Optimisation and applications of chemical exchange saturation transfer MRI techniques for cancer imaging on clinical scanners

Vincent Evans
UCL Centre for Medical Imaging
Division of Medicine

Thesis submitted for the degree of
Doctor of Philosophy (Ph.D)

University College London
2020

I, Vincent Evans, confirm that the work presented in this thesis is my own. Where information has been derived from other sources, I confirm that this has been indicated in the thesis.

Abstract

Chemical Exchange Saturation Transfer (CEST) is receiving growing attention in the field of cancer imaging due to its ability to provide molecular information with good spatial resolution within clinically acceptable scan-times.

Translation to the clinic requires a solid evidence-base demonstrating the clinical utility and a range of anatomical regions and pathologies have already been studied. These have traditionally been evaluated in terms of asymmetry-based metrics, the most common of which is the magnetization transfer ratio. However, alternative and potentially more informative metrics are also possible.

Investigation of fitting metrics has not been reported at clinical field strengths and there is currently no standard approach for optimising the acquisition and post-processing protocols. The work described in this thesis focuses on the practical development and implementation of z-spectrum fitting methods *in vivo* at 3.0T.

After the technical and clinical introductory chapters, chapter three describes the evaluation and comparison of the use of two different lineshapes for modelling the water direct saturation effect.

Chapter four describes the optimization of an acquisition and post-processing protocol suitable for CEST imaging of the human prostate at 3.0T. The repeatability of the method is evaluated and in chapter five the optimized protocol is applied in two cancer patients.

In chapter six a method is proposed for identification of CEST and NOE resonances in z-spectra acquired at low-field strengths.

Chapter seven describes a pre-clinical study of healthy rat brains at 9.4T highlighting the need to consider the interplay between CEST and perfusion effects.

In chapter eight the effects of gadolinium administration on CEST signal and contrast in glioma patients is investigated.

I hope that the work described herein and the contributions stemming from it will be of some practical benefit to scientists and clinicians interested in exploring the future potential of the growing field of CEST imaging.

Impact Statement

MRI plays a central role in cancer imaging and well-established imaging methods with T1-weighted, T2-weighted and diffusion-weighted contrast mechanisms are carried out routinely around the world due to their proven ability to provide clinically useful information.

However, the MRI field is relatively young and there are still many potential imaging techniques to be explored. The focus of this thesis is to explore the practical aspects of implementing chemical exchange saturation transfer (CEST) MRI which can provide chemically-derived information to clinicians which may aid in tumour diagnosis, prognosis and monitoring of response to treatment. Endogenous CEST is entirely non-invasive. Therefore if it is proven to be a valuable complementary cancer imaging technique it may help to improve patient management and outcomes and save money for healthcare providers such as the NHS with minimal cost or risk to the patient.

For CEST researchers, the work discussed in this thesis may prove useful in guiding the design of imaging protocols and post-processing analysis as it explores many of the challenges that are faced during the optimization of acquisition and post-processing protocols suitable for z-spectrum fitting.

Part of the work described includes analysis of contrast generated by z-spectrum fitting in both prostate cancer and glioma in humans. These are the first known descriptions of z-spectrum fitting on clinical data and will therefore be of interest to researchers aiming to study either of these pathologies using CEST at 3.0T.

The steps outlined to optimize fitting algorithms may also be of interest to MRI software developers who wish to build on the ideas outlined here to automate the post-processing of CEST data at the scanner console. Implementation of an automated fitting algorithm for CEST z-spectra acquired at clinical field strengths would provide an advantage over competitors in the CEST space.

The work described in this thesis has been presented at UCL, national and international conferences and has stimulated many productive conversations with people from the research and medical communities.

Table of Contents

ABSTRACT 5

IMPACT STATEMENT 7

LIST OF FIGURES 15

LIST OF TABLES 25

ACKNOWLEDGEMENTS 27

1 TECHNICAL INTRODUCTION 29

1.1 NMR THEORY ESSENTIALS 29

1.1.1 Thermal equilibrium 29

1.1.2 Equation of motion 29

1.1.3 Relaxation 30

1.1.4 Bloch equations 31

1.1.5 Bloch equations in the rotating frame 31

1.2 CHEMICAL EXCHANGE SATURATION TRANSFER APPLICATIONS 32

1.3 CHEMICAL EXCHANGE SATURATION TRANSFER THEORY 33

1.3.1 What can CEST tell us? 34

1.3.2 Chemical Shift 34

1.3.3 Chemical Exchange and Exchange Rates 36

1.3.4 Exchange Rate pH-dependency 38

1.3.5 Quantification of exchange rates 39

1.3.6 Z-spectrum contributors 39

1.3.7 Saturation 41

1.3.8 Saturation Transfer and the Bloch-McConnell equations 43

1.3.9 The z-spectrum 44

1.3.10 Post-processing 45

1.4 CHALLENGES AND CONSIDERATIONS 48

1.4.1 B_0 field inhomogeneities 48

1.4.2 B_1 inhomogeneities 51

1.4.3 Z-spectrum sampling and signal-to-noise 52

1.4.4 Post-processing pipeline 52

2 CLINICAL INTRODUCTION 55

2.1 PHYSIOLOGICAL BASIS OF CEST SIGNAL IN CANCER 56

2.1.1 *Endogenous CEST contrast* 56
2.1.2 *Dynamic CEST contrast* 56
2.2 ALTERED METABOLIC PATHWAYS IN CANCER 57
2.2.1 *The Warburg Effect* 58
2.3 CEST APPLICATIONS IN CANCER 59
2.3.1 *Gleason Grading of Prostatic Carcinoma* 59
2.3.2 *Prostate cancer imaging* 61
2.3.3 *Glioma imaging* 63
2.4 CLINICAL FOCUS OF THIS THESIS 64

3 FITTING THE WATER PEAK: LORENTZIAN VS BLOCH 65
3.1 INTRODUCTION 66
3.1.1 *Physical basis of oscillatory effects in the z-spectrum close to 0ppm* 66
3.2 METHODS 69
3.2.1 *Phantom Preparation* 69
3.2.2 *MRI Imaging Protocol* 71
3.2.3 *Post-processing* 71
3.3 RESULTS 73
3.3.1 *Fitted peak heights* 75
3.3.2 *Goodness-of-fit comparisons* 77
3.4 DISCUSSION 79
3.4.1 *Fitted peak heights* 79
3.4.2 *RMSD assessment* 80
3.4.3 *Computation time* 80
3.4.4 *Reflections on the Bloch approach* 81
3.4.5 *Use of nicotinamide* 81
3.4.6 *Future direction* 82
3.5 CONCLUSIONS 82

4 OPTIMIZATION AND REPEATABILITY OF CEST-MRI IN THE PROSTATE 83
4.1 INTRODUCTION 84
4.1.1 *Prostate anatomy and function* 85
4.2 MATERIALS AND METHODS 86
4.2.1 *Ethics* 86
4.2.2 *Subjects* 86
4.2.3 *MRI Protocol* 87

4.2.4 Offset sampling frequencies ... *87*
4.2.5 WASABI ... *88*
4.2.6 Data Analysis ... *88*
4.2.7 Saturation scheme and TR optimisation ... *89*
4.2.8 Region of interest analysis ... *90*
4.2.9 Repeatability in healthy volunteers ... *90*
4.3 RESULTS ... 91
4.3.1 MRI Sequence Optimisation ... *91*
4.3.2 Repeatability in Healthy Volunteers ... *93*
4.4 DISCUSSION ... 96
4.5 CONCLUSIONS ... 100
4.6 CHAPTER SUPPLEMENTARY FIGURES ... 101
5 INITIAL EVALUATION OF CEST CONTRAST IN PROSTATE CANCER ... 103
5.1 PROSTATE CANCER OVERVIEW ... 103
5.1.1 Prostate Imaging – Reporting and Data System (PI-RADS v2) ... *104*
5.1.2 Clinical Treatment Pipeline ... *105*
5.1.3 Motivation for measuring prostate cancer CEST contrast ... *105*
5.2 METHODS ... 105
5.2.1 Ethics and recruitment ... *105*
5.2.2 Recruitment pipeline ... *106*
5.2.3 Comments on recruitment ... *107*
5.2.4 MRI Protocol ... *108*
5.2.5 Regions-of-interest (ROIs) ... *108*
5.2.6 Data Analysis ... *109*
5.3 RESULTS ... 109
5.4 DISCUSSION ... 113
5.5 SUPPLEMENTARY FIGURES ... 115
6 PEAK-FINDER: A STATISTICAL APPROACH TO CEST-PEAK IDENTIFICATION ... 117
6.1 INTRODUCTION ... 117
6.2 METHODS ... 118
6.2.1 Over-fitting approach ... *118*
6.2.2 Histogram analysis ... *119*
6.2.3 Sum-of-amplitudes analysis ... *119*

6.2.4 Simulated z-spectra *120*
6.2.5 Phantoms *120*
6.2.6 MRI protocol at 9.4T *121*
6.2.7 MRI protocol at 3.0T *121*
6.2.8 Data analysis *121*
6.3 RESULTS 121
6.3.1 Simulations *121*
6.3.2 Phantom results at 9.4T *128*
6.3.3 Phantom data at 3.0T *134*
6.4 DISCUSSION 137
7 CARBOGEN CHALLENGE IN RATS AT 9.4T 141
7.1 INTRODUCTION 142
7.1.1 GlucoCEST *142*
7.1.2 Arterial Spin Labelling (ASL) *143*
7.1.3 ^{31}P spectroscopy *143*
7.2 MATERIALS AND METHODS 143
7.2.1 Animal model and ethics *143*
7.2.2 MRI Protocol *144*
7.2.3 Data Analysis *145*
7.3 RESULTS 145
7.3.1 MTR_{asym}, CBF, T2 and ^{31}P when breathing different gases *146*
7.3.2 Tuning the Fitting Algorithm *147*
7.3.3 Changes in the fitted peak heights *154*
7.4 DISCUSSION 159
7.4.1 Sources of altered CEST signals when breathing carbogen *161*
7.5 CONCLUSIONS 163
8 THE EFFECT OF GADOLINIUM CONTRAST ON THE CEST SIGNAL IN GLIOMA PATIENTS 165
8.1 INTRODUCTION 166
8.2 MATERIALS AND METHODS 166
8.2.1 Study participants and ethics *166*
8.2.2 MRI protocol *167*
8.2.3 Fitting algorithm optimisation *167*
8.2.4 Analysis and post-processing *168*

8.3 RESULTS 169
8.3.1 MT offset frequency *169*
8.3.2 Tuning of the fitting-algorithm using a sum-of-amplitudes approach *170*
8.3.3 Repeatability in healthy volunteers *172*
8.3.4 Absolute peak heights pre- and post-Gd *174*
8.3.5 Tumour contrast pre- and post-Gd *177*
8.4 DISCUSSION 184
8.4.1 Peak-assignment *184*
8.4.2 Absolute signal changes *184*
8.4.3 Contrast changes *185*
8.4.4 Recommendations *186*
9 SUMMARY AND FUTURE DIRECTIONS 187
9.1 THESIS SUMMARY 187
9.2 FUTURE DIRECTIONS 188
10 REFERENCES 191
11 APPENDIX A – SEQUENCE OPTIMIZATION IN THE PROSTATE AT 3.0T .. 203
11.1.1 Readout *203*
11.1.2 Saturation Scheme *203*
12 APPENDIX B – ISMRM 2018 (PARIS) INTERACTIVE E-POSTER 206
13 APPENDIX C – ESMRMB 2017 (BARCELONA) E-POSTER 209
14 APPENDIX D – BC-ISMRM 2016 (LEEDS) TRADITIONAL POSTER 210
15 CONTRIBUTIONS FROM THIS WORK AND FUNDING 211

List of Figures

Figure 1-1: Precession of a nuclear spin around the externally applied B0-field. Figure reproduced from Figure 2.8 in [1]. 30

Figure 1-2: Showing (a) the nutation of the magnetisation into the xy-plane in the laboratory frame, and (b) the same nutation from the perspective of a frame rotating at the Larmor frequency. Figure reproduced from 1.2.1 in [2] 32

Figure 1-3: Schematic illustration of exchange between two pools. Each pool has its own set of properties, including the equilibrium net magnetisation, T1 and T2. The two-way exchange is governed by two different pool-specific exchange rates. 36

Figure 1-4: Exchange rates of the side chain hydroxyl proton of avcetyl-threonine-OCH_3 in aqueous solution. The proton exchange rate constants are plotted versus the pH for data measured at 4℃ (circles), 10℃ (squares), 20℃ (diamonds), 30℃ (triangles), and 36℃ (stars). The pH was corrected for the temperature dependence of the dissociation constant of water. The fitted curves assume exchange catalysis by H^+ and OH^- only. Figure reproduced from [30]. 38

Figure 1-5: An illustration of the layers of binding that water molecules may experience in the presence of a large macromolecule. The boundaries between the bound, intermediate and free water layers are continuous and this gives rise to a significant spread in the chemical shifts of the hydrogen protons across the whole sample. The T2 values are also very short closer to the bound layer, where interactions between neighbours accelerate the de-phasing process. Figure reproduced from [42]. 40

Figure 1-6: Schematic diagrams illustrating CW saturation and pulsed (or 'multi-step') saturation. Figure reproduced from [45]. 42

Figure 1-7: Z-spectra acquired in the healthy rat brain at 9.4T at 0.5μT (red), 1.0μT (blue) and 1.5μT (green). Amide, amine and NOE resonances are marked at 3.5ppm, 1.9ppm and -3.5ppm respectively. Black lines represent Lorentzians fitted to the data to account for the direct water saturation. Figure reproduced from from [47]. 45

Figure 1-8: Simulated z-spectrum (blue) for a two-pool system (water at 0.0ppm and amide at 3.5ppm). The red line is the MTR_{asym} which represents the contribution to the z-spectrum from the exchanging amide pool. In this case the non-zero MTR_{asym} is purely due to the amide contribution. When multiple pools are present their overlapping contributions to the measured z-spectrum mean that there are several contributions to the final MTR_{asym} value. 46

Figure 1-9: A fitted z-spectrum showing the contributions from water direct-saturation (cyan), amide (blue), amine (brown), NOE (green) and MT (red) effects. The black dashed line represents the vertical offset which accounts for imperfect normalization. Figure reproduced from [55]. 47

Figure 1-10: Gd-enhanced T1-weighted image of a glioblastoma at 7T along with pixel-wise generated amplitude maps of the MT, NOE, amide and amine pools. Figure reproduced from [55]. 48

Figure 1-11: MR images of a patient with WHO grade III oligodendroglioma. **A** shows the T2w image with the tumour core highlighted with the red arrow. **B** shows the water centre-frequency offset in Hz (arising due to B0 inhomogeneities). Clear inhomogeneities are seen near air-tissue interfaces (sinus, ear). **C** shows the uncorrected asymmetry map at 3.5 ppm (APTw) where large artefacts are visible (white stars) due to the B0-inhomogeneities. **D** shows the same map after B0 correction using a basic method of shifting the z-spectrum so that the point of lowest intensity is at 0 ppm. Even using this basic correction technique, the results are significantly improved. Figure reproduced from [19]. 49

Figure 1-12: Precession of the magnetisation around the effective field. The rotation angle $\phi = \omega\text{eff}.\tau\text{p}$ depends on the pulse duration τ_p, the amplitude of the B_1 excitation field, and the frequency offset $\Delta\omega$. Figure reproduced from [57]. 50

Figure 1-13: A simulated WASABI z-spectrum (solid blue line) at B_0 = 3.0T generated by saturation by means of a single rectangular pulse with duration τ_p = 5ms and amplitude B_1 = 3.7μT. The maxima occur when the phase (dashed green line) is a multiple of 2π. In this case the magnetization is rotated back in its initial orientation parallel to B_0. Information about the water-frequency shift $\delta\omega$ and the RF amplitude B_1 is encoded in the shift of the symmetry axis and the periodicity of the function $Z(\Delta\omega)$, respectively. Figure reproduced from [57]. 51

Figure 1-14: Schematic flow-diagram showing the key steps taken in the acquisition and post-processing of CEST data throughout the work outlined in this thesis. 53

Figure 2-1: The number of articles on PubMed containing either “chemical exchange saturation transfer” or “amide proton transfer” in the title or abstract, aggregated by year. The first occurrences are in 2002 and 2003 respectively, growing to 120 and 39 in 2018. 55

Figure 2-2: A schematic illustration highlighting the differences between oxidative phosphorylation, anaerobic glycolysis, and aerobic glycolysis, also known as the Warburg effect. Figure reproduced from [66]. 59

Figure 2-3: The current most recent consensus-meeting-driven Illustration of five categories of cell patterns that may be found in tissue from prostate biopsy and their numerical score within the Gleason grading system. At higher scores the cells are less well-differentiated, with more stroma between glands, and the masses become more neoplastic and irregular with only occasional gland formation. Typically, more than one pattern will be present in a given sample. Figure reproduced from [70]. 60

Figure 2-4: Histology images for a range of Gleason scores showing the classical Gleason scores and the recently proposed Grade Groups. Figure reproduced from [71]. 61

Figure 2-5: Results from Jia et al who measured differences in APTR between prostate cancer and benign peripheral zone tissue in twelve patients. Figure reproduced from [82]. 62

Figure 2-6: Results from Takayama et al, who found that APT signal was significantly raised in Gleason 7 lesions compared to regions of benign prostate hyperplasia (BPH), and Gleason 6 and 9 lesions. Data acquired from 66 patients. Figure reproduced from [24]. 62

Figure 3-1: Calculated values of the post-B1 M_z after the application of a single, rectangular B1-pulse of power 2.0μT and duration $\tau p = 40\text{ms}$ at 3.0T. The oscillatory nature of 'M_z post-B_1' illustrates how moving from CW to pulsed-saturation introduces additional complexity to the z-spectrum. 69

Figure 3-2: T2-weighted image labelled to show the configuration of the phantom. 70

Figure 3-3: Four weighting schemes used to fit nicotinamide phantom data. 73

Figure 3-4: Z-spectra (solid-lines) and MTR_{asym} (dashed-lines) from 200mM nicotinamide solution at pH 8, scanned at four different saturation powers (see legend). 74

Figure 3-5: Maps of MTR_{asym} at 2.75ppm. Concordant with the representative z-spectra shown in Figure 3-4, the asymmetry increases with saturation power and also with pH for these samples. The water tube shows no visibly discernible asymmetry. 74

Figure 3-6: A representative z-spectrum (pH8 at maximum saturation $B1_{eq}$ = 1.47μT) with fit results for (**A)** a Lorentzian for the water peak with all data-points equally weighted, (**B)** a Lorentzian for the water peak with data-points in the±1ppm range weighted to zero, (**C)** a Bloch simulation for the water peak with all data-points equally weighted, and (**D)** a Bloch simulation for the water peak with all data- points in the±1ppm range weighted to zero. 75

Figure 3-7: Fitted peak heights for the **(A)** amide and **(B)** NOE peaks when fitting the water peak with either a Lorentzian lineshape or a lineshape generated through Bloch simulations. Both the amide and NOE peak heights increase at increasing pH with the amide height in particular showing a strong agreement between all fitting approaches. 76

Figure 3-8: Representative RMSD values for each weighting scheme from the 1.14μT dataset. Results for the Lorentzian fits and Bloch fits are shown in the top and middle panels, respectively. The lower panel shows the difference between the RMSDs of the Lorentzian and Bloch results. Positive values of $RMSD_{diff}$ correspond to the Lorentzian fit outperforming the Bloch fit for a given z-spectrum (i.e. yielded a lower RMSD value) and conversely negative values of $RMSD_{diff}$ mean that the Bloch fit outperformed the Lorentzian fit. 77

Figure 3-9: Boxplots of all $RMSD_{diff}$ values for each weighting method, aggregated over all four pH-values and four saturation powers. Significance was tested between data-points from all weighting schemes using a Mann-Whitney U-test. The null hypothesis is that the two sets of data to be tested are drawn from a continuous distribution with equal medians. Significance threshold was 0.05 and is indicated in the figure with an asterisk. The null hypothesis was rejected in tests comparing the data from weighting scheme 1 with schemes 2, 3 and 4. 78

Figure 4-1: Illustration of the primary features of the male reproductive tract showing the position of the prostate gland relative to the bladder, seminal vesicles, urethra and rectum. Image reproduced from [101]. 85

Figure 4-2: Schematic diagram highlighting the key zones of the prostate. Figure reproduced from [103]. 86

Figure 4-3: Z-spectra from large ROIs drawn over the whole prostate when using saturation trains with N = 20, 30, 40, 50 and 60 Gaussian pulses. The error bars show the standard deviation of the signal across all voxels within each ROI. The z-spectrum approaches saturation steady-state with increasing N. 91

Figure 4-4: Histogram showing the distribution of offset frequencies of the fitted MT super-Lorentzian across prostate voxels taken from 5 healthy volunteers when fitting only data-points outside of the +/-15ppm range. 92

Figure 4-5: A plot of the mean heights of the fitted amide, NOE and MT peaks over all voxels of a whole prostate for a range of saturation flip-angles. Error-bars show the standard deviation over all voxels. The amide and NOE signals were both maximised using a flip-angle of 1133°. 93

Figure 4-6: Representative normalized z-spectra, fit results and fit residuals from ROIs drawn in the PZ, TZ and muscle in a single healthy volunteer, showing only the ±7ppm range. The 4-pool fit results include contributions from water, amide, NOE and MT. The MTR_{asym} has been scaled x5 for improved visibility. The residual differences between the raw data and the fits are all less than 0.028. 94

Figure 4-7: Bland-Altman plots showing the inter-session repeatability of the heights of the fitted (A) amide, (B) NOE and (C) MT peaks and (D) the MTR_{asym} measurements, using ROI's drawn by reader 1. Plots include the 95% limits of agreement (LOA) expressed in absolute terms and as a percentage, the bias, and the coefficient of variation (CV). 95

Figure 4-8: Representative maps and histograms of the fitted horizontal and vertical offset terms. It can be seen that the horizontal offset varies smoothly across the image. The vertical offset does not vary smoothly but as it is intended to account for noise in the reference image this is expected. The values are both fairly tightly constrained to close to zero. 101

Figure 5-1: The recruitment pipeline for this study including the numbers of candidates that reached each stage. 107

Figure 5-2: Voxel-wise maps of the heights of the fitted amide, NOE and MT peaks, and the MTR_{asym} measurements for (A-F) patient 1 with a transition zone (TZ) tumor and (G-L) patient 2 with a peripheral zone (PZ) tumor. The tumor and apparently-uninvolved-tissue (AUT) regions of interest are highlighted in red and blue respectively and the tumors are highlighted with a red arrow on the T2w images. Visually, slight hypo-intensities are observed in the amide and NOE signal in the region of TZ tumor with corresponding hyper-intensity in the MT signal and no significant change in the MTR_{asym}. Conversely, hyper-intensities in the amide and NOE signals and hypo-intensities in both the MT and MTR_{asym} signals are observed in the region of PZ tumor. It should be noted that the regions of signal change associated with the tumor ROIs are not localized only to the region of tumor and appear to be part of broader structural features in these two cases. 110

Figure 5-3: Boxplots showing the fitted amide, NOE and MT peak heights and MTR_{asym} measurements from all voxels within tumor and AUT ROIs drawn by reader 1 for **(A)** both scans of patient 1 with a TZ tumor, **(B)** both scans of patient 2 with a PZ tumor. The red line indicates the median value of all voxels within the ROI, with the bottom and top edges of the blue box indicating the 25th and 75th percentiles, respectively. The whiskers extend to the most extreme data points not considered outliers. Data points that were more than 1.5x the interquartile range away from the top or bottom of the box were classed as outliers and are plotted individually using red crosses. Significant signal differences between tumor and AUT within a given scan (as calculated using the Mann-Whitney U test) are denoted using single, double or triple asterisks representing $p<0.05$, $p<0.01$ and $p<0.001$ respectively.. 111

Figure 5-4: Scatter-plots of the MT-amplitude vs the signal from the T2-weighted image for voxels across two scans of two prostate cancer patients. No inverse relationship is obvious, suggesting that there is no clear interplay between the MT-signal and the T2 of water..... 115

Figure 6-1: Simulated z-spectra for a three-pool system at two field strengths with added Gaussian-distributed noise (σ = 0.01). 122

Figure 6-2: Simulated z-spectra from 9.4T and 3.0T fitted using 33 Lorentzian lineshapes (SNR=100). 122

Figure 6-3: Histograms showing the distribution of fitted parameters across (A) 500 simulated z-spectra at 9.4T and (B) 500 simulated z-spectra at 3.0T, both with added noise and B_0 inhomogeneities of up to 0.1ppm. The top left histograms showing the distributions of the chemical shifts are of primary interest with the FWHM, vertical and horizontal offsets included for completeness. Maxima are observed in the chemical shift distributions close to 2.8ppm and 3.5ppm where the simulated CEST pools are located. As expected, the FWHM values are smaller at 9.4T.. 123

Figure 6-4: Scatterplots showing the relationship between the amplitude of fitted lineshapes and the chemical shift at which they are centred. For simluations at both (A) 9.4T and (B) 3.0T, fitted lineshapes were distributed across the whole chemical shift range.

For the 9.4T data, ignoring the ±1ppm range and the upper and lower-bounds of ±4.75ppm the highest amplitudes are seen at 2.8ppm and 3.5 ppm corresponding to the two amide groups. At 3.0T, a broader feature is observed consistent with an underlying maximum at 3.5ppm, albeit less pronounced than at 9.4T. It is unlikely that the maximum at 2.8ppm could be identified with confidence from this 3.0T dataset. 125

Figure 6-5: Sum-of-amplitudes plots for data from (A) 9.4T and (B) 3.0T. The two amide resonances are clearly visible in both cases. Of note, the maxima previously visible on the NOE-side of the z-spectrum are far-reduced in the 3.0T case. 126

Figure 6-6: Boxplots showing the distributions of the fitted chemical shift values for the cis and trans isomers in simulated data at two field strengths when fitted using a 3-pool model. 127

Figure 6-7: Representative z-spectra from 100mM nicotinamide solution at pH7.8, scanned at both 3.0T and 9.4T with respective $B1_{cwpe}$ values of 0.97μT and 1.17μT respectively.. 129

Figure 6-8: A fitted z-spectrum from the pH7.8 compartment with saturation flip-angle of 3000°. The sum of the Lorentzian lineshapes generated a good fit of the z-spectrum. Water-supporting peaks in the ±1ppm range are attributed to the oscillatory effects described in chapter 3. 130

Figure 6-9: Histograms showing the distributions of fit parameters of 4,131 voxels across multiple compartments of a Nicotinamide and water phantom scanned at 9.4T. 131

Figure 6-10: A plot of the sum of amplitudes of all peaks fitted within each 0.01ppm range across all fits. Maxima corresponding to the cis and trans amide resonances are marked in red and the ‘water-supporting’ peaks are highlighted in blue. Results from outside the ±5.8ppm range are judged to be strongly affected by fitting artefacts and are excluded. . 132

Figure 6-11: A z-spectrum acquired at 9.4T, fitted using a 3-pool fitting model with offset frequencies determined using the sum-of-amplitudes method. 133

Figure 6-12: A map of the height of the trans-isomer amide peak in different compartments of the phantom scanned at 9.4T. 133

Figure 6-13: Histograms showing the distributions of fit parameters from the pH7.8 compartment of a Nicotinamide and water phantom scanned at 3.0T. 134

Figure 6-14: Sum-of-amplitudes analysis for the pH 7.0 compartment scanned at 3.0T showing clear resonances close to 3.38ppm and 2.55ppm. Maxima corresponding to the cis and trans amide resonances are marked in red and the ‘water-supporting’ peaks are highlighted in blue. 135

Figure 6-15: A fitted z-spectrum acquired from 100mM nicotinamide solution scanned at 3.0T. pH7.8, $B1_{CWPE}$ = 0.97μT. Fit parameters were tuned using sum-of-amplitudes analysis. 136

Figure 6-16: Map of the trans-isomer amide signal across multiple compartments at 3.0T. It is suspected that the stripe artefacts in the image are due to interactions between the B_0 and B_1 field inhomogeneities as they appear broadly concentric and consistent with typical field homogeneity maps. They are not attributed to Gibbs ringing as the pattern does not resemble the shape of each sub-compartment where there are boundaries between plastic and water. 136

Figure 6-17: Chemical shift assignments for the cis- and trans-isomers of nicotinamide over a range of pH values and saturation powers as assigned by a sum-of-amplitudes analysis. Results from 9.4T show the tightest agreement at different pH and saturation powers with no substantial pH-drift observed. Results from 3.0T show increased variation compared to the 9.4T data and this is particularly evident for the cis-isomer. 137

Figure 7-1: A schematic illustration of calculation of the glucoCEST enhancement (GCE) following administration of exogenous glucose. Subtraction of the post-administration MTR_{asym} from the pre-administration MTR_{asym} yields the GCE. Figure reproduced from [135]. 142

Figure 7-2: Representative z-spectra **(A)** and MTR_{asym} **(B)** from four gas phases (Oxygen – Carbogen x2). The MTR_{asym} spectra show similar behaviors for both repetitions of the gas cycle. The solid lines show the mean MTR_{asym} from within regions of interest, with dashed lines indicating the standard deviation. Figure created by FT and MR and reproduced from [135]. 146

Figure 7-3: Changes in the median MTR_{asym}, CBF and T2 measurements as a function of the gas input for ROIs drawn in the cortex and hippocampus. A clear dependency is observed in the MTR_{asym} and CBF measurements but no trend is obvious in T2. Figure created by FT and MR and reproduced from [135]. 146

Figure 7-4: Changes in the MTR_{asym} (A) in the cortex and hippocampus with intravenous administration of a 2DG bolus, and (B) in the cortex with intravenous administration of a 2DG bolus alongside the changes seen when alternately breathing oxygen and carbogen. The magnitude of changes caused by changing the gas being breathed are larger than those of a 2DG bolus suggesting that the CEST effect is influenced by perfusion. Figure created by FT and MR and reproduced from [135]. 147

Figure 7-5: Fitted z-spectra (**A**) where the fitted value of the NOE 2 FWHM was found to be 11.33ppm, and (**B**) where it was found to be 1.77ppm. It can be seen that while the peaks fitted on the aliphatic side of the z-spectrum in (**B**) look more physically realistic, the amine peak has also grown in size and width raising questions about whether we have got things right on the CEST side of water. 149

Figure 7-6: Scatter plots of the amplitude of all fitted peaks vs the FWHM of the NOE 2 pool. The amine and NOE 1 pools show a strong negative correlation between amplitude and the NOE 2 FWHM. A similar trend is observed in the MT amplitude. This suggests that the high values of NOE 2 FWHM are a fitting artefact whereby a broad, high amplitude NOE 2 peak is being fitted preferentially to a narrow, low amplitude peak (which is more physically realistic) and as a result the heights of the other adjacent fitted peaks in particular (ie the NOE 1 and amine peaks) are reduced. The negative impact of this artefact could be limited by restricting the FWHM range of the NOE 2 pool to a more physically realistic range. 150

Figure 7-7: Histogram of the offsets frequencies of 29 fitted peaks (excluding water) over many voxels. It can be seen that this analysis suggests the presence of 3 CEST pools and 2 NOE peaks. MT excluded for full visibility of the NOE2 peak. 151

Figure 7-8: Sum-of-amplitudes analysis offset over many voxels (excluding water). It can be seen that this analysis suggests the presence of 3 CEST pools and 2 NOE peaks. MT is shown in green to distinguish between MT and NOE2 which have similar offsets. 152

Figure 7-9: A representative fitted z-spectrum taken from a single-voxel in the rat hippocampus along with the fit residuals which are all less than 0.01. Due to the high saturation power, the MT effect is dominant. 154

Figure 7-10: Representative maps of the heights of Lorentzian lineshapes fitted to data acquired during oxygen inhalation. Cortex (top) and hippocampus (bottom) ROIs for cortex and hippocampus are overlaid in light and dark orange over the reference image respectively. 155

Figure 7-11: Representative maps of the FWHM of Lorentzian lineshapes fitted to data acquired during oxygen inhalation. Cortex (top) and hippocampus (bottom) ROIs for cortex and hippocampus are overlaid in light and dark orange over the reference image respectively. 156

Figure 7-12: Distribution of the amplitudes and widths of Lorentzian lineshapes fitted to z-spectra acquired in the rat brain cortex at 9.4T. Signal changes correlating with the breathing of each gas are observed in the amide and amine amplitudes and FWHM, the NOE1 amplitude and in the hydroxyl FWHM. 157

Figure 7-13: Distribution of the amplitudes and widths of Lorentzian lineshapes fitted to z-spectra acquired in the rat brain hippocampus at 9.4T. The NOE1 amplitude is the only parameter that is observed to correlate with the breathing of each gas. 158

Figure 7-14: Relative and absolute concentrations of amine and hydroxyl-containing metabolites when breathing different concentrations of CO_2. This study used 5% CO_2 which the data in this figure suggest would cause a reduction in the amine concentration and an increase in the hydroxyl concentration. Figure generated using data from [152]. 163

Figure 8-1: Boxplots and a histogram showing the fitted MT offset frequencies from whole brain data of a single healthy volunteer. The median offset frequency of -1.63ppm was found to be stable both when including and excluding fit results at the boundary conditions (outside the ±9.99ppm range). It was therefore selected as the offset frequency of the MT pool for subsequent fitting in this chapter. 169

Figure 8-2: Distribution of the fitted MT height and FWHM parameters from a single volunteer. 170

Figure 8-3: Sum-of-amplitudes for a whole-brain fit using 23-Lorentzian lineshapes for each z-spectrum. Maxima are observed close to 3.5ppm, 1.5ppm, -1.5ppm which would be ascribed to amide, hydroxyl and NOE2 effects, but there is not sufficient resolution to select offset frequencies for further fitting with confidence based on these results. No clear contributions from the amine and NOE1 effects are observed. 171

Figure 8-4: Fitted peak heights derived from repeated measurements in four healthy volunteers. Results are shown for all seven pools in both grey and white-matter and are normalised to the mean of the two sets of measurements. Good agreement is observed on visual inspection. 173

Figure 8-5: Normalised z-spectra taken from a single voxel in a Gd-enhancing region both pre- and post-administration of Gd. The post-Gd z-spectrum appears less saturated than the pre-Gd z-spectrum which is consistent with a reduction in T1. 174

Figure 8-6: The median absolute fitted peak heights, pre- and post-Gd administration, in five anatomical regions of interest over all five patients. The purple line with heavier weighting indicates the median of the heights aggregated over all patients. Post-Gd signal changes are larger in tumour and Gd-enhancing regions than in apparently uninvolved regions of grey and white-matter. 175

Figure 8-7: Boxplots showing the distribution of fitted peak heights from all voxels in Gd-enhancing regions from all seven patients. Normality was checked using the Kolmogorov-Smirnov test and significance was calculated using a two-sample t-test. 176

Figure 8-8: Masks for the tumour-related ROIs, and grey and white-matter ROIs for slice 5 of volunteer 6. These are provided for reference to help with interpretation of the subsequent CEST maps. 178

Figure 8-9: CEST signal maps showing the amplitude and FWHM of the fitted lineshapes in volunteer 5 both pre-and post-Gd for **A** water, **B** amide, **C** amine, **D** hydroxyl, **E** NOE1, **F** NOE2 and **G** MT. The core of the tumour is most clearly identifiable in the post-Gd cases in the amplitude of the amide, NOE1, NOE2 and MT pools, and in the FWHM of the amide, amine, NOE1, NOE2 and MT pools. The FWHM of the NOE2 pool also shows some distinction between the tumour core and periphery. 182

Figure 8-10: Signal differences between regions of tumour and grey- and white-matter for all patients, pre- and post-Gd. In all cases apart from GM-tumour amine contrast, WM-tumour hydroxyl contrast and GM-tumour MT contrast, the administration of Gd increases the absolute signal differences between GM or WM, and tumour. 183

Figure 11-1: measured signal from repeated measurements for a range of TR values. .. 204

Figure 11-2: Repeated unsaturated acquisitions showing that longer TR's yield higher absolute signal. 204

List of Tables

Table 1-1: Approximate CEST exchange properties for amide, amine and hydroxyl groups. Figure reproduced from [28]. 35

Table 3-1: Description of nicotinamide phantom compartments 70

Table 3-2: Fitting parameters used when fitting z-spectra acquired in the Nicotinamide phantom. 72

Table 3-3: Mean and median root-mean-square deviation (RMSD) differences between Lorentzian and Bloch approaches to fitting the water peak for four different weighting schemes. Other parameters include minima and maxima, 25th and 75th percentiles, and the percentage of the 16 data-points for each weighting scheme which were above zero. 79

Table 4-1: Starting values and upper and lower bounds for all parameters used by the z-spectrum fitting algorithm. 93

Table 4-2: The coefficients of variation (CV), 95% limits of agreement (LOA) and bias of the intra-session and inter-session Bland-Altman plots generated for the amide, nuclear Overhauser effect (NOE), magnetization transfer (MT) and asymmetric magnetization transfer ratio (MTR_{asym}) signals in 5 healthy volunteers. Results are shown for analysis done using regions of interest drawn by two separate readers. The intra-class correlation (ICC) coefficients are also provided. 96

Table 5-1: PI-RADS assessment categories for prostate lesions identified in multi-parametric MRI. 104

Table 5-2: Recruitment criteria for patients being enrolled into the study. 106

Table 5-3: Median amide, NOE, MT and MTR_{asym} signal measurements in TZ AUT and TZ tumor (patient 1) and PZ AUT and PZ tumor (patient 2). Data are shown for both scans of both patients using ROIs drawn by both readers. The signal difference, Δ, is expressed both as an absolute value and also as a percentage of the AUT signal. All associated p-values were calculated using the Mann-Whitney U test and are included. Significant differences in signal between tumor and AUT are highlighted in bold. Differences in repeated signal difference measurements (Δ) between scans and readers are broadly in-line with the LOA values calculated earlier. The most consistent signal differences are found in the MT pool where signal in tumor often varies by over 0.04 thereby exceeding the best-case intra-session LOA for MT. The second scan of patient 2 shows the largest overall signal differences and consistency between readers where both the amide and MT signal changes in PZ tumor are greater than the LOA for these two pools. 112

Table 6-1: Chemical shifts assigned to the cis- and trans-isomers using simulated three-pool z-spectra at two field strengths in the SNR=100 case. The histogram and sum-of-amplitudes both show very close (<0.02ppm) agreement with the ground truth. The three-pool method which was originally expected to improve the fit results appears to give worse results than the histogram and sum-of-amplitudes steps. The closest chemical shift value for each isomer at each field strength is marked in bold and underlined. In the case of the trans-isomer at 9.4T the histogram and sum-of-amplitudes assignments were identical to 2.d.p. 128

Table 7-1: Mean and median offset frequencies of fitted MT-peaks using both Lorentzian and super-Lorentzian lineshapes. 148

Table 7-2: Fitting parameter lower-bounds, upper-bounds and starting-values for the 7-pool model used for fitting z-spectra from rat brain data at high saturation power........ 153

Table 7-3: The effect of 10 and 30% CO2 exposure on brain metabolite concentration after 5 mins. All values are means ± standard error of the mean (S.E.M.) with the number of observations indicated in parentheses. Symbols * and ** indicate statistical significance at the 5% and 1% levels respectively. Figure reproduced and adapted from [152]........ 162

Table 8-1: Lorentzian fitting parameters for data acquired from brain glioma patients at 3.0T........ 172

Table 8-2: The standard deviation of the variation in median fitted peak heights over repeated scans in healthy volunteers expressed as a percentage. 173

Table 8-3: Absolute and percentage-changes in median signal post-Gd administration aggregated over all patient volunteers. Percentage-changes exceeding the maximum standard deviation values previously calculated in healthy volunteers are underlined and highlighted in bold........ 177

Table 15-1: Contributions from this work........ 213

Acknowledgements

I would like to thank my supervisors David Atkinson, Xavier Golay and Shonit Punwani for their continued support over the last four years. David in particular provided expert technical advice and thoughtful guidance on several fronts and with extraordinary patience. His balanced and considered approach has been a great influence on me and is one that I aspire to carry with me beyond the PhD.

I would have been lost on this journey far more often than I was without the guidance and understanding so generously provided by Patxi Torrealdea and Marilena Rega, the comradeship of Aaron Kujawa, and the friendship of all three.

Throughout, the work was underpinned by the dedicated community of people within the UCL Centre for Medical Imaging and thanks are due to Alex Menys for helping to drive things forward in the closing months.

I must also take this opportunity to acknowledge the inestimable support of those not already mentioned, at home, in London and farther afield, who I am fortunate enough to count as friends. Your encouragement took many forms and has been more valuable to me than I may have made clear – thank you.

Finally, I’d like to thank my parents, Steve and Anne, and my sister Charlotte. They have shown incredible patience and unwavering support for me both during and outside of the PhD for which I will forever be grateful.

1 Technical Introduction

The technical aspects of the work outlined in the thesis are primarily focused on the development of practical guidelines for the application of lineshape-based fitting of z-spectra. In order to understand the fundamental concepts underpinning the work and CEST imaging in general it is first of all necessary to provide a brief overview of the fundamentals of MRI theory. These are covered in the first part of this chapter which moves on to discuss the key technical and practical aspects that must be considered during CEST protocol design.

1.1 NMR Theory Essentials

This section outlines some of the key magnetic resonance (MR) concepts that are required in order to fully understand the CEST theory described in section 1.2.

1.1.1 Thermal equilibrium

When a macroscopic system of many spins is placed in an external magnetic field, a net magnetisation, **M**, develops that is parallel to the applied field (convention is to refer to this direction as the *z*-direction). The value of **M** at a given point in space is the vector sum of the individual magnetic moments in the system. At thermal equilibrium this magnetisation vector has its maximum magnitude along the *z*-axis (ie d**M**/dt = 0) and has no transverse component in the *xy*-plane. The magnitude of equilibrium magnetisation is denoted as M_0.

1.1.2 Equation of motion

According the classical vector model, the evolution of **M** within the external magnetic field is described by the following equation of motion:

$$\frac{d\boldsymbol{M}(t)}{dt} = \gamma \boldsymbol{M}(t) \times \boldsymbol{B}(t) \tag{1-1}$$

Where γ is the gyromagnetic ratio of the spin of interest, $\boldsymbol{M}(t)$ is the net magnetisation vector, and $\boldsymbol{B}(t)$ is the magnetic field experienced by the spins. The resulting behaviour is that $\boldsymbol{M}(t)$ rotates (or '*precesses*') around $\boldsymbol{B}(t)$ at a frequency known as the Larmor frequency, ω_0 which is given at any instant by:

$$|\omega_0| = \gamma |B| \tag{1-2}$$

Where B is the magnitude of the magnetic field experienced by the nucleus. Figure 1-1 illustrates the classical vector model of precession where **B₀** is the main static magnetic field through the bore of the scanner.

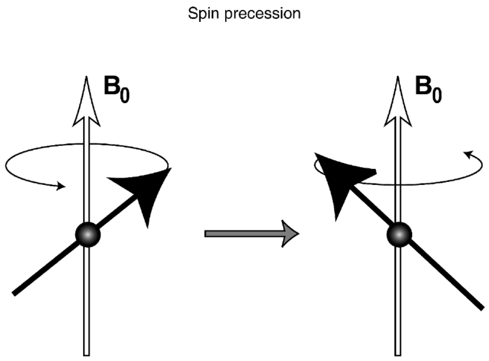

Figure 1-1: *Precession of a nuclear spin around the externally applied B_0-field. Figure reproduced from Figure 2.8 in [1].*

1.1.3 Relaxation

Two relaxation effects occur as the net magnetization vector returns to thermal equilibrium following a perturbation. These are known as spin-lattice and spin-spin relaxation.

Spin-lattice (longitudinal) T_1-relaxation acts to re-grow the *z*-component of M_0 back towards the thermal equilibrium value over time. The effect is described by the relation:

$$M_z(t) = M_0 - [M_0 - M_z(0)]e^{-t/T_1} \tag{1-3}$$

Where $M_z(0)$ is the *z*-component of ***M*** at some initial time-point t = 0 and T_1 is a tissue or material-specific constant that determines the rate of the T_1 recovery. T_1 values are typically on the order of seconds for human tissue at 3.0T.

Spin-spin (transverse) T_2-relaxation (also referred to as T_2-dephasing) arises due to B_0 inhomogeneities and interactions between neighbouring spins that cause them to lose coherence with each other, leading to a reduced net transverse magnetisation. The decay of the transverse component of **M**, $M_\perp$, over time is described by the relation:

$$M_\perp(t) = M_\perp(0)e^{-t/T_2} \tag{1-4}$$

Where $M_\perp(0)$ is the magnitude of the transverse (*x*-*y*) component of the magnetisation at some initial time-point *t* = 0 and T_2 is another system-specific constant that determines the rate of T_2-dephasing. T_2 values are typically on the order of tens of milliseconds in human tissue at 3.0T and the value of T_2 is necessarily lower than the value of T_1 in any given system.

1.1.4 Bloch equations

Adding terms to account for T_1 and T_2 relaxation processes to the equation of motion 1-1 yields an expression referred to as the Bloch equation:

$$\frac{d\boldsymbol{M}(t)}{dt} = \gamma\boldsymbol{M}(t) \times \boldsymbol{B}(t) - \frac{M_{\parallel} - M_0}{T_1} - \frac{M_{\perp}}{T_2} \tag{1-5}$$

As the static $\mathbf{B_0}$ field is conventionally taken to lie along the *z*-axis, equation 1-5 can be separated into its Cartesian components to produce a set of linked Bloch equations that fully describe the evolution of the magnetisation vector, $\boldsymbol{M}(t)$, of an isolated set of spins in the presence of a time-varying magnetic field, $\boldsymbol{B}(t)$ in three orthogonal directions:

$$\frac{dM_x(t)}{dt} = \gamma[M_y(t)B_{\boldsymbol{z}}(t) - M_z(t)B_{\boldsymbol{y}}(t)] - \frac{M_x(t)}{T_2} \tag{1-6}$$

$$\frac{dM_y(t)}{dt} = \gamma[M_z(t)B_{\boldsymbol{x}}(t) - M_x(t)B_{\boldsymbol{z}}(t)] - \frac{M_y(t)}{T_2}$$

$$\frac{dM_z(t)}{dt} = \gamma[M_x(t)B_{\boldsymbol{y}}(t) - M_y(t)B_{\boldsymbol{x}}(t)] - \frac{M_z(t) - M_0}{T_1}$$

1.1.5 Bloch equations in the rotating frame

For the purposes of simplifying calculations, reducing computational load in simulations, and more easily visualising the effects of RF pulses during MRI sequences, it is often helpful to re-imagine the Bloch equations from the perspective of a rotating frame of reference. This frame rotates around the *z*-axis with a frequency ω_{rot}. When the rotation is at the same frequency as the Larmor precession (i.e. $\omega_{rot} = \omega_0$), and is in the same direction, the effects of precession are completely removed from the model. This gives rise to a much simplified, yet equally valid description of the evolution of **M**. Mathematically, the transformation of the laboratory frame Bloch equations (1-6) into the rotating-frame requires the following substitution $B_z(t) \rightarrow B_z(t) - \frac{\omega_{rot}}{\gamma}$. The equations can also be simplified further by removing the time-dependence of B_z as the magnet strength in MRI scanners does not vary (at least in theory) i.e. $B_z(t) \rightarrow B_0$. Applying these two transformations, the Bloch equations in the rotating frame are:

$$\frac{dM'_x(t)}{dt} = M_y(t)\Omega - \gamma M_z(t)B_y(t) - \frac{M_x(t)}{T_2} \tag{1-7}$$

$$\frac{dM'_y(t)}{dt} = -M_x(t)\Omega + \gamma M_z(t)B_x(t) - \frac{M_y(t)}{T_2}$$

$$\frac{dM'_z(t)}{dt} = \gamma[M_x(t)B_y(t) - M_y(t)B_x(t)] - \frac{M_z(t)-M_0}{T_1}$$

Where $\Omega = \omega_0 - \omega_{rot}$.

The usefulness of the rotating frame is illustrated by considering the evolution of the magnetisation as a result of an on-resonance B_1 pulse i.e. B_1 rotates at the same rate as ω_0. In the laboratory frame the direction of B_1 is constantly changing and the trajectory of **M** as it nutates downwards is a spiral as shown in Figure 1-2 (a). In the rotating frame this translates to a constant pulse being applied along the *x*-axis and the apparent complexity of the behaviour of **M** is reduced, as illustrated in Figure 1-2 (b).

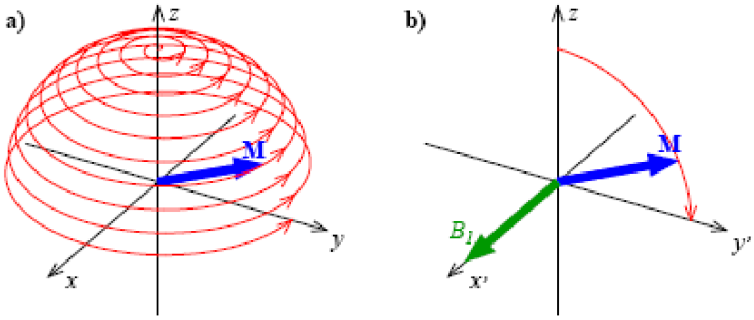

Figure 1-2: *Showing (a) the nutation of the magnetisation into the xy-plane in the laboratory frame, and (b) the same nutation from the perspective of a frame rotating at the Larmor frequency. Figure reproduced from 1.2.1 in [2]*

The nutation frequency of **M** around an on-resonance pulse in the rotating frame may be simply expressed as:

$$|\omega_1| = \gamma|B_1| \tag{1-8}$$

1.2 Chemical Exchange Saturation Transfer Applications

CEST has started to receive increased attention as a novel imaging methodology in recent years. Successful demonstrations of CEST imaging have broadly been focused within three main fields: differentiating cancerous tissue from healthy or necrotic tissue using contrast generated using both endogenous [3][4][5] and exogenous metabolites [6][7]; measuring ischemia/hypoxia in stroke [8], and pH mapping [5]. However, the potential applications are not limited to these fields. Work has also been done demonstrating the potential utility of CEST in measuring cartilage degradation in the human knee and lumbar inverterbral disc through the glycosaminoglycan signal (gagCEST) [9][10], monitoring glycogen levels in human muscle [3][11] and the mouse-liver (glycoCEST) [12] and measuring liposome concentrations in phantoms (lipoCEST) [13] as well as other applications including glutamine (gluCEST) [14], hyperCEST [15] and paraCEST [16].

A great deal of work demonstrating the potential utility of CEST has been done in the pre-clinical setting at field strengths between 4.7T and 9.4T [12][17]. This is primarily due to the higher SNR (CEST is an inherently low-signal technique), finer spectral resolution, and greater flexibility in terms of SAR limitations. The use of animal models also has several benefits when compared to human volunteers, including the possibility of longer scan-times, minimizing motion with anaesthesia, tighter regulation of physiological parameters (e.g. levels of sedative, breathing gases) and the option to artificially induce pathological conditions (e.g. tumour xenografts or ischemia).

However, for any benefits to be realised in clinical cancer imaging, the technique must be shown to be feasible on clinical MRI scanners. Early demonstrations of this have been described in several anatomical regions including the brain [18][19][20][21], head and neck [22] and the prostate [23][24].

1.3 Chemical Exchange Saturation Transfer Theory

CEST is a method of probing the chemical environments of ^{1}H nuclei using MR techniques. The core principle is to measure small changes in the water signal intensity as a result of applying off-resonance RF saturation prior to the MRI read-out. CEST belongs to a family of NMR techniques known as saturation transfer (ST) experiments, which have been well-understood in the context of spectroscopy for many years. Overhauser first proposed that ST effects may arise between electrons and nuclei [25]. Soon after this it was realised that ST effects also arise between nuclei, and this was termed the Nuclear Overhauser Effect (NOE) [26]. ST can occur via two mechanisms: dipolar mediated cross-relaxation through space, or chemical exchange, the latter first being described by Forsen and Hoffman [27]. Both effects are well modelled by the Bloch-McConnell equations (see 1.3.8) which describe the evolution of the magnetisation vectors of multiple pools that are undergoing chemical exchange (see section 1.3.3).

1.3.1 What can CEST tell us?

CEST is sensitive to the presence of chemical groups containing exchangeable protons. The most common of these within biological systems are amide (-NH), amine ($-NH_2$) and hydroxyl (-OH) chemical groups and many biological molecules contain one or more of these. Endogenous CEST imaging contrast arises from the interaction of these relatively low-concentration chemical groups with the much more abundant water pool. The biochemical basis of CEST contrast between different tissues is complex and depends on chemical concentrations, pH, T1, T2, saturation schemes and even temperature. Sections 1.3.2 through to 1.3.10 will outline the key components of the technique before subsequent sections describe some of the challenges that must be overcome to carry out CEST imaging effectively.

1.3.2 Chemical Shift

Diamagnetic chemical-shielding effects arise due to interactions between the magnetic field and the electrons surrounding a given atomic nucleus. In MRI, these effects act to modify the magnitude of the magnetic field experienced by a given ^{1}H-proton such that the field it experiences is smaller than the magnitude of the externally applied field. This leads to protons in different chemical environments (e.g. water, amide, amine, hydroxyl protons) experiencing different effective fields and therefore, as per equation 1-2, exhibiting different characteristic resonant frequencies even in the presence of the same externally applied B_0 field. The chemical shielding effect can be expressed in a simple form as:

$$B_{effective} = (1 - \sigma)B_0 \tag{1-9}$$

Where σ is a dimensionless magnetic shielding constant taking values between 10^{-6} and 10^{-2} over all MR-active nuclei (but is generally in the range 10^{-6} to 10^{-5} for protons).

The small variation in the Larmor frequency arising due to this effect is referred to as ‘chemical shift’. The chemical-shielding effect is the dominant cause of this chemical shift. Other NMR effects (such as J-coupling, dipolar-coupling and quadrupolar-coupling) influence the spectroscopic signatures of MR-active nuclei. These effects are well-documented in the magnetic resonance spectroscopy (MRS) literature and are not of direct relevance to CEST imaging, where the magnitude of the chemical shift effect is the primary parameter of interest for distinguishing between different chemical environments, and therefore are not discussed further here.

As chemical shifts are typically on the order of millionths of the Larmor frequency they are usually reported in terms of ‘parts per million’ which is typically abbreviated to ‘ppm’. In CEST the convention is to express chemical shifts relative to the Larmor frequency of the water pool, with 0ppm being on-resonance with water. This means that the chemical shift, in ppm, of some other chemical group A may be expressed as:

$$Chemical\ Shift_A = 10^6 * \frac{\omega_{0A} - \omega_{0W}}{\omega_{0W}} \tag{1-10}$$

Where ω_{0A} is the Larmor frequency of pool A and ω_{0W} is the Larmor frequency of the water pool.

The ppm scale is useful as it allows for B_0-independent quantification of chemical shifts such that, for example, the amide proton resonance at 3.0T (448 MHz) and at 9.4T (1404 MHz) may both be referred to as being located at 3.5 ppm. This means that CEST data from scanners of different field strengths may be easily compared and that data processing can be performed the same way regardless of scanner field strength.

Table 1-1 contains the chemical shifts of the amide, amine and hydroxyl chemical groups along with other CEST properties, including: exchange rates; common endogenous metabolites containing each chemical group; the approximate magnitude of the obtainable CEST asymmetry signal for each group (asymmetry analysis is discussed in section 1.3.10.1); pH sensitivity, and the potential clinical applications of CEST imaging of those metabolites.

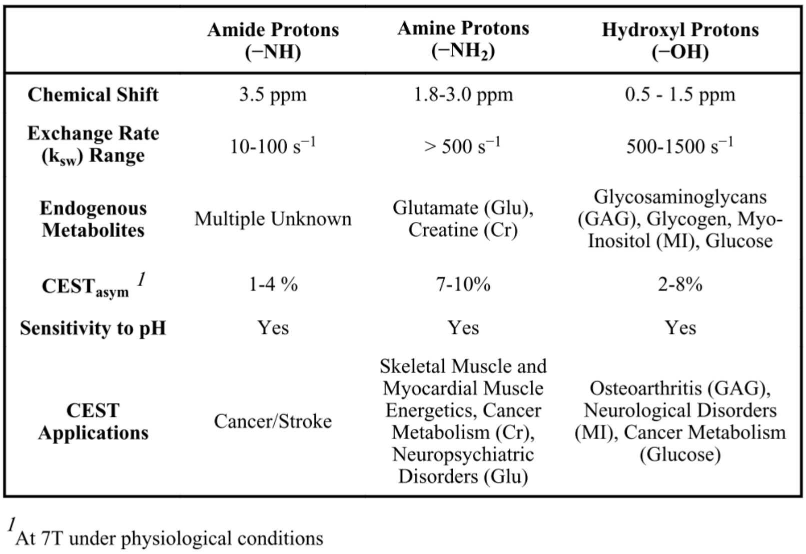

	Amide Protons (−NH)	**Amine Protons (−NH$_2$)**	**Hydroxyl Protons (−OH)**
Chemical Shift	3.5 ppm	1.8-3.0 ppm	0.5 - 1.5 ppm
Exchange Rate (k_{sw}) Range	10-100 s^{-1}	> 500 s^{-1}	500-1500 s^{-1}
Endogenous Metabolites	Multiple Unknown	Glutamate (Glu), Creatine (Cr)	Glycosaminoglycans (GAG), Glycogen, Myo-Inositol (MI), Glucose
$CEST_{asym}$ ^{1}	1-4 %	7-10%	2-8%
Sensitivity to pH	Yes	Yes	Yes
CEST Applications	Cancer/Stroke	Skeletal Muscle and Myocardial Muscle Energetics, Cancer Metabolism (Cr), Neuropsychiatric Disorders (Glu)	Osteoarthritis (GAG), Neurological Disorders (MI), Cancer Metabolism (Glucose)

^{1}At 7T under physiological conditions

Table 1-1: *Approximate CEST exchange properties for amide, amine and hydroxyl groups. Figure reproduced from* [28].

The chemical shift effect is fundamental to the CEST technique as it allows for the delineation of multiple proton chemical environments in the post-analysis of the acquired data on the basis of their frequency-offset from water. This will be discussed in more detail when introducing the z-spectrum in section 1.3.9.

1.3.3 Chemical Exchange and Exchange Rates

> *"In magnetic resonance, the term chemical exchange has a specific meaning. It means that a chemical system is at macroscopic equilibrium, but at the microscopic level, an individual nucleus is exchanging its environment with another nucleus. The process causes no net change in the sample, but from the point of view of a particular nucleus, a chemical reaction has occurred."*
>
> **Modern Magnetic Resonance, Webb, 2006** [29]

For the simplest two-pool model (an aqueous solution of solute A, which contains an exchangeable proton), protons are in constant exchange between the pools. The transition rate, k_{AW}, for protons moving from pool A to water is a measure of the rate at which magnetisation leaves that pool, or put another way, is the inverse of the mean time that a proton spends in pool A before exchanging to a water site $(1/\tau_{AW})$. A corresponding transition rate, k_{WA}, exists for the reverse process of water protons moving to pool A. A schematic illustration of the process is shown in Figure 1-3.

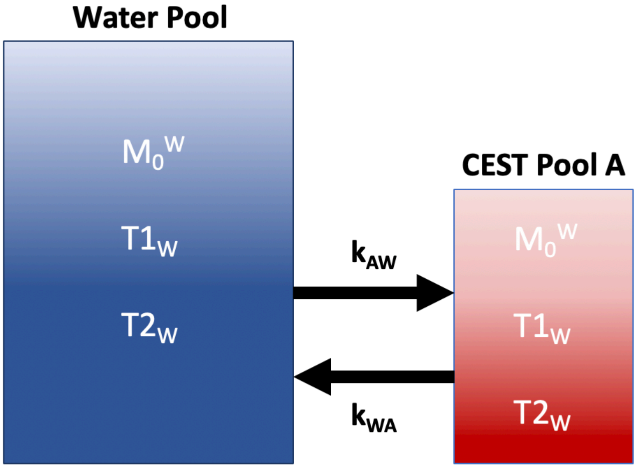

Figure 1-3: *Schematic illustration of exchange between two pools. Each pool has its own set of properties, including the equilibrium net magnetisation, T1 and T2. The two-way exchange is governed by two different pool-specific exchange rates.*

Magnetisation is exchanged between the two pools through the chemical exchange mechanism according to:

$$\frac{d\boldsymbol{M^W}}{dt} = k_{AW}\boldsymbol{M^A} - k_{WA}\boldsymbol{M^W} \tag{1-11}$$
$$\frac{d\boldsymbol{M^A}}{dt} = k_{WA}\boldsymbol{M^W} - k_{AW}\boldsymbol{M^A}$$

And the total number of protons is conserved such that:

$$k_{AW}M_0^A = k_{WA}M_0^W \tag{1-12}$$

Where M_0^W is the magnitude of the equilibrium magnetisation for the water pool, and similarly for pool A. An exchange rate for the system may be defined as $k_{ex} = k_{AW} + k_{WA}$. Saturation transfer due to cross-relaxation may be expressed in the same form [26]. For this reason, it is possible to model both chemical exchange and cross-relaxation based effects using the same mathematical model. This allows for an easy way to account for CEST, NOE and magnetisation transfer (MT) effects within the same theoretical framework.

For models with more than two pools the same principles apply and the number of exchange terms grows multiplicatively. However, as the CEST, NOE and MT pools are all small compared to the water pool, the dominant exchange effects are between these pools and water. Therefore, when dealing with multi-pool systems it is common to neglect exchange terms between the non-water pools.

CEST effects are observed optimally in the 'intermediate-exchange regime' i.e. when k_{ex} for a given species is approximately equal to the chemical shift between that species and water:

$$k_{ex} \approx \Delta\omega \tag{1-13}$$

If exchange rates are too slow, reductions in water M_z do not accumulate quickly enough to overcome T1 relaxation during saturation. If exchange rates are too high, the time-averaged Larmor frequency of a given proton sits somewhere between the frequencies of the water pool and solute pool and the pools become spectrally merged and indistinguishable. The presence of a fast-exchanging solute also acts to shorten the T2 due to exchange effects.

1.3.4 Exchange Rate pH-dependency

Exchange rates depend on pH in a manner that is both acid- and base-catalysed. The dependency is expressed by the general relationship:

$$k = k_a \times 10^{-pH} + k_b \times 10^{pH-pk_w} + k_0 \qquad (1\text{-}14)$$

Where k_a and k_b are the acid- and base-catalysed rate constants respectively, and $k_0$is a term to contain contributions from a range of possible exchange catalysts [30]. pk_w is the water auto-dissociation constant (approximately 14 at 25℃). This expression gives rise to a pH-dependency that can take the form of that shown in Figure 1-4. At physiological pH ranges (typically pH 6 to 8 [31]) and temperatures, chemical exchange rates are base-catalysed.

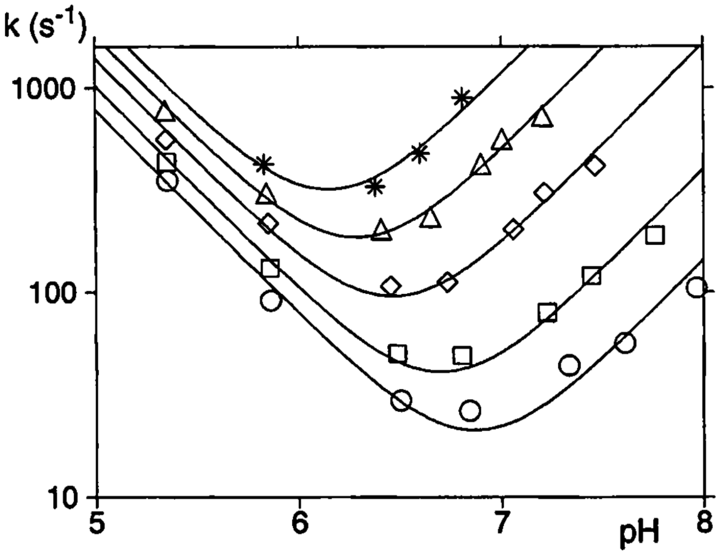

Figure 1-4*: Exchange rates of the side chain hydroxyl proton of avcetyl-threonine-OCH$_3$ in aqueous solution. The proton exchange rate constants are plotted versus the pH for data measured at* 4℃ *(circles),* 10℃ *(squares),* 20℃ *(diamonds),* 30℃ *(triangles), and* 36℃ *(stars). The pH was corrected for the temperature dependence of the dissociation constant of water. The fitted curves assume exchange catalysis by H^+ and OH^- only. Figure reproduced from* [30].

In specific reported cases the relationship between the exchange rates of amides and amines have been reported to be [5][32]:

$$k_{amide} = 5.57 * 10^{pH-6.4} \qquad (1\text{-}15)$$
$$k_{amine} = 10^{pH-4.2}$$

The relationship between pH and exchange rates has been exploited to perform pH mapping using CEST [33]. Zhou et al [5] proposed the amide proton transfer (APT) technique to measure pH by observing changes in the amide signal at 3.5 ppm and several groups have successfully used APT contrast to acquire pH-weighted MR images which correlate well with lactic acidosis [34][35]. However, the APT signal is also affected by cellular water content, protein and peptide content, NOE effects and relaxation constants of the water pool [5][36].

1.3.5 Quantification of exchange rates

Several CEST-based approaches to quantifying exchange rates exist. “Quantification of exchange rate using varying saturation power” (QUESP) and “quantification of exchange rate using varying saturation time” (QUEST) both acquire z-spectra over several saturation powers or saturation durations then solve sets of linked Bloch-McConnell (BM) equations to quantify the exchange rates [37][38].

Ratiometric approaches for measuring pH have also been developed whereby signal from different exchange sites are used to calculate the pH. Ward and Balaban initially suggested a method whereby the two exchangeable sites are parts of the same exogenous compound [39]. More recently, McVicar et al proposed a technique named amine and amide concentration-independent detection (AACID) [32] which is able to measure absolute pH using a ratiometric approach between the amide and amide protons from endogenous mobile peptides and proteins, then using ^{31}P-MRS to calibrate the results. This technique has the benefit of not requiring the assumption of constant water content and solute concentrations, which are limitations of APT.

1.3.6 Z-spectrum contributors

1.3.6.1 CEST pools

Exchangeable protons in biological systems are generally found within amide, amine and hydroxyl groups, the chemical shifts and exchange rates of which are shown in Table 1-1. The contribution to the z-spectrum from each pool is influenced by the physical concentrations of each pool, temperature, exchange rates, T1 and T2, and the choice of saturation scheme (discussed in section 1.3.7).

1.3.6.2 Nuclear Overhauser Effect (NOE)

The Nuclear Overhauser Effect (NOE) is a mechanism by which magnetisation is transferred by the through-space dipolar interaction i.e. no physical chemical exchange actually occurs but nearby spins interact magnetically either through space or via some relay mechanism along the chemical chain. The NOE effect was originally seen to be a confounding effect in generating accurate asymmetry measurements (asymmetry analysis is discussed in section 1.3.10.1) but has since been re-framed as a potential source of additional useful information. In CEST it has been traditionally considered to manifest on the aliphatic side of the water resonance around -3.5ppm but recent work has identified a second NOE peak close to -1.6ppm [40] and additional work suggests that there may be an additional contribution overlapping with the amide resonance [41]. Long chain or complex organic molecules contribute to the NOE effect. Exchange rates associated with the NOE effect are slow therefore the effect is predominantly observed at low saturation powers.

1.3.6.3 Magnetisation Transfer (MT)

The MT effect arises due to water molecules in a semi-bound state in the hydration layers around large macromolecules (eg proteins) as illustrated in Figure 1-5 and it is the most spectrally broad contributor to the z-spectrum.

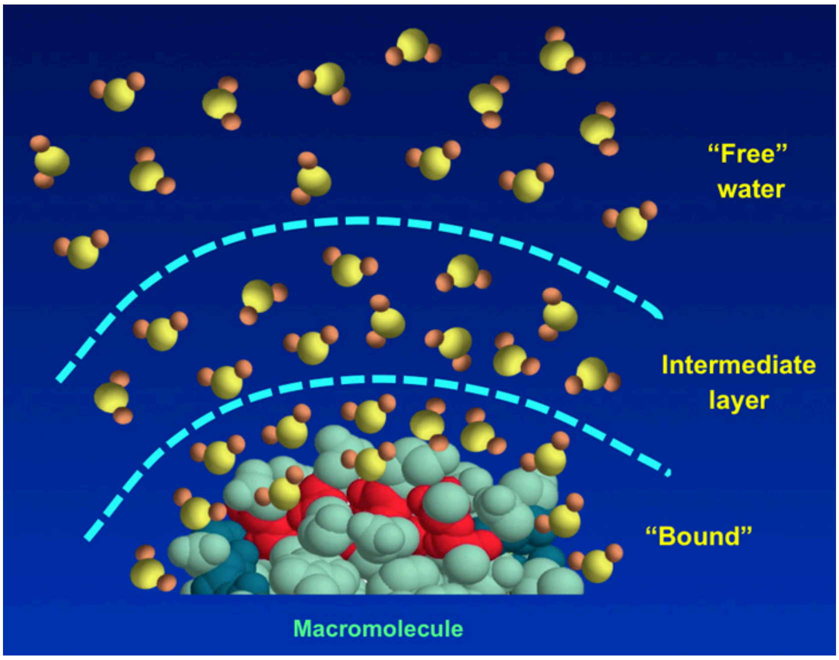

Figure 1-5*: An illustration of the layers of binding that water molecules may experience in the presence of a large macromolecule. The boundaries between the bound, intermediate and free water layers are continuous and this gives rise to a significant spread in the chemical shifts of the hydrogen protons across the whole sample. The T2 values are also very short closer to the bound layer, where interactions between neighbours accelerate the de-phasing process. Figure reproduced from* [42].

The water molecules close to a macromolecule experience a greater or lesser degree of inter-molecular binding depending on their proximity to the macromolecule itself. The rapid de-phasing of these bound protons means that the MT effect has a very short T2 value (of the order 10's of microseconds) and the interaction of the transverse component of the MT pool magnetisation with the water pool is negligible. However, the bound water molecules experience dipolar relaxation, which manifests itself as a very broad absorption peak in the z-spectrum. The MT absorption profile is typically tens to hundreds of ppm's wide and is reported to be well-described by a super-Lorentzian lineshape although Lorentzians are often used as a simpler alternative to eliminate the complications introduced by the 'pole' that occurs close to the centre of a super-Lorentzian. It has been reported that the MT effect may be asymmetric with a small aliphatic offset frequency [43][44] and that the magnitude and offset of the effect may show some dependency on saturation power.

1.3.7 Saturation

Saturation is defined as the reduction of the net magnetisation of a system through the application of radiofrequency (RF) radiation with a frequency at or close to the Lamor frequency of the spins within the system. This can be done using either continuous-wave (CW), or pulsed-saturation, which are discussed in sections 1.3.7.1 and 1.3.7.2 respectively.

CEST saturation takes place any time that the magnetization of a system with multiple exchanging pools has been perturbed from thermal equilibrium by the RF. T1 relaxation acts to reduce $|M|$ only when the *z*-component of **M** is negative (otherwise it acts to re-grow the magnetisation and $|M|$ increases). T2 relaxation acts to reduce $|M|$ at any time when the magnetisation vector has a component within the *xy*-plane. T2 acts over shorter time-scales than T1 and only ever acts to reduce $|M|$.

At full saturation the net magnetisation of a pool of protons reaches zero i.e. the distribution of spin-vectors is indistinguishable from thermal equilibrium in the absence of a B_0 field. However, in practice, T1 relaxation, chemical exchange between pools with differing chemical shifts, and the choice of possible RF saturation parameters limit how close to zero the magnitude of the magnetization can be pushed and the system approaches 'saturation steady-state'. This refers to the condition whereby, during saturation, the reduction in $|M|$ due to the application of saturation RF is exactly counteracted by the effects of T1 relaxation. The true saturation steady-state condition occurs for CW saturation only. For pulsed saturation, 'pseudo-steady-state' is achieved where the recovery of M_z during the inter-pulse delay due to T1 effects exactly equals the reduction of M_z during the application of each pulse.

1.3.7.1 Continuous-wave saturation

Continuous-wave (CW) saturation is the application of a long (typically several seconds) RF pulse centred at a specific frequency. A schematic pulse-sequence diagram of a CW-CEST acquisition is shown in Figure 1-6. CW saturation is highly frequency-selective due to the long pulse durations. The CW-saturation scheme may be fully described by the frequency and magnitude of the B_1, and the pulse duration. B_1 values are typically required to be in the range 0.5-5uT for endogenous CEST. High frequency selectivity (low bandwidth) is desirable when performing CEST, as will become clearer when discussing the z-spectrum in section 1.3.9. However, hardware limitations and SAR restrictions on clinical scanners mean that CW-CEST is often not feasible in the clinical setting and that pulsed-saturation must be used instead.

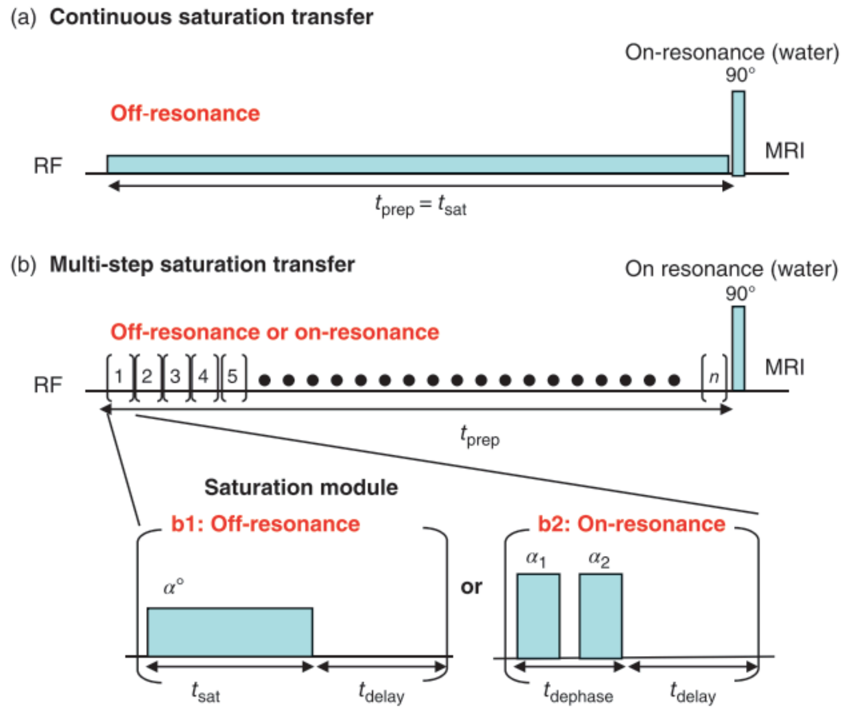
(a) Continuous saturation transfer
On-resonance (water)
90°
Off-resonance
RF
MRI
$t_{prep} = t_{sat}$
(b) Multi-step saturation transfer
On resonance (water)
90°
Off-resonance or on-resonance
RF
1
2
3
4
5
n
MRI
t_{prep}
Saturation module
b1: Off-resonance
$\alpha°$
or
b2: On-resonance
α_1
α_2
t_{sat}
t_{delay}
$t_{dephase}$
t_{delay}

Figure 1-6: *Schematic diagrams illustrating CW saturation and pulsed (or 'multi-step') saturation. Figure reproduced from* [45]*.*

1.3.7.2 Pulsed saturation

Pulsed saturation involves applying multiple RF-pulses that form a 'saturation train'. A schematic pulse-sequence diagram for a pulsed-CEST acquisition is shown in Figure 1-6. A pulsed saturation scheme is fully described by five parameters: the pulse duration τ_{pd} (typically order of ms), the inter-pulse delay τ_{ipd} (typically order of ms and commonly smaller than τ_{pd}) the number of pulses N (typically of the order 10's to 100's), the pulse-shape (of the envelope within which the sinusoidal carrier frequency oscillates) and the amplitude. The B_1 amplitude varies in time during pulsed saturation so it is commonly expressed as a continuous wave power equivalent B_{1CWPE} i.e. the power of a continuous-wave that would impart the same amount of energy per unit time as the pulsed scheme. Due to the shorter pulses, pulsed saturation is less frequency-selective than CW saturation and is more susceptible to Fourier artefacts such as sidebands. When designing pulsed schemes, it is desirable that the frequency response of the scheme does not extend much further than the spacing between z-spectrum sampling frequencies.

The optimisation of pulsed saturation schemes is a complex problem with a multi-dimensional parameter space. Recently Yoshimaru et al have applied a genetic algorithm approach to derive sets of parameters that maximise CEST asymmetry measurements [46].

1.3.8 Saturation Transfer and the Bloch-McConnell equations

During exchange, a proton can be modelled as if it exchanges instantaneously, and it is assumed that the process of exchange does not itself alter the magnetisation vector. When exchanging between two sites at different chemical shifts, the *x*, *y* and *z*-components of the magnetisation are preserved, but the Larmor frequency will change as a result of the difference in the magnitude of the magnetic field at each site.

This saturation transfer effect (described by equation 1-11) can be combined with the Bloch equations in the rotating frame (equation 1-7) by adding exchange terms that couple multiple pools via the exchange mechanism. The resulting equations are called the Bloch-McConnell equations and may be expressed for a two-pool model as:

$$\begin{aligned}
\frac{dM_x^W(t)}{dt} &= M_y^W(t)\Omega^W - \gamma M_z^W(t)B_{\boldsymbol{y}}(t) - \frac{M_x^W(t)}{T_2^W} - k_{WA}M_x^W + k_{AW}M_x^A \qquad (1\text{-}16)\\
\frac{dM_y^W(t)}{dt} &= -M_x^W(t)\Omega^W + \gamma M_z^W(t)B_{\boldsymbol{x}}(t) - \frac{M_y^W(t)}{T_2^W} - k_{WA}M_y^W + k_{AW}M_y^A\\
\frac{dM_z^W(t)}{dt} &= \gamma\left[M_x^W(t)B_{\boldsymbol{y}}(t) - M_y^W(t)B_{\boldsymbol{x}}(t)\right] - \frac{M_z^W(t)-M_0^W}{T_1^W} - k_{WA}M_z^W + k_{AW}M_z^A\\
\frac{dM_x^A(t)}{dt} &= M_y^A(t)\Omega^A - \gamma M_z^A(t)B_{\boldsymbol{y}}(t) - \frac{M_x^A(t)}{T_2^A} - k_{AW}M_x^A + k_{WA}M_x^W\\
\frac{dM_y^A(t)}{dt} &= -M_x^A(t)\Omega^A + \gamma M_z^A(t)B_{\boldsymbol{x}}(t) - \frac{M_y^A(t)}{T_2^A} - k_{AW}M_y^A + k_{WA}M_y^W\\
\frac{dM_z^A(t)}{dt} &= \gamma\left[M_x^A(t)B_{\boldsymbol{y}}(t) - M_y^A(t)B_{\boldsymbol{x}}(t)\right] - \frac{M_z^A(t)-M_0^A}{T_1^A} - k_{AW}M_z^A + k_{WA}M_z^W
\end{aligned}$$

Where the primes have been dropped for simplicity and M^W is the magnetisation of the water pool and M^A is the magnetisation of pool A. This can be expressed in matrix form as:

$$\begin{aligned}
\frac{d\boldsymbol{M^W}}{dt} &= \boldsymbol{A^W}.\boldsymbol{M^W} + \boldsymbol{B^W} + k_{WA}\boldsymbol{M^W} \qquad (1\text{-}17)\\
\frac{d\boldsymbol{M^A}}{dt} &= \boldsymbol{A^A}.\boldsymbol{M^A} + \boldsymbol{B^A} + k_{AW}\boldsymbol{M^A}
\end{aligned}$$

Where $\boldsymbol{M} = \left[M_x(t), M_y(t), M_z(t)\right]^T$; $\boldsymbol{B} = [0{,}0, R_1 M_0]^T$ and

$$\boldsymbol{A} = \begin{bmatrix} -R_2 & \Omega & 0 \\ -\Omega & -R_2 & \omega_1 \\ 0 & -\omega_1 & -R_2 \end{bmatrix}$$

And ^{T} denotes the transpose of the matrix, $R_1 = 1/T_1$ and $R_2 = 1/T_2$.

Therefore, in a multi-pool model, it is possible to influence the magnetisation of one pool of protons (e.g. the water pool) by saturating another pool (pool A) where pool A is undergoing chemical exchange with the water pool. If one pool of protons with a non-zero chemical shift relative to water undergoes efficient saturation, and exchanges some number of 'saturated' protons with water prior to the MRI readout, the measured signal from water (determined by M_{zw}) will be reduced by an amount proportional to the number of protons that have exchanged and related to the net magnetisation of both pools (ignoring T1 recovery). This is the essence of the CEST principle: to measure the reduction in the water signal as a result of chemical exchange between exchangeable pools of protons and the water proton pool. To extract information, we must analyse the z-spectrum, which is outlined in the following section.

1.3.9 The z-spectrum

In CEST imaging, each slice of the image is acquired multiple times, each time applying saturation at a different offset frequency. The z-spectrum is a plot of the measured signal (which comes primarily from water) as a function of the saturation offset frequency. Each voxel has its own z-spectrum, and these may be combined using region of interest (ROI) analysis to minimise noise. Figure 1-7 shows ROI-averaged z-spectra acquired in the rat brain at 9.4T using three saturation powers. A minimum in the measured signal is observed when the saturation is on-resonance with water at 0 ppm. This is because the water pool itself has been saturated, therefore there is very little signal to be acquired by the read-out. Conversely, when saturation is at a far-away offset, the observed signal tends towards the un-saturated intensity. CEST analysis lies in the post-processing of the z-spectrum with a particular focus on understanding features seen within the ± 5ppm range, namely features arising due to the CEST, NOE and MT effects.

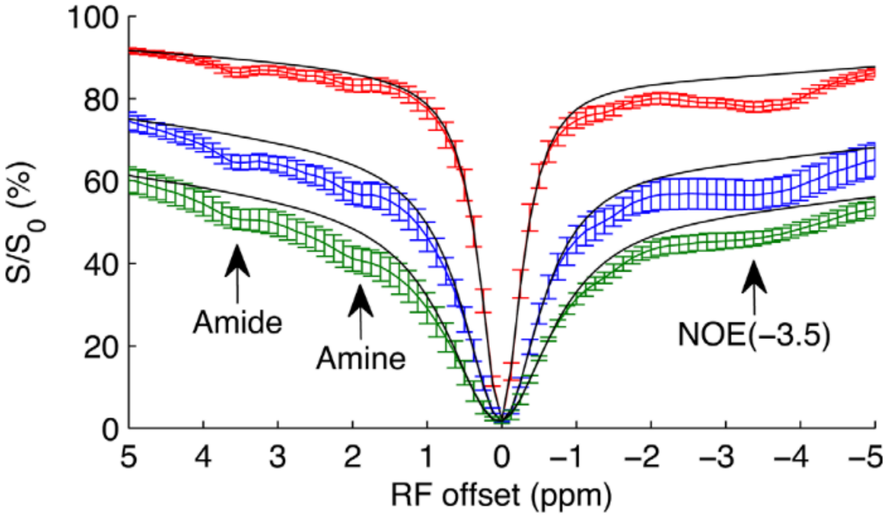

Figure 1-7: *Z-spectra acquired in the healthy rat brain at 9.4T at 0.5μT (red), 1.0μT (blue) and 1.5μT (green). Amide, amine and NOE resonances are marked at 3.5ppm, 1.9ppm and -3.5ppm respectively. Black lines represent Lorentzians fitted to the data to account for the direct water saturation. Figure reproduced from from* [47].

1.3.10 Post-processing

Several approaches have been outlined for the post-processing of CEST data. These can broadly be separated into two groups: asymmetry analysis and fitting analysis.

1.3.10.1 Asymmetry Analysis

Contributions from various DS, CEST, NOE and MT effects give rise to an asymmetric z-spectrum. Asymmetry analysis is a method of quantifying this asymmetry at a given saturation frequency or over a range of frequencies. The asymmetric magnetization transfer ratio (MTR$_{asym}$) is the most commonly used metric and is calculated by subtracting one side of the z-spectrum from the other, with the water frequency (conventionally 0ppm in CEST imaging) as the central point. This is expressed as:

$$MTR_{asym}(\omega) = \frac{M_z(-\omega)-M_z(\omega)}{M_0} \tag{1-18}$$

Where $M_z(\omega)$ is the measured water signal at the offset ω and $M_0$is the unsaturated signal. A normalised simulated z-spectrum for a two-pool system (including water at 0ppm and amide at 3.5ppm), and the corresponding MTR$_{asym}$ is shown in Figure 1-8.

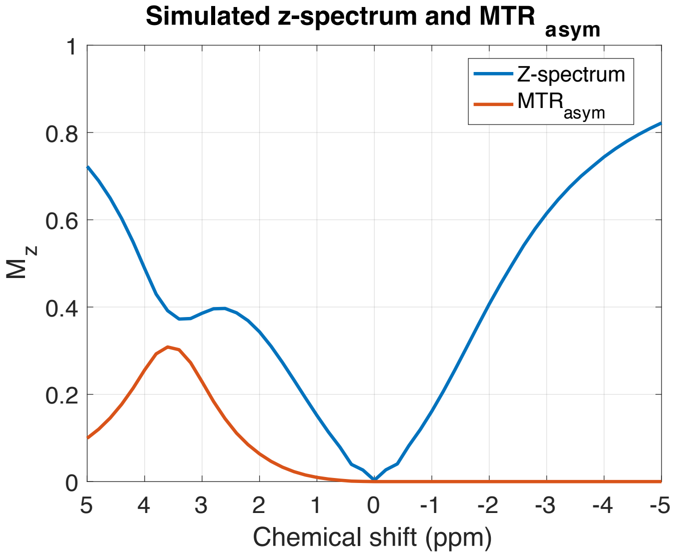

Figure 1-8*: Simulated z-spectrum (blue) for a two-pool system (water at 0.0ppm and amide at 3.5ppm). The red line is the MTR$_{asym}$ which represents the contribution to the z-spectrum from the exchanging amide pool. In this case the non-zero MTR$_{asym}$ is purely due to the amide contribution. When multiple pools are present their overlapping contributions to the measured z-spectrum mean that there are several contributions to the final MTR$_{asym}$ value.*

The asymmetry analysis approach using MTR$_{asym}$ removes the symmetrical water contribution from the z-spectrum and allows us to visualise the sum of contributions from the other exchangeable pools. Asymmetry can be quantified either as the height of the MTR$_{asym}$ curve at a given ppm value, or as the integral over a ppm range. Alternative asymmetry calculations have been proposed but these are not considered any further within this thesis [48].

.

1.3.10.2 Lorentzian z-spectrum fitting

Z-spectrum features due to CEST, DS and NOE pools have been shown to be well-modelled using Lorentzian lineshapes [49][50][51][52]. The equation for a Lorentzian is:

$$L_i(\omega, \omega_{0i}, \Gamma_i, A_i) = A_i \frac{1}{2\pi} \frac{\Gamma_i}{(\omega-\omega_{0i})^2+(0.5\Gamma_i)^2} \qquad (1\text{-}19)$$

Where ω_{0i} is the offset frequency of pool *i*, Γ_i is the full-width-half-maximum (FWHM) and A_i is a scaling factor.

The MT contribution is reported to be well-described by a super-Lorentzian lineshape [53][54]:

$$SL(\omega, \omega_{0SL}, T_2^b, A_{SL}) = A_{SL} \int_0^{\frac{\pi}{2}} d\theta \, sin\theta \sqrt{\frac{2}{\pi}} \frac{T_2^b}{|3cos^2\theta-1|} e^{-2\left(\frac{(\omega-\omega_{0SL})T_2^b}{|3cos^2\theta-1|}\right)^2} \qquad (1\text{-}20)$$

Where T_2^b is the T2 of the MT pool, ω_{0SL} is the central offset frequency of the lineshape relative to water, and A_{SL} is a scaling factor.

It follows that the general overall fit equation for a normalised z-spectrum with contributions from *n* pools (including DS, CEST and NOE effects) and an MT contribution is given by:

$$M_z(\omega) = 1 - \sum_{i=1}^{n} L_i(\omega - h, \omega_{0i}, \Gamma_i, A_i) - SL(\omega - h, \omega_{0SL}, T_2^b, A_{SL}) \qquad (1\text{-}21)$$

Where *h* is a whole-fit horizontal offset term to account for imperfect B_0 inhomogeneity correction (discussed in section 1.4.1).

The contributions to the z-spectrum from amide, amine and hydroxyl groups are centred approximately in the 1-3.5ppm range with significant overlap at lower field strengths and *in vivo*. Z-spectrum fitting allows for de-convolution of the contributions from each pool. For illustration, Figure 1-9 shows a normalised z-spectrum (data shown as circular data-points) which has been fitted using multiple Lorentzian lineshapes to account for each of the contributing pools. The pools are: water direct saturation (cyan), the amide resonance (blue), amine resonance (maroon), nuclear-Overhauser effect (NOE) (green) and magnetisation transfer (MT) (red). The overall fit (the sum of contributions over fitted pools) is shown by the black line. A measured *in vivo* z-spectrum is comprised of the sum of contributions from each of these pools, plus the hydroxyl group (excluded in this example).

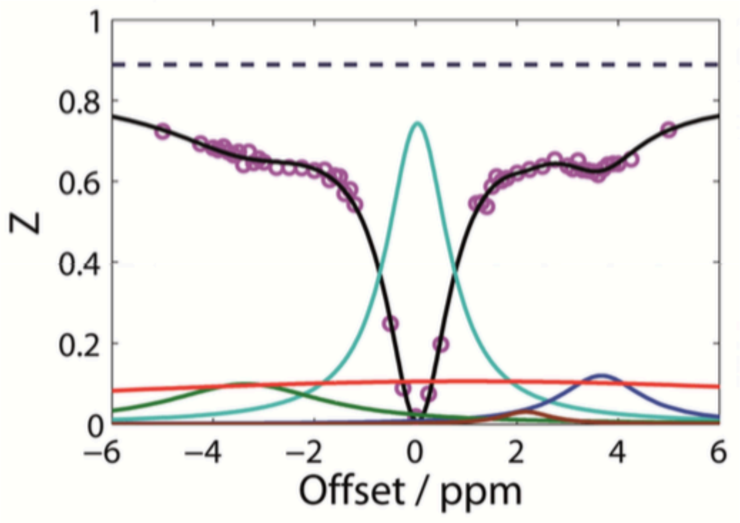

Figure 1-9: *A fitted z-spectrum showing the contributions from water direct-saturation (cyan), amide (blue), amine (brown), NOE (green) and MT (red) effects. The black dashed line represents the vertical offset which accounts for imperfect normalization. Figure reproduced from* [55].

Fitting each voxel in an image in this manner allows CEST maps to be produced similar to that shown in Figure 1-10 whereby the signal within each voxel in a given image corresponds to the amplitude of a particular fitted Lorentzian lineshape. In this case, the signal contrast in the rim and core of a glioblastoma are delineated from the surrounding tissue differently by different pools. In particular the MT signal shows hypo-intensity in the core and rim of the tumour, the NOE signal shows hypo-intensity in the core only, and the amide signal shows a clear hyper-intensity around the tumour rim.

Full-fitting of the BM equations can also be done either numerically or analytically, as discussed in chapter 3.

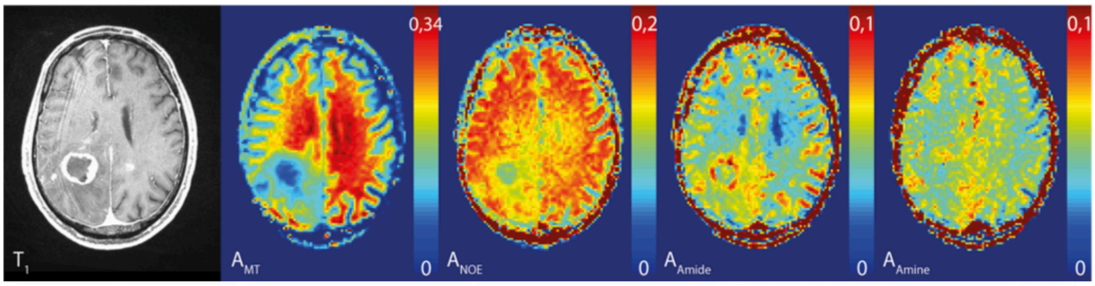

Figure 1-10: *Gd-enhanced T1-weighted image of a glioblastoma at 7T along with pixel-wise generated amplitude maps of the MT, NOE, amide and amine pools. Figure reproduced from* [55].

1.4 Challenges and considerations

Previous sections have described the key theoretical aspects of CEST imaging. The following sub-sections address some of the practical challenges that must be considered during the design of real-world CEST protocols, along with descriptions of some common approaches to overcoming them.

1.4.1 B_0 field inhomogeneities

Due to the frequency-selective nature of the off-resonance CEST saturation pulses, uniform saturation across the imaging slab can only be achieved when there is a good shim. In CEST, deviations of the B_0-field from the centre-frequency of the scanner (f_0) manifest as horizontal shifts in the position of the z-spectrum such that it is no longer centred at 0ppm. This can skew results, particularly when performing asymmetry-based analysis.

B_0 inhomogeneities occur due to imperfect shimming and are exacerbated by motion. They are typically of the order 10's of Hz at 3.0T. This can directly affect CEST measurements and therefore it is common practice to perform voxel-wise B_0 field corrections of CEST data.

Figure 1-11 shows a T2w image, a water centre-frequency inhomogeneity map, and the uncorrected and B_0-corrected asymmetry maps at 3.5 ppm from a patient with a WHO grade III oligodendroglioma, imaged at 3.0T. The shim is relatively good over the bulk of the brain but shows a large inhomogeneity close to the sinuses and two smaller deviations on either side of the head, above the ears. The difference between the un-corrected and corrected APT-weighted (APTw) images illustrate the importance of correcting for B_0 inhomogeneities during post-processing [19].

In cases of extremely high deviations from f_0 the acquired data may no longer be usable after B_0-field corrections especially if the range of sampling frequencies is small compared to the magnitude of the frequency shift.

Several methods have been proposed to correct for B_0 inhomogeneities. Some of these are purely mathematical, and others such as water saturation shift referencing (WASSR) [56] require the acquisition of additional data to generate B_0 maps which are subsequently used to correct the CEST data on a voxel-wise basis. In this work, correction was done using B_0 maps which were generated by two different methods: traditional dual-echo B_0 maps, and the recently described water-shift and B1 (WASABI) method which is outlined below. These scans were interleaved in-between the main CEST scans in order to capture spatial and temporal B_0 fluctuations.

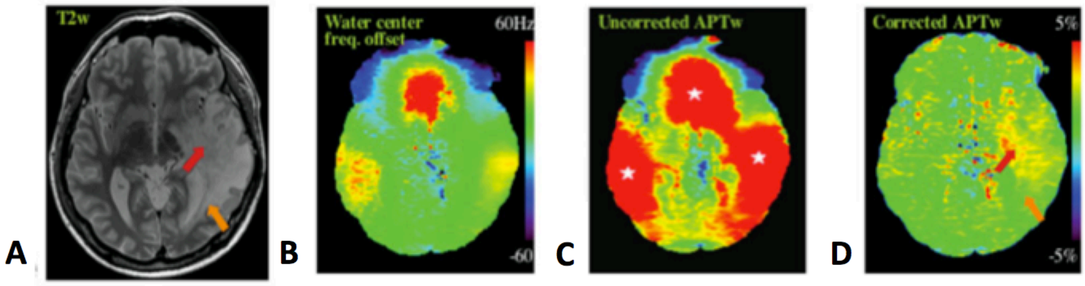

Figure 1-11: *MR images of a patient with WHO grade III oligodendroglioma.* ***A*** *shows the T2w image with the tumour core highlighted with the red arrow.* ***B*** *shows the water centre-frequency offset in Hz (arising due to B0 inhomogeneities). Clear inhomogeneities are seen near air-tissue interfaces (sinus, ear).* ***C*** *shows the uncorrected asymmetry map at 3.5 ppm (APTw) where large artefacts are visible (white stars) due to the B0-inhomogeneities.* ***D*** *shows the same map after B0 correction using a basic method of shifting the z-spectrum so that the point of lowest intensity is at 0 ppm. Even using this basic correction technique, the results are significantly improved. Figure reproduced from* [19].

1.4.1.1 Simultaneous water shift and B_1 (WASABI) acquisition

The WASABI method was first proposed by Schuenke et al in 2016 [57]. The approach involves acquiring a z-spectrum saturating using a single high-power, short-duration rectangular pulse. When off-resonance, this pulse causes precession of the magnetization vector around an effective field B_{eff} as illustrated in Figure 1-12.

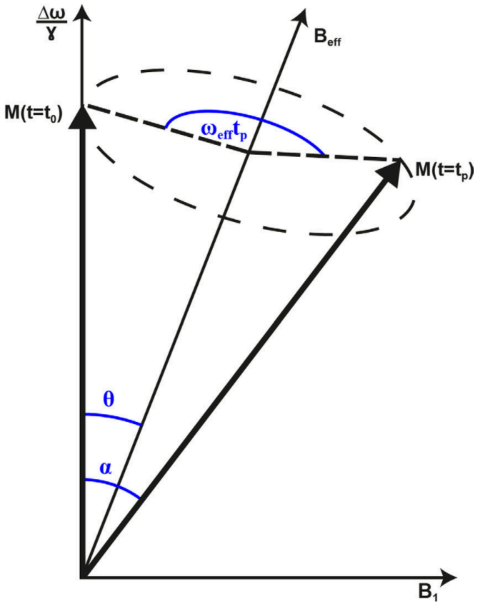

***Figure 1-12**: Precession of the magnetisation around the effective field. The rotation angle $\phi = \omega_{eff}.\tau_p$ depends on the pulse duration τ_p, the amplitude of the B_1 excitation field, and the frequency offset $\Delta\omega$. Figure reproduced from* [57].

The rotation angle $\phi = \omega_{eff}.\tau_p$ depends on the pulse duration τ_p, the amplitude of the B_1 excitation field, and the frequency offset $\Delta\omega$. These saturation parameters give rise to an oscillatory z-spectrum, an example of which is shown in Figure 1-13.

Schuenke et al derived an equation with four free parameters (see equation 1-22) that describes the observed lineshape and which can be fitted to WASABI data to simultaneously extract B_0 and B_1 field maps.

$$Z(\Delta\omega) = \left\| c - d.sin^2\left(tan^{-1}\left(\frac{\gamma.B_1}{\Delta\omega-\delta\omega}\right)\right).sin^2\left(\sqrt{(\gamma.B_1)^2 + (\Delta\omega-\delta\omega)^2}.\frac{\tau_p}{2}\right)\right\| \quad \text{(1-22)}$$

Parameter $\delta\omega$ represents the B_0-shift (relative to f_0) and B_1 is the absolute frequency of the applied RF. Parameters *c* and *d* have no field-map significance and relate only to amplitude modulation of the lineshape.

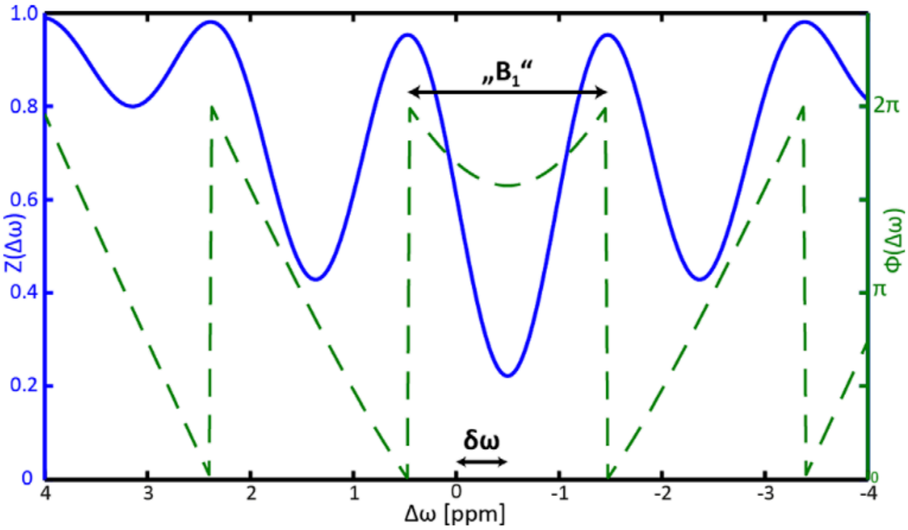

Figure 1-13: *A simulated WASABI z-spectrum (solid blue line) at B_0 = 3.0T generated by saturation by means of a single rectangular pulse with duration τ_p = 5ms and amplitude B_1 = 3.7μT. The maxima occur when the phase (dashed green line) is a multiple of 2π. In this case the magnetization is rotated back in its initial orientation parallel to B_0. Information about the water-frequency shift $\delta\omega$ and the RF amplitude B_1 is encoded in the shift of the symmetry axis and the periodicity of the function $Z(\Delta\omega)$, respectively. Figure reproduced from* [57].

WASABI scans were performed in 41 seconds. Fitting of single-slice WASABI images to extract $\delta\omega$ and B_1 values took typically less than 20 seconds per image using a custom-written Matlab script.

1.4.2 B_1 inhomogeneities

B_1 inhomogeneities lead to spatial variation in the saturation efficiency, which may lead to poor data integrity. Multi-transmit options are available on some scanners and are able to improve the homogeneity of the B_1 field. The problems caused by inhomogeneous B_1 are of more significance when imaging metabolites (or exogenous CEST contrast agents) with fast exchange rates, which require higher saturation powers to achieve high saturation efficiency, α, where α can be approximated by:

$$\alpha = \frac{(\gamma B_1)^2}{(\gamma B_1)^2 + (k_{sw})^2} \tag{1-23}$$

Several approaches to B_1-corrections have been proposed [58][59][60]. The simplest is to acquire CEST data at multiple saturation powers along with a B_1-map, and then to linearly interpolate the z-spectrum within each voxel using the corresponding B_1-map value.

B_1-corrections at least double the length of the CEST acquisition time in a protocol. For endogenous CEST, the slow-exchanging amides are less affected by B_1 inhomogeneity, but the amine and hydroxyl groups may be affected.

1.4.3 Z-spectrum sampling and signal-to-noise

Finely-sampled z-spectra are desirable, especially for z-spectrum fitting, but the total scan-time is directly proportional to the number of sampling frequencies and the number of signal averages (NSA). As with all MRI techniques, there are trade-offs in CEST imaging that must be balanced in an application-specific manner. Acquiring multiple signal averages improves the signal-to-noise (SNR) ratio, but this again increases the scan-time and it is important for clinical CEST protocols to be well-tolerated by patients so they cannot be excessively long.

Partial z-spectrum sampling shortens acquisition times but has limitations. At the extreme end of this, Xu et al recently acquired dynamic glucose enhanced (DGE) CEST data repeatedly at a single offset frequency to monitor the change in the hydroxyl signal as a result of glucose infusion [7]. However, this method is very susceptible to the confounding effects of B_0 drift. Partial z-spectrum sampling in general precludes subsequent peak-fitting analysis due to the sparsity of data points across the whole offset frequency range of interest.

1.4.4 Post-processing pipeline

A schematic pipeline that outlines the key CEST acquisition and post-processing steps used throughout this thesis is shown in Figure 1-14.

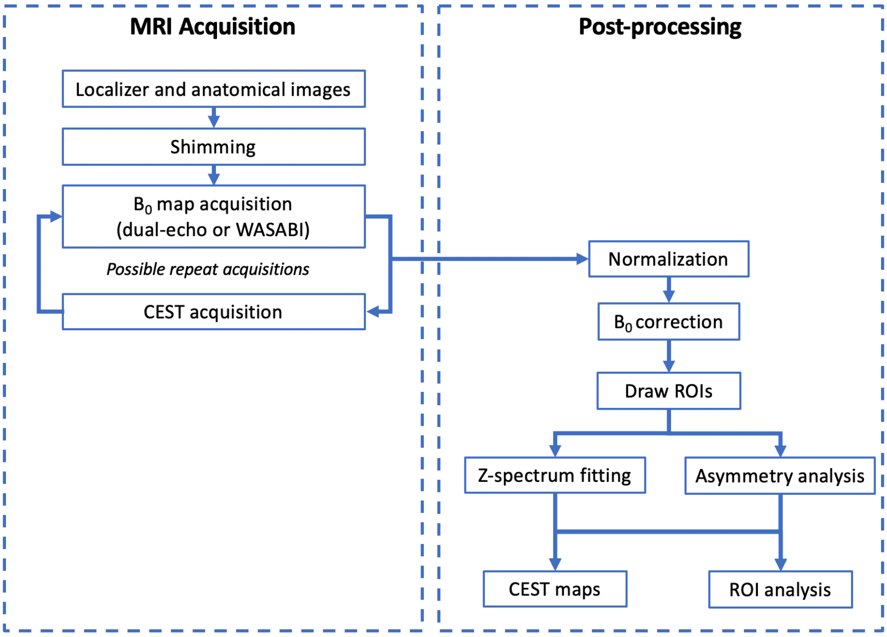
MRI Acquisition
Localizer and anatomical images
Shimming
B_0 map acquisition (dual-echo or WASABI)
Possible repeat acquisitions
CEST acquisition
Post-processing
Normalization
B_0 correction
Draw ROIs
Z-spectrum fitting
Asymmetry analysis
CEST maps
ROI analysis

Figure 1-14: *Schematic flow-diagram showing the key steps taken in the acquisition and post-processing of CEST data throughout the work outlined in this thesis.*

2 Clinical Introduction

CEST has received growing research attention since the early 2000's. The PubMed search results in Figure 2-1 show that the terms "chemical exchange saturation transfer" and "amide proton transfer" first appeared in article titles or abstracts in 2002 and 2003 respectively with one publication each. In 2018 there were 120 and 39 published articles containing each of these respective terms.

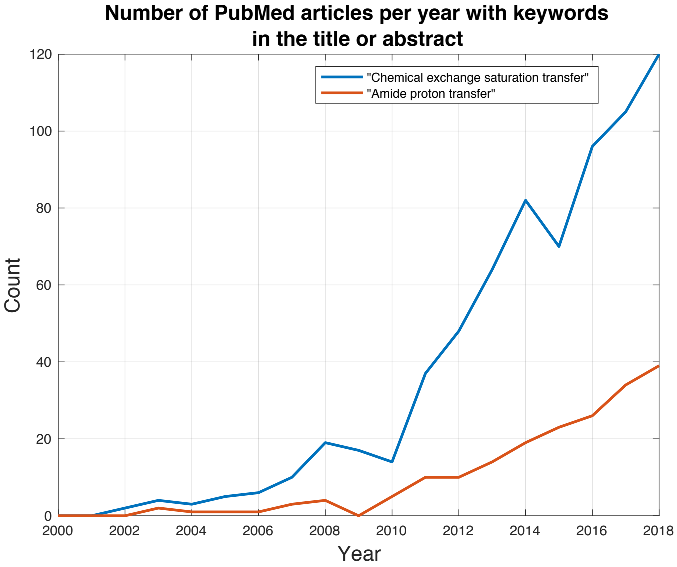

Figure 2-1: *The number of articles on PubMed containing either "chemical exchange saturation transfer" or "amide proton transfer" in the title or abstract, aggregated by year. The first occurrences are in 2002 and 2003 respectively, growing to 120 and 39 in 2018.*

The growth of the CEST corpus reflects increasing interest from scientists and clinicians. As discussed in this chapter, the technique is sensitive to changes in metabolite concentrations and pH, factors which make it particularly relevant for cancer imaging as well as in pathologies involving ischemia (e.g. stroke) and arthritis [61].

Philips has responded to the increased interest in CEST by including an "APTx" feature in the latest version of their proprietary software, thereby reducing the technical barrier to undertaking CEST-related research studies. CEST could potentially become a non-invasive source of metabolomic information to support diagnosis, prognosis and treatment monitoring for a range of conditions.

This thesis is concerned with cancer imaging so below we discuss some of the principal metabolomic changes that occur in cancer which may give rise to CEST imaging contrast.

2.1 Physiological basis of CEST signal in cancer

The two mechanisms underlying the generation of CEST contrast are: (1) concentration differences, and (2) exchange rate differences (which are driven primarily by the pH of the immediate chemical environment). These may be assessed in terms of their spatial variation within the acquired images or dynamically across time. The thesis concerns itself mostly with the former, but the analysis of dynamic CEST signals is central to the analysis in chapter 7.

2.1.1 Endogenous CEST contrast

Amide, amine and hydroxyl chemical groups feature abundantly *in vivo* as constituent parts of many proteins, peptides and other metabolites. As seen in Table 1-1, each species has an associated range of possible chemical shifts. The chemical shift of a given exchangeable proton may be influenced by both the molecular configuration and the chemical environment (including both concentration and pH).

Given the vast number of molecules present within the volume of a typical MRI voxel and the complex and dynamic physiological processes that are taking place, the identification of specific endogenous metabolites *in vivo* using CEST is a challenge. However, image contrast may still be generated endogenously through assessment of the signal variations across the field-of-view which can be used to generate exchange-weighted images.

Demonstrations of endogenous CEST imaging at clinical field strengths *in vivo* have tended to focus on asymmetry measurements. More recently, and partly due to the relatively low-saturation powers that must be used when performing CEST on clinical scanners, the sizeable contribution of the NOE effect has been acknowledged. It is shifting from being viewed as a confounding factor to a potential source of useful information.

In asymmetry assessments, many contributions are folded up into the single number that is expressed by each voxel. The use of z-spectrum fitting, as outlined in the previous chapter, may be able to deconvolve the multiple overlapping contributions to be produce a richer understanding of the endogenous contrast that is observed.

2.1.2 Dynamic CEST contrast

The administration of exogenous contrast media can be used to generate time-varying CEST contrast. Signal changes observed across a time-series of images which were acquired both pre and post the administration of some external contrast agent may be attributed with confidence to the introduction of that particular agent into the system (or, conceivably, to downstream effects which were instigated by the initial agent). CEST scans can be repeated over time while a CEST agent is administered and the signal-changes can be interpreted as direct effects of the agent.

Glucose, carrier of five hydroxyl groups, has great potential as a biologically active exogenous CEST contrast agent in cancer imaging. This is due to its rapid uptake into regular metabolic pathways and due to the altered dynamics of glucose caused by the Warburg Effect (see section 2.2.1).
Chelated paramagnetic CEST (PARACEST) contrast agents have also been created with exchangeable protons at chemical shifts far from water. These are very easy to identify in the z-spectrum but the information they can provide is limited because they are not readily processed as part of any pre-existing biochemical pathways.

2.2 Altered Metabolic Pathways in cancer

The metabolic processes that give rise to altered CEST contrast in cancer are complex and interdependent but understanding of the relevant pathways is increasing over time. In 2000, Hanahan and Weinberg published a seminal review paper in ‘Cell’ [62] (revisited in 2011 [63]) which identified six phenotypic ‘*Hallmarks of Cancer’*:

1) Sustaining proliferative signaling
2) Evading growth suppressors
3) Activating invasion and metastasis
4) Enabling replicative immortality
5) Inducing angiogenesis
6) Resisting cell death

Moving from the phenotypic to the metabolomic, in 2016 Pavlova and Thompson proposed an additional set of six hallmarks of cancer **metabolism** relating to intra-cellular processes which are disrupted in tumour cells [64]:

1) Deregulated uptake of glucose and amino acids
2) Use of opportunistic modes of nutrient acquisition
3) Use of glycolysis/TCA cycle intermediates for biosynthesis and NADPH production
4) Increased demand for nitrogen
5) Alterations in metabolite-driven gene regulation
6) Metabolic interactions with the microenvironment

While not all hallmarks are exhibited in every tumour, they comprise a set of traits observed across tumours more generally. The disruption of key processes such as glycolysis, oxidative carboxylation and the citric acid cycle (the Krebs cycle), combined with the

Warburg effect (see section 2.2.1) cause a complex chain of biochemical changes which are in principle detectable using CEST through changes in metabolite concentrations and pH.

For example, glutamine concentrations have been found to increase by factors of up to 100-fold in experiments carried out on a range of types of cancer cells including *in vitro* HeLa cells [65], and *in vivo* carcinomas, hepatomas and carcinosarcomas. It follows, necessarily, that there is a corresponding increase in the concentration of glutamine-based amine chemical groups. However, as glutamine is also involved in the synthesis of a diverse range of compounds containing exchangeable protons (such as purine, pyrimidine, glucosamine-6-phosphate and nonessential amino acids), each involved in multiple other pathways, the interpretation of reported concentration changes and their correlation with the observed CEST signal must be done with caution [64].

Alterations to the metabolomic profile are likely to trigger a cascade of effects altering the concentrations or kinematics of amide, amine and hydroxyl-containing compounds. In addition, the pH of the micro-environment, the fatty-acid content and, both through altered metabolism and poor vascularity, the water-content may also be affected. As CEST is sensitive to precisely these types of changes there is a strong basis for further investigation of its diagnostic utility.

2.2.1 The Warburg Effect

In the presence of abundant oxygen, nonproliferating tissues (labelled as “differentiated tissue” in Figure 2-2) first metabolize glucose to pyruvate via glycolysis and then completely oxidize most of that pyruvate in the mitochondria to CO_2 during the process of oxidative phosphorylation.

When the oxygen supply is limited, for example in tumors due to poor vascular supply of oxygenated blood, cells can redirect the pyruvate generated by glycolysis away from mitochondrial oxidative phosphorylation by generating lactate through a process known anaerobic glycolysis. This allows glycolysis to continue (by cycling NADH back to NAD+) but results in the production of far less ATP (4 moles of ATP per molecule of glucose compared to 36 moles under oxidative phosphorylation).

Warburg observed that cancer cells tend to convert most glucose to lactate regardless of whether oxygen is present, in a process referred to as ‘aerobic glycolysis’ which is also observed in normal proliferative tissues [66]. In both cancer cells and normal proliferating cells, while mitochondria remain functional, oxidative phosphorylation is reduced in favor of more lactate production. This process of ‘aerobic glycolysis’ is less energy efficient than oxidative phosphorylation, but it is faster and provides the cell with copious amounts of necessary metabolites for proliferation [66][67].

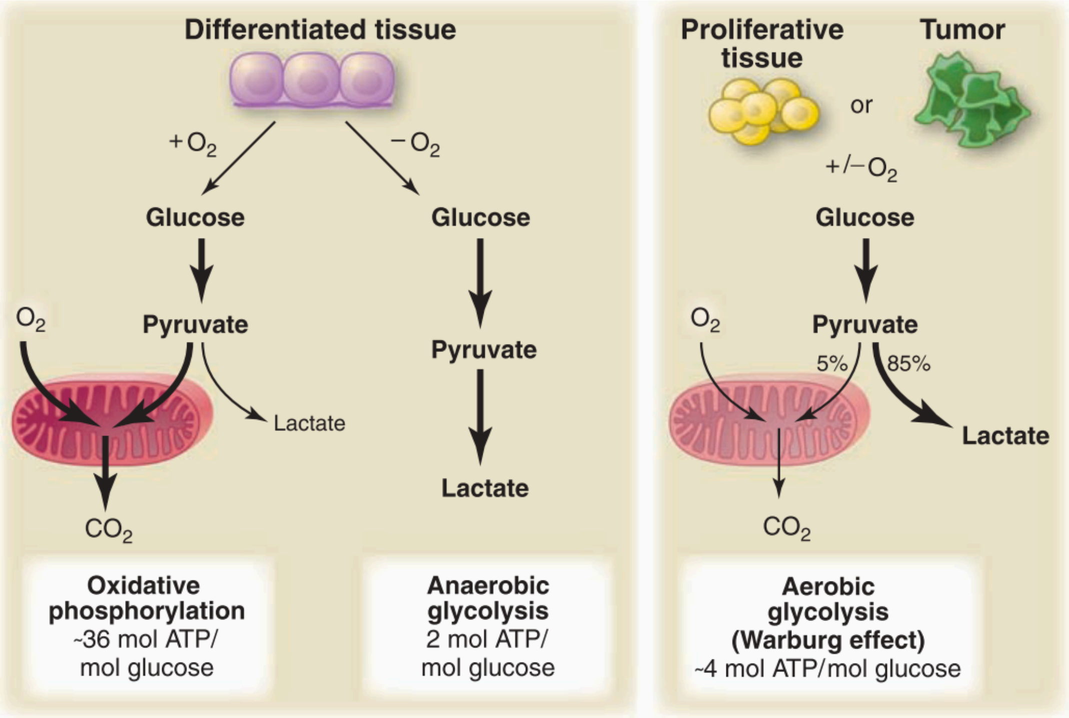
Differentiated tissue
+O2
−O2
Glucose
Glucose
O2
Pyruvate
Pyruvate
Lactate
Lactate
CO2
Oxidative phosphorylation
~36 mol ATP/ mol glucose
Anaerobic glycolysis
2 mol ATP/ mol glucose
Proliferative tissue
Tumor
or
+/−O2
Glucose
O2
Pyruvate
5%
85%
Lactate
CO2
Aerobic glycolysis (Warburg effect)
~4 mol ATP/mol glucose

Figure 2-2: *A schematic illustration highlighting the differences between oxidative phosphorylation, anaerobic glycolysis, and aerobic glycolysis, also known as the Warburg effect. Figure reproduced from* [66].

2.3 CEST applications in cancer

2.3.1 Gleason Grading of Prostatic Carcinoma

Histopathology is the gold-standard for prostate lesion categorization and the established scoring system for prostate biopsies is known as ‘Gleason Grading’, so-named after Donald Gleason who worked to develop the system at the Minneapolis Veterans Administration Hospital in the 1960s [68]. The system forms a key part of standard practice for predicting cancer outcomes and is periodically reviewed and adapted at global consensus meetings to ensure that it serves the community of clinicians that rely on it optimally [69][70][71][72].

To obtain a Gleason score, a biopsy sample is viewed under a microscope and the cell patterns are assessed. A range of cell patterns are illustrated in Figure 2-3 and these have been split into five categories, each with a numeric label.

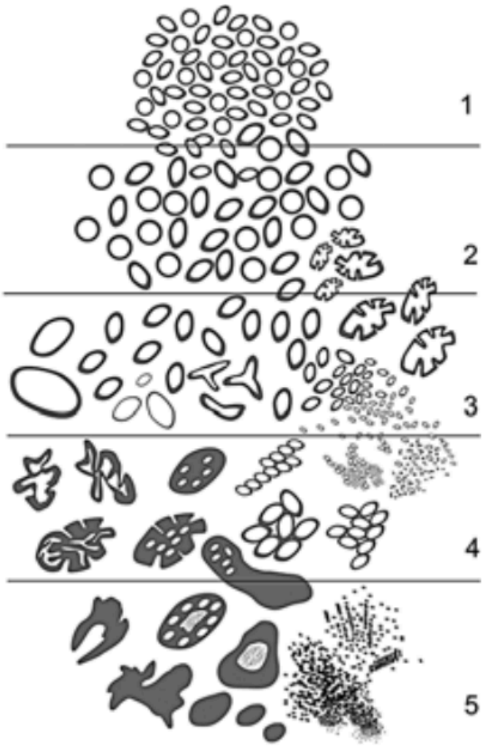

***Figure 2-3**: The current most recent consensus-meeting-driven Illustration of five categories of cell patterns that may be found in tissue from prostate biopsy and their numerical score within the Gleason grading system. At higher scores the cells are less well-differentiated, with more stroma between glands, and the masses become more neoplastic and irregular with only occasional gland formation. Typically, more than one pattern will be present in a given sample. Figure reproduced from* [70].

Corresponding examples from histology are shown in Figure 2-4. The final Gleason score is the sum of the grades of (1) the most predominant pattern observed in the sample, and (2) the highest grade of the secondary or (if present) tertiary patterns [70][71][73]. Both constituent numbers are retained as these also have individual predictive value. For example, both Gleason 3+4 and Gleason 4+3 have a total Gleason score of 7, but the latter is associated with less favourable outcomes than the former [74]. Gleason scores of 6 or above are considered to be of clinical interest. A revised scoring system has recently been proposed and is being introduced alongside the existing system [71]. In both systems, higher scores are associated with poorer prognosis.

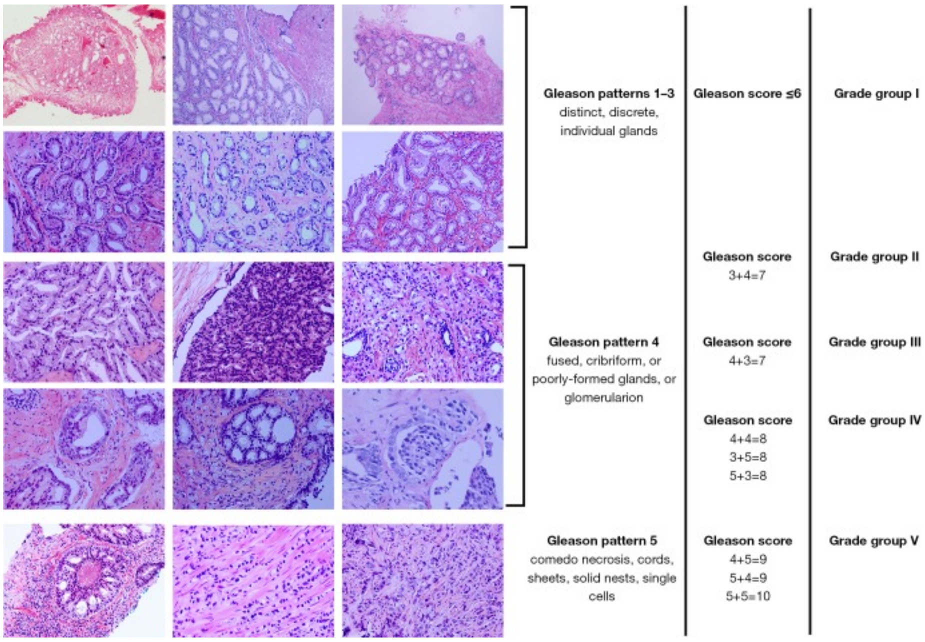
Gleason patterns 1–3
distinct, discrete, individual glands
Gleason score ≤6
Grade group I
Gleason score 3+4=7
Grade group II
Gleason pattern 4
fused, cribriform, or poorly-formed glands, or glomerularion
Gleason score 4+3=7
Grade group III
Gleason score 4+4=8 3+5=8 5+3=8
Grade group IV
Gleason pattern 5
comedo necrosis, cords, sheets, solid nests, single cells
Gleason score 4+5=9 5+4=9 5+5=10
Grade group V

Figure 2-4: *Histology images for a range of Gleason scores showing the classical Gleason scores and the recently proposed Grade Groups. Figure reproduced from* [71].

2.3.2 Prostate cancer imaging

The National Institute for Health and Care Excellence (NICE) reports that as of 2014 prostate cancer was the most common cancer in men in the UK (excluding non-melanoma skin cancer) and accounted for 26% of all male cancers in England and Wales in 2010 [75].

A key diagnostic tool in the prostate cancer detection and treatment pipeline is the use of multi-parametric MRI (mp-MRI) protocols and radiologist scoring schemas, which are becoming increasingly harmonized across sites as radiological consensus continues to emerge [76][77].

While mp-MRI has been shown to improve detection of clinically significant prostate cancer [78] approximately a third of cases remain equivocal [79][80]. There is a clear clinical need to improve prostate cancer diagnosis and simultaneously reduce the need for biopsies by developing new non-invasive imaging methods. CEST may be able to provide metabolic information to support existing mp-MRI protocols.

Prior to the publication of the work outlined in chapters 4 and 5 of this thesis [81], only two published studies had focused on the applications of CEST in prostate cancer imaging. The first of these by Jia et al published in 2011 [23] demonstrated that amide proton transfer ratio (APTR) measurements in regions of prostate cancer were significantly higher than in benign peripheral zone (PZ) regions as shown in Figure 2-5. In 2016, Takayama et al [24] published results from the analysis of CEST data from 66 prostate tumors which suggested that amide proton transfer (APT) measurements in Gleason 7 lesions are significantly higher than in Gleason 6, 8 and 9 lesions and in regions of benign prostate hyperplasia (BPH). These results are reproduced in Figure 2-6.

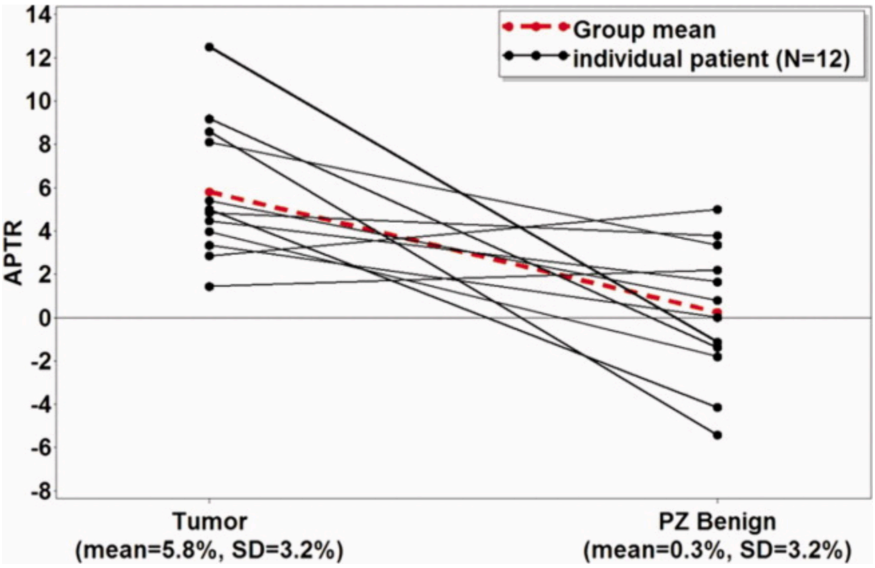

Figure 2-5: *Results from Jia et al who measured differences in APTR between prostate cancer and benign peripheral zone tissue in twelve patients. Figure reproduced from* [82].

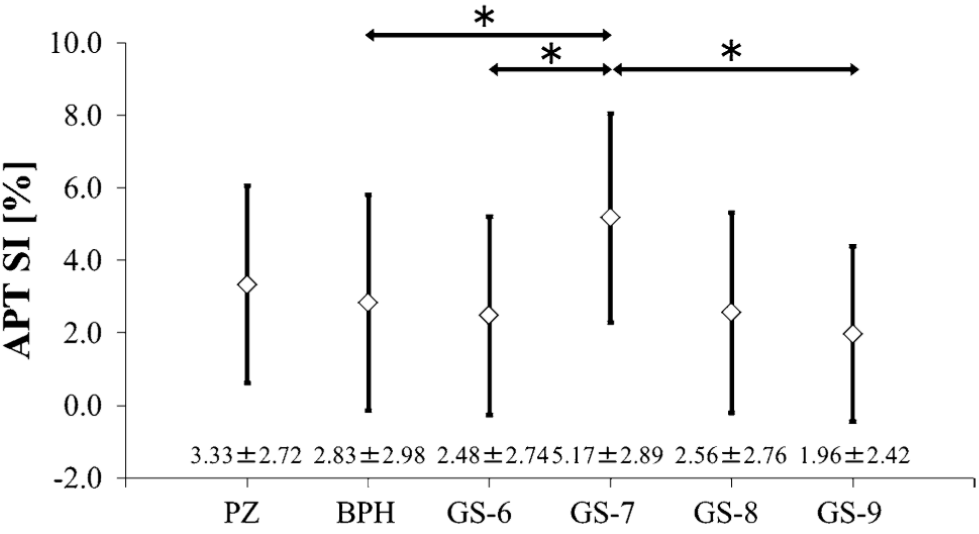

Figure 2-6: *Results from Takayama et al, who found that APT signal was significantly raised in Gleason 7 lesions compared to regions of benign prostate hyperplasia (BPH), and Gleason 6 and 9 lesions. Data acquired from 66 patients. Figure reproduced from* [24].

These two sets of results provided the initial motivation for the further investigation into the possibilities of CEST imaging of the prostate described in this thesis. In particular, the aim was to understand whether Lorentzian fitting of CEST z-spectra, which has previously only been applied at pre-clinical field strengths, is feasible using data acquired in the prostate at 3.0T.

In order for the clinical potential of the technique to be explored fully, an optimization of the acquisition and analysis, and evaluation of the repeatability of the results is needed. This technical development, carried out in a cohort of healthy volunteers, is described in chapter 4. The optimised protocol is then applied in prostate cancer patients in chapter 5 and the initial results are evaluated. This work was published as a piece of original research in the Journal for Magnetic Resonance Imaging (JMRI) in February 2019 [81].

2.3.3 Glioma imaging

Gliomas are the most common primary intracranial tumours, representing 81% of malignant brain tumours, and are associated with poor prognosis. A 2014 review by Ostrom *et al* reported a 5-year relative survival rate for glioblastomas (the most common histological subtype of gliomas, constituting ~45% of all glioma diagnoses), of ~5% [83].

MRI usually plays a central role in the diagnosis, characterisation, surveillance and monitoring of gliomas. High resolution T1-weighted and T2-weighted imaging are supplemented with gadolinium enhanced sequences to obtain high-resolution multiplanar structural information. While MRI has tended to become the imaging modality of choice for imaging gliomas, supplanting contrast-enhanced CT, the low specificity means it can still be difficult to delineate tumour from healthy brain tissue, with up to one third of non-enhancing gliomas being malignant [84]. An additional problem in glioma imaging is that of ‘pseudoprogression’ whereby new or enlarging areas of contrast agent enhancement are observed in imaging after radiotherapy treatment, which subside or stabilise without additional therapy [85]. Several methods for distinguishing between real progression and pseudoprogression have been suggested [85] but even when applied in combination these are not fully accurate. CEST is a strong contender and has already received some attention in light of this problem [86][87].

This provides a basis for further investigation into imaging methods that exploit not just the tissue T1 and T2 properties, or diffusion characteristics but metabolically-based contrast mechanisms such as CEST. Indeed, several studies have investigated the utility of CEST in delineation of glioma from healthy tissue [18][19][21][88][89][90], correlation with histopathological grade [91][92], and differentiation of radiation necrosis from tumour recurrence [4][93].

Some of the concentration changes reported in metabolomic studies of glioma are large enough to be in principle detectable by CEST imaging. For example, cancer-associated mutations on the isocitrate dehydrogenase 1 (IDH1) gene can lead to increased levels of 2-hydroxyglutarate (2HG) [94]. Dang *et al* showed significant 100-fold increases in 2HG concentration of up to 10 mMol L^{-1} in malignant gliomas in humans containing R132 mutations [94]. When compared to the expected amino acid concentration in normal brain of approximately 20–25 mMol L^{-1} [95], these concentration changes are clearly relevant to the observed CEST contrast and recent work by Paech *et al* has demonstrated that CEST MRI at 7.0T is able to predict IDH mutation status in human glioma patients [96].

Consensus recommendations for a standardized brain tumor MRI protocol from the European Organization of Research and Treatment of Cancer (EORTC) Brain Tumor Group (BTG) include the administration of gadolinium-based contrast media [97]. If CEST is to be adopted clinically it is therefore crucial to understand whether or not *in vivo* CEST measurements are sensitive to the effects of Gd-administration both in terms of the absolute signal measurements and the tumour image contrast and this subject is explored in chapter 8.

2.4 Clinical focus of this thesis

In summary, the clinical questions explored in the remaining chapters of this thesis on 3.0T clinical scanners are the following:

- Sequence optimisation for prostate imaging
- Repeatability of prostate metrics from Lorentzian fitting
- Preliminary assessment of prostate cancer image contrast
- Evaluation of the effects of Gd on glioma CEST image contrast

3 Fitting the water peak: Lorentzian vs Bloch

The direct saturation of water in the z-spectrum is well-modelled by Lorentzian lineshape when applying a single long continuous-wave saturation pulse, but when using pulsed-saturation (as we must on clinical scanners if saturation durations are to exceed ~1s) additional complexity is introduced to the z-spectrum which is not accounted for by the Lorentzian lineshape. This is a confounding effect that can directly impact on the fitted parameters of the water, CEST and NOE peaks. Questions to be answered include: what is the magnitude of the impact on the final fitting parameters? And is a better-performing, practically implementable alternative available?

The work outlined in this chapter approaches these questions by comparing the fitted parameters and the goodness-of-fit when fitting the water peak using two different lineshapes:

- a standard Lorentzian lineshape, and
- a lineshape generated by numerically solving the Bloch equations

Chapter Contributions:

I designed the experiment and planned, created and scanned the phantoms and wrote the analysis scripts.

David Atkinson (Reader, primary supervisor)[1]: Provided initial training using the Philips 3.0T Achieva at UCLH and provided continual support with the CEST patch used throughout this thesis.

Francisco Torrealdea (Postdoctoral Researcher and Clinical Scientist)[1,2], Marilena Rega (Clinical Scientist)[3] and Eleni Demetriou (Postdoctoral Researcher)[4]: Institute of Neurology laboratory training.

Francisco Torrealdea[1,2], Marilena Rega[3]: Provided guidance when implementing the Bloch equations and ode45 function for solving them in Matlab.

James Fairney and Catherine Morgan: Provided initial input on the development of the CEST patch during their time at UCL.

Contributor affiliations:

[1] Centre for Medical Imaging, University College London, 43-45 Foley St, Fitzrovia, London, W1W 7TS, United Kingdom

[2] UCLH Medical Physics and Biomedical Engineering, Elizabeth Garrett Anderson Wing, University College Hospital, 25 Grafton Way, London, WC1E 6DB

[3] Institute of Nuclear Medicine, University College London Hospital NHS Foundation Trust, 5th Floor Tower, University College Hospital, 235 Euston Road, London, NW1 2BU

[4] Institute of Neurology, University College London, Queen Square, London, WC1N 3BG

3.1 Introduction

There are two common approaches to fitting the CEST z-spectrum: fitting using multiple lineshapes or fitting to solutions of the Bloch-McConnell (BM) equations.

A Lorentzian lineshape is defined by three parameters: the offset frequency, the full width at half maximum (FWHM) and the amplitude. These parameters may vary independently in the model and they influence the fit result in relatively predictable ways. The fitted parameters do not directly relate to physical parameters, but are instead useful for semi-quantitative evaluation of the contributions to the z-spectrum from each exchangeable pool [49][88].

BM-fitting involves exploration of a much larger parameter space than the sum-of-Lorentzians approach. The fitting parameters relate to both physical and saturation parameters. Physical parameters include pool chemical shifts, relative pool concentrations, exchange rates (both between solute pools and water, and sometimes between solute pools) and T1 and T2 values of each pool. The saturation parameters are also required, including pulse-shape and duration, inter-pulse delay, B_1 amplitude and the total number of pulses (assuming a repeated train of identical saturation pulses). BM-models comprised of linked differential equations may be solved either numerically or analytically and the fitted parameters relate directly to physical quantities. Numerical solutions involving fewer approximations produce results that are closer to the mathematical ground-truth of the system as defined by the equations but can be very computationally-intensive. Various analytical solutions have been proposed [98][99] each of which make different approximations in order to reduce the parameter space that needs to be explored.

Oscillatory effects arise in the z-spectrum close to 0ppm when using pulsed saturation schemes. The basis of these oscillations are discussed below and representative examples are shown in Figure 3-4.

3.1.1 Physical basis of oscillatory effects in the z-spectrum close to 0ppm

Saturation at far-off-resonant frequencies has little direct influence on the M_z of water but close to 0ppm, spill-over effects cause the width of the water resonance to be non-zero. In the case of CW saturation, the spill-over effect can be modelled as a relatively simple and smoothly varying effect, but in the pulsed-saturation case the value of the z-spectrum develops an oscillatory component which is strongly dependent on the saturation frequency, saturation timings, B_1 power and T1 and T2 values.

The commonly used "cone-model", outlined in Figure 1-12, illustrates the evolution of **M** in the rotating-frame during the application of an off-resonance B_1-pulse. As the frequency of the applied B_1 is off-resonant with the Larmor frequency of water ($\omega_{RF} \neq \omega_0$), a non-zero 'effective B_0' exists in the rotating frame. This B_{0eff} is expressed as $\frac{\Delta\omega}{\gamma}$ where $\Delta\omega = \omega_{RF} - \omega_0$. The emergence of B_{0eff} within the rotating frame means that the vector around which the **M** now precesses, B_{eff}, is comprised of two orthogonal components such that:

$$\boldsymbol{B_{eff}} = \boldsymbol{B_{0eff}} + \boldsymbol{B_1} \tag{3-1}$$

The magnitude of which is:

$$B_{eff} = \sqrt{{B_0}^2 + {B_1}^2} = \frac{\omega_{eff}}{\gamma} \tag{3-2}$$

The inclination of B_{eff} relative to the z-axis is:

$$\theta = \text{ARCTAN}\left(\frac{B_1}{B_{0eff}}\right) \tag{3-3}$$

And the flip-angle, ϕ_{OnRes}, of **M** around B_1 after an on-resonance pulse of power duration τ_p is expressed as:

$$\phi_{OnRes} = \omega_1 . \tau_p \tag{3-4}$$

Which, for an off-resonance pulse becomes:

$$\phi_{OffRes} = \omega_{eff} . \tau_p \tag{3-5}$$

In the off-resonance case, **M** does not precess only in one plane (conventionally labelled the *y*-*z*-plane as B_1 is applied along the *x*-axis), but instead sweeps out a cone-shape, as shown in Figure 1-12. Assuming **M** has no transverse component prior to a B_1 pulse (i.e. **M**(0) = $\mathbf{M_{zinit}}$), the M_z-component of **M** will oscillate throughout the pulse in a sinusoidal fashion between its initial value M_{zinit} and some minimum value, M_{zmin}, which is determined by θ and calculated trigonometrically as:

$$M_{zmin} = M_{zinit}.\cos(2\theta) \tag{3-6}$$

An equation describing the oscillation of M_z between the initial value of M_{zinit} and the lower-bound of M_{zmin} over time during a constant B_1 pulse (excluding T1, T2 and exchange effects) may therefore be written:

$$M_z(t) = A.cos\left(\phi_{OffRes}\right) + C \tag{3-7}$$

Where:

$$A = \frac{(M_0 - M_{zmin})}{2} \tag{3-8}$$

And:

$$C = \frac{(M_0 + M_{zmin})}{2} \tag{3-9}$$

Figure 3-1 illustrates the behaviour described by equation 3-7. The derivation above neglects T1, T2 and exchange effects in order to illustrate the principle that underpins the emergence of the zig-zag pattern. The spill-over effect in the presence of pulsed off-resonance saturation is highly variable and dependent on the offset-frequency and the B_1.

The concern is that data-points close to 0ppm may skew the fitting results of other pools, reducing the accuracy of reported fit results. To better understand these risks, a hybrid fitting approach is tested whereby CEST and NOE pools are fitted using Lorentzian lineshapes while the water resonance is fitted using a lineshape generated using a Bloch-simulation. The hypothesis is that this approach may be able to account for the confounding features close to 0ppm better than a fit using only Lorentzian lineshapes, and without having to perform a full BM fit. The fit results and goodness-of-fit measures obtained when using the hybrid approach are compared to those obtained when using the standard sum-of-Lorentzians approach in phantom data. Alternative weighting schemes are also considered and these are outlined in the methods section.

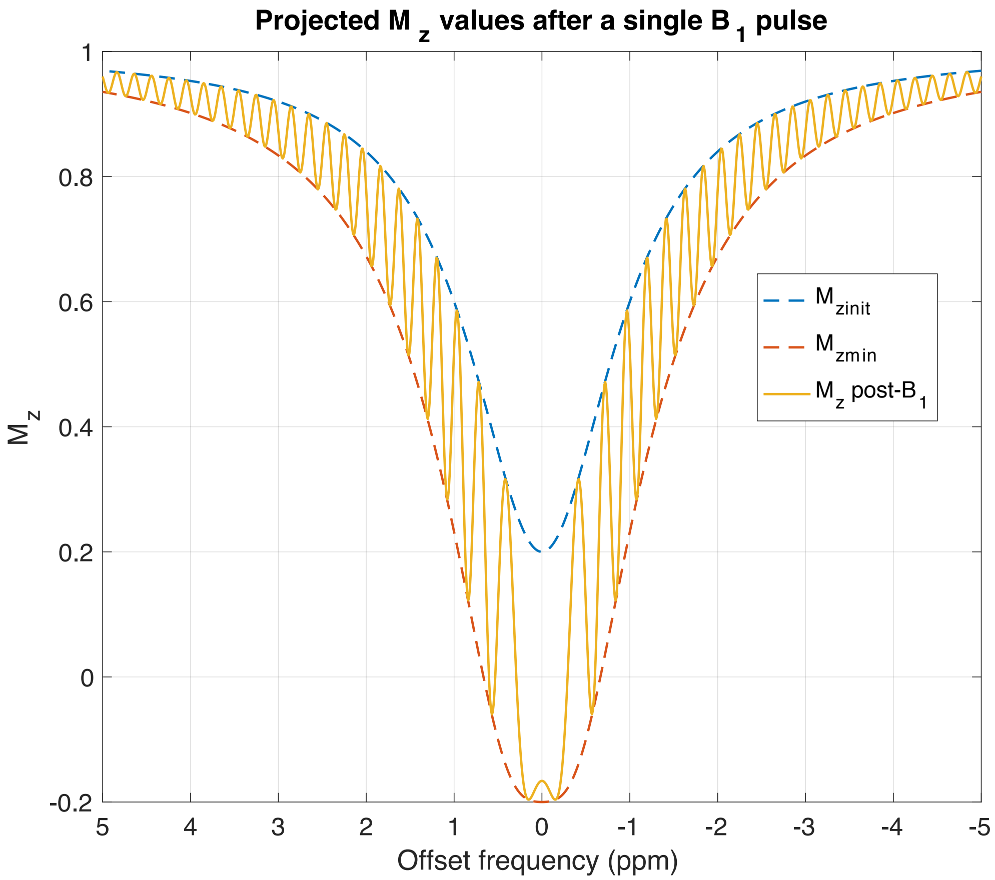

Figure 3-1: *Calculated values of the post-B1 M_z after the application of a single, rectangular B1-pulse of power 2.0μT and duration $\tau_p = 40ms$ at 3.0T. The oscillatory nature of 'Mz post-B_1' illustrates how moving from CW to pulsed-saturation introduces additional complexity to the z-spectrum.*

In addition to comparing results when using the two lineshapes, novel approaches to the weighting of data-points to 0ppm is also investigated as a means of improving accuracy of fits.

3.2 Methods

3.2.1 Phantom Preparation

A multi-compartment phantom was prepared consisting of five 50ml Falcon tubes, four of which contained a 200mM solution of nicotinamide (Sigma-Aldrich, St. Louis, MO) [88][100] and one of which contained water only. CEST effects at slower exchange rates are more likely to be observable using clinical scanners (with the associated RF limitations) than those at higher exchange rates. Therefore an amide-containing molecule was selected due to the slow exchange rate of amides compared to amine and hydroxyl groups.

The optimum pH for observing the amide peak in nicotinamide was not known, therefore the compartments containing nicotinamide were controlled to pH values of 5, 6, 7 and 8 (see Table 3-1) using HCl and NaOH. Measurements were made with a digital pH-meter (Mettler Toledo International, Inc).

Tube #	Description	Concentration (mMol l^{-1})	pH	Gd
Tube 1	Nicotinamide solution	200	5	No
Tube 2	Nicotinamide solution	200	6	No
Tube 3	Nicotinamide solution	200	7	No
Tube 4	Nicotinamide solution	200	8	No
Tube 5	Water only	0	-	No

Table 3-1: *Description of nicotinamide phantom compartments*

The falcon tubes were fixed in place within a larger plastic container, which was filled with water and sealed. A T2-weighted image of the phantom, labelled to indicate the tube configuration, is shown in Figure 3-2.

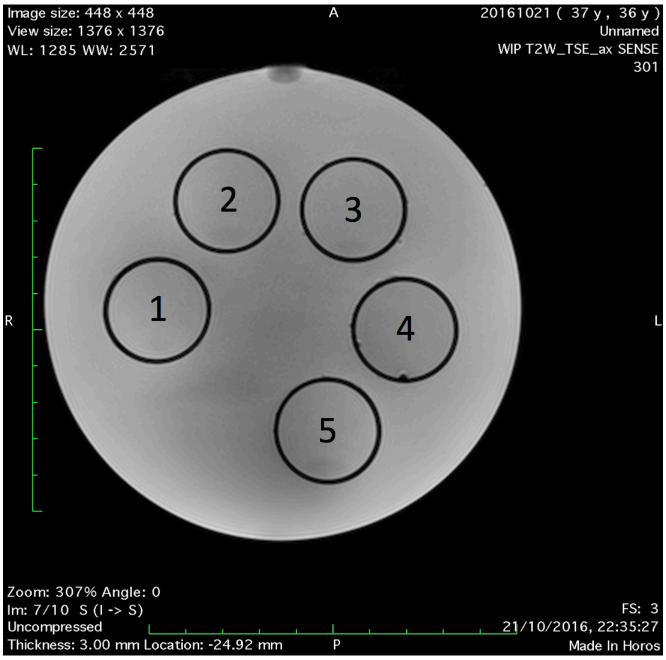
Image size: 448 x 448
View size: 1376 x 1376
WL: 1285 WW: 2571
A
20161021 (37 y , 36 y)
Unnamed
WIP T2W_TSE_ax SENSE
301
2
3
1
4
5
R
L
Zoom: 307% Angle: 0
Im: 7/10 S (I -> S)
Uncompressed
Thickness: 3.00 mm Location: -24.92 mm
P
FS: 3
21/10/2016, 22:35:27
Made In Horos

Figure 3-2: *T2-weighted image labelled to show the configuration of the phantom.*

3.2.2 MRI Imaging Protocol

Data were acquired using a 3.0T Achieva MRI scanner (Philips Healthcare, Best, The Netherlands). The phantom was scanned within 3 hours of preparation to minimize any degradation of the contents due to biological contaminants.

A single-slice spoiled gradient echo read-out (voxel-size 2x3x4mm) with flip-angle 10° was used. The saturation scheme comprised of a train of 40 sinc-Gaussian RF pulses with pulse duration (τ_p) = 40ms and inter-pulse-delay (τ_d) = 40ms. Images were acquired over 81 frequency offsets separated by 0.0625ppm between ± 1ppm, and by 0.125ppm outwards to ± 5ppm, with additional data-points at ± 7.5, ± 10.0, ± 12.5, ± 15.0, ± 20.0, ± 25.0, and ± 300.0ppm. Four different saturation powers were used between with B_{1eq} ranging from 0.49μT to 1.47μT. The saturation power was varied by changing the saturation flip-angle only. The flip angles used were 600°, 976°, 1400° and 1800°.

Dual-echo phase-maps were acquired interleaved between CEST acquisitions to allow for the generation of B_0-maps for field inhomogeneity corrections.

3.2.3 Post-processing

All data processing was done using home-written software developed using Matlab R2016a (Mathworks, Natick, MA, USA).

B_0-corrections were performed by calculating B_0-maps from the dual-echo phase maps and shifting each z-spectrum the required amount. Normalization of each z-spectrum was done using the M_z value at 300ppm. Regions-of-interest (ROIs) were drawn over each falcon tube and all z-spectra within the ROI were averaged to generate a single z-spectrum for each tube at each $B1_{eq}$.

The fit model contained lineshapes to account for the water, amide and NOE contributions. A whole-fit vertical offset was included to correct for imperfect normalization.

All data were fitted twice. The first fit was done using a Lorentzian to account for the direct saturation, and the second used a lineshape generated from the numerically-solved Bloch equations. Fitting parameters and their constraints are shown in Table 3-2. A non-linear-least-squares algorithm was applied to minimize the difference between the measured z-spectrum and the fit results.

Water Lorentzian	**Min**	**Max**	**Initial**
Scaling factor (A.U)	1.00	10.0	2.00
FWHM (ppm)	0.10	4.00	2.00
Frequency offset (ppm)	-0.01	0.01	0.00
Water Bloch Simulation			
Scaling factor	0.80	1.20	1.00
T1 of water (s)	2.10	3.90	3.00
T2 of water (s)	0.04	0.75	0.15
Saturation flip-angle (°)	150	2500	500
Amide Lorentzian			
Scaling factor (A.U)	0.01	3.00	0.20
FWHM (ppm)	1.00	4.00	1.50
Frequency offset (ppm)	2.50	3.00	2.70
NOE Lorentzian			
Scaling factor (A.U)	0.10	1.50	1.00
FWHM (ppm)	0.50	6.00	1.50
Frequency offset (ppm)	-3.50	-2.70	-3.10
Whole fit			
Vertical offset	-0.10	0.10	0.00

***Table 3-2**: Fitting parameters used when fitting z-spectra acquired in the Nicotinamide phantom.*

3.2.3.1 Weighting schemes

As the oscillatory behavior only occurs close to 0ppm (and is typically constrained to the ±1ppm range), a secondary research question was whether or not we could compensate for it by reducing the weighting of data-points in this chemical shift range. It was considered that ignoring or down-weighting these points may provide an alternative method for minimising the disruption caused to the fit results by the oscillatory data-points.

Four weighting schemes, illustrated in Figure 3-3, were tested:

1) All points weighted equally.
2) Points between ± 1ppm were completely ignored (assigned a weighting of zero).
3) Weighting of points between ± 1ppm was linearly tapered such that the weighting was zero at 0ppm.
4) Weighting of points between ± 1ppm followed an inverse Lorentzian-profile with a FWHM of 0.5ppm and an amplitude of 1, such that the weighting was at 0ppm was zero.

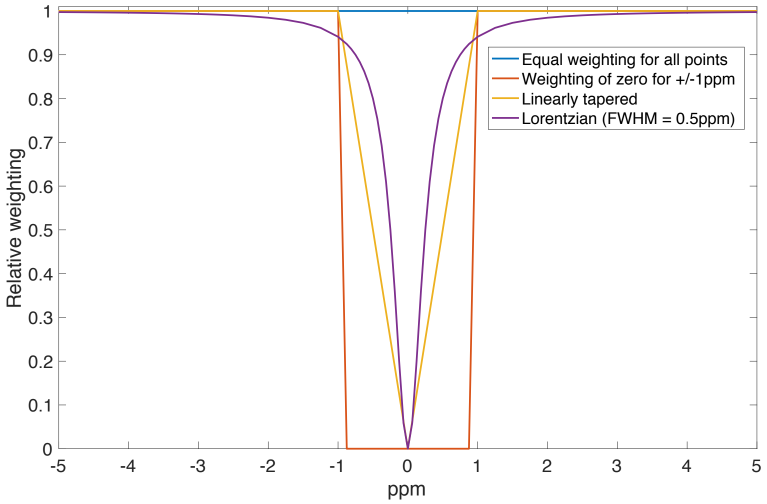

Figure 3-3: *Four weighting schemes used to fit nicotinamide phantom data.*

3.2.3.2 Data Analysis

The heights of the fitted amide and NOE peaks were compared across methods and weighting schemes to assess the level of variation. The goodness-of-fit (GOF) was quantified using the root-mean-square deviation (RMSD):

$$RMSD = \sqrt{\frac{\sum_{t=1}^{T}(\hat{y}_t - y_t)^2}{T}} \tag{3-10}$$

Where $\hat{y}_t$ is the model-predicted value corresponding to real observation y_t which is one element of a set comprised of *T* data-points. An RMSD of zero would indicate a perfect fit to the data.

The RMSD was evaluated using data-points between ±5ppm, excluding points between ±1ppm where our weighting varied between schemes. The RMSD from each model-type (Lorentzian vs Bloch) and each weighting scheme are compared for every z-spectrum.

3.3 Results

Figure 3-4 shows representative B_0-corrected z-spectra (solid-lines) and MTR_{asym} (dashed-lines) from the pH 8 tube at all four saturation powers. The maximum MTR_{asym} is observed close to 2.8ppm consistent with previous work [100] and the oscillations close to 0ppm are clearly visible.

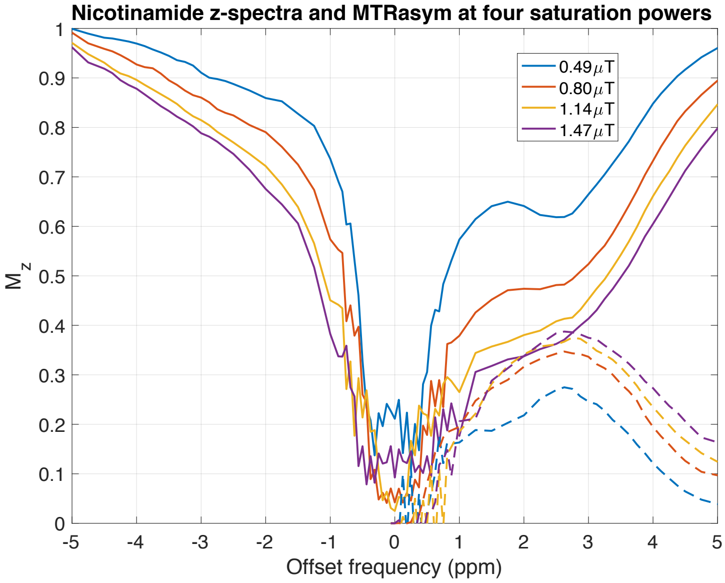

Figure 3-4: *Z-spectra (solid-lines) and MTR_{asym} (dashed-lines) from 200mM nicotinamide solution at pH 8, scanned at four different saturation powers (see legend).*

Asymmetry maps were calculated using the MTR_{asym} at 2.75ppm and are shown in Figure 3-5 and Figure 3-6 shows a representative z-spectrum which has been fitted using both Lorentzian and Bloch methods. Results are shown both for weighting scheme 1 (all data-points weighted equally) and weighting scheme 2 (data-points in the ±1ppm range weighted to zero). The associated fit residuals are also shown.

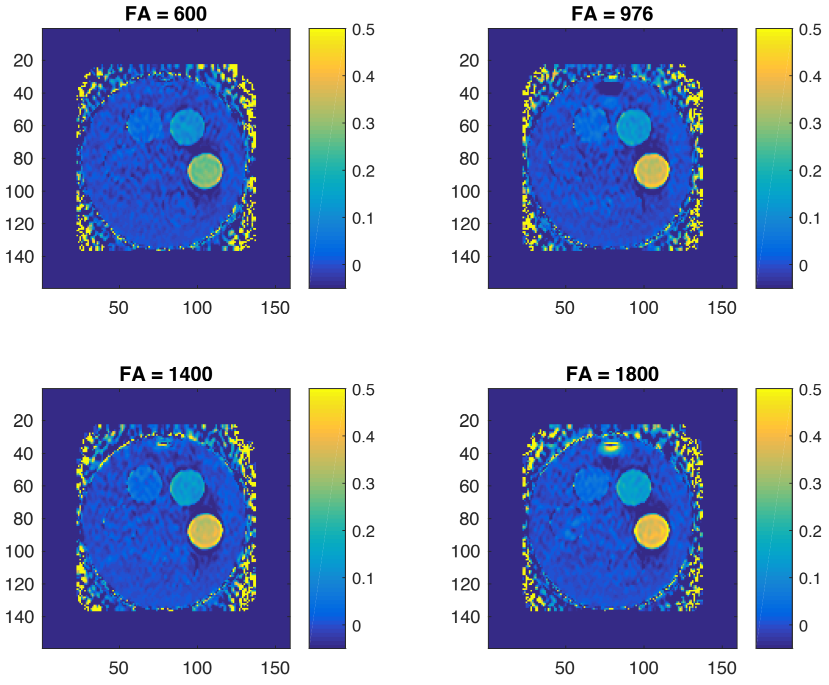

Figure 3-5: *Maps of MTR_{asym} at 2.75ppm. Concordant with the representative z-spectra shown in Figure 3-4, the asymmetry increases with saturation power and also with pH for these samples. The water tube shows no visibly discernible asymmetry.*

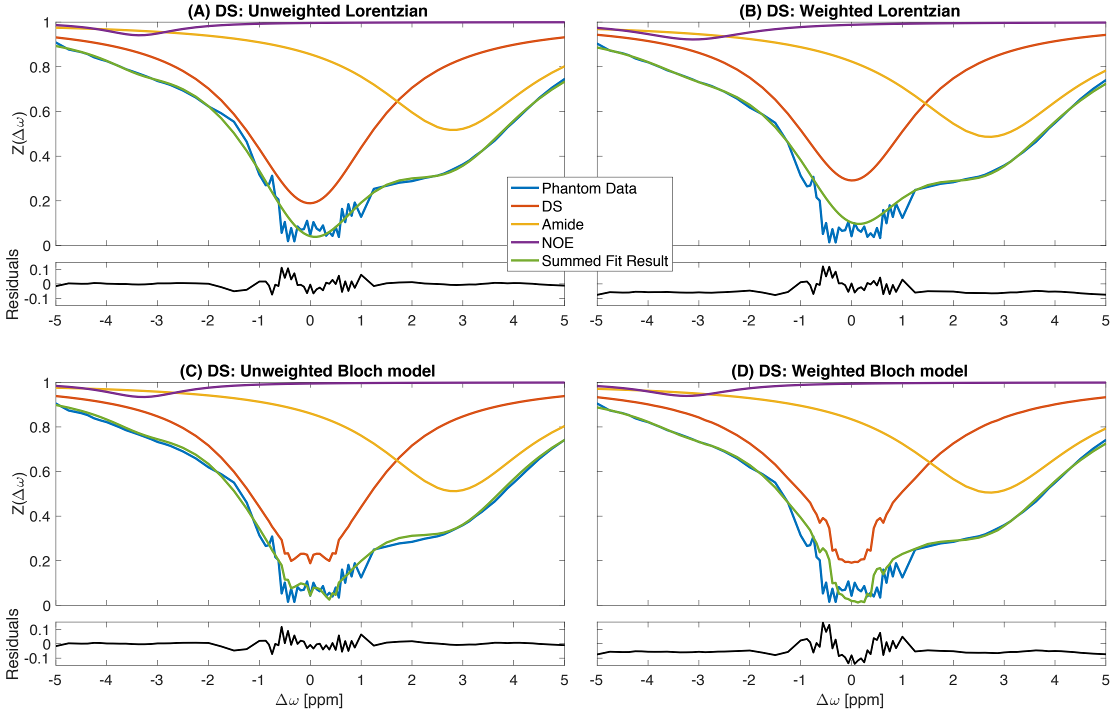

Figure 3-6: *A representative z-spectrum (pH8 at maximum saturation $B1_{eq}$ = 1.47μT) with fit results for (**A)** a Lorentzian for the water peak with all data-points equally weighted, (**B)** a Lorentzian for the water peak with data-points in the±1ppm range weighted to zero, (**C)** a Bloch simulation for the water peak with all data-points equally weighted, and (**D)** a Bloch simulation for the water peak with all data- points in the±1ppm range weighted to zero.*

3.3.1 Fitted peak heights

Figure 3-7 shows the heights of the fitted amide and NOE peaks as a function of pH for Lorentzian fits and Bloch fits over all four weighting schemes for the B_{1eq} = 1.14μT case. Both the amide and NOE data show good agreement between methods with variations in peak heights on the order of 0.001. In both the amide and NOE data, and for both the Lorentzian and Bloch-based fitting approaches, the results when using weighting scheme 2 (all points in the ±1ppm range weighted to zero) show the greatest deviations from the group mean.

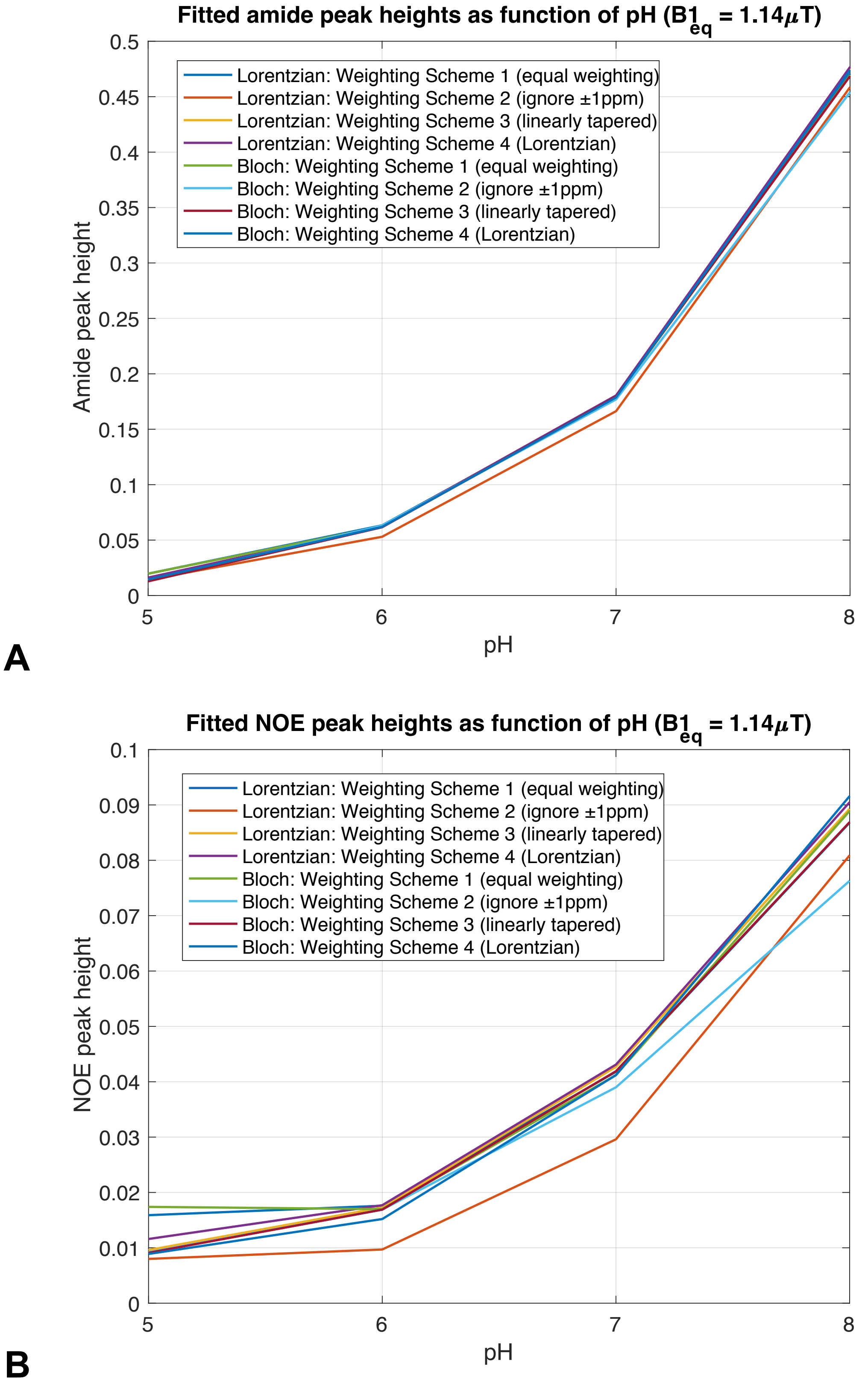

***Figure 3-7:** Fitted peak heights for the **(A)** amide and **(B)** NOE peaks when fitting the water peak with either a Lorentzian lineshape or a lineshape generated through Bloch simulations. Both the amide and NOE peak heights increase at increasing pH with the amide height in particular showing a strong agreement between all fitting approaches.*

3.3.2 Goodness-of-fit comparisons

Representative RMSD values for both Lorentzian and Bloch-fits of the 1.14μT data are shown in Figure 3-8. The bottom panel contains the difference between the RMSD values from the Lorentzian and Bloch fits such that $RMSD_{diff} = RMSD_{Bloch} – RMSD_{Lorentzian}$. Therefore, as low RMSD values are desirable, in cases where $RMSD_{diff}$ takes a positive value we may conclude that Lorentzian fitting outperformed Bloch fitting.

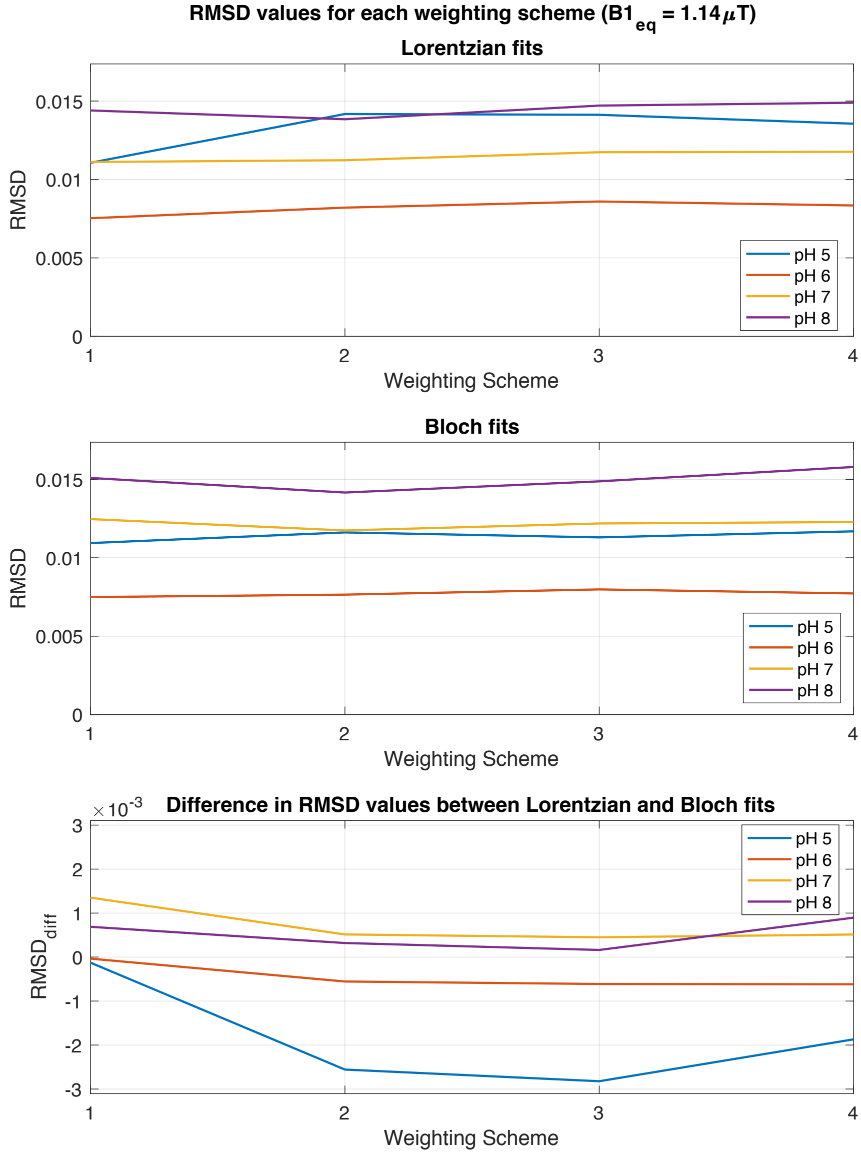
RMSD values for each weighting scheme ($B1_{eq}$ = 1.14μT)

Lorentzian fits

Bloch fits

Difference in RMSD values between Lorentzian and Bloch fits

***Figure 3-8**: Representative RMSD values for each weighting scheme from the 1.14μT dataset. Results for the Lorentzian fits and Bloch fits are shown in the top and middle panels, respectively. The lower panel shows the difference between the RMSDs of the Lorentzian and Bloch results. Positive values of $RMSD_{diff}$ correspond to the Lorentzian fit outperforming the Bloch fit for a given z-spectrum (i.e. yielded a lower RMSD value) and conversely negative values of $RMSD_{diff}$ mean that the Bloch fit outperformed the Lorentzian fit.*

Boxplots of the $\mathrm{RMSD_{diff}}$ values for each weighting scheme, aggregated over all pH values and saturation powers, are shown in Figure 3-9. The red horizontal line indicates the median value of the 16 data-points, the lower and upper horizontal lines of the blue box correspond to the 25th and 75th percentiles respectively, and the black horizontal lines at the end of the dotted stems mark the minimum and maximum values. Outliers are defined as any data-points which are more than 1.5x the interquartile range away from the top or bottom of the blue box and these are marked using a red cross.

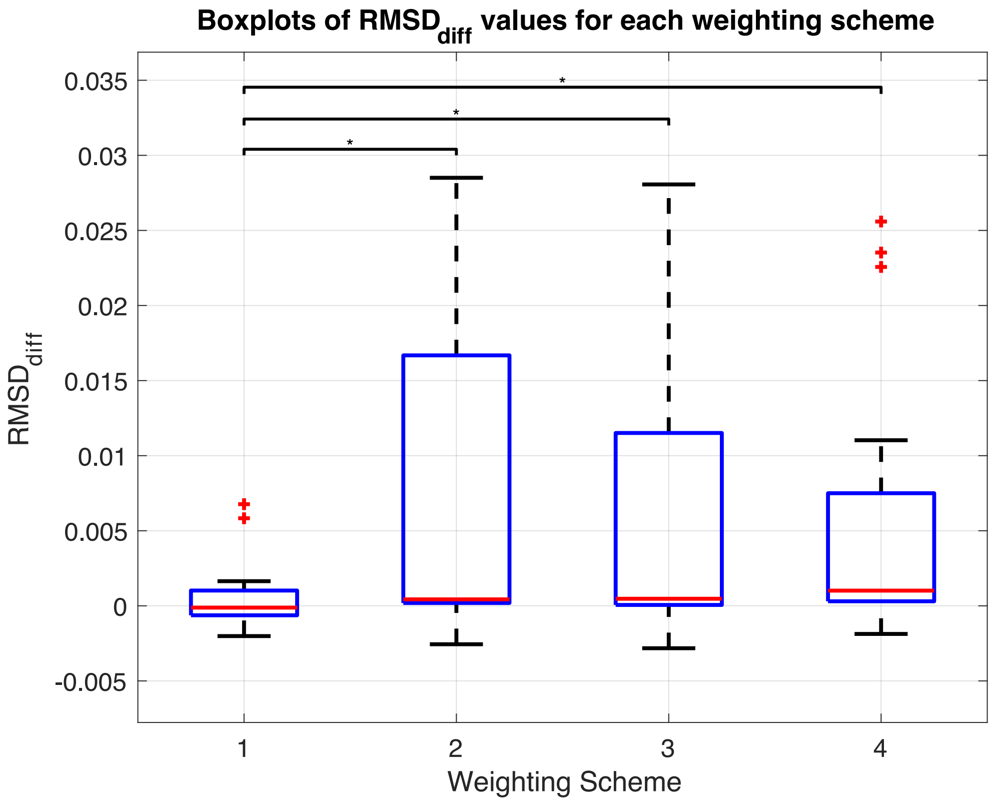

Figure 3-9: *Boxplots of all $\mathrm{RMSD_{diff}}$ values for each weighting method, aggregated over all four pH-values and four saturation powers. Significance was tested between data-points from all weighting schemes using a Mann-Whitney U-test. The null hypothesis is that the two sets of data to be tested are drawn from a continuous distribution with equal medians. Significance threshold was 0.05 and is indicated in the figure with an asterisk. The null hypothesis was rejected in tests comparing the data from weighting scheme 1 with schemes 2, 3 and 4.*

Weighting scheme 1 shows the tightest clustering of $\mathrm{RMSD_{diff}}$ values over all pH-values and saturation powers with a median value of -0.1×10^{-3} and a range of 1.6×10^{-3} (excluding two outliers). Weighting schemes 2, 3 and 4 show similar median values of 0.4×10^{-3}, 0.4×10^{-3} and 1.0×10^{-3}, respectively, but with higher 75th percentiles and maximum extents ranging up to a maximum value of 29.0×10^{-3} in the case of weighting scheme 2. This broader spread of the data is taken to be the underlying reason for the level of statistical significance observed between weighting scheme 1 and the other three schemes as indicated in Figure 3-9. Full tabulation of the values contained in the boxplots plus the mean $RMSD_{diff}$ values are shown in Table 3-3.

Significance tests were performed to compare the differences between results obtained using the four weighting schemes. Only data-points from the first set (weighting scheme 1) were found to be normally distributed (as tested using the one-sample Kolmogorov-Smirnov test) which suggested that significance could not be tested using a two-sample t-test. Instead, the non-parametric Mann-Whitney U-test was applied with significance threshold set at 0.05. The $RMSD_{diff}$ values from all four weighting schemes were tested against each other and the null hypothesis was rejected when comparing weighting scheme 1 to weighting schemes 2, 3 and 4 with p-values of 0.028, 0.048 and 0.028, respectively. These are indicated with asterisks in Figure 3-9.

RMSD ($\times10^{-3}$)	**Weighting scheme 1**	**Weighting scheme 2**	**Weighting scheme 3**	**Weighting scheme 4**
Minimum	-2.01	-2.56	-2.82	-1.87
Lower Adjacent	-2.01	-2.56	-2.82	-1.87
25th percentile	0.63	0.19	0.06	0.30
Median	-0.12	0.43	0.47	1.01
Mean	0.63	7.40	6.60	5.80
75th percentile	1.01	16.7	11.5	7.50
Upper Adjacent	1.64	28.5	28.1	11.0
Maximum	6.77	28.5	28.1	25.6
Percentage data-points > 0	31.3	87.5	75.0	81.3

Table 3-3: *Mean and median root-mean-square deviation (RMSD) differences between Lorentzian and Bloch approaches to fitting the water peak for four different weighting schemes. Other parameters include minima and maxima, 25th and 75th percentiles, and the percentage of the 16 data-points for each weighting scheme which were above zero.*

3.4 Discussion

3.4.1 Fitted peak heights

The fitted amide and NOE peak heights showed very little variation when using different lineshapes and weighting methods. The trend lines (examples shown in Figure 3-7) showed good agreement and the full-range of deviation of fitted peak heights across all powers and weighting schemes was typically no greater than 0.02.

While the NOE contribution was smaller than the amide contribution, it was not expected that there would be any such signal and indeed none is described in other CEST work using nicotinamide phantoms by Zhou et al and Jin et al [88][100]. While Jin et al used a relatively high saturation B_{1eq} power of approximately 4.0μT (which would lead to far less visible NOE peak), Zhou et al used B_{1eq} = 0.75μT which is in the same regime as the data collected here. It is assumed here that Zhou et al neglected to take the NOE into account.

3.4.2 RMSD assessment

As illustrated in the boxplots in Figure 3-9 and data presented in Table **3-3**, the goodness-of-fit was generally better when using a Lorentzian lineshape. The mean $RMSD_{diff}$ values across all four weighting schemes were positive yet very close to zero, suggesting a slight tendency for improvement of the goodness-of-fit when using the Lorentzian method compared to using the Bloch method. Weighting scheme 1 was the only one to have a median $RMSD_{diff}$ less than zero, although this was by a very small margin.

The greatest benefit from using the Lorentzian approach versus the Bloch approach was achieved on data from the pH 6 compartment when saturating with B_{1eq} = 1.47μT and fitting applying weighting scheme 2 (all points in the ±1ppm range weighted to zero). In this case a peak $RMSD_{diff}$ value of 0.0285 was reached produced by RMSD values for Lorentzian and Bloch fitting of 0.009 and 0.038 respectively (data not shown).

The upper limits of $RMSD_{diff}$ were found to be lower for weighting scheme 1 than for the other weighting schemes. This may not be surprising given the fact that weighting schemes 2, 3 and 4 use the same number of fitting parameters as weighting scheme 1 to fit the same number of data-points but some of these data-points have reduced relative-weightings and therefore less influence on the goodness-of-fit. Discrepancies in the goodness-of-fits would have been more worthy of analysis had the variation in the amide and NOE peak heights been greater.

3.4.3 Computation time

The script that was used for data-fitting was run on a Macbook Pro (mid-2015, 2.5GHz Intel Core i7 processor, 16GB 1600MHz DDR3 memory). The only change in the script configuration between the Lorentzian and Bloch-based fitting approaches was to replace a function which calculated a Lorentzian lineshape for a set of parameters with a call to a function which run a set of ordinary differential equations (ODEs) using the ‘ode45’ Matlab solver. Solutions for several Lorentzian fits could be reached per second, while a single Bloch-fit for 93 frequency offsets could take up to 10 hours even after the Bloch simulation codes had been streamlined several times using the Matlab ‘Profiler’ tool to improve computing efficiency. While it would no doubt be possible to speed-up the performance either through code improvements, conversion to C, or use of superior processing power, the CPU-load remains a limitation of the numerical ODE approach to fitting, especially when performing voxel-by-voxel fitting as would be required for any clinical implementations.

3.4.4 Reflections on the Bloch approach

It was hypothesized that using the Bloch approach may improve the goodness-of-fit measures compared to using the Lorentzian approach, allowing for a more accurate modelling of the z-spectrum by taking account of the complex behavior that emerges close to 0ppm in the pulsed-saturation case. It has been shown that this behaviour is sensitive to small deviations in B_0 and B_1.

Despite the greater number of parameters and therefore broader range of possible lineshapes generated using the Bloch method, it does not appear to confer any notable advantage in terms of fit accuracy (the fitted amide and NOE peaks show good agreement between methods) or in terms of goodness-of-fit where it is generally either outperformed by or matched by the Lorentzian approach.

This may be attributed to the physical limitations of spectral and spatial resolution that can be achieved using CEST-MRI. Even in the simple case of nicotinamide solution phantoms, small field fluctuations manifest not only across the image but also at the sub-pixel level. The sum total of these effects is what is processed during image reconstruction thereby presenting a ‘pixel-average’ which may not be sufficiently high resolution for the effects that we are trying to model. These problems will only be exacerbated *in vivo* due to the effects of movement.

Bloch-McConnell fitting, which includes CEST and NOE pools in the simulations, may be able to improve overall goodness-of-fit measures by better modelling the exchange interactions between water and other pools. However, due to the higher-order parameter spaces that need to be explored by the fitting algorithm it would be likely to further increase computation time.

3.4.5 Use of nicotinamide

The decision to use nicotinamide for this study was predicated on it being a simple molecule containing a single amide group and no MT effect. It is also biologically relevant as it is involved in the metabolic pathway as part of nicotinamide adenine dinucleotide (NADH).

After this analysis had been completed it was realized that the single amide group in nicotinamide has two isomeric configurations, each with a different resonant frequency (approximately 2.8ppm and 3.5ppm). Jin et al [100] used nicotinamide in a CEST study with no mention of multiple resonances, and Zhou et al [88] also used it in a CEST study and treated it explicitly as a single resonance.

Therefore, an extra peak was present that was not factored in to the analysis. This was not visibly obvious from the data we acquired due to the broad resonances therefore this analysis was performed using only a single amide peak. It is not expected that this seriously affects the outcome of this study where the two resonances show considerable overlap. Work described in chapter 6 goes on to exploit the fact that there are two amide resonances in nicotinamide.

3.4.6 Future direction

The Lorentzian and Bloch lineshapes are both approximations when it comes to the fitting of pulsed-saturation CEST data. Based on analysis of this data, acquired in phantoms at 3.0T, it appears that the fit results from other fitted pools are generally consistent between methods, with a slight bias in favour of the Lorentzian approach when using alternative weighting schemes. Given the lack of benefit paired with the computationally expensive nature of generating numerically-solved Bloch lineshapes, the Lorentzian approach appears to be a more practical and pragmatic choice for future CEST fitting analysis.

Alternative weighting schemes including weighting all data-points in the ±1ppm range to zero (scheme 2), linearly tapered weighting (scheme 3), and Lorentzian-shaped weighting (scheme 4) may confer some benefit in terms of goodness-of-fit of the remainder of the z-spectrum, but this would need further validation *in vivo* prior to any recommendation to deviate from a uniformly weighted fit.

3.5 Conclusions

Lorentzian fitting of the water peak generates results that are comparable to those obtained when using a Bloch-simulation based approach and do so in computation times that are over four orders of magnitude faster. On this basis, it was decided to fit the water peak using a Lorentzian lineshape for the remainder of the work outlined in this thesis.

4 Optimization and repeatability of CEST-MRI in the prostate

Chemical exchange saturation transfer (CEST) can potentially support cancer imaging with metabolically-derived information. Multi-parametric prostate MRI has improved diagnosis but may benefit from additional information to reduce the need for biopsies.

The work outlined in this chapter has two primary objectives: Firstly, optimising an acquisition and post-processing protocol for 3.0T multi-pool CEST analysis of prostate data, and secondly to evaluate the repeatability of the technique in five healthy volunteers scanned at multiple sessions.

The optimized saturation scheme was found to be 60 sinc-Gaussian pulses with 40ms pulse duration, at 50% duty-cycle with continuous-wave pulse equivalent B1 power ($B1_{CWPE}$) of 0.92μT. The magnetization transfer (MT) contribution to the fit-model was centered at -1.27ppm.

Inter-session coefficients of variation (CVs) of the amide, NOE and Magnetization Transfer (MT) and asymmetric magnetization transfer ratio (MTR_{asym}) signals of 25%, 23%, 18% and 200% respectively were observed. Fit-metric and MTR_{asym} CVs agreed between readers to within 4 and 10 percentage points respectively.

Differences in the amplitudes of fitted Lorentzian lineshapes of between 0.03-0.10 (17-43%) were found to be detectable depending upon pool, with the MT measurement being the most repeatable (differences of 17-22% detectable).

The work described in this chapter and the subsequent chapter (where the optimized sequence is applied in prostate cancer patients) was accepted for publication as a piece of original research in the Journal of Magnetic Resonance Imaging (JMRI) in February 2019 [81].

Chapter Contributions:

I planned out the study and carried out all optimization, analysis and statistics. I also recruited all volunteers, liaised with bookings teams to arrange scan-times and briefed all radiographers prior to scanning sessions. I received informed consent from all volunteers and filed all consent forms in the site file.

David Atkinson (Reader)[1]: Development and technical support for the CEST patch.

Francisco Torrealdea (Postdoctoral Researcher and Clinical Scientist)[1,2] and Marilena Rega (Clinical Scientist) [3]: Technical support and support with out-of-hours scanning.
Mrishta Brizmohun Appayya, MD (Radiologist)[1], Arash Latifoltojar, MD (Radiologist)[1], Harbir Sidhu, MD, FRCR (Radiologist)[1,4]: Support with slice-planning and ROI drawing.
Xavier Golay (Professor of MRI Physics)[5], Shonit Punwani (Radiologist)[1], Mina Kim (Senior Postdoctoral Researcher)[5]: Study design guidance.
Aaron Kujawa (PhD student)[5]: Proof reading and technical support throughout the project.
Teresita Beeston (Research Nurse)[6]: Ethics and recruitment support

Contributor affiliations:
[1] Centre for Medical Imaging, University College London, 43-45 Foley St, Fitzrovia, London, W1W 7TS, United Kingdom
[2] UCLH Medical Physics and Biomedical Engineering, Elizabeth Garrett Anderson Wing, University College Hospital, 25 Grafton Way, London, WC1E 6DB
[3] Institute of Nuclear Medicine, University College London Hospital NHS Foundation Trust, 5th Floor Tower, University College Hospital, 235 Euston Road, London, NW1 2BU
[4] Radiology Department, University College London Hospital NHS Foundation Trust, Ground Floor North, University College Hospital, 235 Euston Road, London, NW1 2BU
[5] Institute of Neurology, University College London, Queen Square, London, WC1N 3BG
[6] University College London Hospitals NHS Foundation Trust Imaging Research Department, 235 Euston Road, London NW1 2BU

4.1 Introduction

As discussed in detail in the introductory chapters, Lorentzian fitting of CEST z-spectra allows for semi-quantitative measurements relating to several different exchange effects and the technique has not previously been explored in the prostate at 3.0T.

The work described in this chapter has two primary objectives. The first is to optimise an acquisition and post-processing protocol suitable for z-spectrum fitting analysis of prostate data acquired at 3.0T with clinically feasible scan-times. The second is to evaluate the intra- and inter-session repeatability of both the fitting and asymmetry metrics derived from the optimized protocol. It is hypothesised that the repeatability scores of the CEST fitting metrics will out-perform those from asymmetry analysis.

4.1.1 Prostate anatomy and function

The prostate gland is part of the male reproductive and urinary systems. Its primary function is to produce and secrete proteins and ions that form the bulk of the seminal fluid, including the prostate-specific antigen (PSA). The prostate itself surrounds the urethra and sits below the urinary bladder and in front of the rectum, as illustrated in Figure 4-1.

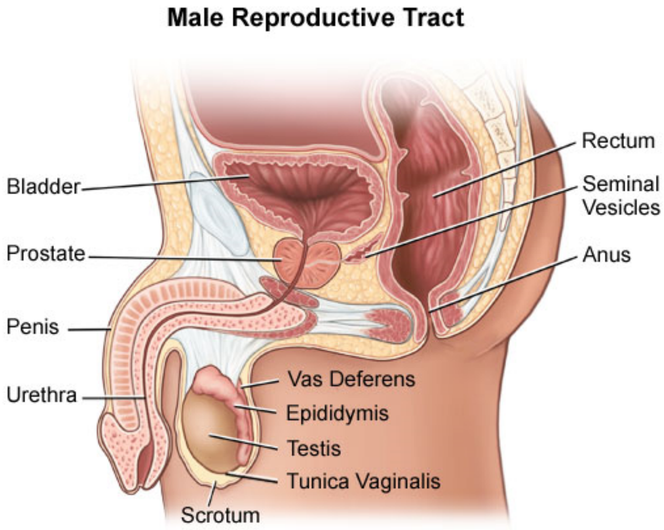

Figure 4-1: *Illustration of the primary features of the male reproductive tract showing the position of the prostate gland relative to the bladder, seminal vesicles, urethra and rectum. Image reproduced from* [101].

The human prostate in childhood is small, weighing around 2g. During puberty it undergoes a phase of exponential growth, increasing in mass to about 20g and to approximately the size of a walnut [102][103]. This occurs with a corresponding rise in serum testosterone to adult levels [102]. Mean prostatic mass then remains fairly constant until the end of the third decade of life when mean prostatic weight begins to rise slowly in a process known as benign prostatic hyperplasia (BPH) [104]. This growth may place pressure on the prostatic urethra, giving rise to restricted urinary flow. Increased cell proliferation in the transition zone (TZ) during BPH increases the risk of the development of cancer.

The prostate anatomy is shown in Figure 4-2 and is broadly divided into four regions:

1) **Peripheral zone (PZ):** The largest area of the prostate. Most prostate cancers start in the peripheral zone.
2) **Transition zone (TZ):** Surrounds the prostatic urethra. This is the zone that enlarges during benign prostatic hyperplasia (see below).
3) **Central zone:** Lies behind the TZ and surrounds the ejaculatory ducts, which run from the seminal vesicles to the prostatic urethra. Very few prostate cancers start in the central zone.

4) **Anterior fibromuscular stroma:** A thickened area of tissue that surrounds the apex (lower section) of the prostate. Made of muscle fibres and fibrous connective tissue. This area of the prostate does not contain any glands and prostate cancer is rarely found in this region.

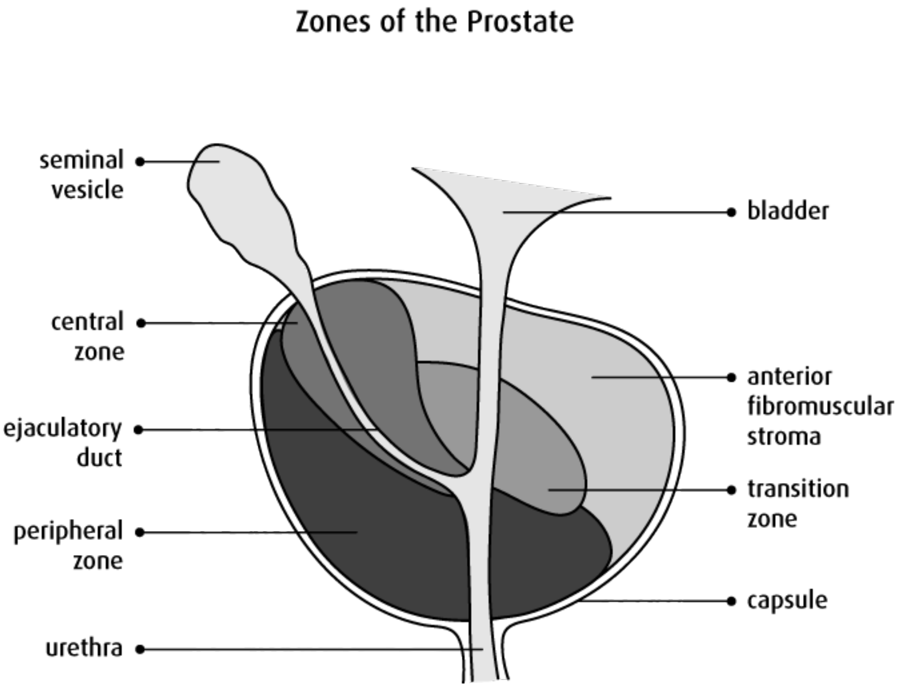
Zones of the Prostate
seminal vesicle
central zone
ejaculatory duct
peripheral zone
urethra
bladder
anterior fibromuscular stroma
transition zone
capsule

Figure 4-2: *Schematic diagram highlighting the key zones of the prostate. Figure reproduced from* [103].

The PZ and TZ are of particular interest in cancer imaging as they are the regions within which most cancerous growths occur. As such, the primary focus of this chapter and the subsequent chapter is in these regions.

4.2 Materials and Methods

4.2.1 Ethics

Local ethics board approval allowing for the scanning of up to 10 individuals for the purposes of sequence development was granted. Written informed consent was obtained prior to all examinations.

4.2.2 Subjects

Five healthy male volunteers (age range 24-47yrs; median age: 28yrs) were recruited. Two of these volunteers were initially scanned as part of the sequence and post-processing optimization steps and all five volunteers subsequently underwent two MRI sessions (interval range: 7-27 days; median interval: 20 days) to allow for evaluation of the repeatability, as described in more detail in subsequent sections.

4.2.3 MRI Protocol

Data were acquired on a 3.0T Achieva MRI scanner (Philips Healthcare, Best, The Netherlands) using a 32-channel cardiac coil. All scans were performed axially in the feet-first position. A T2-weighted whole-volume TSE acquisition and a diffusion weighted imaging (DWI) acquisition were performed at the start of the session. These were then used to plan the CEST scans. A single-slice was positioned at the largest axial cross-section of the prostate. The shim volume was aligned with the imaging-plane.

The T2-weighted scan was an axial multi-shot TSE (TSE factor = 16). TE=100ms, TR=4000ms, field-of-view (FOV)=180x180mm^2, resolution=224x218 with 30, 3mm thick slices. Refocusing control and fat suppression were off. A parallel imaging acceleration (SENSE) factor of 1.3 (RL) was used. The number of signal averages (NSA) was 1. Scan duration was 3m 27s.

The DWI scan used an axial multi-slice Cartesian single-shot EPI readout. TE=79ms, TR=2360ms, FOV = 220 x 220mm^2, resolution = 168x168 with 14, 5mm slices. NSA=6. Images were acquired using a single b-factor of 2000 s mm^{-2}. Spectral pre-saturation with inversion recovery (SPIR) fat suppression was applied. Scan duration was 2m 10s.

4.2.3.1 *CEST Scan Readout*

Turbo-spin-echo (TSE) and turbo-field-echo (TFE) readouts were initially compared for image quality, z-spectrum noisiness and read-out duration. The signal-to-noise ratio (SNR) was higher in the TSE so therefore it was chosen for improved CEST repeatability.

The CEST scan read-out was an axial single-shot TSE readout. TE=14ms, TR=5100ms, FOV=140x140mm^2, resolution=64x63 with a single slice of thickness 4mm. Refocusing control was set to 120° and SPIR fat suppression was applied. No parallel imaging acceleration was used. NSA=1. The scan duration was 5min 42s.

4.2.4 Offset sampling frequencies

Saturated images were acquired with 0.25ppm spacing between ±5ppm, with additional measurements at ±5.5, ±6.0, ±6.5, ±7.0, ±7.5, ±10.0, ±15.0, ±20.0, ±25.0, ±30.0, ±100.0 and ±300.0ppm allowing for sampling of the broad semi-solid MT contribution. An unsaturated reference image was acquired for z-spectrum normalization.

4.2.5 WASABI

B_0 maps were acquired using a WASABI (water shift and B_1) sequence which was adapted from parameters outlined in the literature [57]. Data were acquired at 20 saturation frequency offsets, evenly spaced between ±3ppm. A 5ms block saturation pulse of flip-angle 284° (B_{1CWPE} = 3.7μT) was applied before each read-out. The read-out parameters and slice-planning were the same as for the CEST scan. The duration of each WASABI scan was 41s.

4.2.6 Data Analysis

All data were processed using in-house developed software in Matlab R2016a (MathWorks, Natick, MA, USA).

B_0 inhomogeneity corrections were carried out by interpolating the CEST z-spectra to 1Hz (0.008ppm) frequency intervals and shifting the spectra on a voxel-by-voxel basis using B_0 maps generated using WASABI data.

4.2.6.1 Lorentzian Fitting

The direct saturation (DS), CEST and Nuclear Overhauser Effect (NOE) [28][105][106] pools were modelled using Lorentzian lineshapes [49][50][51], previously described by equation 1-19.

Spectral features at 3.0T are sufficiently broad, in particular *in vivo*, that over-fitting is a concern. To mitigate the risk of over-fitting using several Lorentzians, the CEST effects down-field of water (i.e. those with positive chemical shifts) were jointly modelled using a single Lorentzian. This Lorentzian was centred at the APT frequency offset of 3.5ppm and is henceforth referred to as the amide pool. Similarly, a single Lorentzian, located at -3.5ppm up-field was used to account for the NOE effect [50][52].

The MT contribution to the z-spectrum was modelled using a super-Lorentzian lineshape [51][53][54], previously described by equation 1-20.

The offset frequency of the MT contribution to the z-spectrum has been seen to vary across tissues [52][44][107]. This issue is discussed by van Zijl et al [108] and Hua et al [44] and is likely due to a combination of causes including differences in the constituents of the macromolecular pool across tissues, which is thought to contain both slow and fast-exchanging contributors. The MT offset frequency was estimated by fitting the z-spectra from many voxels using only data points outside of the ±15ppm range, where CEST and

NOE contributions are negligible. The median offset from this analysis was used for all subsequent fits and the super-Lorentzian lineshape was symmetrically interpolated between ±20ppm using a cubic-spline to remove the pole that occurs close to its central frequency.

A whole-fit frequency offset term, h, was included in the fit equation to account for imperfect B_0-field inhomogeneity corrections and a vertical constant signal term v was also included to account for the effects of noise during z-spectrum normalization. After fitting, both the normalized data points and the amplitude parameters extracted from the fit were re-normalized using the fitted vertical offset value (using a voxel-wise multiplication by 1/(1-v)). This ensured the data and fit results were properly normalized.

The general overall fit equation for a re-normalised z-spectrum with contributions from n pools (including DS, CEST and NOE effects) and an MT contribution is given by:

$$M_z(\omega) = 1 - \sum_{i=1}^{n} L_i(\omega - h, \omega_{0i}, \Gamma_i, A_i) - SL\left(\omega - h, \omega_{0SL}, T_2^b, A_{SL}\right) \qquad (4\text{-}1)$$

Fitting analyses were performed using a non-linear least squares algorithm and the fit expression described in equation 4-1 customised for a four-pool model (DS, amide, NOE, MT), with all data points weighted equally. The primary output metrics of interest from the fitting were taken to be the heights of the amide, NOE and MT peaks.

4.2.6.2 Asymmetry Analysis

The MTR_{asym} (see equation 1-18) for this analysis was calculated at 3.5ppm.

4.2.7 Saturation scheme and TR optimisation

A pulsed-saturation scheme was used, defined by the following parameters: pulse duration (τ_p), inter-pulse-delay (τ_d), saturation flip-angle (θ) and the number of pulses (N).

Prior experimentation had shown that, due to the safety restrictions and limitations on the hardware, 50% duty-cycle was the maximum that could be achieved when applying saturation trains for longer than approximately 1s on the Philips Achieva 3.0T. As saturation efficiency is improved with higher duty-cycle, the maximum of 50% was used for the saturation scheme. The Philips '*sg_100_100_0'* sinc-truncated Gaussian pulse-shape was used, which has a profile designed to minimise sidebands. The pulse duration τ_p and inter-pulse delay τ_d were both selected to be 40ms.

To determine the number of pulses required to achieve saturation steady-state z-spectra were acquired in a healthy volunteer using a range of values of N (20, 30, 40, 50 and 60) with a nominal saturation flip-angle of 1000°. The dynamic scan time was set to be long at 10s to allow for full recovery between each dynamic.

The saturation flip-angle was subsequently optimised by acquiring data in a healthy volunteer using a range of values of flip-angle θ and selecting the flip-angle that maximised signals from the fitted amide and NOE pools.

A range of TR values between 2 and 6 seconds were explored by acquiring un-saturated images repeatedly in a healthy volunteer and comparing the total absolute signal observed in each case. These results were cross-referenced with values quoted in the literature for the T1 of the prostate at 3.0T (found to be ~1.6s by de Bazelaire et al [109]) and a selection was made to allow for >95% signal recovery between TSE read-outs.

4.2.8 Region of interest analysis

Regions of interest (ROIs) were drawn on all unsaturated CEST reference scans by two post-FRCR board-certified radiologists with extensive prostate experience. This was done with a graphical user interface (GUI) which was created using an in-house developed Matlab script. ROIs were drawn in the right and left PZ, right and left TZ and right and left obturator internus muscles.

4.2.9 Repeatability in healthy volunteers

The B_0-corrected z-spectra from all voxels within each ROI were averaged to generate a single z-spectrum per ROI which was fitted using the 4-pool model to extract amide, NOE and MT measurements, and the MTR_{asym} was calculated. Bland-Altman plots were used to evaluate the intra-session and inter-session repeatability of the technique [110]. For intra-session repeatability, the results from the first scan of each session were compared with the results from the second scan of the same session, with scans being separated by a total of 6m 23s. For inter-session repeatability, the results from the first scan of the first session were compared with the results of the first scan of the second session, and similarly with the second scan of each session. The coefficient of variation (CV) was calculated in the standard way for each metric (amide, NOE, MT and MTR_{asym}). The 95% limits of agreement (LOA), derived in each case from the Bland-Altman analysis, are the values within which 95% of the differences between measurements are expected to lie, and the bias is the mean difference between scans. In the ideal case of perfect repeatability with no noise, the LOA, bias and CV are all zero.

4.3 Results

4.3.1 MRI Sequence Optimisation

Figure 4-3 shows the z-spectra from an ROI drawn over the whole prostate for different numbers of saturation pulses, N. Saturation steady-state is approached with increasing N and differences between subsequent z-spectra became smaller with each increment of 10 pulses. The trade-off between small gains in saturation and increased scan-time led to the selection of 60 pulses for the final saturation scheme. For the given saturation timings ($\tau_p = \tau_d = 40$ms) this corresponds to 4.8 seconds of total saturation time.

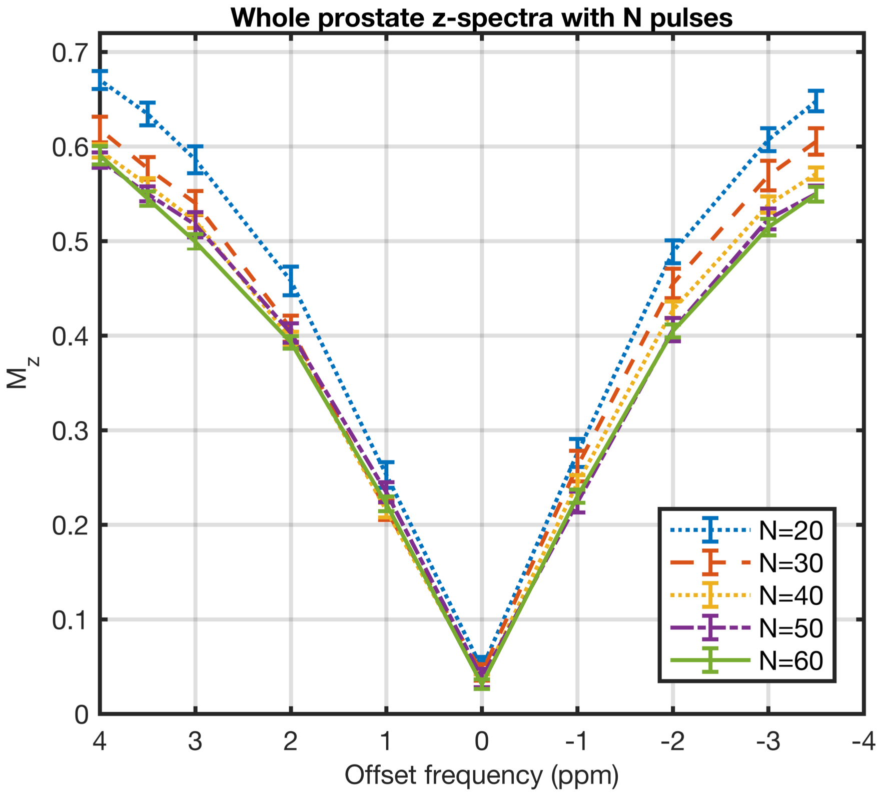

Figure 4-3: *Z-spectra from large ROIs drawn over the whole prostate when using saturation trains with N = 20, 30, 40, 50 and 60 Gaussian pulses. The error bars show the standard deviation of the signal across all voxels within each ROI. The z-spectrum approaches saturation steady-state with increasing N.*

In keeping with reference values from the literature [109] and data that was acquired in a healthy volunteer (see Appendix A), a TR of 5s or above was found to allow for >95% signal recovery of M_z between readouts. The final TR was chosen to be 5.1s to accommodate the TSE readout (245ms) and 4.8s of saturation.

Figure 4-4 shows the histogram distribution of super-Lorentzian offset frequencies when fitting only MT data points outside of the ±15ppm range. The median offset frequency was -1.27ppm with 25th and 75th percentiles at -2.04ppm and -0.04ppm respectively. Based on this data, the offset of the super-Lorentzian was fixed at -1.27ppm for all subsequent analysis. This is similar to values used in other Lorentzian fitting work [52].

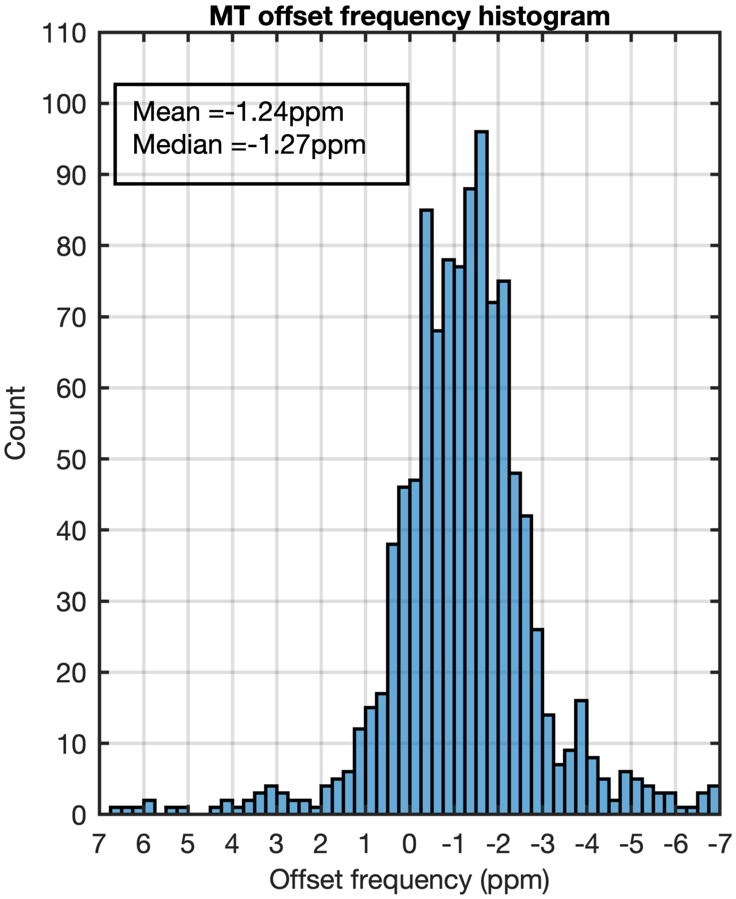

Figure 4-4: *Histogram showing the distribution of offset frequencies of the fitted MT super-Lorentzian across prostate voxels taken from 5 healthy volunteers when fitting only data-points outside of the +/-15ppm range.*

A healthy volunteer was scanned several times using a range of saturation-pulse flip-angles and the z-spectra from all voxels were fitted using the 4-pool model. The heights of the fitted amide, NOE and MT peaks as a function of saturation flip-angle are shown in Figure 4-5. The MT signal increased with increasing saturation power and the mean signals from the amide and NOE pools across the whole prostate were jointly maximised with a saturation flip-angle of 1133°, corresponding to a B_{1CWPE} of 0.92μT. The fit parameters used in the final analysis are summarised in Table 4-1.

Z-spectrum contributor	**Lineshape**	**Parameter**	**Starting Value**	**Lower Bound**	**Upper Bound**
Water	Lorentzian	ω_0 (ppm)	0.0000	-0.0001	0.0001
		Γ (ppm)	1.0	0.5	12.0
		A (A.U)	0.8	0.1	1.0
Amide	Lorentzian	ω_0 (ppm)	3.500	3.499	3.501
		Γ (ppm)	2.0	0.5	12.0
		A (A.U)	0.1	0.0	1.0
NOE	Lorentzian	ω_0 (ppm)	-3.500	-3.501	-3.499
		Γ (ppm)	2.0	0.5	12.0
		A (A.U)	0.1	0.0	1.0
MT	Super-Lorentzian	ω_{0SL} (ppm)	-1.27000	-1.27001	-1.26999
		T_2^b (μs)	10	1	50
		A_{SL} (A.U)	0.500	0.001	1.000
Horizontal Offset (whole-fit)	Constant	h (ppm)	0.0	-0.3	0.3
Vertical Offset (whole-fit)	Constant	v (A.U)	0.0	-0.1	0.1

Table 4-1: *Starting values and upper and lower bounds for all parameters used by the z-spectrum fitting algorithm.*

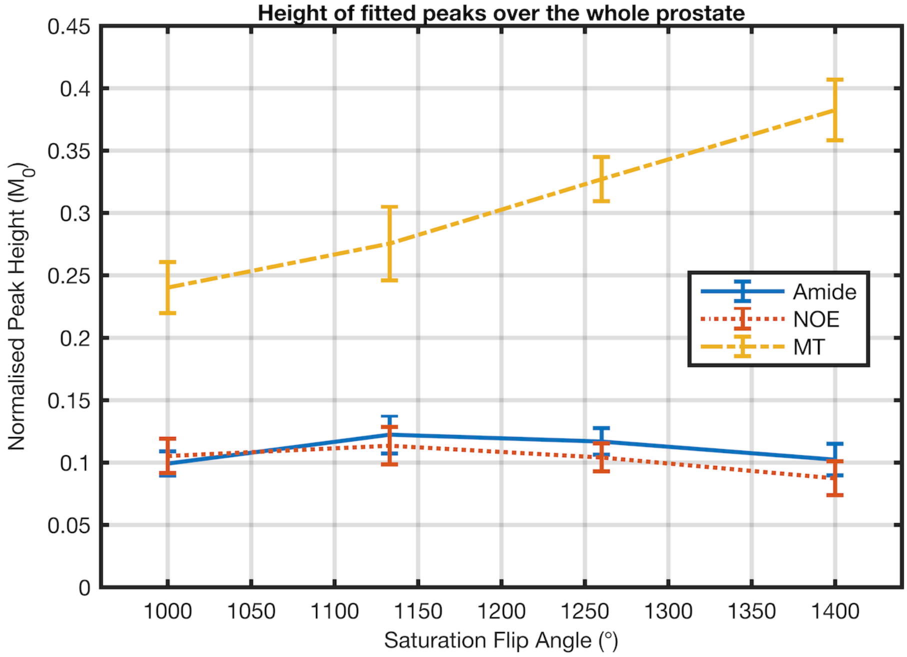

Figure 4-5: *A plot of the mean heights of the fitted amide, NOE and MT peaks over all voxels of a whole prostate for a range of saturation flip-angles. Error-bars show the standard deviation over all voxels. The amide and NOE signals were both maximised using a flip-angle of 1133°.*

4.3.2 Repeatability in Healthy Volunteers

Representative fitted z-spectra from ROIs drawn in the PZ, TZ and obturator internus muscle of a single healthy volunteer are shown in Figure 4-6.

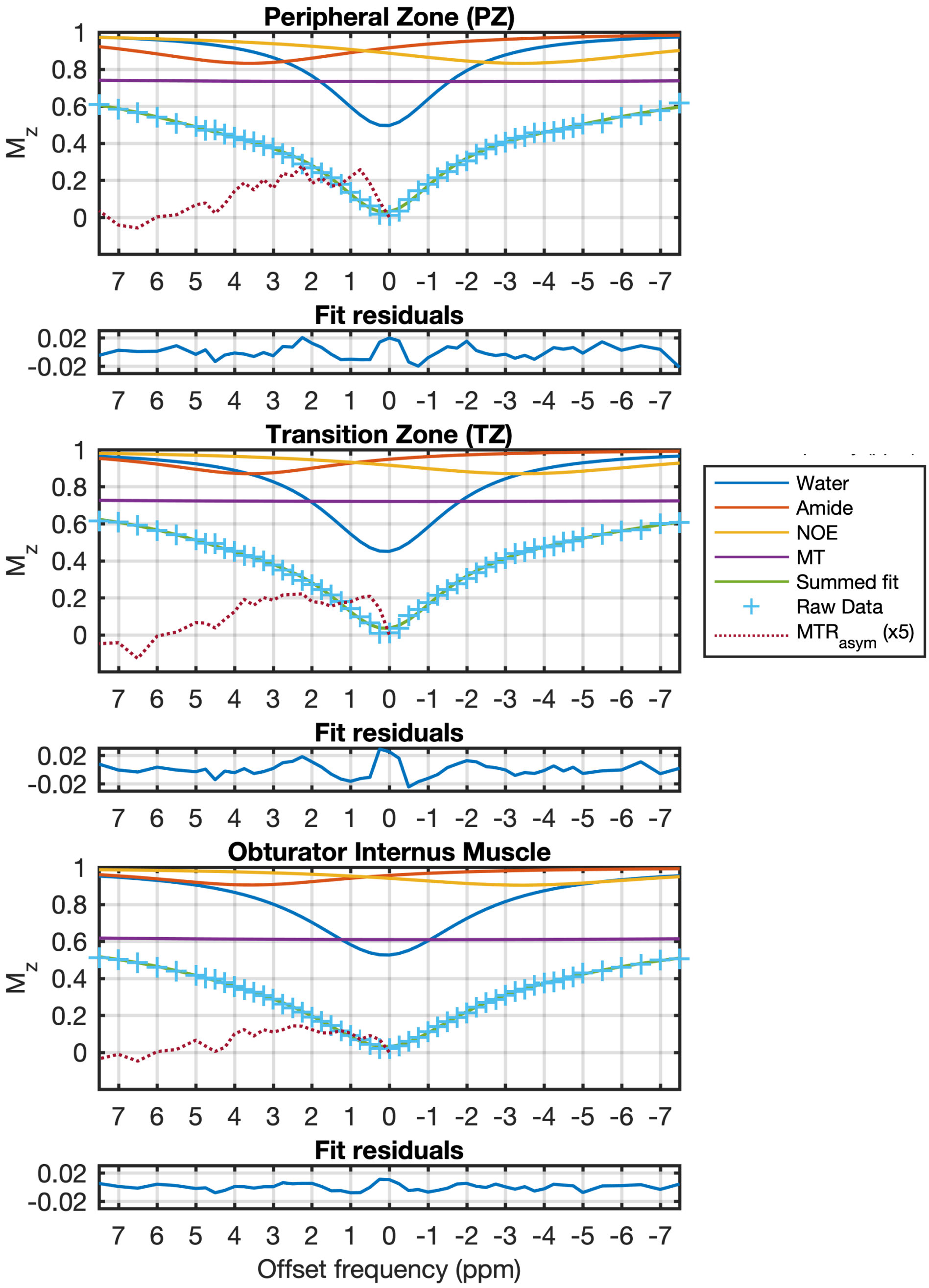

Figure 4-6: *Representative normalized z-spectra, fit results and fit residuals from ROIs drawn in the PZ, TZ and muscle in a single healthy volunteer, showing only the ±7ppm range. The 4-pool fit results include contributions from water, amide, NOE and MT. The MTR_{asym} has been scaled x5 for improved visibility. The residual differences between the raw data and the fits are all less than 0.028.*

Figure 4-7 (A-D) shows Bland-Altman plots for the inter-session repeatability of the heights of the fitted amide, NOE and MT lineshapes and the MTR_{asym} measurements respectively, using the ROIs drawn by reader 1 (intra-session plots are not shown). The plots include the CV and the LOA expressed in units of M_0, which equates to $M_z(\infty)$ = 1 for a normalized z-spectrum.

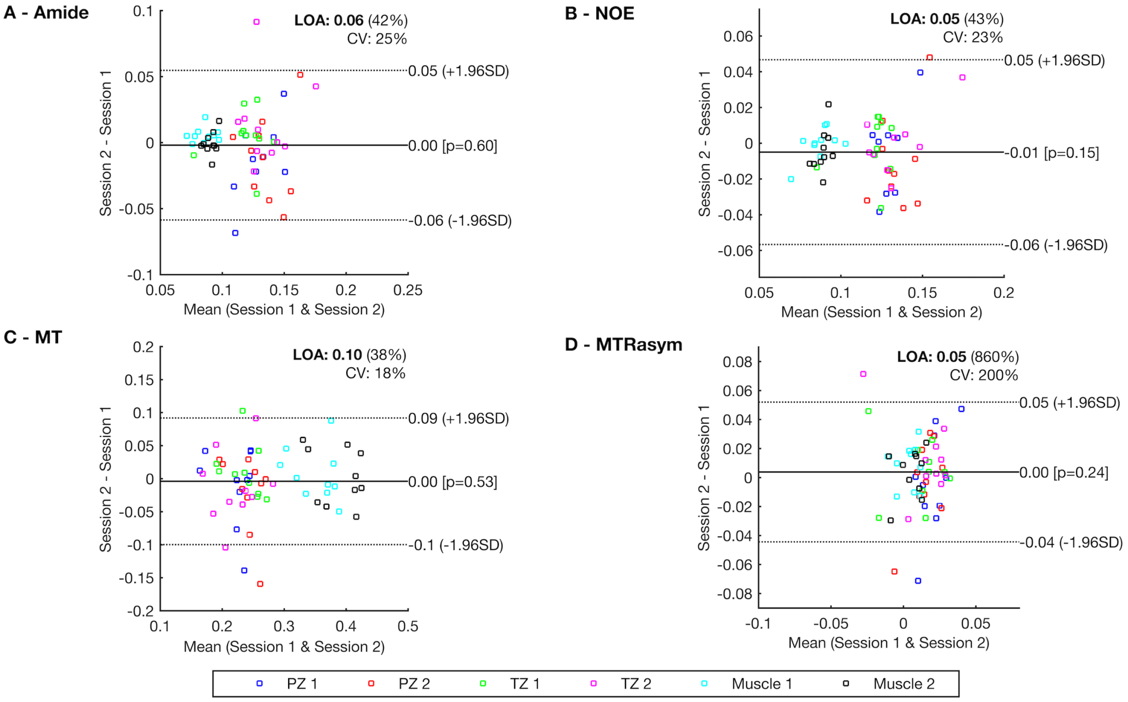

Figure 4-7: *Bland-Altman plots showing the inter-session repeatability of the heights of the fitted (A) amide, (B) NOE and (C) MT peaks and (D) the MTR$_{asym}$ measurements, using ROI's drawn by reader 1. Plots include the 95% limits of agreement (LOA) expressed in absolute terms and as a percentage, the bias, and the coefficient of variation (CV).*

The intra-session coefficients-of-variation (CVs) of the amide, NOE, MT and MTR$_{asym}$ measurements in healthy volunteers using ROIs drawn by reader 1 were found to be 20%, 19%, 9.5% and 150% respectively. The corresponding inter-session CVs were found to be 25%, 23%, 18% and 200% respectively.

The full CV, LOA and bias values for amide, NOE, MT and MTR$_{asym}$ measurements made using ROIs drawn by both readers are shown in Table 4-2 along with the intra-class correlation (ICC) coefficients between readers.

The LOA gives an indication of the threshold for reliable detectability of signal differences. Therefore, based on this data, we would expect to be able to reliably detect differences in the amplitudes of the fitted peaks from repeated scans within a single session of 0.04-0.05 (33-38% for amide and NOE and 17-22% for MT) or higher. The bias is close to zero in every case.

	Intra-session					
	CV		**LOA**		**Bias**	
CEST Metric	Reader 1	Reader 2	Reader 1	Reader 2	Reader 1	Reader 2
Amide	20%	20%	0.05	0.05	0.00	0.00
NOE	19%	18%	0.04	0.04	0.00	0.00
MT	9.5%	7.4%	0.05	0.04	0.00	0.00
MTR$_{asym}$	150%	140%	0.04	0.03	0.00	0.00
ICC	0.997		0.539		-	
	Inter-session					
	Reader 1	Reader 2	Reader 1	Reader 2	Reader 1	Reader 2
Amide	25%	22%	0.06	0.05	0.00	-0.01
NOE	23%	19%	0.05	0.04	-0.01	0.00
MT	18%	15%	0.10	0.08	0.00	0.00
MTR$_{asym}$	200%	200%	0.05	0.05	0.00	0.00
ICC	0.999		0.835		-	

Table 4-2: *The coefficients of variation (CV), 95% limits of agreement (LOA) and bias of the intra-session and inter-session Bland-Altman plots generated for the amide, nuclear Overhauser effect (NOE), magnetization transfer (MT) and asymmetric magnetization transfer ratio (MTR$_{asym}$) signals in 5 healthy volunteers. Results are shown for analysis done using regions of interest drawn by two separate readers. The intra-class correlation (ICC) coefficients are also provided.*

4.4 Discussion

In the current work we optimised an acquisition and post-processing pipeline for multi-pool CEST imaging of the prostate at 3.0T and evaluated the repeatability of the technique in healthy volunteers.

CEST sequence parameters including number of pulses, saturation powers, and the TR were tuned to maximise the heights of the fitted CEST and NOE peaks and the offset frequency of the fitted MT peak was also estimated.

The combined scan-time of the CEST and WASABI scans was clinically acceptable at 6m 23s. The pulse-duration and inter-pulse delay parameters were not explored during the optimization as prior experimentation on this scanner had indicated that saturation trains of longer than ~1s were not possible when using duty-cycles above 50% due to SAR and hardware restrictions. A pulse-duration of 40ms was chosen because it gives rise to spectral selectivity approximating the frequency sampling that was used (0.25ppm or 32Hz in the central region of the z-spectrum).

As expected, the intra-session repeatability scores are found to be superior to the inter-session repeatability scores in every case as indicated by lower CV and LOA values.

Bland-Altman analysis showed that the CV values for all fit results (both intra-session and inter-session) were 25% or lower. The intra-session 95% LOA for amide, NOE and MT amplitude differences were found to be between 0.04-0.05 (17-38%). The corresponding inter-session values for amide and NOE were between 0.04-0.06 (35-43%) and for MT this rose to 0.08-0.10 (33-38%). Therefore the threshold for detectable differences in fitted peak amplitudes in all cases, ranged from 0.04-0.10 (17-43% depending on pool). While inspection of the LOA values between readers suggests reasonable inter-reader agreement, the ICC coefficient calculated for the intra-session variability between readers was particularly low, in part due to a low number of observations over a small range.

By comparison, a recent study of the repeatability of apparent diffusion coefficient (ADC) measurements in prostate mp-MRI at 3.0T found limits of agreement ranging from 13.91% to 60.49% using an endorectal coil [111]. This puts the repeatability of CEST fitting metrics within the repeatability range of established ADC scans from the mp-MRI protocol.

The fitted MT peak was found to be the most repeatable measurement as quantified by CV. This is perhaps not surprising as it is the broadest contribution to the z-spectrum and all other contributions sit nested within it in the ±5ppm range. Magnetization transfer imaging (MTI) traditionally involves acquiring unsaturated images and images saturated at an offset typically >1kHz off-resonance. Recent work by Arlinghaus et al [112] showed good repeatability of quantitative MT (qMT) imaging of the breast at 3.0T and Barrett et al [113] demonstrated that MTI shows promise as for prostate cancer detection at 3.0T.

The inter-reader differences in CV measurements for the fitted pools (amide, NOE, MT) are all smaller than four percentage points, with ICC coefficients of >0.99 suggesting that inter-reader variability is not the main source of variation.

As hypothesised, there is a marked difference between the levels of repeatability found when applying the fitting method, which showed maximum intra-session and inter-session CV values of 20% and 25% respectively, and the repeatability of the $\mathrm{MTR}_{\mathrm{asym}}$ measurements, which showed maximum intra-session CV of 150% and an inter-session CV of 200%.

The CV values for $\mathrm{MTR}_{\mathrm{asym}}$ repeatability are poorer than for the fitting metrics. The LOA values for $\mathrm{MTR}_{\mathrm{asym}}$, while larger than those reported in other endogenous CEST repeatability studies [114][115] were similar to or slightly lower than those of the fitted amide and NOE peaks. Both of these values may be improved by using a sequence optimized for $\mathrm{MTR}_{\mathrm{asym}}$ imaging but that lies outside the scope of this work which is primarily focused on z-spectrum fitting.

All MTR_{asym} calculations in this work were made using the single-offset approach described in previous prostate APT work [23][24]. As an alternative, the use of multiple offset frequency points in the MTR_{asym} calculation may reduce the effects of noise and therefore improve the repeatability. For illustration the CV values were re-calculated using the mean MTR_{asym} values over three offset frequencies (3.25, 3.5 and 3.75ppm) and the intra-session CV values from both readers were reduced to 110%, with the inter-session CV values dropping to 170% and 160%. These changes are attributed to noise averaging although the optimal choice of integration range and its physiological significance would require further optimization and consideration. The comparison of CV values between single and multi-offset MTR_{asym} calculations is included here for illustration. For more equivalent comparisons, future studies may wish to acquire a dedicated multi-offset acquisition for MTR_{asym} calculations and to compare these results to results from a single-offset acquisition (with the same sequence timings) which is repeated for the same duration as the multi-offset acquisition and therefore achieves higher SNR per MTR_{asym} measurement.

Our results suggest that, when using the acquisition protocol outlined in this work, the fit-model described produces more repeatable CEST measurements than MTR_{asym} analysis. This is attributed to a reduction in the influence of noise when using whole z-spectrum fitting methods.

There are several limitations of the study. No anti-spasmodic drug was given as part of this research and bowel motion may affect the results. Motion correction of CEST data can be difficult due to changes in image contrast between saturation frequencies however methods currently being developed to address this could be applied in future work [116].

To prevent overfitting, the number of free parameters cannot be too high. For this reason, in this work we used a 4-pool model with a single CEST pool and a single NOE pool. Optimization of the offset frequencies of these two pools was attempted by fitting many voxels with relaxed constraints on the upper and lower bounds of the offset frequencies, but the analysis did not converge (data not shown). We believe this to be due to the use of a reduced number of pools, the broadness of CEST resonances at 3.0T, and the fact that different sub-regions of the prostate may have different CEST pool offsets. In response to this, reference values were used for the CEST and NOE offset frequencies [50][52] . In particular the amide resonant frequency of 3.5ppm was selected because at the low B1 saturation powers we used, the saturation efficiency for the slow-exchanging amides is higher than for amine and hydroxyl groups. Future CEST studies at field strengths above 3.0T may better characterise z-spectrum features in the prostate which will inform future fitting models. Generalization of these models across sites will require the consolidation of in-house post-processing scripts after sufficient technical development and validation has taken place.

The horizontal offset term varied smoothly across the images and values were largely contained within the -0.02ppm to 0.04ppm range (see Figure 4-8 in the supplementary figures for this chapter) suggesting that fitting artefacts in the prostate due to poor B_0 correction are not a major concern when performing z-spectrum fitting with a horizontal offset. For this reason, regularization of the horizontal offset constant (for example, using IDEAL-fitting as per Zhou et al [88]) was not applied although this could be applied in future work. Variation of the vertical offset parameter across the prostate (with values largely confined to within a range of ±0.01, also shown in supplementary Figure 4-8) was not smoothly varying across the field of view, but as this term is included to correct for noise, this was expected.

A single-slice readout was chosen for the benefit of having a shorter read-out time and the slice thickness was 4mm. Partial volume effects may have influenced the results although the slice positioning was centred at the largest cross-section of the gland and it is expected that this will have helped to minimise these effects within this study. As a clinical tool, the protocol would benefit from an increased number of slices with thickness <4mm to provide greater coverage and minimise these effects.

Optimization of saturation parameters for maximal absolute amide and NOE signals was performed in healthy volunteers using data from the whole prostate, including PZ and TZ sub-regions. The chosen saturation power of 0.92μT was broadly consistent with saturation powers used in other endogenous CEST studies utilizing z-spectrum fitting which utilize $B1_{CWPE}$ in the region of 1.0μT [52][88]. For optimal cancer detection, a protocol needs to provide an adequate level of signal and contrast between AUT and tumor and variations in T1 and T2 values, pH and metabolite concentrations between regions may influence the optimal parameter set. Further work in patients may refine the protocol for cancer detection.

Early engagement with the team of radiographers ensured that everybody knew what to expect at scan time including consenting the volunteers, positioning in the scanner and ensuring availability of prior imaging on nearby PACS workstations to support slice-planning for the second scans. To minimse the chances of any drop-outs, all healthy volunteers were sent reminder messages both one week and one day prior to their scans.

No proprietary CEST sequences were available on the version of the scanner therefore an in-house developed patch was applied. Use of the patch involved re-starting the scanner software which meant that the scan-slots for this study had to be chosen to be long enough to allow for the extra steps and possibility of issues arising and to avoid disruption to clinical services.

Use of proprietary CEST scan protocols would have ensured a simpler and faster scanning protocol and would have allowed these scans to be added to the end of other clinical prostate MRI research protocols. This lack of proprietary CEST software would need to be addressed if multi-centre studies were to be undertaken. Philips has since released an ‘APTx’ sequence that allows for some CEST sequences to be run off-the-shelf, this may benefit similar future CEST studies on clinical machines.

4.5 Conclusions

In summary, we have optimized a full-z-spectrum acquisition and fitting protocol suitable for prostate imaging on a 3.0T scanner within clinically feasible scan-times. The repeatability of the fitting metrics are comparable to other mp-MRI scans and are seen to be more repeatable than MTR_{asym}. This demonstration of z-spectrum fitting at 3.0T and quantification of the repeatability of *in vivo* CEST metrics on a clinical scanner [114][115][117] is a necessary step towards the translation of CEST techniques to the clinic.

The results from this study provide a benchmark for CEST fitting repeatability in the human prostate at 3.0T and may be used to power future prostate CEST studies.

4.6 Chapter supplementary figures

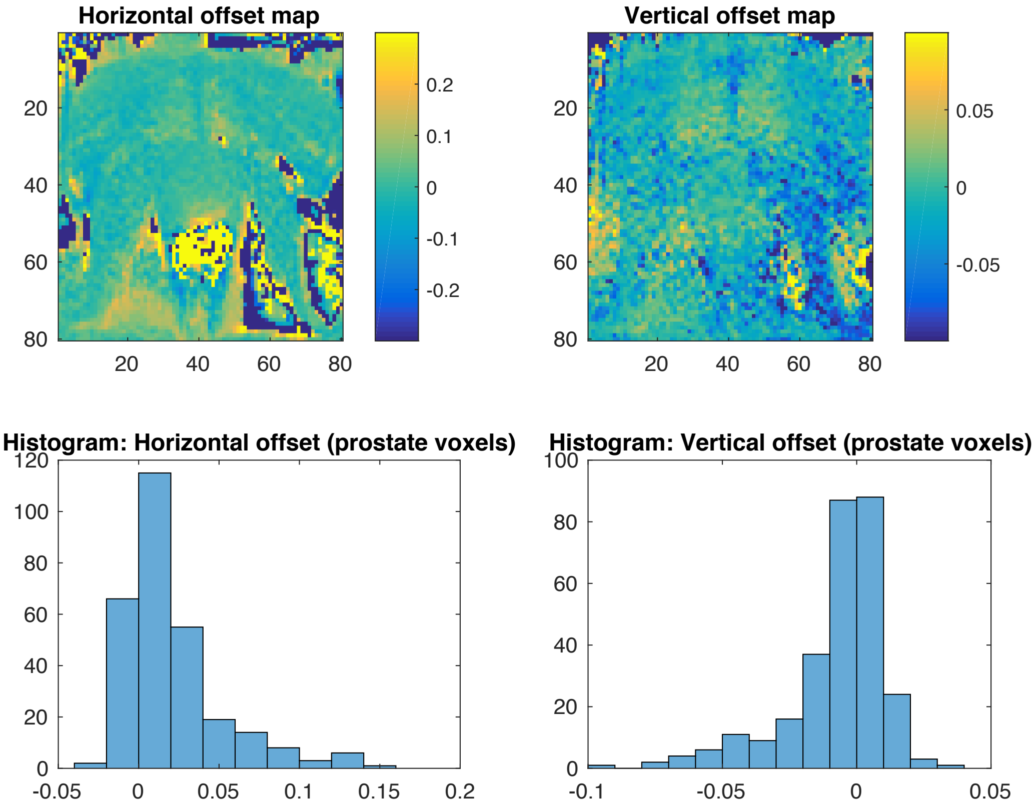

Figure 4-8: *Representative maps and histograms of the fitted horizontal and vertical offset terms. It can be seen that the horizontal offset varies smoothly across the image. The vertical offset does not vary smoothly but as it is intended to account for noise in the reference image this is expected. The values are both fairly tightly constrained to close to zero.*

5 Initial evaluation of CEST contrast in prostate cancer

The optimised protocol from the previous chapter is applied in one transition zone (TZ) cancer patient and one peripheral zone (PZ) cancer patient and a preliminary assessment of the signal differences between regions of tumour and apparently-uninvolved tissue (AUT) is made.

Chapter Contributions:

I contacted and recruited all patients, booked them in for scans, received informed consent, and carried out all data analysis and statistics.

Shonit Punwani (Radiologist)[1]: Support with patient identification.
Mrishta Brizmohun Appayya (Radiologist)[1], Arash Latifoltojar (Radiologist)[1], Harbir Sidhu (Radiologist)[1,2]: Support with slice-planning and ROI-drawing.
Teresita Beeston (Research Nurse)[2], Joey Clemente (Research Practitioner)[2], Wivijin Piga (Research Practitioner)[2], Katerina Soteriou (Research Practitioner)[2]: Ethics and recruitment support

Contributor affiliations:

[1] Centre for Medical Imaging, University College London, 43-45 Foley St, Fitzrovia, London, W1W 7TS, United Kingdom
[2] University College London Hospitals NHS Foundation Trust Imaging Research Department, 235 Euston Road, London NW1 2BU

5.1 Prostate Cancer Overview

Prostate cancer ranks among the top five cancers for both incidence and mortality worldwide and a range of genetic, lifestyle and dietary factors have been associated with prostate cancer risk. It is the most commonly diagnosed cancer in men and incidence rates are increasing globally [118].

The vast majority of diagnoses occur in patients over 50 years of age [119] and most are first detected either by elevated levels of prostate-specific antigen (PSA) during blood-test screening or via abnormal results of a digital rectal exam (DRE) [120]. The majority of detected prostate cancer is located within the peripheral zone (PZ), with the second most common location being the transition zone (TZ) and third the central zone (CZ) [121][122][123][124].

5.1.1 Prostate Imaging – Reporting and Data System (PI-RADS v2)

The Prostate Imaging – Reporting and Data System version 2 (PI-RADS v2) is a set of guidelines for multi-parametric prostate MRI and radiological reporting produced by international collaboration and consensus between the American College of Radiology (ACR), European Society of Uroradiology (ESUR) and the AdMeTech Foundation [125][126]. First developed in the early 2010s, version 2 was published in 2015.

The PI-RADS v2 system is used by radiologists while reporting mp-MRI scans which typically consist of T2-weighted (T2W) scans, diffusion-weighted imaging (DWI) and derived apparent-diffusion coefficient (ADC) maps, dynamic contrast-enhanced (DCE) images and in some cases, 1H-spectroscopy.

The reporting typically includes prostate gland volume; mapping, sizes and characterisation of abnormal lesions, and comments about other findings (e.g. cysts, calcifications, fibrosis). Abnormal lesions are assigned a score based on findings across the range of scans that were acquired. In PI-RADS this assessment is done using a 5-point scale which is based on the likelihood that findings from each lesion correlate with the presence of a clinically significant cancer. The guidelines describe how scores from different imaging methods should be combined and the overall assessment categories are as follows [125]:

Category	Cancer likelihood assessment
PI-RADS 1	Very low (clinically significant cancer is highly unlikely to be present)
PI-RADS 2	Low (clinically significant cancer is unlikely to be present)
PI-RADS 3	Intermediate (the presence of clinically significant cancer is equivocal)
PI-RADS 4	High (clinically significant cancer is likely to be present)
PI-RADS 5	Very high (clinically significant cancer is highly likely to be present)

Table 5-1: *PI-RADS assessment categories for prostate lesions identified in multi-parametric MRI.*

PI-RADS v2 Assessment Categories are based on mp-MRI findings only and should not incorporate other factors such as PSA, DRE, clinical history or choice of treatment.

At urology multi-disciplinary team meetings (MDTs) within the NHS, radiologist findings are often crucial when making subsequent treatment decisions.

5.1.2 Clinical Treatment Pipeline

Detection and staging of suspected prostate cancer may involve mp-MRI scans, biopsies and repeat PSA measurements. In cases with high-risk of metastasis a positron-emission-tomography (PET) scan may be performed [127].

Men with low-risk prostate cancer may be enrolled onto an ‘active surveillance’ (AS) program [128]. These programs aim to reduce overtreatment by instead opting to provide periodic follow-ups where disease progression can be monitored through repeated mp-MRI scans and PSA measurements.

Patients who are offered treatment may be recommended one of a range of interventions including high-intensity focused ultrasound (HIFU) for cancer ablation, radiation therapy, cryotherapy, or prostate removal (radical prostatectomy). Hormonal treatments such androgen deprivation therapy (ADT) may also be offered, typically as an adjunct to other treatments [129].

5.1.3 Motivation for measuring prostate cancer CEST contrast

By scanning prostate cancer patients using an optimized CEST sequence we are aiming to make a preliminary evaluation of signal changes observed in the amide, NOE, MT and MTR_{asym} signals.

5.2 Methods

5.2.1 Ethics and recruitment

Local ethics board approval allowing for the scanning of up to 10 individuals for the purposes of sequence development was granted. Written informed consent was obtained prior to all examinations.

The recruitment criteria for this single-attendance imaging study are outlined in Table 5-2. Patients were invited to attend a single scanning session using a surface coil with no requirement for administration of Gadolinium contrast.

Criterion #	Description	Comments
1	Lesion size > 10mm	Ensure that the lesion is clearly visible in the CEST scans.
2	PI-RADS $\geq$ 4	Radiologist reports high or very high likelihood of presence of clinically significant cancer.
3	Candidate has received no prior treatment	The effects of prior treatment will introduce confounding factors into interpretation of the results.
4	Candidate not currently undergoing hormone therapy	Hormone therapy will influence tumor metabolomics and confound interpretation of the results.
5	Any historical biopsies > 3 months ago	Reduce the likelihood of interference from post-biopsy haemorrhage.
6	If biopsied: biopsy confirms presence of cancer (Gleason $\geq$ 7)	Confirmed presence of cancer through histology is gold standard.

Table 5-2: *Recruitment criteria for patients being enrolled into the study.*

5.2.2 Recruitment pipeline

Patients were primarily identified at local MDT meetings held at UCLH and Harley St Hospitals, with the support of SP (radiologist with > 10 years of experience), with additional patients being identified through liaison with clinical research practitioners JC, WP and KS.

A total of 90 patients were screened. Of these 4 were scanned, and data from 2 are included in this analysis. The recruitment pipeline is outlined in Figure 5-1 along with numbers that reached each stage.

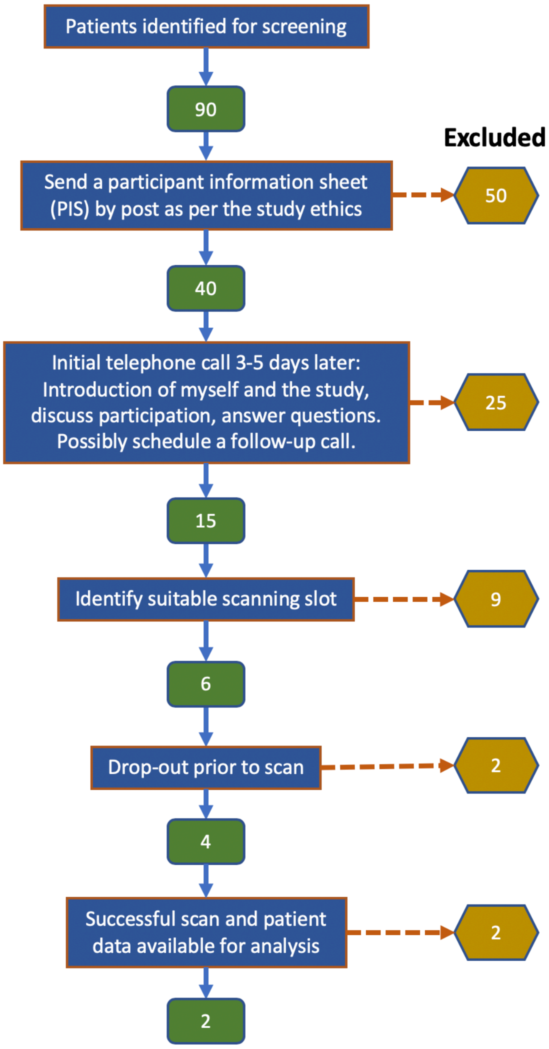
Patients identified for screening
90
Excluded
Send a participant information sheet (PIS) by post as per the study ethics
50
40
Initial telephone call 3-5 days later: Introduction of myself and the study, discuss participation, answer questions. Possibly schedule a follow-up call.
25
15
Identify suitable scanning slot
9
6
Drop-out prior to scan
2
4
Successful scan and patient data available for analysis
2
2

Figure 5-1: *The recruitment pipeline for this study including the numbers of candidates that reached each stage.*

5.2.3 Comments on recruitment

Forty of the ninety identified patients passed the initial screening. There were several reasons for exclusion. Some had received prior treatment or were undergoing ADT and therefore did not meet the recruitment criteria. Patients who had undergone biopsy in the preceding three months were adding to a waiting list and were sent a PIS once they had cleared the three-month window, if they were still eligible at that point.

The ethics required that a participant information sheet (PIS) be sent in the post to the patient, and that the patient must have at least 24hrs to consider their participation before giving informed consent. These times constraints meant that some patients with procedures scheduled were excluded because there was not enough time for successful approach, recruitment and scanning before their procedure (i.e. in less than approximately

3-4 days). In a small number of cases, research practitioners, the urology research nurse or the managing clinician requested that a suitable patient not be approached for circumstantial reasons typically relating to participation in other clinical trials or personal circumstances.

In general, patients were interested to hear about the study and those who were not interested in participation politely declined. In some cases, follow-up calls were scheduled to give the patient time to consider their participation but most of the time the level of interest or otherwise was established within a single phone-call. Approximately 5 patients were not contactable either because they did not answer the phone or because no telephone details were available in the electronic patient records (EPR) system.

Data from two of the four recruited patients was used during set-up and led to modifications in the sequence. The initial plan was to optimize the sequence directly in patients but as recruitment was slower than expected. it was decided to optimize the sequence in healthy volunteers, as described in the previous chapter.

Ultimately, two patients were successfully recruited and scanned using the optimised sequence. Both had TRUS biopsy-proven tumors, both of whom were under active surveillance for lesions scoring 5/5 on PI-RADS, with maximum lesion size >10mm and whose biopsies had taken place over 4 months prior to recruitment. Patient 1 (71 years) had a right-sided Gleason 3+4 TZ tumor with prostate specific antigen (PSA) concentration of 8.4ng/ml and patient 2 (55 years) had a right-sided Gleason 4+3 PZ tumor with PSA concentration of 6.2ng/ml. PSA measurements were made 2 months prior to the research scans.

5.2.4 MRI Protocol

Two patients were scanned twice at a single attendance (time between scans approximately 8 minutes) using the protocol outlined in the previous chapter.

Both patients had known and previously classified tumors and prior mp-MRI imaging which was made available to support in the slice-planning. The slice was positioned at the largest axial cross-section of the tumor as determined by radiology research fellows (AL and HS).

5.2.5 Regions-of-interest (ROIs)

Readers had access to prior clinical mp-MRI reports and pathology results and the T2w and DWI images acquired during this study to support the drawing of ROIs. This was to ensure that the tumor was localized in the acquired images as accurately as possible to allow for accurate evaluation of the signal differences between different regions.

For the patient with a TZ tumour, both readers drew ROIs in the right and left-hand PZ, in the TZ tumour, in healthy TZ and in right and left-hand obturator internus muscles.

For the patient with a PZ tumour, both readers drew ROIs in the right and left-hand TZ, in the PZ tumour, in healthy-appearing PZ and in right and left-hand obturator internus muscles.

5.2.6 Data Analysis

Maps of the amide, NOE and MT peak-heights, and the MTR_{asym} were generated by performing voxel-wise analysis of the patient scans.

Boxplots of the signal from all voxels within tumor and AUT ROIs were also created. The significance of the observed image contrast between tumor and AUT in patient scans was evaluated by treating each group of voxels within an image as an independent sample and applying a non-parametric Mann-Whitney U test with $p < 0.05$ taken to be significant.

5.3 Results

Maps of the amide, NOE, MT and MTR_{asym} signal intensities from each patient are shown in Figure 5-2 alongside the corresponding T2-weighted and DWI (b=2000) images. DWI is particularly useful for identifying regions of PZ tumor as seen in the figure. Tumor and AUT ROIs are overlaid onto the images, with tumor marked with a red arrow on the T2w images.

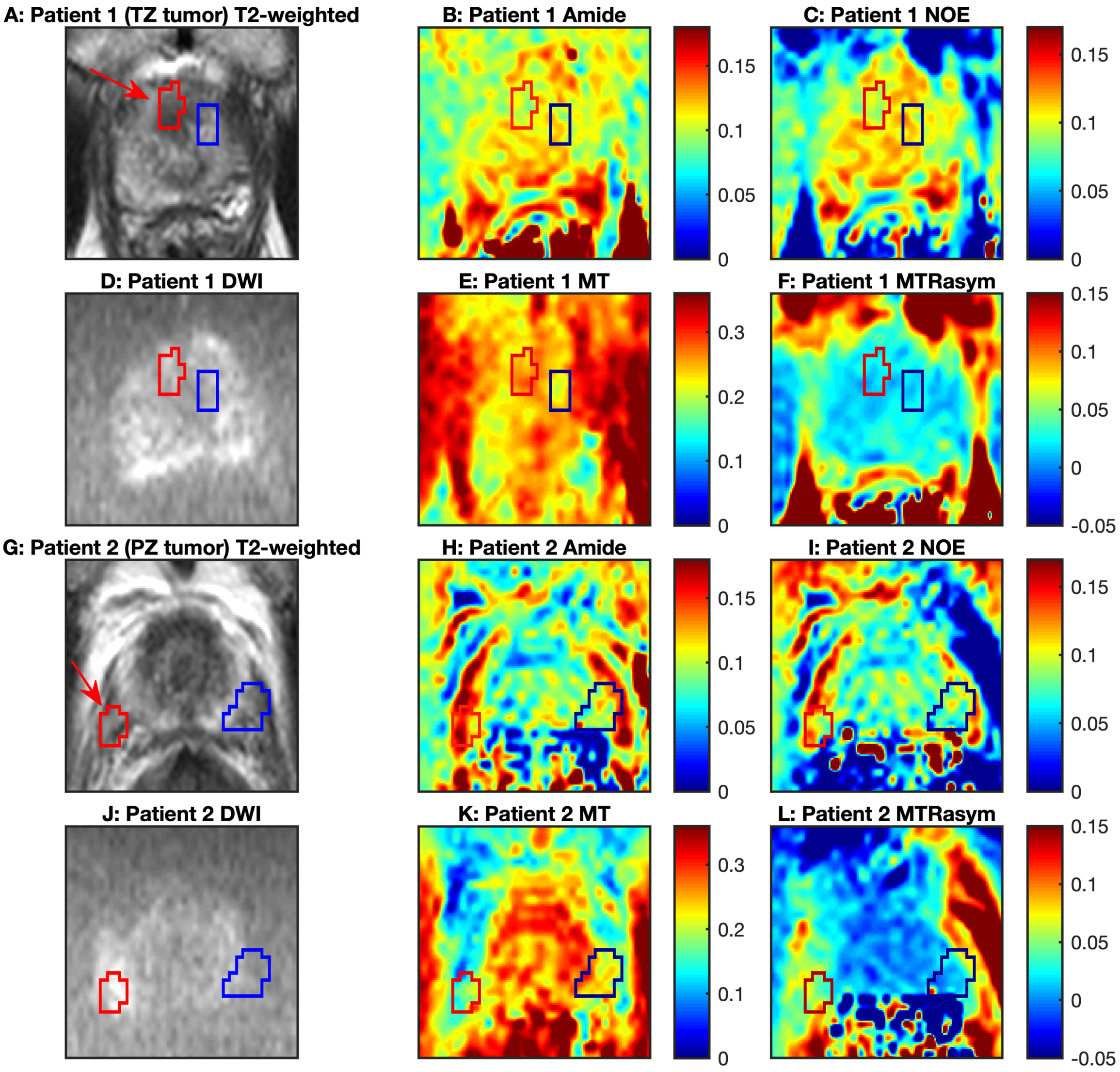
A: Patient 1 (TZ tumor) T2-weighted
B: Patient 1 Amide
C: Patient 1 NOE
D: Patient 1 DWI
E: Patient 1 MT
F: Patient 1 MTRasym
G: Patient 2 (PZ tumor) T2-weighted
H: Patient 2 Amide
I: Patient 2 NOE
J: Patient 2 DWI
K: Patient 2 MT
L: Patient 2 MTRasym
0.15
0.1
0.05
0
0.3
0.2
0.1
-0.05

Figure 5-2: *Voxel-wise maps of the heights of the fitted amide, NOE and MT peaks, and the MTR$_{asym}$ measurements for (A-F) patient 1 with a transition zone (TZ) tumor and (G-L) patient 2 with a peripheral zone (PZ) tumor. The tumor and apparently-uninvolved-tissue (AUT) regions of interest are highlighted in red and blue respectively and the tumors are highlighted with a red arrow on the T2w images. Visually, slight hypo-intensities are observed in the amide and NOE signal in the region of TZ tumor with corresponding hyper-intensity in the MT signal and no significant change in the MTR$_{asym}$. Conversely, hyper-intensities in the amide and NOE signals and hypo-intensities in both the MT and MTR$_{asym}$ signals are observed in the region of PZ tumor. It should be noted that the regions of signal change associated with the tumor ROIs are not localized only to the region of tumor and appear to be part of broader structural features in these two cases.*

Boxplots of the amide, NOE and MT signal, and the MTR$_{asym}$ values from all voxels in AUT and tumor ROIs are shown in Figure 5-3 for both patients and both readers. Statistical significance of signal differences between regions were assessed using a non-parametric Mann-Whitney U test with significance levels of $p<0.05$, $p<0.01$ and $p<0.001$ denoted in the boxplots by *, ** and *** respectively.

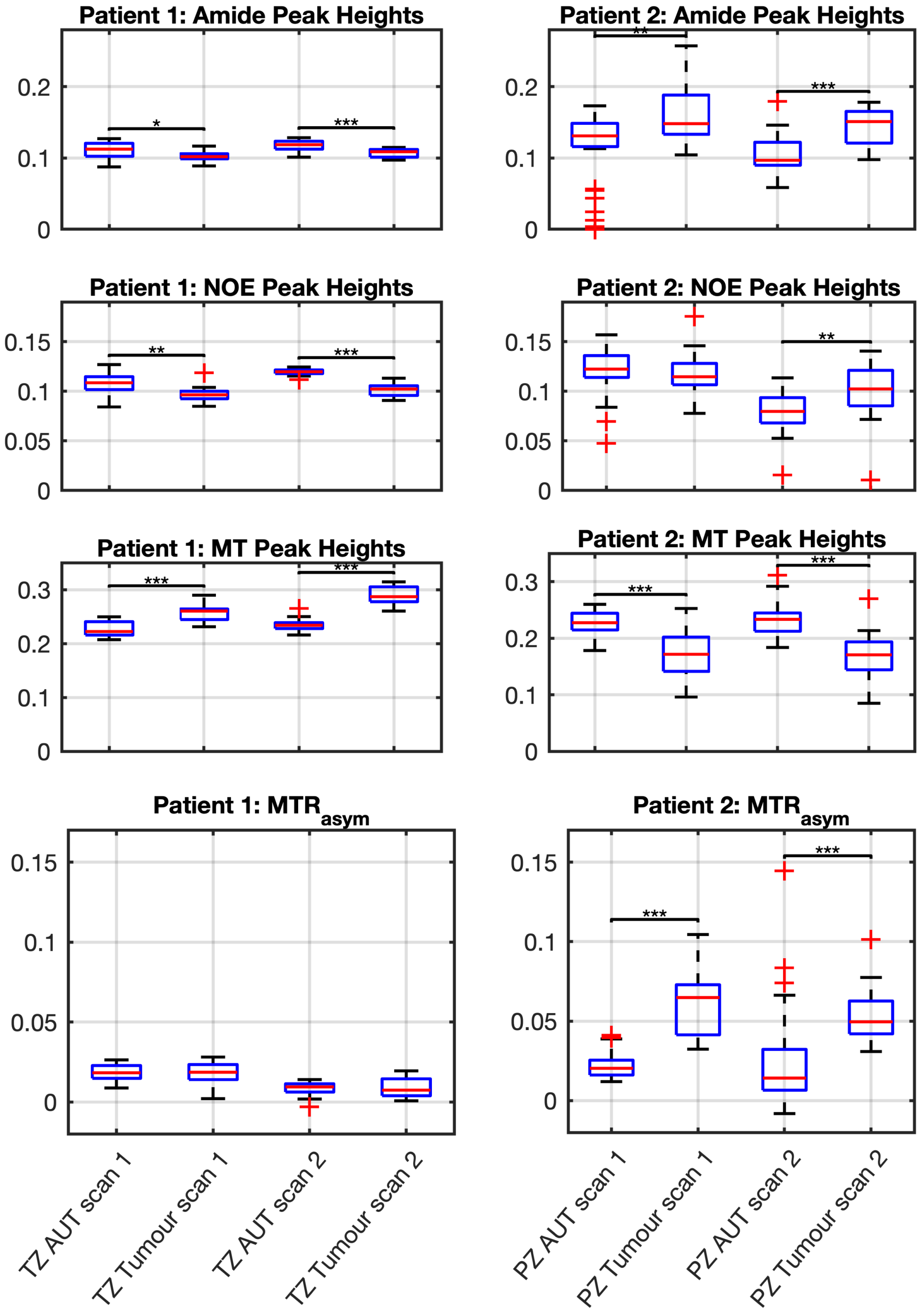

Figure 5-3: *Boxplots showing the fitted amide, NOE and MT peak heights and MTR$_{asym}$ measurements from all voxels within tumor and AUT ROIs drawn by reader 1 for* ***(A)*** *both scans of patient 1 with a TZ tumor,* ***(B)*** *both scans of patient 2 with a PZ tumor. The red line indicates the median value of all voxels within the ROI, with the bottom and top edges of the blue box indicating the 25th and 75th percentiles, respectively. The whiskers extend to the most extreme data points not considered outliers. Data points that were more than 1.5x the interquartile range away from the top or bottom of the box were classed as outliers and are plotted individually using red crosses. Significant signal differences between tumor and AUT within a given scan (as calculated using the Mann-Whitney U test) are denoted using single, double or triple asterisks representing $p<0.05$, $p<0.01$ and $p<0.001$ respectively.*

The median amide, NOE, MT and MTR$_{asym}$ signals in regions of tumor and AUT, the difference in median signals between these regions (∆), and the corresponding significance values, p, are fully tabulated in Table 5-3. Measurements showing significant differences between tumor and AUT are highlighted in bold.

Patient 1 (TZ tumor)								
Median signal	**Scan 1**							
	Reader 1				Reader 2			
	TZ AUT	TZ Tumor	∆	p	TZ AUT	TZ Tumor	∆	p
Amide	**0.113**	**0.102**	**-0.011 (-9.7%)**	**0.020**	**0.116**	**0.104**	**-0.012 (-10.3%)**	**0.042**
NOE	**0.109**	**0.096**	**-0.012 (-11.0%)**	**0.001**	**0.116**	**0.098**	**-0.018 (-15.5%)**	**0.016**
MT	**0.222**	**0.260**	**0.038 (17.1%)**	**<0.001**	0.247	0.254	0.007 (2.8%)	0.357
MTR$_{asym}$	0.018	0.019	<0.001 (0.0%)	0.928	**0.014**	**0.023**	**0.009 (64.3%)**	**0.017**
Median signal	**Scan 2**							
	Reader 1				Reader 2			
	TZ AUT	TZ Tumor	∆	P	TZ AUT	TZ Tumor	∆	p
Amide	**0.119**	**0.109**	**-0.010 (-8.4%)**	**<0.001**	0.112	0.112	<0.001 (0.0%)	0.668
NOE	**0.120**	**0.102**	**-0.017 (-14.2%)**	**<0.001**	0.114	0.104	-0.010 (-8.8%)	0.065
MT	**0.234**	**0.287**	**0.053 (22.7%)**	**<0.001**	0.261	0.275	0.014 (5.4%)	0.342
MTR$_{asym}$	0.009	0.007	-0.002 (-22.2%)	0.884	**0.007**	**0.015**	**0.008 (114.3%)**	**0.029**
Patient 2 (PZ tumor)								
Median signal	**Scan 1**							
	Reader 1				Reader 2			
	PZ AUT	PZ Tumor	∆	p	PZ AUT	PZ Tumor	∆	p
Amide	**0.131**	**0.148**	**0.017 (13.0%)**	**0.010**	0.142	0.140	-0.002 (-1.4%)	0.456
NOE	0.122	0.115	-0.008 (-6.6%)	0.334	0.122	0.123	<0.001 (0.00%)	0.898
MT	**0.227**	**0.172**	**-0.056 (-24.7%)**	**<0.001**	**0.242**	**0.203**	**-0.039 (-16.1%)**	**<0.001**
MTR$_{asym}$	**0.020**	**0.065**	**0.045 (225%)**	**<0.001**	**0.018**	**0.028**	**0.010 (55.6%)**	**0.042**
Median signal	**Scan 2**							
	Reader 1				Reader 2			
	PZ AUT	PZ Tumor	∆	p	PZ AUT	PZ Tumor	∆	p
Amide	**0.097**	**0.151**	**0.054 (55.7%)**	**<0.001**	**0.091**	**0.127**	**0.036 (39.6%)**	**<0.001**
NOE	**0.080**	**0.102**	**0.023 (28.8%)**	**0.004**	**0.075**	**0.100**	**0.025 (33.3%)**	**<0.001**
MT	**0.233**	**0.171**	**-0.063 (-27.0%)**	**<0.001**	**0.273**	**0.188**	**-0.085 (-31.1%)**	**<0.001**
MTR$_{asym}$	**0.014**	**0.050**	**0.035 (250%)**	**<0.001**	**0.009**	**0.038**	**0.030 (333.3%)**	**<0.001**

Table 5-3: *Median amide, NOE, MT and MTR$_{asym}$ signal measurements in TZ AUT and TZ tumor (patient 1) and PZ AUT and PZ tumor (patient 2). Data are shown for both scans of both patients using ROIs drawn by both readers. The signal difference, ∆, is expressed both as an absolute value and also as a percentage of the AUT signal. All associated* p*-values were calculated using the Mann-Whitney U test and are included. Significant differences in signal between tumor and AUT are highlighted in bold. Differences in repeated signal difference measurements (∆) between scans and readers are broadly in-line with the LOA values calculated earlier. The most consistent signal differences are found in the MT pool where signal in tumor often varies by over 0.04 thereby exceeding the best-case intra-session LOA for MT. The second scan of patient 2 shows the largest overall signal differences and consistency between readers where both the amide and MT signal changes in PZ tumor are greater than the LOA for these two pools.*

Visually, hypo-intensities of both the amide and NOE signals are observed in the region of TZ tumor when compared to apparently uninvolved TZ (patient 1), with corresponding hyperintensity of the MT signal.

For patient 2 the opposite contrast effect is observed, with hyper-intensity of amide and NOE signals within the region of PZ tumor relative to apparently uninvolved PZ and a corresponding relative hypo-intensity of the MT signal. However, it should be noted in this case that the hyper-intensities of amide and NOE signals within the tumor ROI appear to be part of broader structural features that are not localized to the tumor itself.

In the five healthy volunteers scanned in the previous chapter, MT was the most repeatable parameter (see Table 4-2) with the lowest CV values and a threshold for signal detection of 0.04-0.05 (17-22%) or higher. In the PZ tumor patient, MT showed significant amplitude decreases for both scans and for both readers with signal changes in the range -0.039 to -0.085 (16-31%), consistent with the repeatability threshold.

5.4 Discussion

Signal differences between tumor and AUT were most pronounced and showed the best agreement between readers for the second scan of the PZ tumor patient. In this case the amide, NOE and MTR_{asym} signals all showed significant increases in the region of tumor, and the MT signal was significantly reduced. While not all of these signal differences were larger than the previously measured LOAs for respective pools, the statistical significance was evaluated between groups of voxels drawn from within individual images and therefore relate to image contrast from a single subject and timepoint, not absolute signal measurements across multiple subjects and multiple timepoints. Results of the statistical significance tests should be interpreted in these terms.

The MTR_{asym} measurements are lower than those reported by Takayama et al [24] who observed MTR_{asym} values in the approximate range of 0.5-6% in PZ tissue and 3-8% in Gleason 7 tissue using a higher saturation power of 2.0μT. However, the MTR_{asym} signal enhancement in the PZ tumor (found to be approximately 3% of M_0, averaged over readers and scans), was broadly consistent in magnitude with the signal changes observed by Takayama et al [24]. The magnitude of the significant signal differences between AUT and both tumor types were found to be in the range 0.01-0.06 which is consistent with the magnitude of changes expected based on previous studies [23][24].

Partial volume effects may have had some small influence on the results although the slices were positioned at the largest cross section of the tumors (which were both >10mm in diameter) and it is expected that this will have served to minimise these effects.

It was considered whether the fitting model would be able to distinguish decreases in tissue T2 (which would cause broadening of the water peak) from increases in MT signal, which would cause a similar effect in the chemical shift ranges of interest for CEST and NOE peaks as these are two of the broadest features of the z-spectrum. If the distinction could not be made we would expect to see an inverse correlation between the T2w signal and MT height across the prostate voxels. No such correlation was observed (see Figure 5-4 in the supplementary figures for this chapter), which allayed concerns that the model was unable to distinguish between these two effects. This is attributed to the fact that MT points acquired between ±5.5 and ±300ppm allowed for proper characterisation of the broad MT resonance.

In terms of diagnostic prostate imaging, a comparison can be drawn between CEST and magnetic resonance spectroscopy (MRS), which are sources of alternative but complementary metabolic information. CEST provides chemically- and pH-weighted information derived from exchangeable protons across many metabolites, while MRS provides metabolite-specific profiling [115], often focusing on the ratio of choline to citrate [115]. While MRS has already been discussed in the context of mp-MRI [76] CEST is an imaging technique capable of providing higher spatial resolution than MRS in comparable scan-times (the CEST voxel size for this work is 2.2mm^2 compared to 6.9mm^2 [130] and 5.9mm^2 [115] in two studies on prostate MRS). MRS is well-suited to the characterization of known lesions or tumors under active surveillance, but the higher in-plane resolution of CEST is an advantage when screening for unconfirmed lesions. CEST has already shown promise in cancer imaging [114] [115][117] and further investigation will allow for exploration of its potential utility.

Multi-pool CEST imaging protocols similar to the one outlined in this work may be able to integrate traditional MTI metrics with semi-quantitative CEST measurements to provide more detailed exchange-based parametric information in support of mp-MRI protocols for the imaging of prostate cancer.

The evaluation of CEST contrast in prostate tumors would be improved with the inclusion of more subjects, but the initial results presented in this chapter, in combination with those presented in the previous chapter may provide a benchmark that could help power future prostate CEST studies.

Overall MT had the best repeatability and showed the most consistent change across scans and readers in the PZ tumour patient.

5.5 Supplementary figures

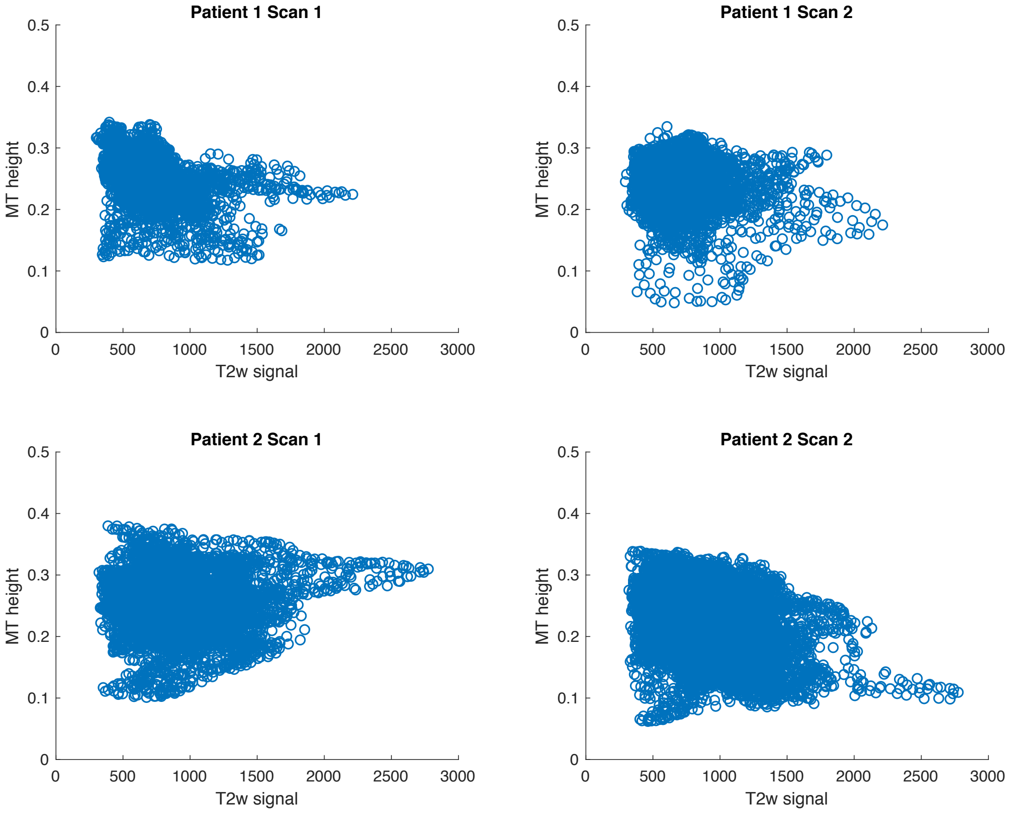

Figure 5-4: *Scatter-plots of the MT-amplitude vs the signal from the T2-weighted image for voxels across two scans of two prostate cancer patients. No inverse relationship is obvious, suggesting that there is no clear interplay between the MT-signal and the T2 of water.*

6 Peak-Finder: A statistical approach to CEST-peak identification

One of the key challenges when performing CEST peak-fitting at 3.0T is the assignment of chemical shift values to each pool in the fitting model. While NMR spectroscopy can be used to accurately identify chemical shift values under specific conditions of pH, temperature and concentration, these conditions show considerable variation in physiological systems and have additional dependences on T1, T2 and saturation parameters. As such there is currently no standard approach to the assignment of chemical shift values for Lorentzian fitting of z-spectra. This is particularly important *in vivo* where the CEST and NOE resonances are broad and overlapping and inaccurate peak-assignments may affect the final results from fitting. In this chapter, a method is proposed to help CEST peak assignment through deliberate over-fitting of z-spectra using many Lorentzian lineshapes. The proof-of-concept is demonstrated in simulated data and phantom data acquired at both 9.4T and at 3.0T.

Specific Chapter contributions:

Eleni Demetriou, PhD (Postdoctoral Researcher)[1]: Provided access to the Institute of Neurology laboratory space for phantom creation and undertook data acquisition at 9.4T.

All other work was undertaken by the author, including developing the idea, creating phantoms, scanning at 3.0T, implementing Matlab scripts and subsequent analysis.

Contributor affiliations:

[1] Institute of Neurology, University College London, Queen Square, London, WC1N 3BG

6.1 Introduction

One of the key steps when performing z-spectrum fitting of CEST data is the assignment of chemical shifts to each CEST or NOE pool. Fixing these parameters reduces the number of degrees of freedom in the final fitting model and reduces the likelihood of over-fitting. While the chemical shifts of CEST and NOE pools sit within narrow and well-defined ranges which are measurable using MRS, in CEST imaging they may appear to shift in the z-spectrum depending on the amplitude of the saturation and the underlying T1 and T2 values of the tissue. It is therefore desirable to select optimal chemical shifts for lineshapes corresponding to each pool when performing z-spectrum fitting.

This process is particularly challenging at clinical field strengths where z-spectrum features are broad and overlapping. This makes visual assessments of the chemical shifts and therefore tuning of the fitting-model challenging. In addition, the oscillatory behavior observed in the ±1ppm range *in vivo* at clinical field strengths can interfere with fit-optimisation because the complex behavior that arises is not modelled by the water Lorentzian so unpredictable parameter interactions may occur in an effort to compensate for this.

Here a method is proposed which involves deliberate over-fitting of z-spectra using many Lorentzian lineshapes. The underlying principle is that, while the over-fitting process allows fitted lineshapes to be centred at any chemical shift value, they will tend to cluster around ‘true’ resonances in the z-spectrum when data is aggregated over many fits and that these lineshapes will tend to have larger amplitudes. It is also suggested that this over-fitting approach may help to correct for the oscillatory behavior close to 0ppm, thereby minimizing the interference that this confounding feature has with the rest of the z-spectrum when assigning chemical shifts. Analysis of the distribution of chemical shifts from this process may allow for a novel approach to chemical shift assignments and for greater confidence in the tuning of fitting algorithms when analyzing CEST data acquired at clinical field strengths.

The purpose of this study is to assess whether the proposed method can be used to identify optimal chemical shift values for the fitting of z-spectra. The method is applied to simulated and phantom data at 9.4T and 3.0T. The hypothesis is that the method will yield chemical shift assignments that agree with the ground truth in the simulation data, and that it will generate consistent chemical shift assignments at both field strengths in phantoms.

6.2 Methods

6.2.1 Over-fitting approach

The fit equation included a whole-fit horizontal shift, *h*, a whole-fit vertical shift, *v*, a Lorentzian lineshape corresponding to the water resonance, which was fixed at 0ppm, and a large number of additional Lorentzian lineshapes with freedom to explore a wide range of chemical shift values.

Given that the maximum number of degrees of freedom in a fitting model cannot exceed the number of data-points, and (as per equation 1-19) a Lorentzian lineshape is defined by three parameters, a z-spectrum consisting of N data-points may be fitted using a maximum of *n* = floor([N-2]/3) Lorentzian lineshapes, the overall fit equation is:

$$M_z(\omega) = 1 - L_{DS}(\omega - h, 0, \Gamma_{DS}, A_{DS}) - \sum_{i=1}^{n-1} L_i(\omega - h, \omega_{0i}, \Gamma_i, A_i) + v \tag{6-1}$$

Where terms with subscript ‘*DS*’ correspond to the Lorentzian lineshape accounting for the water resonance. This peak had a lower limit on its amplitude of $0.5*M_z$. The upper and lower bounds of the FWHM were selected based on the field strength. The chemical shifts of all non-water lineshapes were free to explore the chemical shift range of interest. Fitting was performed using a non-linear-least-squares algorithm to minimse the difference between the points in each measured z-spectrum and the lineshape generated by the overall fit equation.

All z-spectra were fitted in this manner such that simulated data (with 101 sampling frequencies) were fitted with 33 lineshapes, the 9.4T data (with 77 sampling frequencies) were fitted using 25 Lorentzian lineshapes and the 3.0T data (with 50 sampling frequencies) were fitted using a total of 16 Lorentzian lineshapes.

6.2.2 Histogram analysis

Histogram analysis involved plotting histograms of the chemical shifts of all fitted lineshapes across many z-spectra to identify histogram maxima which may correspond to CEST or NOE resonances.

Histograms were also generated for other fit parameters such as the FWHM and amplitude and while these were not explored specifically they were used to support tuning of the upper and lower bounds for each application (simulations and phantoms at both field strengths).

6.2.3 Sum-of-amplitudes analysis

Sum-of-amplitudes analysis is an extension of the histogram analysis which takes into account not just the chemical shift of each fitted lineshape, but also the amplitude. It involves summing the amplitudes of all Lorentzian lineshapes with evenly-spaced bins across the chemical shift range of interest. The results are presented as a bar-chart which, similar to the histograms, can be assessed in terms of maxima which may correspond to CEST or NOE resonances.

6.2.4 Simulated z-spectra

Bloch-McConnell (BM) simulations were used to generate z-spectra for a three-pool system consisting of two amide groups and water. The chemical shifts of the two amide pools were fixed at 2.80 and 3.50ppm (close to reference values of nicotinamide [131]) at concentrations of 200mM and exchange rates of 200Hz. The saturation train consisted of one hundred 40ms duration Gaussian pulses at 80% duty-cycle with a B_{1CWPE} of 1.0μT (saturation flip-angle = 767°) comparable to the power used in subsequently described phantom studies. The offset frequency sampling was at 101 offset frequencies, evenly spaced between ±5ppm. Random Gaussian-distributed noise was added to the z-spectra with standard deviations of σ = 0.001, 0.01 and 0.05 corresponding to SNR levels in the unsaturated regions of the z-spectrum of 1000, 100 and 20, respectively. The σ = 0.01 (SNR=100) level was the most physically realistic noise-level, based on previously acquired CEST data and similar simulation work in the literature [132]. B_0 inhomogeneities were introduced by randomly shifting all z-spectra by up to ±0.01ppm. In total 500 z-spectra were generated at 3.0T and 500 at 9.4T.

6.2.5 Phantoms

Multi-compartment phantoms containing 100mM Nicotinamide solution at pH values of 6.2, 6.6, 7.0, 7.4 and 7.8 were created and scanned at 9.4T and 3.0T within 6 hours of each other. Compartments for the 9.4T phantom were comprised of 1ml syringes which were bundled and tied together. For the 3.0T phantom each compartment was a 50ml falcon tube, and all tubes were fixed in place within a large sealable container which was filled with de-ionised water.

Nicotinamide was selected because it contains a single amide group with two isomeric configurations with different chemical shifts. The *cis*- and *trans*- isomers are known to resonate at 2.88ppm and 3.54ppm respectively when in 1.5 Molar solution at pH 6.5 and have relatively slow exchange rates with water of 125Hz and 111Hz respectively making them suitable for CEST imaging at low saturation powers [131]. Values reported by Birdsall et al suggest that the chemical shifts of both isomers show some dependence on the concentration and pH of the solution. The concentration used in phantoms was 100mM, lower than in Birdsall et al, therefore in keeping with the trends described in their work it was expected that the measured chemical shifts in this work would be slightly lower than those quoted above [131][133].

6.2.6 MRI protocol at 9.4T

At 9.4T, z-spectra were acquired at 77 offsets, evenly spaced between -6.06ppm and +6.06ppm. The saturation scheme was comprised of 151 Gaussian pulses with τ_p = 50ms and τ_d = 5ms (91% duty-cycle). Data were acquired at 9 saturation powers with saturation flip-angles evenly spaced between 600° and 3000° corresponding to $B1_{CWPE}$ values ranging from 0.76μT to 3.91μT.

6.2.7 MRI protocol at 3.0T

At 3.0T z-spectra were acquired at 50 offset frequencies, evenly spaced between ±5ppm. Data were acquired using a saturation scheme comprised of 60 sinc-Gaussian pulses with $\tau_p = \tau_d$ = 40ms. Data were acquired at multiple powers using saturation flip-angles of 200°, 400°, 600°, 800°, 1000°, 1133° and 1190°, with corresponding $B1_{CWPE}$ values ranging from 0.16μT to 0.97μT.

6.2.8 Data analysis

All data were processed using in-house developed software in Matlab R2016a (MathWorks, Natick, MA, USA).

After multiple z-spectra have been fitted, the ppm-range of interest is split into bins of typically 0.01ppm and the amplitude of all lineshapes that fall into each bin are summed. These are presented as bar charts and the maxima are analysed to identify chemical shift ranges which are likely to represent a true resonance in the z-spectrum. This is referred to as the ‘sum-of-amplitudes’ approach in the remainder of this chapter.

6.3 Results

6.3.1 Simulations

Figure 6-1 shows representative z-spectra simulated at 9.4T and at 3.0T with added Gaussian-distributed noise (σ = 0.01). The zig-zag pattern caused by rotation effects close to 0ppm is clearly visible in the 3.0T data.

Representative fits of the 9.4T and 3.0T simulated data using 33 Lorentzians are shown in Figure 6-2. The maximum absolute residual value for the 9.4T data is 0.03 and for the 3.0T data is 0.09 and these values both occur close to 0ppm.

Histogram distributions of all fitting parameters excluding the direct saturation are shown in Figure 6-3 for simulated data from both 9.4T and 3.0T. Maxima are visible in the chemical shift distributions close to 2.8ppm and 3.5ppm where the simulated CEST pools are located. These are more pronounced at 9.4T than at 3.0T. Maxima are also observed in both cases in the ±1ppm range due to the water zig-zag effect.

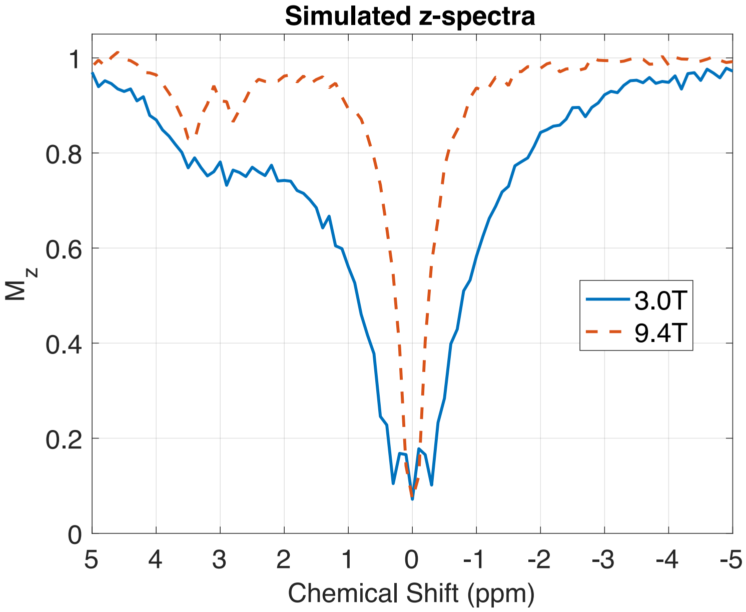

Figure 6-1: *Simulated z-spectra for a three-pool system at two field strengths with added Gaussian-distributed noise (σ = 0.01).*

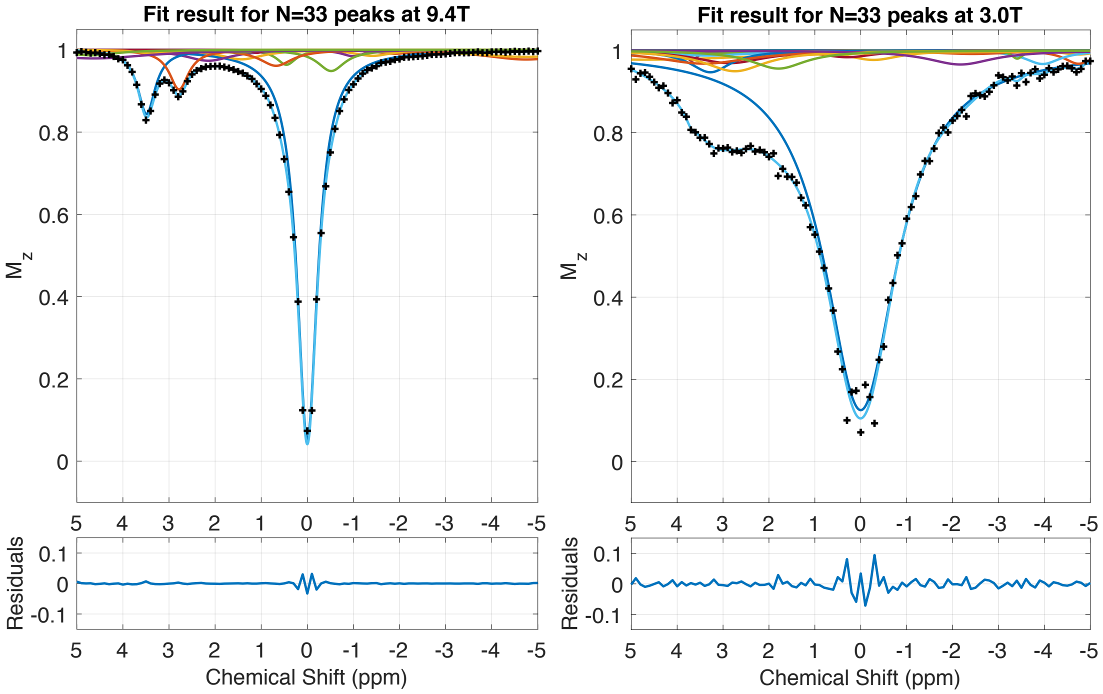

Figure 6-2: *Simulated z-spectra from 9.4T and 3.0T fitted using 33 Lorentzian lineshapes (SNR=100).*

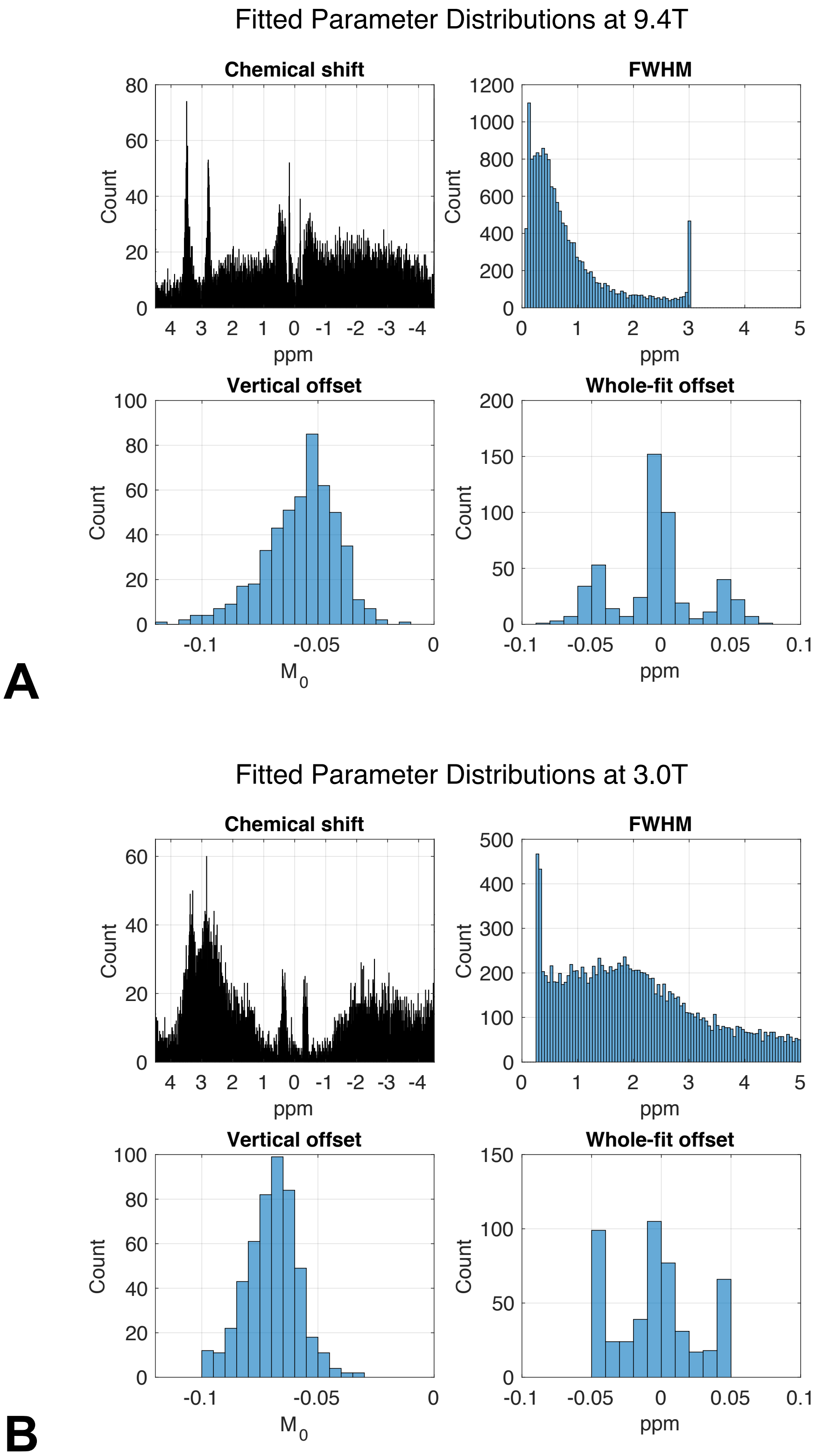

Figure 6-3: *Histograms showing the distribution of fitted parameters across (A) 500 simulated z-spectra at 9.4T and (B) 500 simulated z-spectra at 3.0T, both with added noise and B_0 inhomogeneities of up to 0.1ppm. The top left histograms showing the distributions of the chemical shifts are of primary interest with the FWHM, vertical and horizontal offsets included for completeness. Maxima are observed in the chemical shift distributions close to 2.8ppm and 3.5ppm where the simulated CEST pools are located. As expected, the FWHM values are smaller at 9.4T.*

In the 3.0T simulated data additional maxima are observed in the -3ppm range which could be mistaken for CEST or NOE resonances but which are not caused by exchange effects. These are judged to be fitting artefacts due to the zig-zag effect.

To investigate these effects scatterplots of chemical shift versus peak amplitude are shown in Figure 6-4. At both 3.0T and 9.4T lineshapes have been fitted across the whole chemical shift range. Excluding lineshapes fitted in the ±1ppm range, the highest amplitudes in the 9.4T data are seen at 2.8ppm and 3.5 ppm corresponding to the two amide groups. At 3.0T the maxima are less pronounced, especially at 2.8ppm. Of note is that the maxima previously seen close to -3.0ppm in the chemical shift histogram for 3.0T data (see Figure 6-3) is substantially reduced in the 3.0T data here. On this basis, sum-of-amplitudes plots were created.

The sum-of-amplitudes results are shown in Figure 6-5. Two maxima are clearly observed in the expected chemical shift ranges. The peak sum-of-amplitudes values are found at 2.80ppm and 3.50ppm at 9.4T and 2.85ppm and 3.30ppm at 3.0T. Improvements on the histogram method are seen both in terms of improved delineation of the two true CEST resonances from the ‘sound-floor’ of the plots at both field-strengths, and suppression of the pseudo-NOE signal in the 3.0T data.

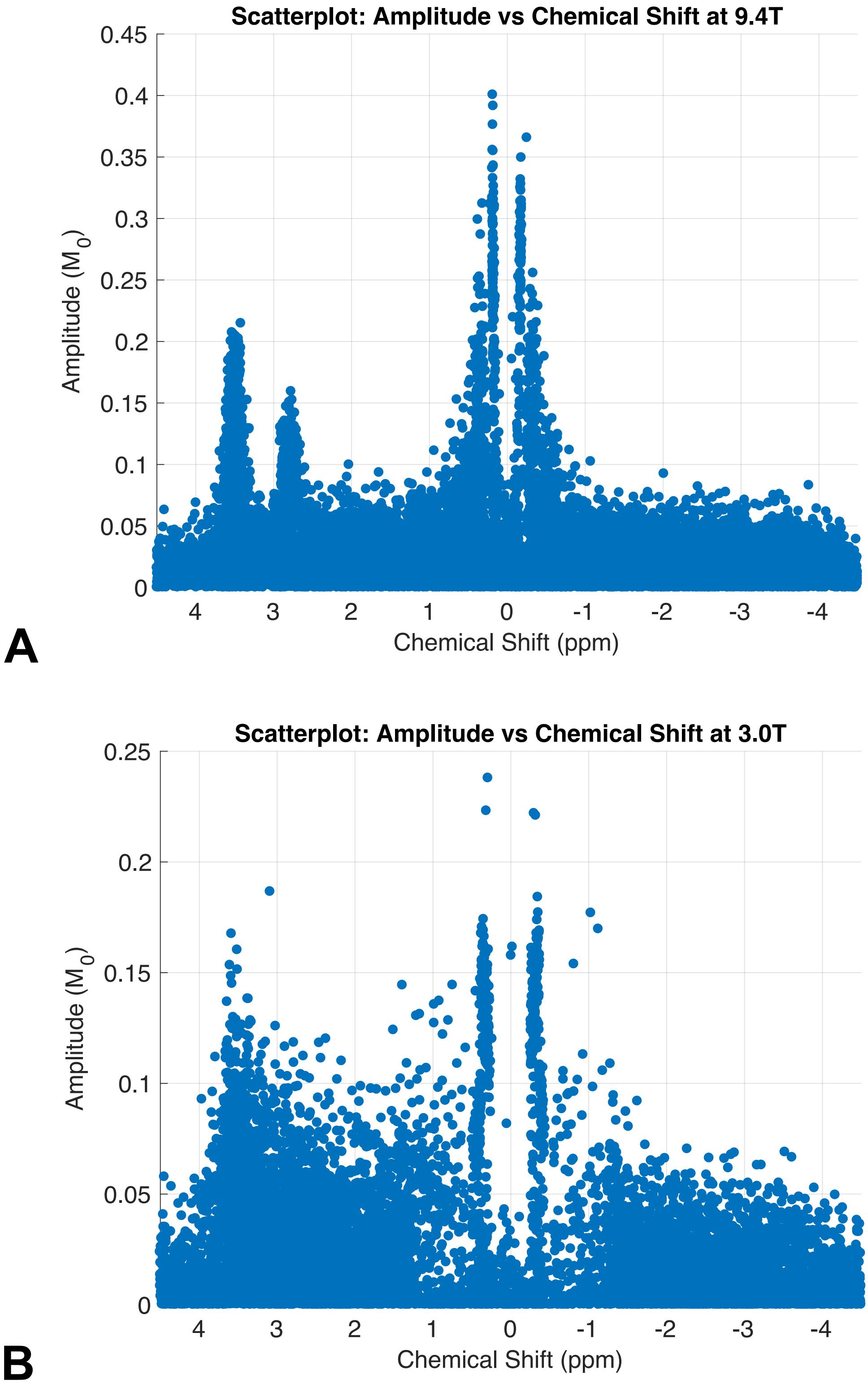

Figure 6-4: *Scatterplots showing the relationship between the amplitude of fitted lineshapes and the chemical shift at which they are centred. For simluations at both (A) 9.4T and (B) 3.0T, fitted lineshapes were distributed across the whole chemical shift range. For the 9.4T data, ignoring the ±1ppm range and the upper and lower-bounds of ±4.75ppm the highest amplitudes are seen at 2.8ppm and 3.5 ppm corresponding to the two amide groups. At 3.0T, a broader feature is observed consistent with an underlying maximum at 3.5ppm, albeit less pronounced than at 9.4T. It is unlikely that the maximum at 2.8ppm could be identified with confidence from this 3.0T dataset.*

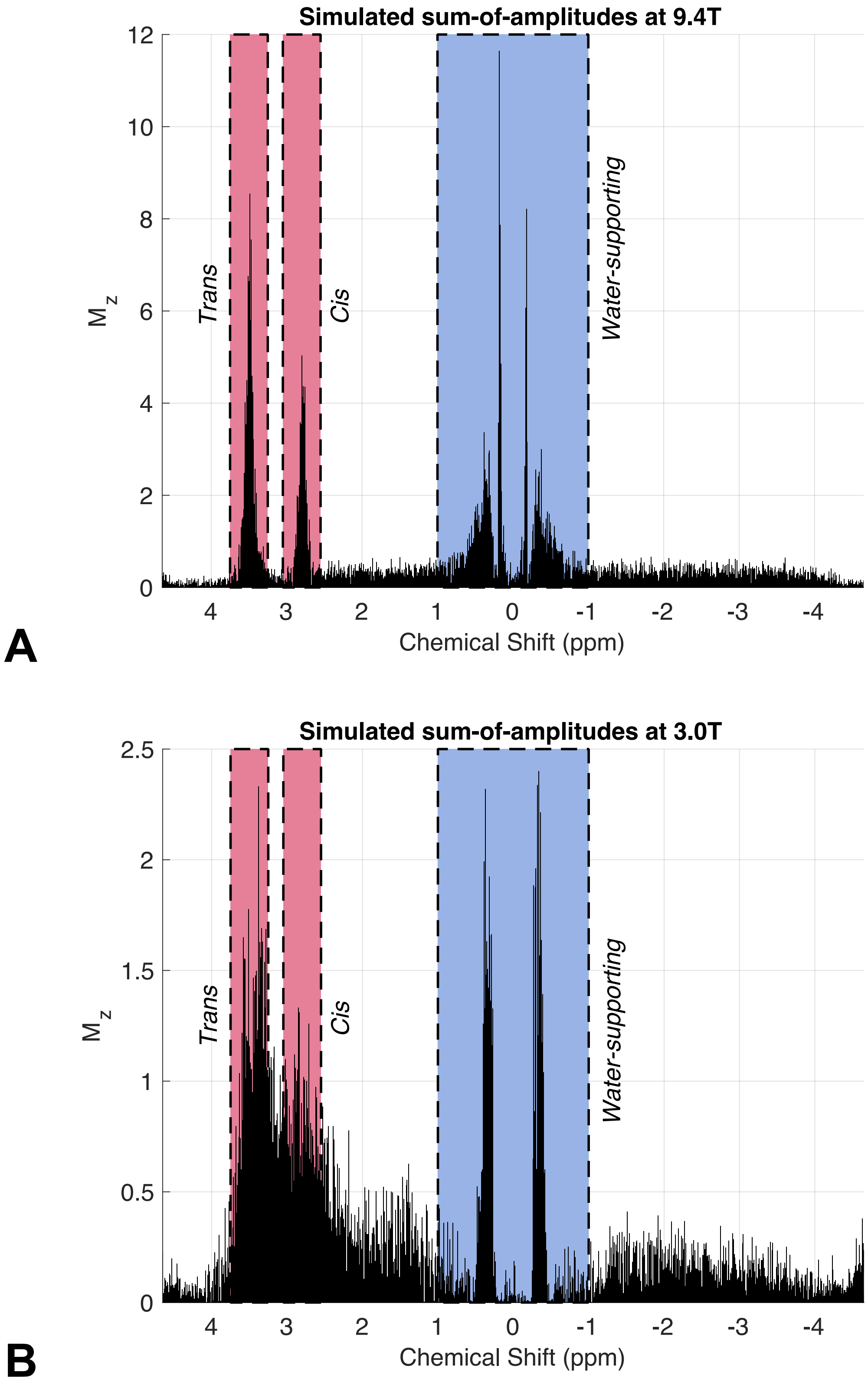

***Figure 6-5:** Sum-of-amplitudes plots for data from (A) 9.4T and (B) 3.0T. The two amide resonances are clearly visible in both cases. Of note, the maxima previously visible on the NOE-side of the z-spectrum are far-reduced in the 3.0T case.*

Having identified from the sum-of-amplitudes analysis that there are two CEST peaks present, the spectra were re-fitted using a three pool model centering the starting values for the chemical shifts of the two CEST pools at the frequencies identified in the sum-of-amplitudes plots with tolerances of ±0.5ppm, based on the widths of the maxima shown in Figure 6-5. The resulting chemical shifts for the two identified CEST peaks are shown in boxplot format in Figure 6-6 where the ground truth chemical shifts of 2.8ppm and 3.5ppm are also indicated by dotted lines.

At 9.4T good agreement is seen between the median fitted chemical shift values and the ground-truth with deviations of 0.02ppm and 0.01ppm for the *cis*- and *trans*-isomers respectively at SNR=100. The clustering is also very tight with inter-quartile ranges for the chemical shifts of the *cis*- and *trans*-isomers of 0.02ppm and 0.03ppm respectively.

At 3.0T the deviations of the median chemical shifts of the *cis*- and *trans*-isomers from ground-truth at SNR=100 were found to be larger at 0.15ppm and 0.06ppm and the interquartile ranges were also found to be larger at 0.21ppm and 0.10ppm, respectively. The boxplots of chemical shifts for the *cis*-isomer across all SNR values does not enclose the ground truth, and the same is true for the *trans*-isomer at SNR=1000.

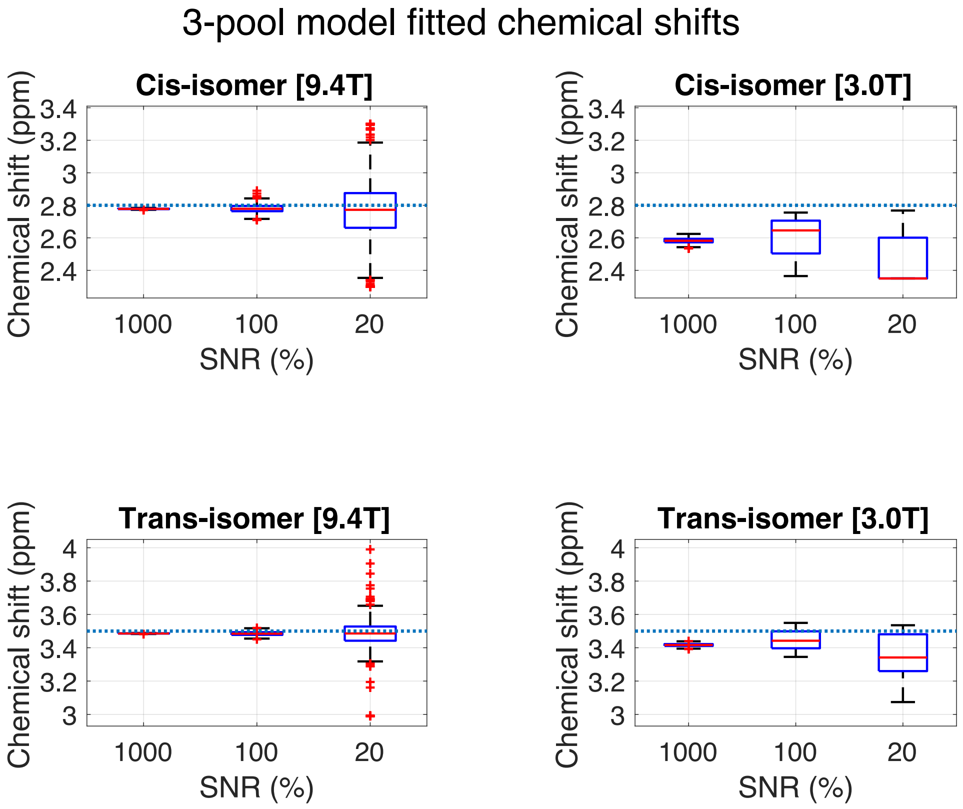

Figure 6-6: *Boxplots showing the distributions of the fitted chemical shift values for the cis and trans isomers in simulated data at two field strengths when fitted using a 3-pool model.*

The results from each stage of this analysis are shown together in Table 6-1. The final result from the three-pool fitting step, whereby the starting values and parameter upper and lower bounds were derived from the sum-of-amplitudes step, was originally expected to improve the fit results but in fact appears to produce worse results (i.e. poorer agreement with the ground truth) than the histogram and sum-of-amplitudes steps. This may be because the over-fitting approach using many lineshapes is able to compensate for the effects of noise and for the zig-zag effects, but when the chemical shifts are fixed and the three-pool model was used, it again became insufficient for modelling the complexity close to 0ppm and the result was that the CEST peaks are 'dragged' closer to 0ppm. These z-spectrum features appear to be at least as important as noise as confounding factors in the overall fits (as the distributions of chemical shifts in Figure 6-6 show).

Assigned chemical shifts (ppm)				
Simulated Field Strength	9.4T		3.0T	
Isomer	Cis	Trans	Cis	Trans
Ground Truth	2.80	3.50	2.80	3.50
Histogram assignment	**2.80**	**3.50**	**2.85**	3.30
Sum-of-amplitudes assignment	**2.80**	3.49	**2.85**	3.38
Three-pool fit assignment	2.78	3.48	2.65	**3.44**

Table 6-1: *Chemical shifts assigned to the cis- and trans-isomers using simulated three-pool z-spectra at two field strengths in the SNR=100 case. The histogram and sum-of-amplitudes both show very close (<0.02ppm) agreement with the ground truth. The three-pool method which was originally expected to improve the fit results appears to give worse results than the histogram and sum-of-amplitudes steps. The closest chemical shift value for each isomer at each field strength is marked in bold and underlined. In the case of the trans-isomer at 9.4T the histogram and sum-of-amplitudes assignments were identical to 2.d.p.*

6.3.2 Phantom results at 9.4T

Representative ROI-averaged z-spectra from 3.0T and 9.4T are shown in Figure 6-7 from compartments at pH 7.8 and $B1_{CWPE}$ of 0.97μT and 1.17μT respectively. Visual inspection of the 9.4T data shows two CEST peaks which are centred at 2.55ppm and 3.35ppm. These values are slightly different to those reported by Birdsall et al [131], however the variation is attributed to dilution shift as referenced in their work.

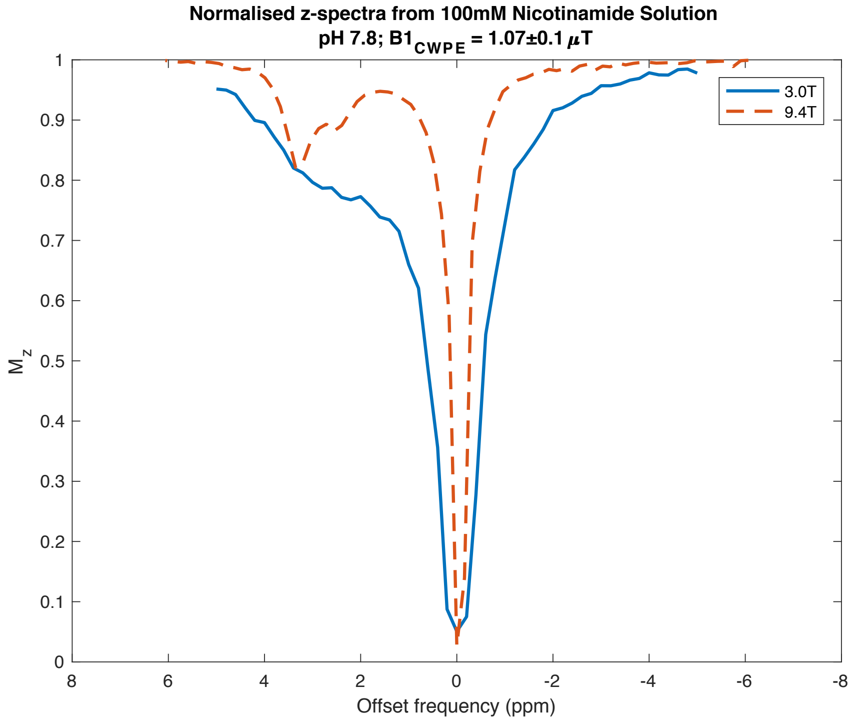

Figure 6-7: *Representative z-spectra from 100mM nicotinamide solution at pH7.8, scanned at both 3.0T and 9.4T with respective B1$_{cwpe}$ values of 0.97μT and 1.17μT respectively.*

The starting values of the chemical shifts of all free-to-roam Lorentzian lineshapes were evenly distributed between ±5ppm. In the first instance the upper and lower bounds were set to be ±6.08ppm. FWHM values were bounded at 0.1ppm and 3ppm, based on initial assessment of the peak widths in the raw data. Figure 6-8 shows a representative z-spectrum from the pH 7.8 compartment at a saturation flip angle of 3000° that has been fitted using 25 Lorentzian lineshapes.

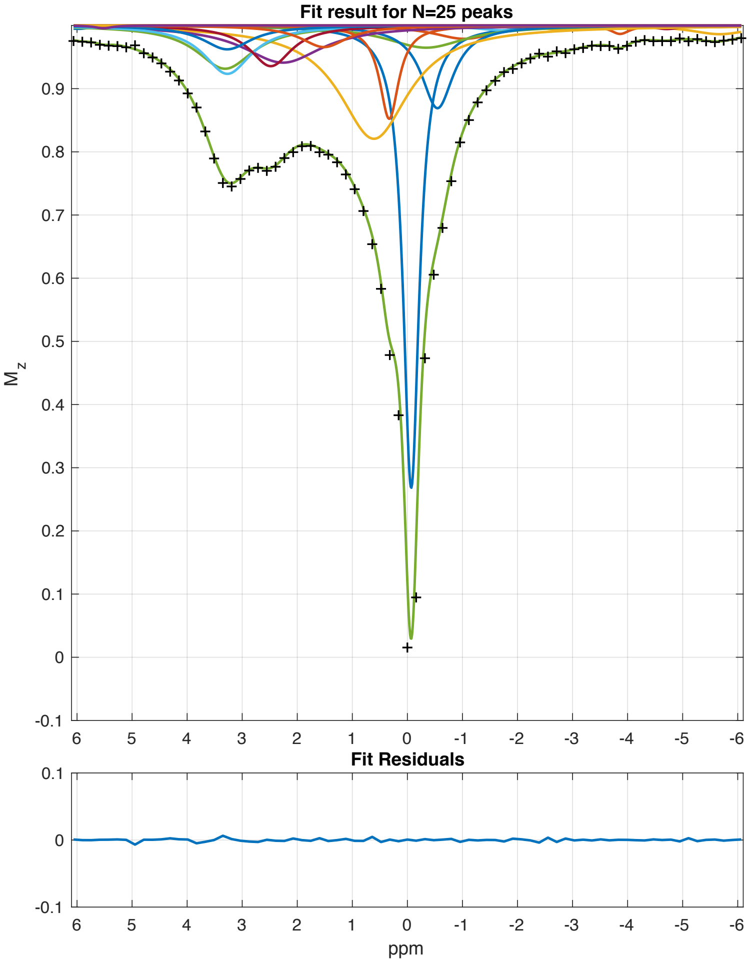

Figure 6-8: *A fitted z-spectrum from the pH7.8 compartment with saturation flip-angle of 3000°. The sum of the Lorentzian lineshapes generated a good fit of the z-spectrum. Water-supporting peaks in the ±1ppm range are attributed to the oscillatory effects described in chapter 3.*

Histograms showing the distribution of the fitted offset frequencies and FWHM values from all peaks excluding water and the whole-fit horizontal and vertical offsets across all compartments and powers (a total of 4,131 voxels) are shown in Figure 6-9. The notable features of the offset frequency histogram are:

1) Two clear histogram peaks with maximum bin heights at 2.56ppm (rising above the noise-floor between 2.49ppm and 2.62ppm) and 3.37ppm (rising above the noise-floor between 3.30ppm and 3.50ppm).
2) A clustering of peaks in the ±1ppm range henceforth referred to as 'water-supporting' peaks. They are attributed to the oscillations in the water peak that arise as a result of using pulsed-saturation. These are fitting artefacts and are not treated as actual CEST or NOE peaks.
3) Maxima at the upper and lower bounds of the fitting range (±6.08ppm). As with the ±1ppm peaks, these are judged to be fitting artefacts.

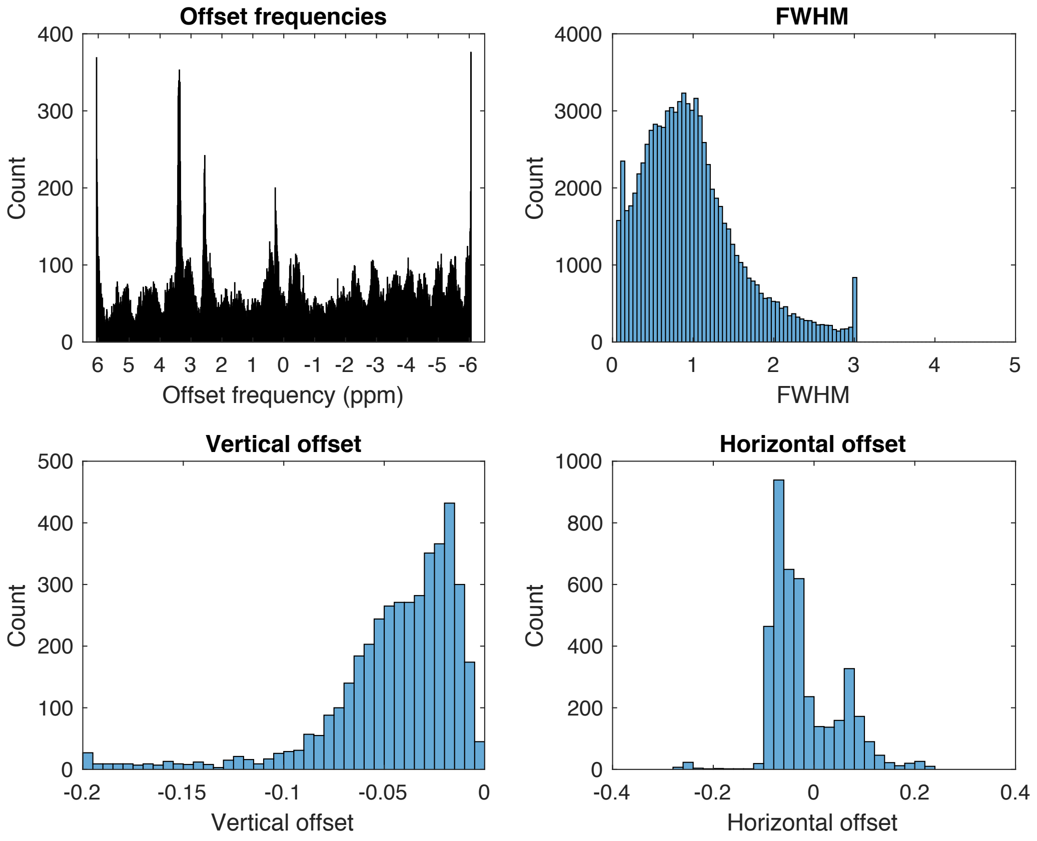

Figure 6-9: *Histograms showing the distributions of fit parameters of 4,131 voxels across multiple compartments of a Nicotinamide and water phantom scanned at 9.4T.*

The effect of using different starting parameters was explored through several iterations. It was concluded that the most well-defined maxima in the histogram and sum-of-amplitudes analyses were obtained when all peaks started at the same offset frequency of 5.0ppm (compared to an initial even distribution across the whole fitting range). This appeared to lower the ‘noise floor’ of the histogram plots.

The sum-of-amplitudes plot for the 9.4T data is shown in Figure 6-10. Compared to the histogram results, the central frequency of the *trans*-isomer remained at 3.37ppm while the central frequency of the *cis*-isomer shifted marginally from 2.56ppm to 2.55ppm.

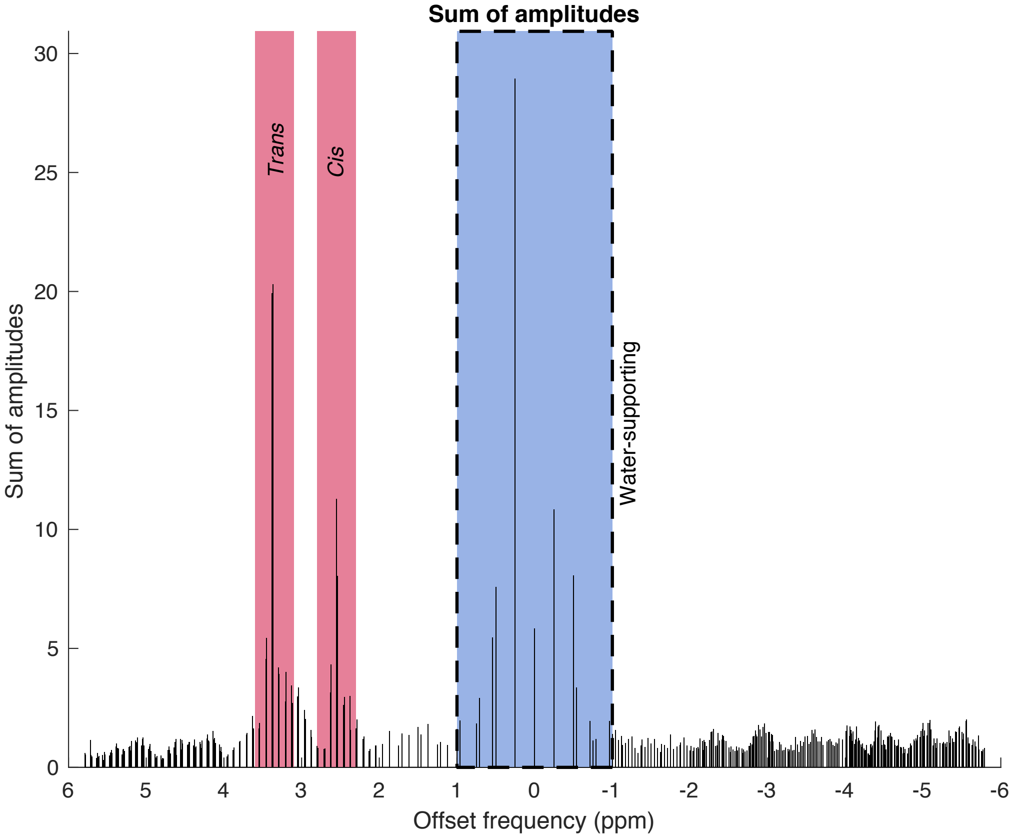

Figure 6-10: *A plot of the sum of amplitudes of all peaks fitted within each 0.01ppm range across all fits. Maxima corresponding to the cis and trans amide resonances are marked in red and the 'water-supporting' peaks are highlighted in blue. Results from outside the ±5.8ppm range are judged to be strongly affected by fitting artefacts and are excluded.*

Having identified that there are two CEST peaks present we have established a 3-pool fitting model with offset frequencies shown in Figure 6-17. Averaged over all powers, the final offset frequencies for the *cis* and *trans* isomers in phantoms at 9.4T were found to be 2.55ppm and 3.30ppm, respectively. A representative fit is shown in Figure 6-11 and Figure 6-12 shows a map of the *trans*-isomer peak height across all compartments. Amide signal appears to increase with pH in this pH range.

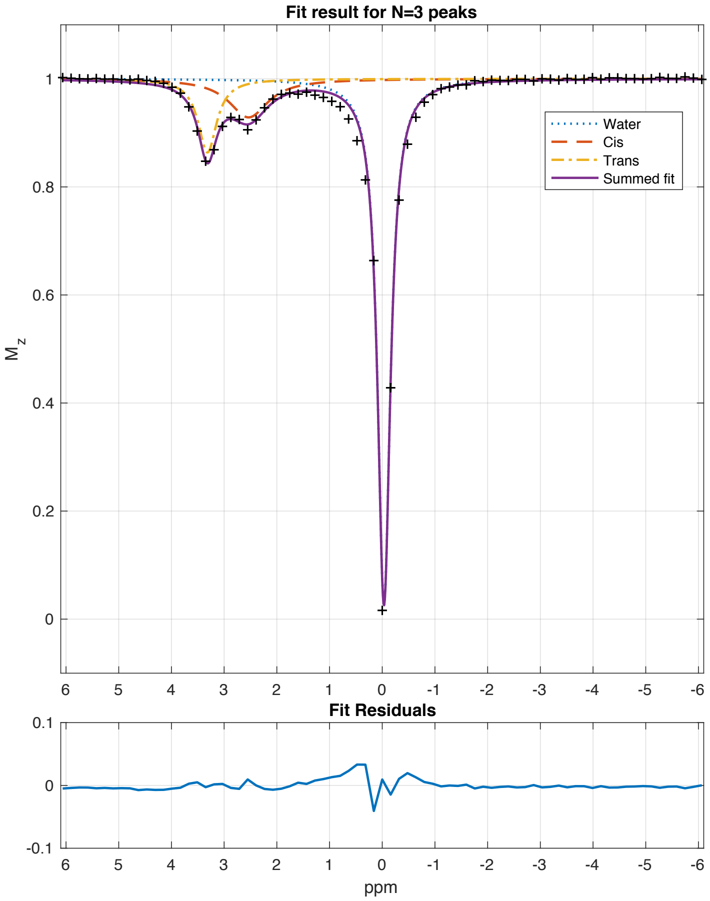

Figure 6-11: *A z-spectrum acquired at 9.4T, fitted using a 3-pool fitting model with offset frequencies determined using the sum-of-amplitudes method.*

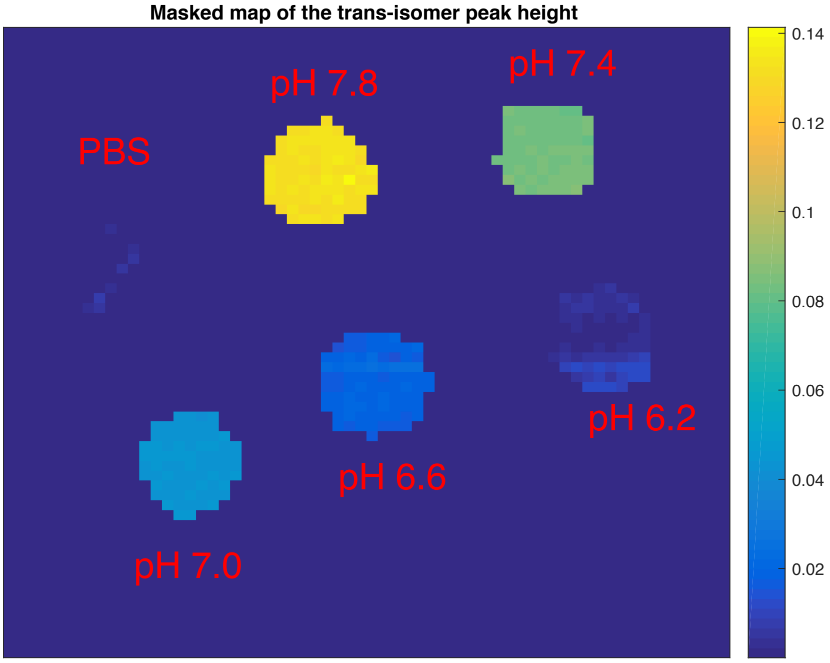
Masked map of the trans-isomer peak height
PBS
pH 7.8
pH 7.4
pH 6.2
pH 6.6
pH 7.0
0.14
0.12
0.1
0.08
0.06
0.04
0.02

Figure 6-12: *A map of the height of the trans-isomer amide peak in different compartments of the phantom scanned at 9.4T.*

6.3.3 Phantom data at 3.0T

At 3.0T the two amide resonances are broader and more overlapping than at 9.4T (see Figure 6-7). Without prior knowledge it would not be obvious that two peaks are present in the spectrum. Various sets of starting values for chemical shifts were tried and the clearest results were found when the starting values of all peaks were at 0.00ppm.

Both the histogram and sum-of-amplitudes analyses for the ph7.0 data are shown in Figure 6-13 and Figure 6-14 respectively. In the sum-of-amplitudes analysis peaks are clearly identifiable close to 2.58ppm and 3.37ppm.

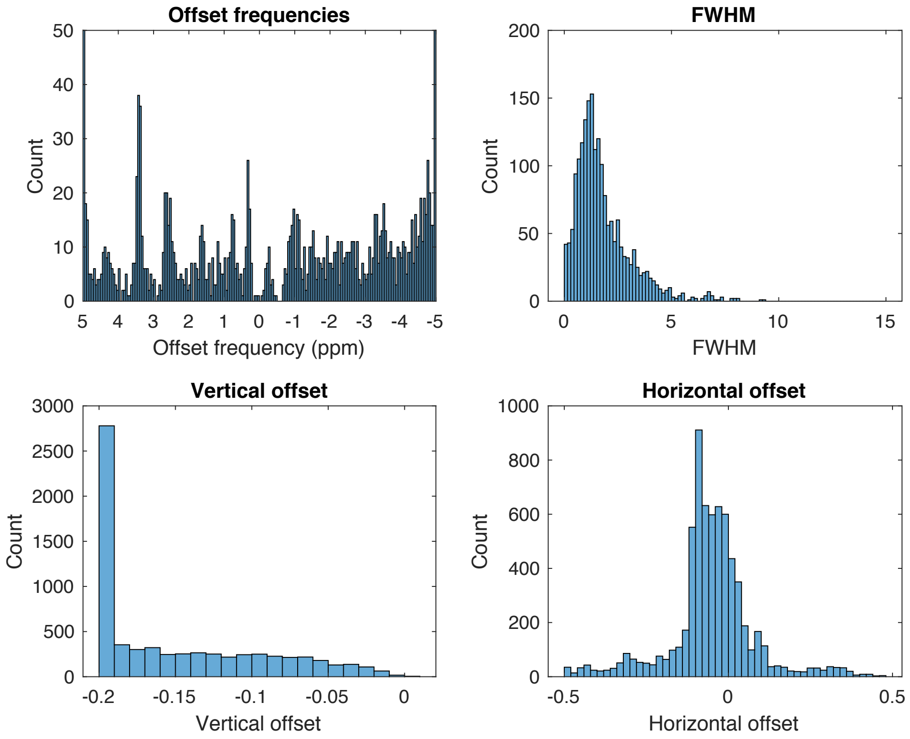

Figure 6-13: *Histograms showing the distributions of fit parameters from the pH7.8 compartment of a Nicotinamide and water phantom scanned at 3.0T.*

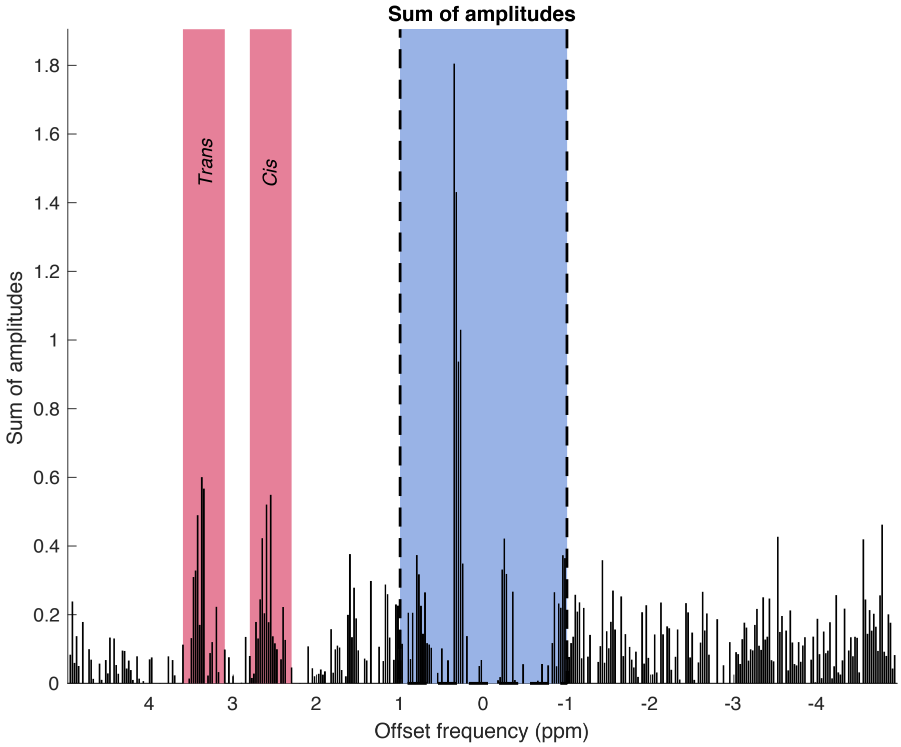

Figure 6-14: *Sum-of-amplitudes analysis for the pH 7.0 compartment scanned at 3.0T showing clear resonances close to 3.38ppm and 2.55ppm. Maxima corresponding to the cis and trans amide resonances are marked in red and the 'water-supporting' peaks are highlighted in blue.*

Having fixed the offset frequencies using the sum-of-amplitudes method the whole dataset was fitted using the 3-pool model. A representative fit of a single voxel taken from the pH 7.8 compartment at 0.97μT saturation power at 3.0T is shown in fFigure 6-15 and a map of the trans-isomer peak heights across the whole phantom is shown in Figure 6-16.

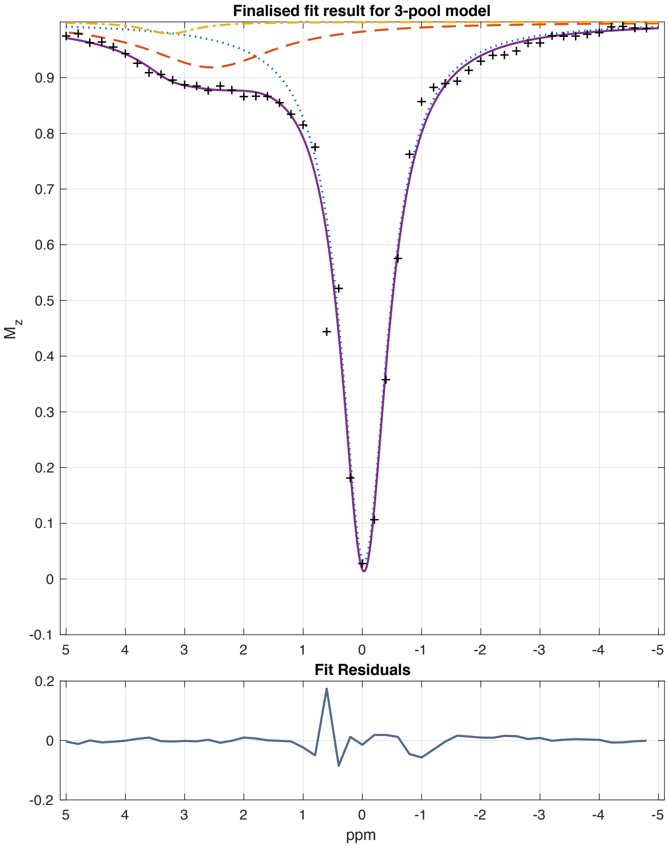

Figure 6-15: *A fitted z-spectrum acquired from 100mM nicotinamide solution scanned at 3.0T. pH7.8, $B1_{CWPE}$ = 0.97μT. Fit parameters were tuned using sum-of-amplitudes analysis.*

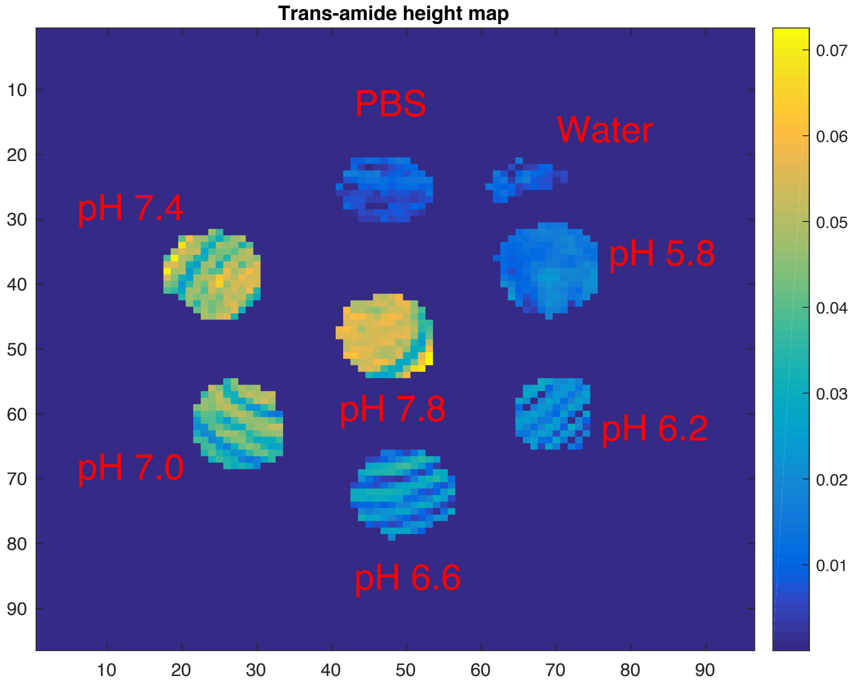
Trans-amide height map
PBS
Water
pH 7.4
pH 5.8
pH 7.8
pH 6.2
pH 7.0
pH 6.6
10
20
30
40
50
60
70
80
90
0.07
0.06
0.05
0.04
0.03
0.02
0.01

Figure 6-16: *Map of the trans-isomer amide signal across multiple compartments at 3.0T. It is suspected that the stripe artefacts in the image are due to interactions between the B_0 and B_1 field inhomogeneities as they appear broadly concentric and consistent with typical field homogeneity maps. They are not attributed to Gibbs ringing as the pattern does not resemble the shape of each sub-compartment where there are boundaries between plastic and water.*

The chemical shift assignments arising from the sum-of-amplitudes analysis for both the *cis*- and *trans*-isomers are shown in Figure 6-17. As anticipated, these *cis*- and *trans*-isomer chemical shift values are slightly smaller than those reported by Birdsall et al (2.88 and 3.54ppm, respectively) and this is attributed to dilution shift [131].

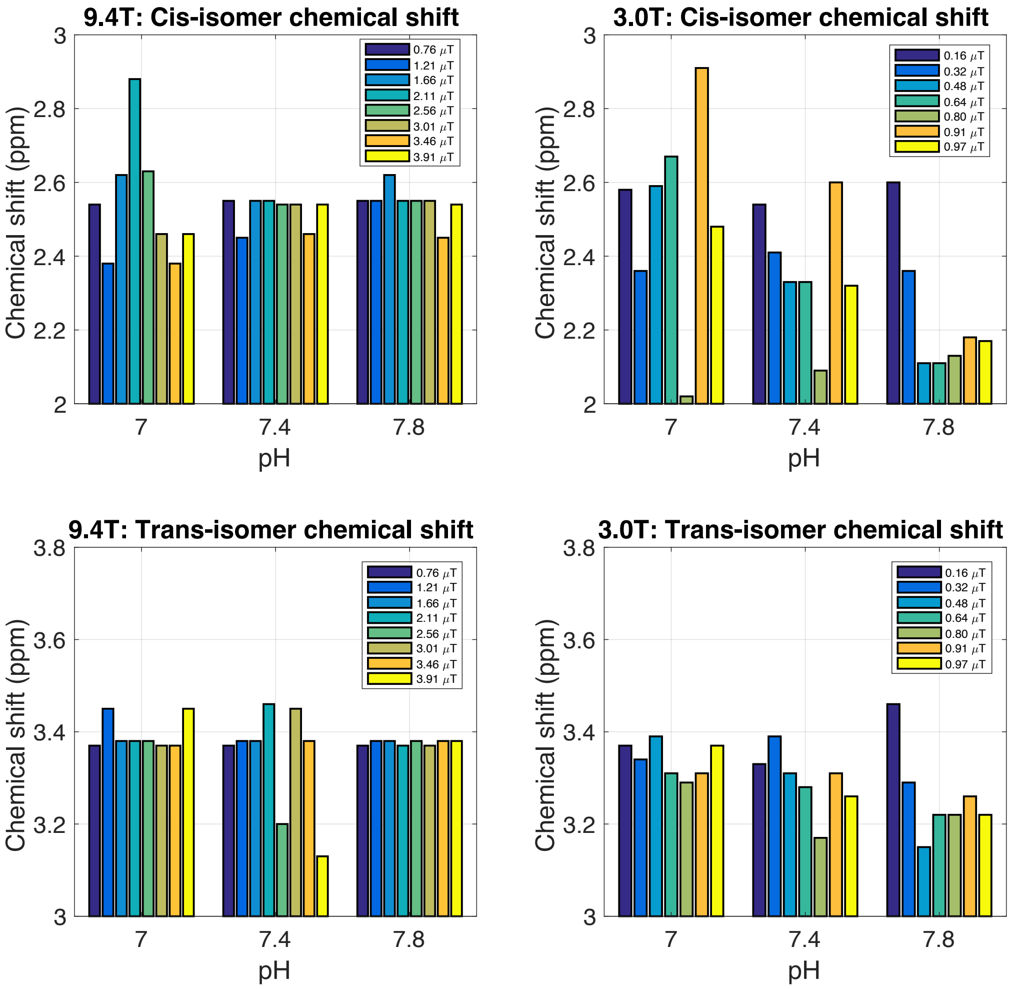

Figure 6-17: *Chemical shift assignments for the cis- and trans-isomers of nicotinamide over a range of pH values and saturation powers as assigned by a sum-of-amplitudes analysis. Results from 9.4T show the tightest agreement at different pH and saturation powers with no substantial pH-drift observed. Results from 3.0T show increased variation compared to the 9.4T data and this is particularly evident for the cis-isomer.*

6.4 Discussion

We have outlined a sum-of-amplitudes approach for identifying and assigning chemical shift values to CEST peaks. The method is an extension of histogram-based analysis and has the added benefit of reducing the effect of starting-values on the final output. The technique was demonstrated both in simulations and in phantoms at two field strengths.

In simulations, the histogram analysis method produced good results for the chemical shift of both isomers but featured pseudo-NOE contributions which complicate the interpretation of the results and will be particularly problematic if the method is to be applied *in vivo*. The extension of the analysis to the sum-of-amplitudes approach still suggested that two CEST peaks were present in the same chemical shift range but had the added benefit of reducing the pseudo-NOE effect at 3.0T.

The sum-of-amplitudes analysis of the simulated data produced good results for both isomers at 9.4T. However, at 3.0T it did not include the ground-truth chemical shift for the *cis*-isomer or for the *trans*-isomer with very little added noise. It is also noted that the method appears more likely to under-estimate rather than over-estimate the chemical shifts of each pool at both field strengths due to interactions with the direct saturation which can shift the apparent chemical shifts of CEST resonances in the z-spectrum.

Three-pool fitting of the simulated data, which was intended to hone-in on a final chemical shift for each pool, gave results showing worse agreement with ground-truth than the histogram or sum-of-amplitudes approaches. This could be due to the specific shape of the oscillatory region of the z-spectrum which, as seen in Figure 6-1, contains large signal fluctuations close to 0ppm which Lorentzian lineshapes are not able to account for. This complex behavior gives rise to parameter interactions that deviate from the ideal (i.e. continuous-wave) saturation case. As we are aiming to implement these methods at clinical field strengths the method must be reliable enough to accommodate these effects. Based on the simulation data it appeared that assigning chemical shifts based on the maxima in the sum-of-amplitudes plots produced the best results at 3.0T.

We may expect to see more consistent peak-assignments at higher fields as the peaks are more separable in terms of absolute Hz and therefore less susceptible to interference from the direct saturation effect. This does appear to be the case in the analysis of the simulated data. However, in counterpoint to this, it may be that the narrower resonances at higher field strengths mean that finer offset sampling is needed to resolve resonances accurately, although the sampling frequency distribution was not explored in this work on simulated data.

In phantom data at 9.4T, the chemical shifts of the amide groups are visible by eye and these were corroborated by the proposed analysis. The results were then validated at 3.0T where the peaks are so broad and overlapping that they are barely separable visually. The finally assigned chemical shifts of the two CEST peaks showed good agreement across a range of pH and saturation powers at 9.4T. At 3.0T the deviations were broadly centred in the correct range but showed considerable variation for the *cis*-isomer in particular. The fact that chemical shift assignments for the *trans*-isomer have smaller errors than the *cis*-isomer assignments is attributed to the *trans*-isomer being further from 0ppm and therefore less affected not only by the direct-saturation but also by rotation-effects in the ±1ppm range [134].

At 3.0T the results at the two lowest saturation powers show better agreement with the 9.4T data than results at the higher saturation powers. This is primarily attributed to the fact that the direct-saturation effect is smaller when using lower values of B_{1cwpe} and is therefore less likely to influence the z-spectrum features in the ppm-ranges of interest for CEST and NOE. On this basis, it is recommended that lower-power data may be best suited for future sum-of-amplitudes analysis.

In addition to this, the watery phantoms used are prone to oscillatory patterns in the z-spectrum close to 0ppm when using pulsed-saturation as a result of rotation effects. These effects are more pronounced in the 3.0T data which was acquired at 50% duty-cycle compared to 91% duty-cycle in the 9.4T data. These effects are anticipated to be less of a concern *in vivo* due to the shorter T1 and T2 values.

The proposed method gives the expected results in a 3-pool system and is suitable for further testing as a method of chemical shift assignments in future CEST experiments. There is the potential to identify peaks that are not visually obvious, especially in z-spectra with broad resonances. The method may therefore be useful for identifying CEST and NOE peaks in *in vivo* datasets at clinical field strengths.

Validation of the technique in other contexts will allow for iterative improvements of the process and evaluation of its efficacy. As expected in the phantom data, the distribution of FWHM values was approximately a third larger at 3.0T than at 9.4T. A possible improvement could be to fix the width of each Lorentzian lineshape during the over-fitting process, thereby reducing the number of free parameters by almost a third and allowing more lineshapes to be fitted to each z-spectrum. This could be done by calculating a characteristic FWHM of a single Lorentzian fitted to the whole spectrum and using that value as the fixed FWHM for all other Lorentzians.

The method will be applied *in vivo* firstly in rats at 9.4T where the CEST and NOE peaks should not only be discernable visually, but also literature values are available for comparison. Subsequently it will be tested in human glioma patients at 3.0T where chemical shift assignment of CEST and NOE peaks is more challenging and where no z-spectrum fitting literature currently exists.

7 Carbogen challenge in rats at 9.4T

In this chapter the Peak-Finder method outlined in the previous chapter is applied to data acquired in healthy rats at 9.4T undergoing a carbogen challenge. The work builds on work presented by FT at ISMRM 2018 which investigated whether or not levels of perfusion (controlled using breathing of carbogen) influence CEST or pH measurements in a rat-model at 9.4T [135]. I re-analyse the same CEST data using z-spectrum fitting to add more detail to the results and understand where in the z-spectrum the observed signal changes originate.

GlucoCEST shows great promise as a metabolic contrast mechanism in cancer imaging where glucose uptake reflects metabolic activity and may be able to direct diagnosis and treatment decisions [6][136][137]. Physiological parameters such as cerebral blood-flow and pH may also be altered in disease therefore, in light of the intrinsically low SNR of glucoCEST methods, it is important to understand the likely impact of concomitant physiological effects that may accompany alterations in glucose concentration *in vivo*.

Specific Chapter contributions:

I undertook all fitting of z-spectra and the subsequent fitting-related analysis.

Francisco Torrealdea, PhD (Postdoctoral Medical Imaging Physicist)[1,2]: Study design, data acquisition, analysis of MTR_{asym}, ASL data and phosphorus spectroscopy data.

Marilena Rega, PhD (Clinical Scientist)[1,3]: Study design, data acquisition, analysis of MTR_{asym}, ASL data and phosphorus spectroscopy data.

Mohamed Tachrount (Postdoctoral Research Fellow)[1] and Magdalena Sokolska (Clinical Scientist)[4]: Technical support.

Contributor affiliations:

[1] Institute of Neurology, University College London, Queen Square, London, WC1N 3BG

[2] Centre for Medical Imaging, University College London, 43-45 Foley St, Fitzrovia, London, W1W 7TS, United Kingdom

[3] Institute of Nuclear Medicine, University College London Hospital NHS Foundation Trust, 5th Floor Tower, University College Hospital, 235 Euston Road, London, NW1 2BU

[4] Medical Physics and Biomedical Engineering, University College London Hospital NHS Foundation Trust, 5th Floor Tower, University College Hospital, 235 Euston Road, London, NW1 2BU

7.1 Introduction

Exogenous glucoCEST has the potential to quantify glucose uptake in tumours [6][7]. As part of this project it is of crucial importance to understand the sensitivity of the glucoCEST technique to changes in the glucose concentration. It is also vital to understand any other concomitant effects that arise due to the exogenous administration of glucose which may cause misinterpretation of the signal changes. Of particular interest are the relationships between signals from CEST, local perfusion as measured by arterial spin labelling (ASL), T2, and pH as measured by ^{31}P-spectroscopy.

7.1.1 GlucoCEST

Glucose ($C_6H_{12}O_6$) contains 5 hydroxyl groups with chemical shifts in the range 0.7-2.1ppm [138]. GlucoCEST refers to the application of CEST imaging methods for the detection of glucose. The technique may be well-suited for cancer imaging due to the preferential uptake of glucose by tumours via the Warburg Effect [62][64][66] (see section 2.2.1). Exogenous glucose may be administered orally, intraperitoneally, or intravenously as a bolus or infusion and, if imaging is repeated at several timepoints, it is possible to calculate the 'glucoCEST enhancement' (GCE) which is the difference between the MTR_{asym} pre and post-adminstration, as illustrated in Figure 7-1. Clinical implementations of glucoCEST may be able to generate contrast comparable to that generated by PET scans using a fluorodeoxyglucose (FDG) tracer and which are markers for glucose uptake. Indeed, one study has already demonstrated a correlation between these two measurements pre-clinically using tumour xenograft mouse models [6]. One of the key challenges of glucoCEST imaging is the low SNR of the method, therefore it is important to understand the likely impact of concomitant effects that may accompany alterations in glucose concentration *in vivo*.

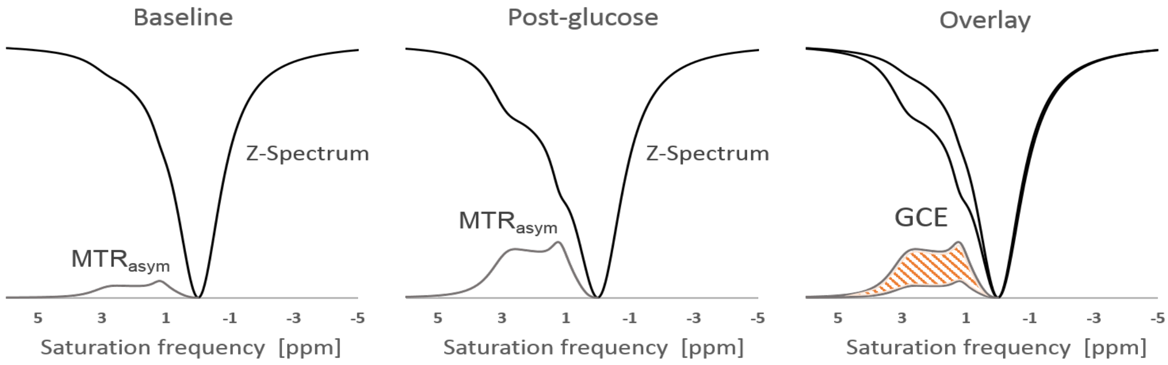

Figure 7-1: *A schematic illustration of calculation of the glucoCEST enhancement (GCE) following administration of exogenous glucose. Subtraction of the post-administration* MTR_{asym} *from the pre-administration* MTR_{asym} *yields the GCE. Figure reproduced from* [135].

7.1.2 Arterial Spin Labelling (ASL)

Arterial Spin Labelling (ASL) involves the use of RF-pulses to magnetically tag protons in arterial blood as they flow towards the imaging slab. The in-flow of these magnetically tagged protons alters the signal in voxels within the slab and the subtraction of images acquired with and without tagging highlights regions of perfusion within the field-of-view. The first implementation of the technique was described by Williams and Detre et al in 1992 [139][140].

Several variations on the ASL method have been developed which utilise different labelling methods to reduce unwanted effects such as from MT [141][142][143]. For this study, pseudo-continuous ASL (pCASL) is used whereby spin-labelling is achieved using a train of many short RF-pulses [144].

7.1.3 ^{31}P spectroscopy

^{31}P-MRS may be used as a non-invasive tool to measure intracellular pH *in vivo*. The pH can be evaluated using the chemical shift of the inorganic phosphate peak (δ_{Pi}, in ppm) in reference to the chemical shift of the phosphocreatine PCr peak (δ = 0ppm) and can be calculated using the following equation [145][146]:

$$pH = pKa + log\frac{\delta_{Pi}-\delta_a}{\delta_b-\delta_{Pi}} \qquad (7\text{-}1)$$

Where the $H_2PO_4^- \leftrightarrow H^+ + HPO_4^{2-}$ deprotonation constant *pKa* = 6.73 and the ^{31}P limiting shifts δ_a = 3.275ppm (for acidic protonated species $H_2PO_4^-$) and δ_b=5.685ppm (for basic deprotonated species HPO_4^{2-}) were used in the analysis. Within physiological pH ranges, δ(P_i) increases by approximately 2ppm as pH drops from 8 to 5 while δ(PCr) remains stable so is used as a reference [147].

7.2 Materials and Methods

7.2.1 Animal model and ethics

Five Sprague-Dawley rats were anaesthetised with 1.75% isoflurane. While in the scanner, body temperature was maintained at 36°C using warm air. All procedures were conducted under a protocol approved by the Home Office.

7.2.2 MRI Protocol

Data were acquired on a 9.4T Agilent pre-clinical scanner.

7.2.2.1 *CEST Preparation*

The saturation parameters were: 80 x Gaussian pulses, B1eq = 3.35μT, τ_p = 50ms, FA = 2000°, 99% duty-cycle. For the first two rats, the z-spectra were sampled at 93 frequency offsets: ±100ppm, ±60ppm, ±50ppm, ±40ppm, ±30ppm, ±20ppm, ±10ppm, ±8ppm, and then at 77 additional offsets evenly spaced between ±6.08ppm. In subsequent rats, z-spectra were sampled at 101 offsets evenly spaced between ±6ppm.

7.2.2.2 *pCASL*

20 interleaved label-control pairs (labelling duration 1.4s, post-labelling delay 1s), gradient-echo EPI readout (TR = 3s, TE=18ms).

7.2.2.3 *T2 maps*

Multi-echo multi-slice spin-echo (ETL=20, TR=3.3s, TEmin = 6.9ms). Maps were calculated by fitting the even echoes to a mono-exponential decay function.

7.2.2.4 *Phosphorous spectroscopy*

Acquired using a single-loop transmit-receive coil (RAPID Biomedical). Global hard pulse. TR=3.3s, 192 averages.

7.2.2.5 *Carbogen challenge*

Carbogen is a mixture of oxygen and carbon dioxide which has been shown to increase radio-sensitivity during tumour radiotherapy by increasing the oxygen-carrying capacity of the blood [148][149]. It is also a reliable agent for inducing increased perfusion by up to 70% in tumour models [150]. In this study, each rat alternately received oxygen and carbogen (a mixture of 95% O_2, 5% CO_2) while MRI data were acquired.

7.2.2.6 *Intravenous bolus of 2-Deoxy-D-glucose (2DG)*

2DG is a glucose molecule where the 2-hydroxyl group has been replaced by a hydrogen atom. It enters cells by the same transporters as glucose and is phosphorylated by hexokinase into 2D-6-phosphate (2DG6P) but undergoes limited further metabolization due to the lack of a hydroxyl group on carbon atom C2 [151]. It therefore becomes trapped in mammalian brain cells for many hours allowing for studies of the glucose metabolic rate by techniques such as CEST. 2-Deoxy-D-glucose (2DG) was administered intravenously to enable a comparison between the magnitude of MTR_{asym} signal changes due to 2DG ('glucoCEST' signal) and the magnitude of changes due to breathing different gases.

7.2.3 Data Analysis

All data were processed using in-house developed software in Matlab R2016a (MathWorks, Natick, MA, USA).

7.2.3.1 Correlation of MTR_{asym} with other measures

Asymmetry analysis was performed in the first instance by FT and MR who correlated MTR_{asym} measurements with calculated values of T2, pH and CBF and made the comparison of glucoCEST signal with the changes due to perfusion induced by breathing carbogen.

7.2.3.2 Applying the Peak-Finder method in vivo

An initial determination of the offset frequency of the MT pool was made by fitting all voxels from the brain at both saturation powers, excluding all data points within the ±10ppm range and analyzing the results. Once this had been provisionally fixed, the sum-of-amplitudes analysis outlined in chapter 6 was performed in order to identify the number and chemical shifts of the remaining CEST and NOE pools thereby generating the tuned fitting model.

7.2.3.3 Full fitting of the z-spectra

Once the chemical shift parameters of the Lorentzian fitting algorithm had been fixed, all z-spectra were fitted voxel-by-voxel over all datasets and the results from different brain regions were evaluated, in particular aiming to identify what underlying changes in CEST and NOE signal give rise to the changes in MTR_{asym} observed by FT and MR.

7.2.3.4 Statistical Tests

When testing for significance between peak heights in different gas phases, data were tested for normality using the one-sample Kolmogorov-Smirnov test. Statistical significance of signal changes was assessed using the two-sample student's t-test with $p < 0.05$ taken to be significant.

7.3 Results

Section 7.3.1 summarises the key results relating to MTR_{asym} measurements, as evaluated in [135]. Sections 7.3.2 and 7.3.3 describe in detail the subsequent fitting analysis that was performed on the same datasets.

7.3.1 MTR$_{asym}$, CBF, T2 and ^{31}P when breathing different gases

Representative z-spectra and MTR$_{asym}$ measurements are shown in Figure 7-2 for four distinct gas phases (Oxygen – Carbogen – Oxygen – Carbogen). The MTR$_{asym}$ from both oxygen phases look similar and from both carbogen phases look similar.

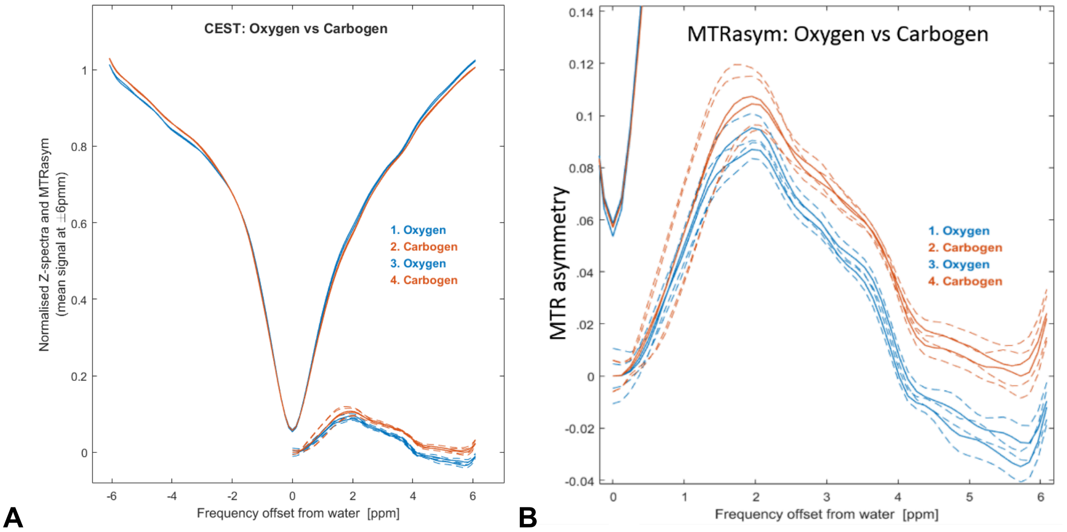

Figure 7-2: *Representative z-spectra* ***(A)*** *and MTR$_{asym}$* ***(B)*** *from four gas phases (Oxygen – Carbogen x2). The MTR$_{asym}$ spectra show similar behaviors for both repetitions of the gas cycle. The solid lines show the mean MTR$_{asym}$ from within regions of interest, with dashed lines indicating the standard deviation. Figure created by FT and MR and reproduced from* [135].

The MTR$_{asym}$, CBF and T2 were calculated in cortex and hippocampus ROIs over the course of the changes of gas inputs. These results are plotted in Figure 7-3. Clear variability in MTRasym and CBF are observed in in response to the change in breathing gases, especially in the well-perfused cortex, but no clear trend is seen in T2.

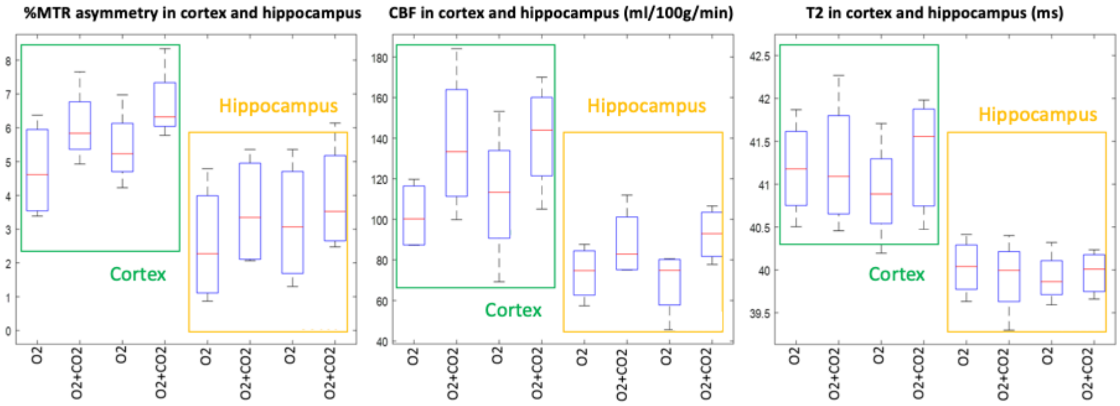

Figure 7-3: *Changes in the median MTR$_{asym}$, CBF and T2 measurements as a function of the gas input for ROIs drawn in the cortex and hippocampus. A clear dependency is observed in the MTR$_{asym}$ and CBF measurements but no trend is obvious in T2. Figure created by FT and MR and reproduced from* [135].

Strong correlation ($p<0.01$) was observed between MTR_{asym} and CBF in both grey and white-matter. No correlation was found ($p>0.1$) between MTR_{asym} and T2 measurements. Correlation plots for these results are found in the original work [135].

Results from ^{31}P spectroscopy showed no changes in the chemical shift between inorganic phosphate and phosphocreatine when breathing O_2 vs CO_2, indicating that the intracellular pH remained steady and suggesting that altered levels of CO_2 were not causing the changes in CEST signal directly.

A comparison between the magnitude of signal changes caused by a 2DG bolus and those caused by switching from oxygen to carbogen is shown in Figure 7-4. The changes in MTR_{asym} are larger for the carbogen challenge than they are for the 2DG IV bolus, suggesting that altered perfusion levels must be taken into consideration in glucoCEST imaging studies. The fitting work in the remainder of this chapter aims to identify the sources of these changes in terms of the specific exchangeable pools that contribute to the z-spectrum.

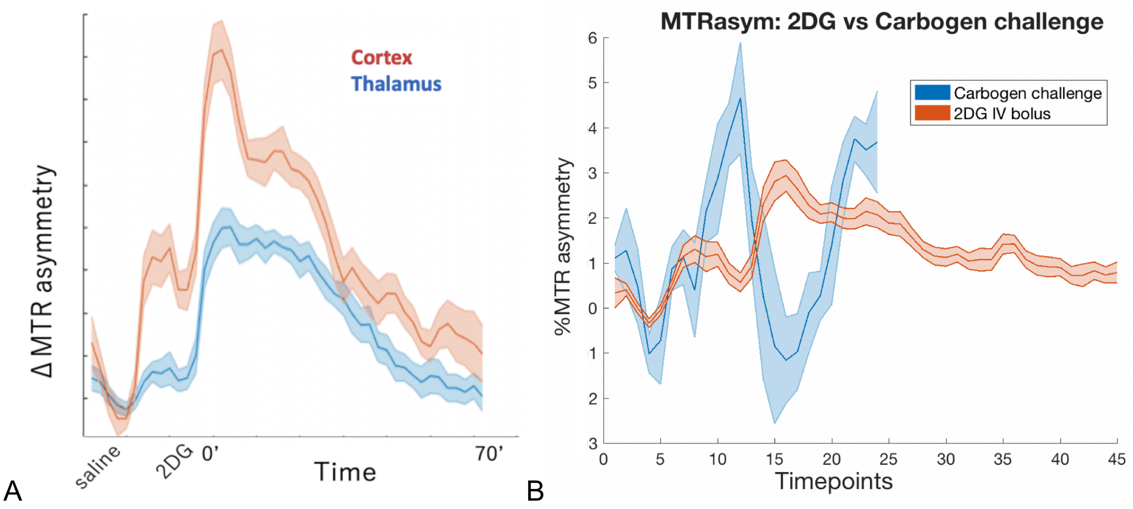

***Figure 7-4:** Changes in the MTR_{asym} (A) in the cortex and hippocampus with intravenous administration of a 2DG bolus, and (B) in the cortex with intravenous administration of a 2DG bolus alongside the changes seen when alternately breathing oxygen and carbogen. The magnitude of changes caused by changing the gas being breathed are larger than those of a 2DG bolus suggesting that the CEST effect is influenced by perfusion. Figure created by FT and MR and reproduced from* [135].

7.3.2 Tuning the Fitting Algorithm

Visual inspection of the z-spectra suggested the presence of a broad MT resonance within which 5 peaks were located approximately at 0ppm, 3.5ppm, 2ppm, -3.5ppm and -1.5ppm, similar to those used in other rat fitting work [88]. The MT offset frequency needed to be fixed and the number of pools verified.

7.3.2.1 Choice of MT lineshape

Lorentzian and super-Lorentzian lineshapes were considered for the fitting of the MT effect. Both were fitted to z-spectra (excluding data-points from within the ±10ppm range to avoid the effects of water, CEST and NOE resonances). The mean and median offset frequencies of these MT-only fits are shown in Table 7-1.

	Mean Offset (ppm)			**Median Offset (ppm)**		
MT Lineshape	Low-power	High-power	Both powers	Low-power	High-power	Both powers
Lorentzian	-1.25	-1.22	-1.24	-1.34	-1.24	-1.27
Super-Lorentzian	-1.51	-1.15	-1.34	-1.56	-1.15	-1.26

Table 7-1: *Mean and median offset frequencies of fitted MT-peaks using both Lorentzian and super-Lorentzian lineshapes.*

The offset frequency range for the Lorentzian fits (-1.34 to -1.22ppm) closely matched the frequency identified for MT in the prostate (-1.27ppm) in chapter 4 and the Lorentzian lineshape produced the best agreement between saturation powers. This is assumed to be because the super-Lorentzian lineshape changes shape with different values of T2b, which may interact with the offset frequency parameter unpredictably. To ensure consistency of the lineshape and offset frequency when fitting data acquired at different powers it was decided to fit the MT using a Lorentzian lineshape.

7.3.2.2 Manually defined fitting-model

Prior to applying the peak-finder method, an initial attempt at defining the fitting algorithm was made through visual inspection of z-spectra and histogram analysis. With water fixed at 0ppm, a 6-pool fit of all voxels was carried out including the peaks that were evident upon visual inspection of the z-spectra (water, amide, amine, NOE1, NOE2, MT). This was done as part of an initial assessment of the offset frequencies of the remaining pools, and to identify whether any peaks were missing. From this analysis, two CEST pools, two NOE pools and an MT contribution were identified.

The distributions of the NOE2 offset frequency, the amine, NOE1 and NOE2 FWHM values, and the NOE1 and NOE2 amplitudes were found to be either bimodal or very broad, both of which may suggested that some fitting artefacts may have been present. In particular, the distribution of the NOE2 FWHM values was strongly bi-modal with some cases of FWHM >5ppm, even exceeding 10ppm, whereas all other Lorentzian FWHM values were below 5ppm.

Figure 7-5 shows two z-spectra: one with a narrow NOE2 peak (FWHM = 1.77ppm) and one with a broad NOE2 peak (FWHM = 11.33ppm). Some interplay with the amplitude of the MT peak was observed as is illustrated in the scatterplots in Figure 7-6.

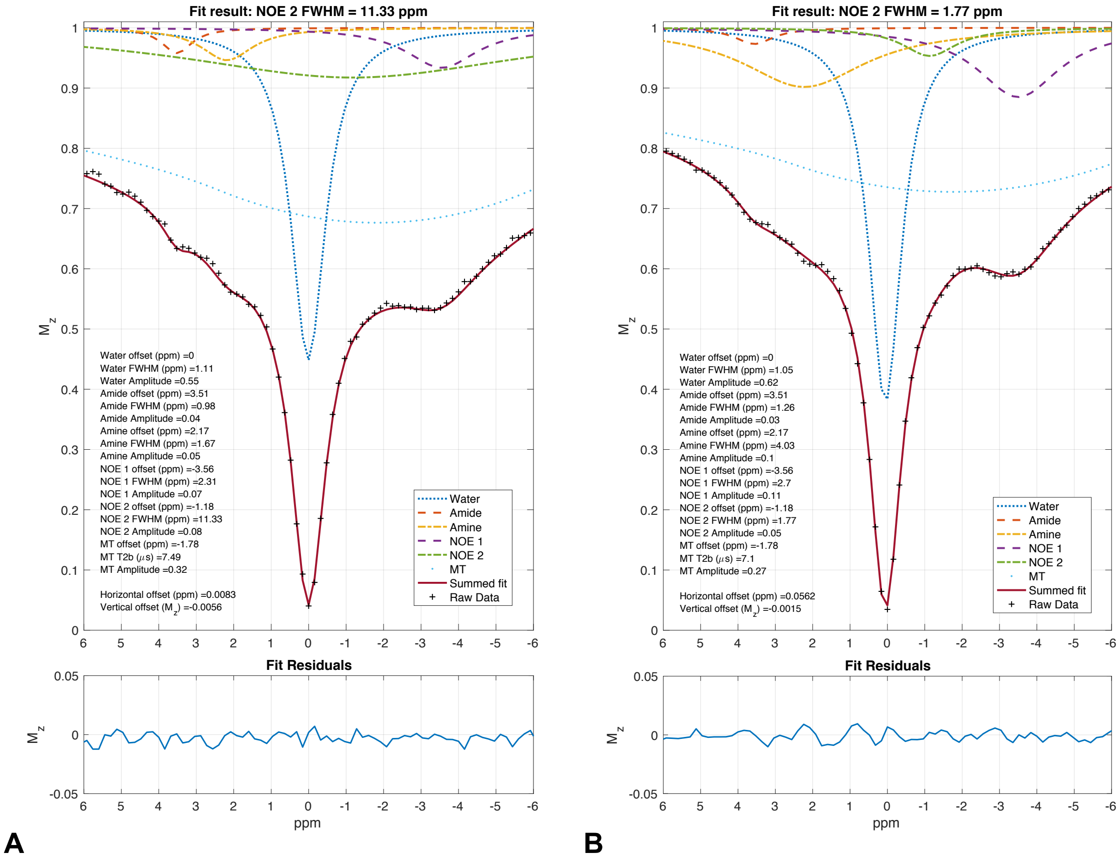

Figure 7-5: *Fitted z-spectra (**A**) where the fitted value of the NOE 2 FWHM was found to be 11.33ppm, and (**B**) where it was found to be 1.77ppm. It can be seen that while the peaks fitted on the aliphatic side of the z-spectrum in (**B**) look more physically realistic, the amine peak has also grown in size and width raising questions about whether we have got things right on the CEST side of water.*

These parameters would be expected to vary independently if the fitting-model was accurate. There also appeared to be an inverse relationship between the width of the NOE 2 peak and the heights of the amine, NOE 1 and MT peaks – its two closest neighbors. This suggests that the peak heights and widths are not varying independently within the model. While we may expect some level of co-variation of peak heights (e.g. voxels with high NOE1 signal may also have high NOE2 signal), a physiological explanation for correlaton between the width of one peak and the height of another *in vivo* is less obvious. T2-broadening effects may go part way to explaining this sort of co-variation, however, it was known from previous fitting experience that the FWHM values in this data tended to be less than 5ppm, which the NOE2 fits in this case often exceeded. Visual inspection of the fit results shown in Figure 7-7 give reason to suspect that an additional CEST peak may be missing from the model between the two CEST peaks that have already been fitted. This was explored using the sum-of-amplitudes approach in the next section.

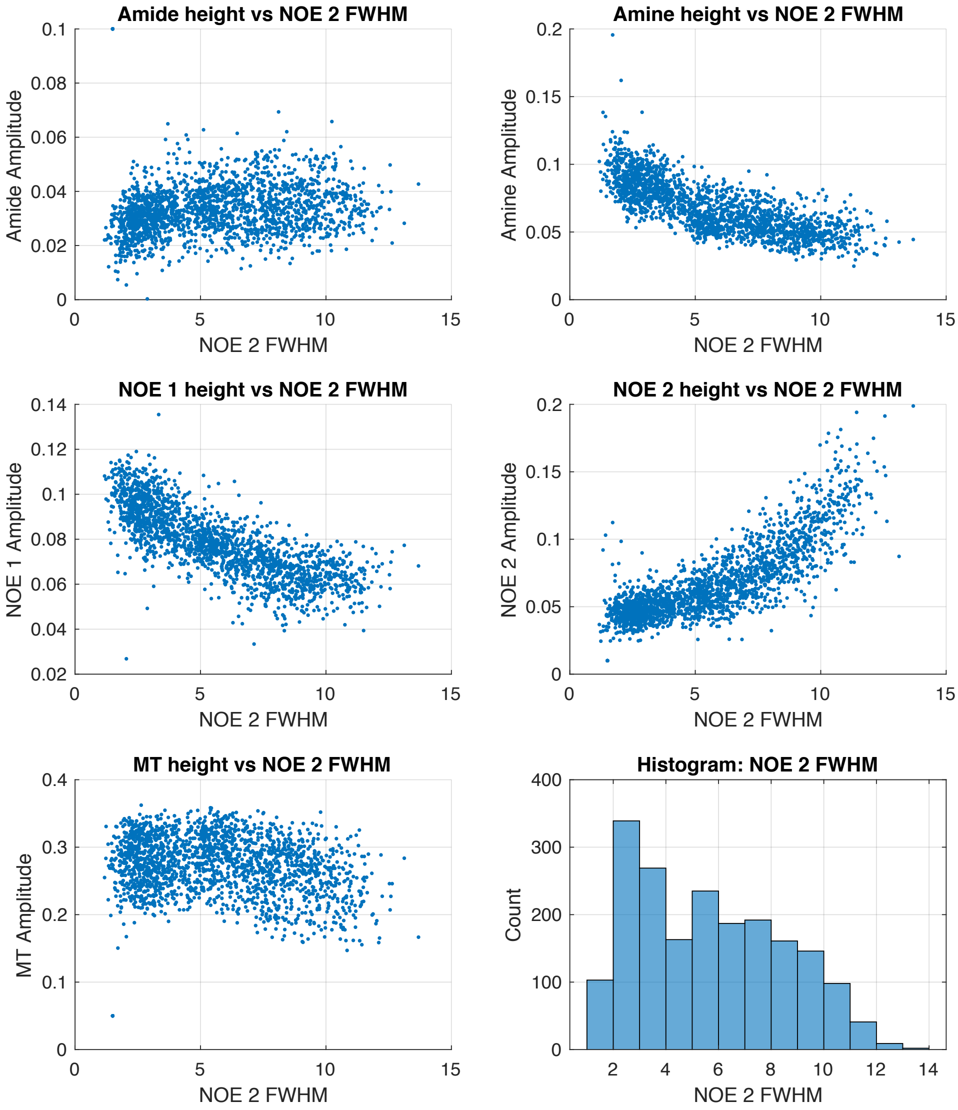

Figure 7-6: *Scatter plots of the amplitude of all fitted peaks vs the FWHM of the NOE 2 pool. The amine and NOE 1 pools show a strong negative correlation between amplitude and the NOE 2 FWHM. A similar trend is observed in the MT amplitude. This suggests that the high values of NOE 2 FWHM are a fitting artefact whereby a broad, high amplitude NOE 2 peak is being fitted preferentially to a narrow, low amplitude peak (which is more physically realistic) and as a result the heights of the other adjacent fitted peaks in particular (ie the NOE 1 and amine peaks) are reduced. The negative impact of this artefact could be limited by restricting the FWHM range of the NOE 2 pool to a more physically realistic range.*

7.3.2.3 *Applying the Peak Finder approach in vivo*

Each z-spectrum contained 93 data-points, therefore all spectra were fitted using 30 lineshapes, a whole-fit horizontal offset term and a whole-fit vertical offset term (92 fitted parameters).

The water pool was fixed at 0ppm and the offset frequencies of all Lorentzians and the MT pool were allowed to freely roam between ±5ppm with the starting positions of all peaks set to 4.9ppm.

Figure 7-7 shows a histogram of the offset frequencies of all fitted pools (excluding water). While some maxima are visible in the expected ppm ranges for amide, amine, hydroxyl and 2 NOE pools, a clear bias towards the starting value of 5ppm is seen in the data which obscures the useful information present. As outlined in the previous chapter, to account for the fact that many of these peaks will have low-amplitude, we perform a sum-of-amplitudes analysis.

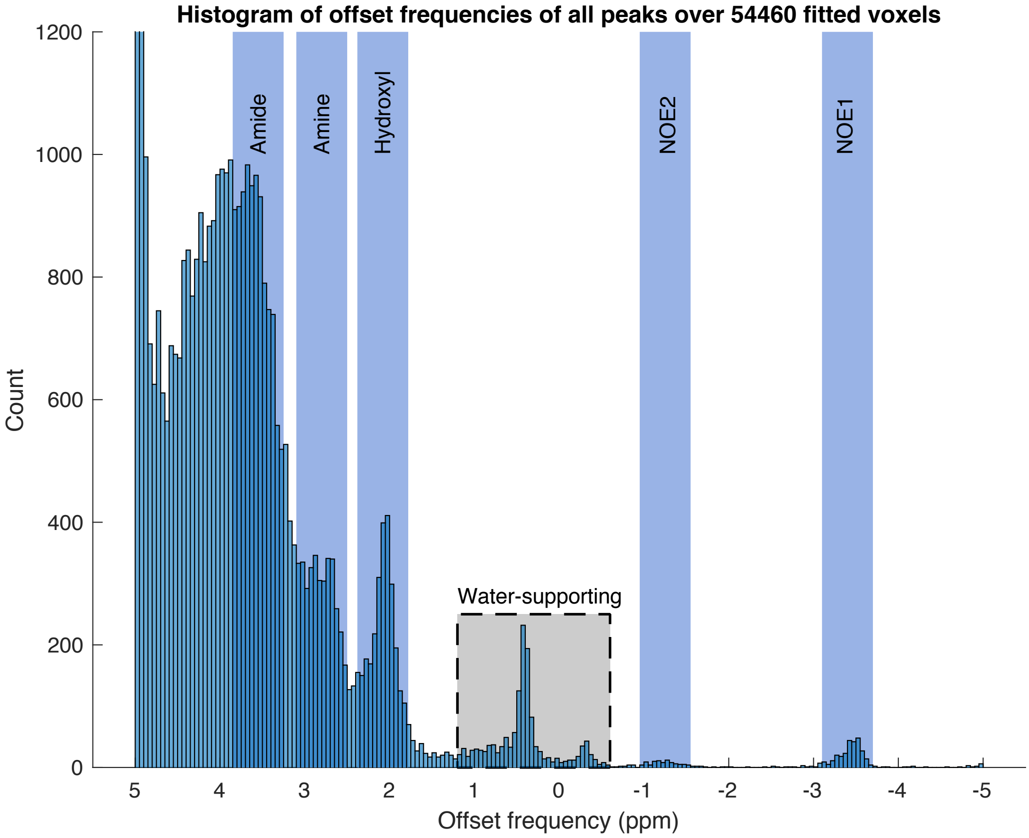

Figure 7-7*: Histogram of the offsets frequencies of 29 fitted peaks (excluding water) over many voxels. It can be seen that this analysis suggests the presence of 3 CEST pools and 2 NOE peaks. MT excluded for full visibility of the NOE2 peak.*

Figure 7-8 shows the results of the sum-of-amplitudes analysis, discretized to a granularity of 0.01ppm. Three CEST peaks and 2 NOE peaks emerge from the analysis – supporting the earlier suspicion that an additional unaccounted for CEST peak was present in the data. The water resonance was fixed at 0ppm and is excluded from the figure and the MT data is shown in green to distinguish it from the co-located NOE2 peak. Some water-supporting peaks are present (the origins of which are outlined in section 3.1.1) but with amplitudes far smaller than observed in phantoms in the previous chapter. The sum-of-amplitudes greatly removes the skewedness of the results towards 5ppm that was observed in the histogram analysis. The three CEST and two NOE offset frequencies observed here are clearly identifiable and fall within the expected ranges from literature values.

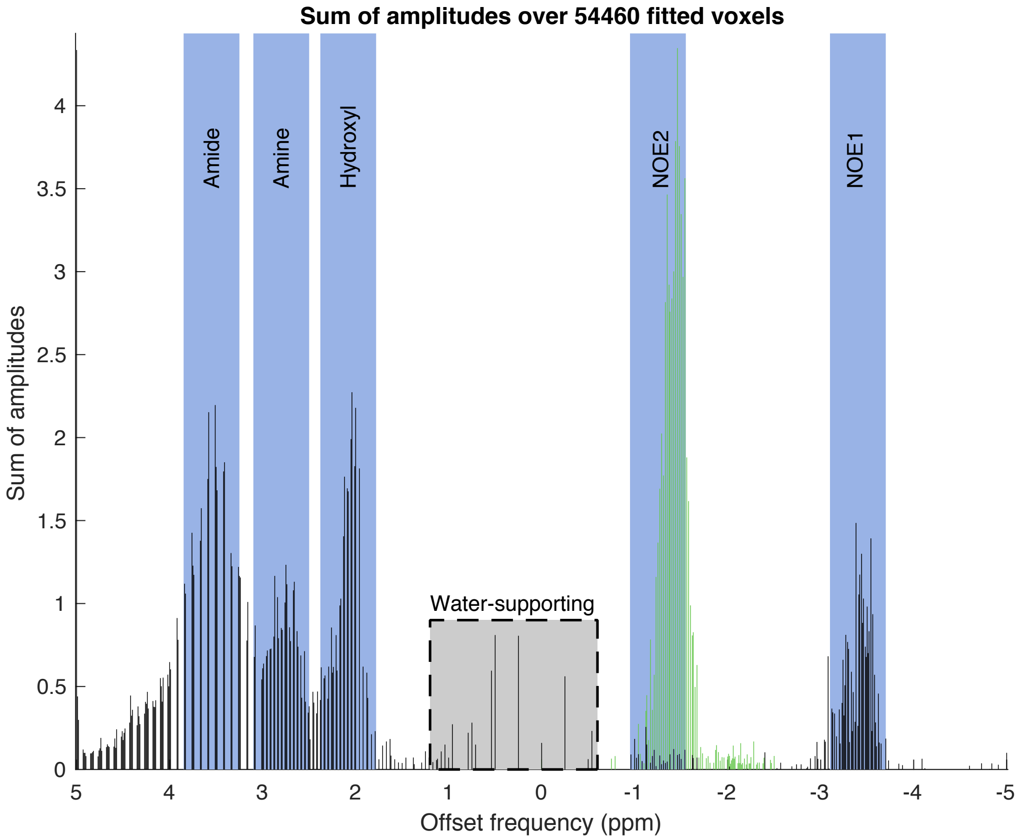

***Figure 7-8**: Sum-of-amplitudes analysis offset over many voxels (excluding water). It can be seen that this analysis suggests the presence of 3 CEST pools and 2 NOE peaks. MT is shown in green to distinguish between MT and NOE2 which have similar offsets.*

The data shown in Figure 7-7 and Figure 7-8 are derived from the low-power dataset where the MT peak is less dominant and the contributions to the z-spectra from the CEST and NOE peaks are proportionally larger.

Having identified approximate offset frequencies for 3 distinct CEST pools, 2 NOE pools, and an MT pool, the process was repeated for different carbogen and oxygen phases at both powers. The finally chosen offset frequency values are shown in Table 7-2.

Z-spectrum contributor	Lineshape	Parameter	Starting Value	Lower Bound	Upper Bound
Water	Lorentzian	ω_0 (ppm)	0.00	-	-
		Γ (ppm)	2.10	1.70	5.00
		A (A.U)	0.25	0.10	0.90
Amide	Lorentzian	ω_0 (ppm)	3.54	-	-
		Γ (ppm)	4.00	0.10	14.0
		A (A.U)	0.03	0.00	0.15
Amine	Lorentzian	ω_0 (ppm)	2.80	-	-
		Γ (ppm)	2.50	0.1	14.0
		A (A.U)	0.03	0.0	0.15
Hydroxyl	Lorentzian	ω_0 (ppm)	1.93	-	-
		Γ (ppm)	2.50	0.10	7.00
		A (A.U)	0.03	0.0	0.15
NOE1	Lorentzian	ω_0 (ppm)	-3.42	-	-
		Γ (ppm)	5.00	0.10	10.00
		A (A.U)	0.03	0.00	0.25
NOE2	Lorentzian	ω_0 (ppm)	-1.38	-	-
		Γ (ppm)	2.00	0.10	10.00
		A (A.U)	0.03	0.00	0.15
MT	Lorentzian	ω_0 (ppm)	-1.40	-	-
		Γ (ppm)	55.0	52.0	60.0
		A (A.U)	0.65	0.55	0.72
Horizontal Offset (whole-fit)	Constant	h (ppm)	0.0	-0.2	0.2
Vertical Offset (whole-fit)	Constant	v (A.U)	0.00	-0.03	0.01

***Table 7-2**: Fitting parameter lower-bounds, upper-bounds and starting-values for the 7-pool model used for fitting z-spectra from rat brain data at high saturation power.*

The MT fit parameter ranges and normalization approaches for subsequent datasets were constrained based on the values observed in the first two rats which showed good consistency across gas phases. This was done to account for the fact that in subsequent rats, data were only acquired in the ±6.08ppm range, without MT points. Normalisation for these datasets was done by calculating the ratio between the signal at 6.08ppm and the faraway offset at 100ppm in the first two rats with MT points. This ratio was between 0.3 and 0.4 for the majority of voxels. Therefore, z-spectra from subsequent rats were normalized such that the signal at 6.08ppm was 0.35*M_0. The vertical offset term in the fitting model allowed for imperfect normalization so this approach to the normalization was judged to be acceptable.

7.3.3 Changes in the fitted peak heights

The tuned fitting algorithm was applied to data from all rats. ROIs were drawn in the cortex and hippocampus which are taken to represent areas of high and low perfusion, respectively. The distributions of fitted peak heights within each ROI were found to be normally distributed. A representative fitted z-spectrum, taken from a voxel in the hippocampus is shown in Figure 7-9. Figure 7-10 shows maps of the heights of the fitted Lorentzians for each pool while breathing O_2.

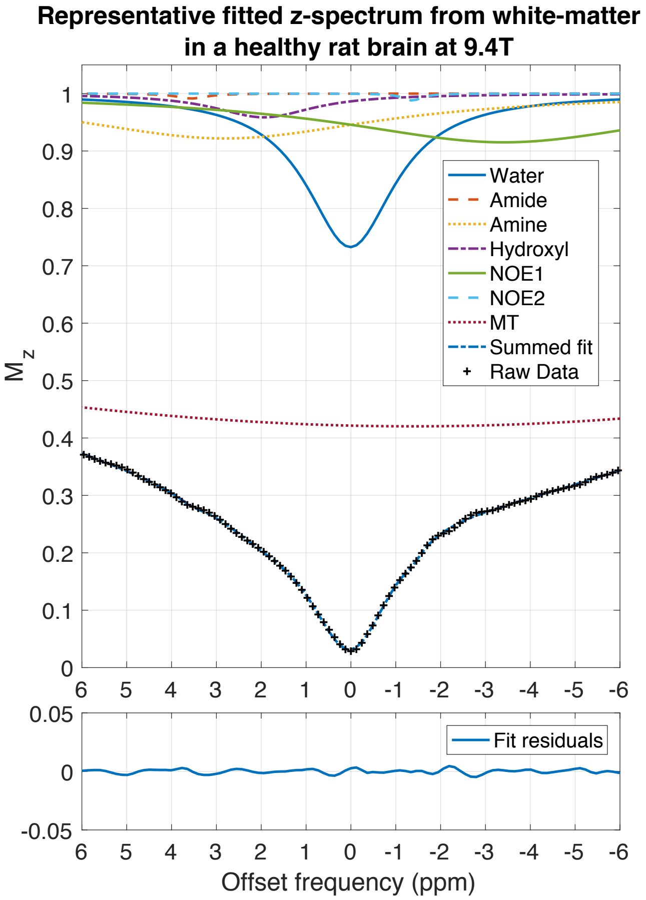

Figure 7-9: *A representative fitted z-spectrum taken from a single-voxel in the rat hippocampus along with the fit residuals which are all less than 0.01. Due to the high saturation power, the MT effect is dominant.*

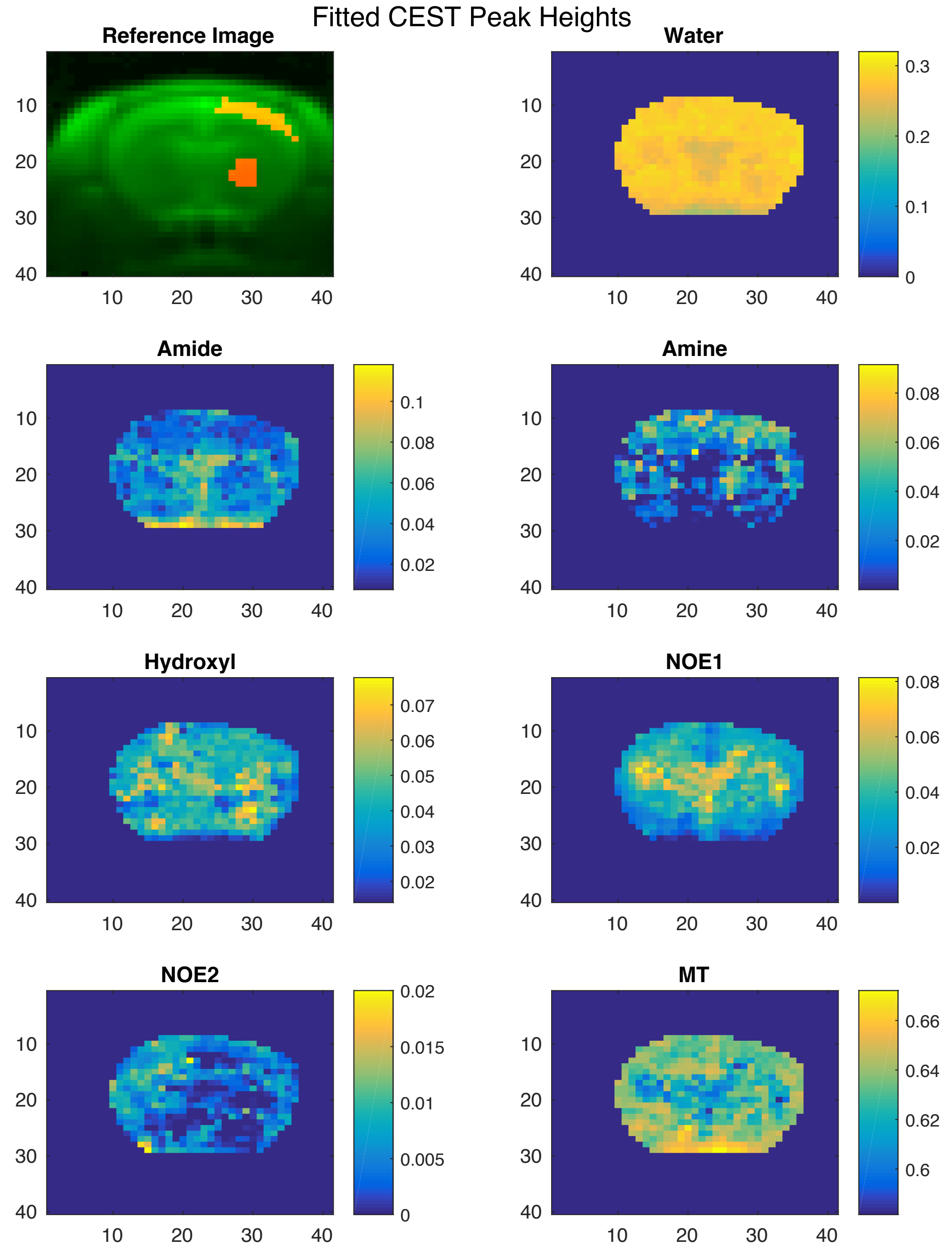
Fitted CEST Peak Heights
Reference Image
Water
Amide
Amine
Hydroxyl
NOE1
NOE2
MT
10
20
30
40
0.3
0.2
0.1
0
0.1
0.08
0.06
0.04
0.02
0.07
0.05
0.03
0.015
0.01
0.005
0.66
0.64
0.62
0.6

Figure 7-10: *Representative maps of the heights of Lorentzian lineshapes fitted to data acquired during oxygen inhalation. Cortex (top) and hippocampus (bottom) ROIs for cortex and hippocampus are overlaid in light and dark orange over the reference image respectively.*

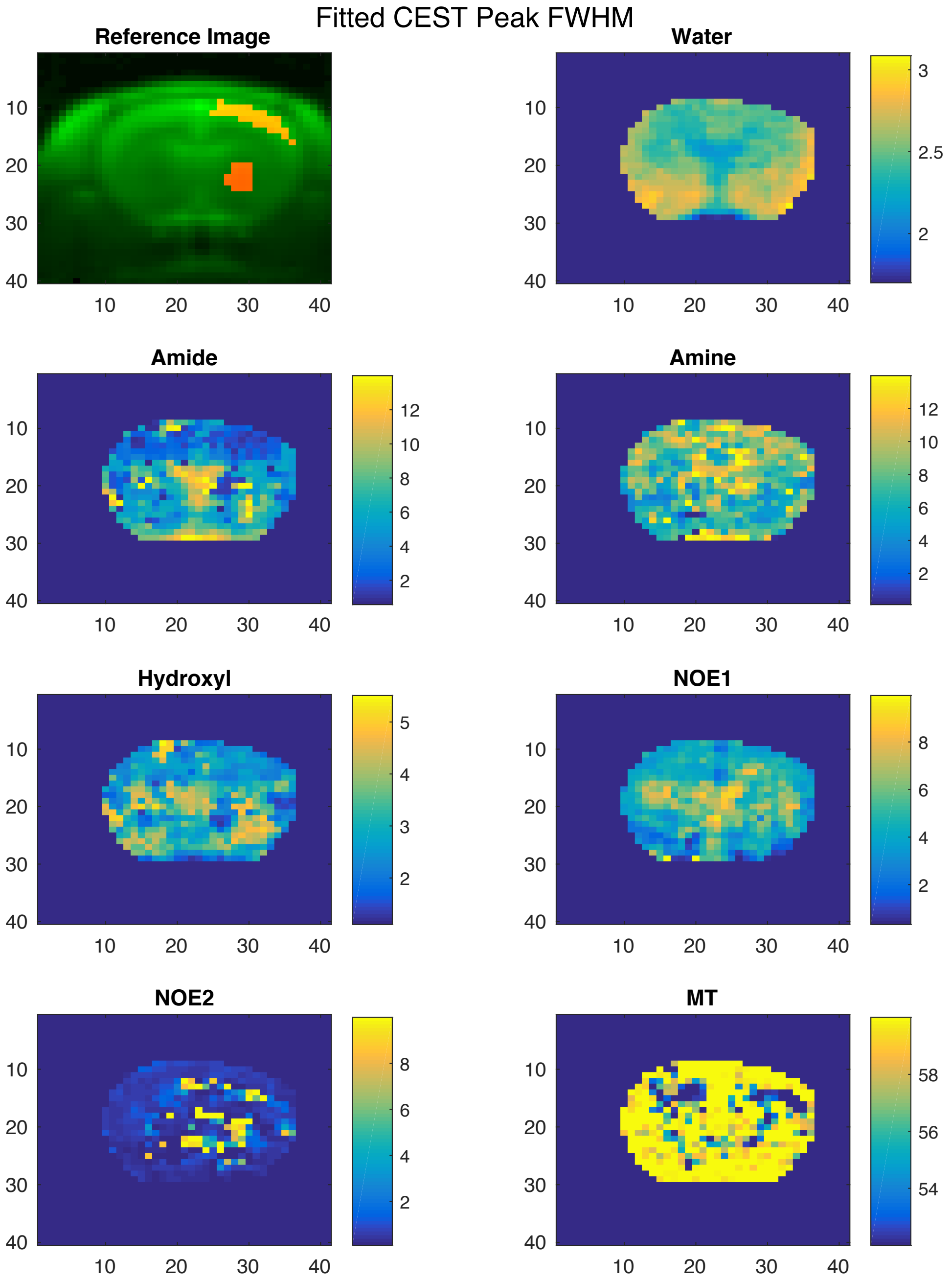
Fitted CEST Peak FWHM
Reference Image
Water
Amide
Amine
Hydroxyl
NOE1
NOE2
MT
10
20
30
40
3
2.5
2
12
10
8
6
4
2
5
58
56
54

Figure 7-11: Representative maps of the FWHM of Lorentzian lineshapes fitted to data acquired during oxygen inhalation. Cortex (top) and hippocampus (bottom) ROIs for cortex and hippocampus are overlaid in light and dark orange over the reference image respectively.

7.3.3.1 Signal changes in the cortex and hippocampus

Variations in the heights and widths of the fitted pools in the cortex when alternating between breathing oxygen and carbogen are shown as boxplots in Figure 7-12 and Figure 7-13. Significance is indicated in the figures with single, double or triple asterisks signifying p <005, <0.01, <0.001 respectively.

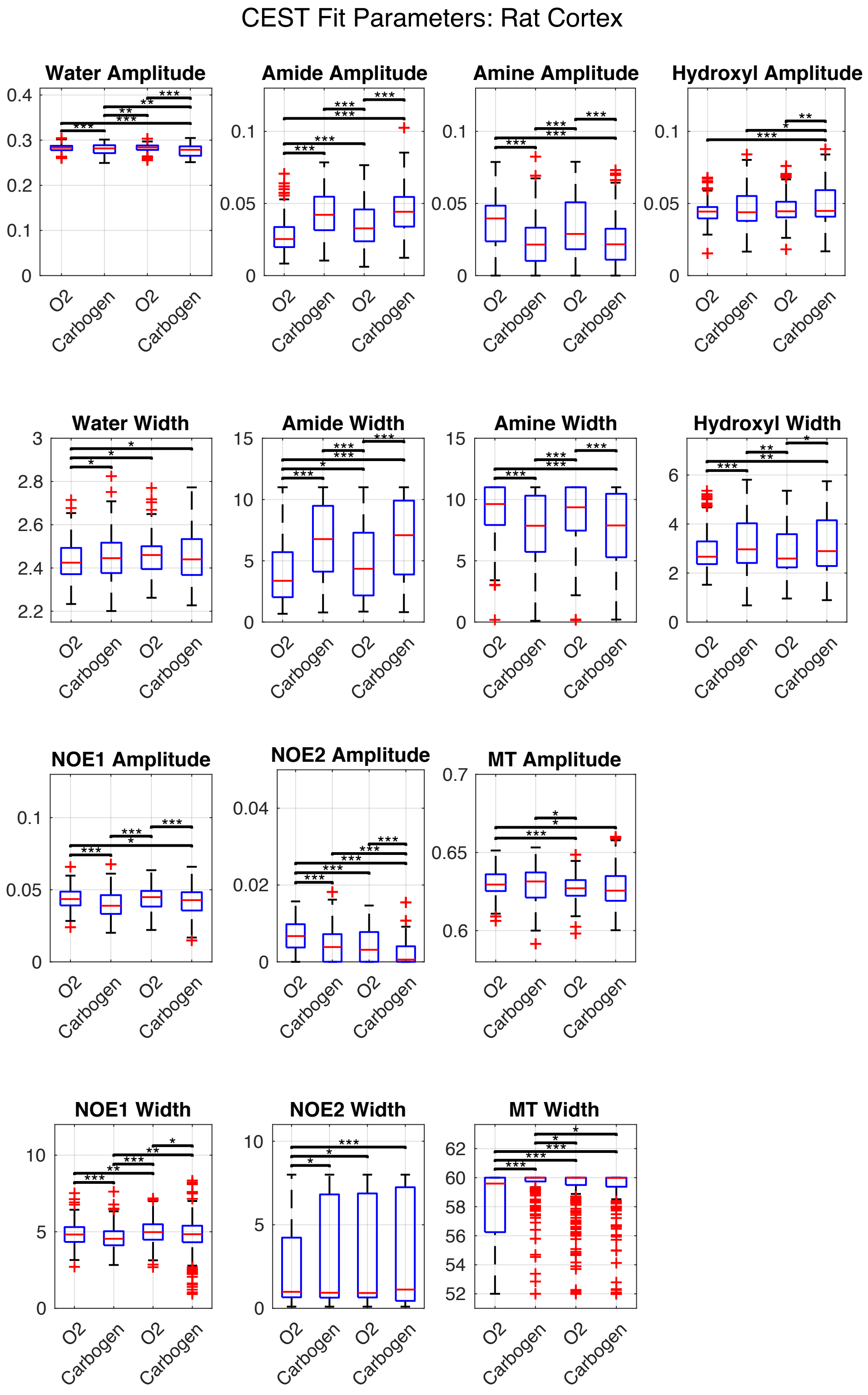

***Figure 7-12**: Distribution of the amplitudes and widths of Lorentzian lineshapes fitted to z-spectra acquired in the rat brain cortex at 9.4T. Signal changes correlating with the breathing of each gas are observed in the amide and amine amplitudes and FWHM, the NOE1 amplitude and in the hydroxyl FWHM.*

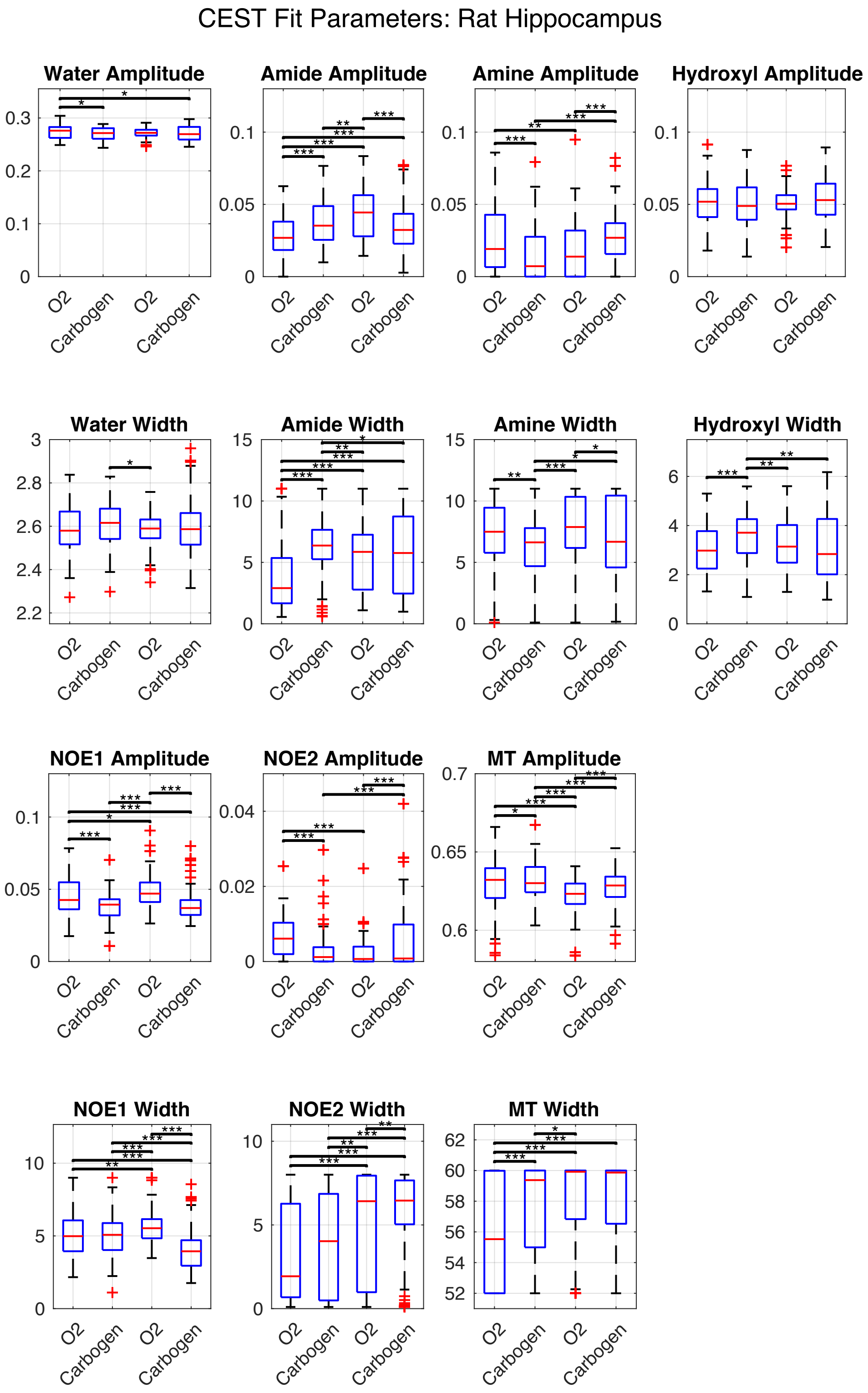

***Figure 7-13**: Distribution of the amplitudes and widths of Lorentzian lineshapes fitted to z-spectra acquired in the rat brain hippocampus at 9.4T. The NOE1 amplitude is the only parameter that is observed to correlate with the breathing of each gas.*

In the cortex, changes correlating with the breathing of each gas are seen most notably in the amide and amine amplitudes (varying by approximately 0.02) and FWHM (varying by 4ppm and 2ppm respectively), the NOE1 amplitudes (variations of approximately 0.05) and possibly in the hydroxyl FWHM (variations of approximately 0.5ppm). In the hippocampus, the clearest trend is seen in the NOE1 amplitude (variations of approximately 0.05), with most other pools showing no obvious correlation with the change of breathing gases. The dependency of the fit results on gas inhalation is smaller in the hippocampus than in the cortex, which is in agreement with the MTR_{asym} changes shown in the results presented in Figure 7-3 and Figure 7-4.

7.4 Discussion

The distribution of T2 and pH measurements remained relatively constant throughout the experiments showing no clear correlation with gas inhalation phases. The constant pH is consistent with work done by Miller *et al* who found that administration of 10% CO_2 (double the concentration used here) produced only a change in pH of 0.1, from 7.1 to 7.0 in the healthy rat brain after five minutes, and that the administration of 30% CO_2 produced a drop to pH 6.6 [152]. This trend appears to be non-linear suggesting that with the use of 5% CO_2 the expected pH change is negligible.

Both CBF and MTR_{asym} contrast showed sizeable signal changes correlating with the changes in gas being inhaled. The MTR_{asym} changes were more pronounced in the cortex than in the hippocampus, suggesting that the administration of carbogen influences the measured CEST effect in regions of high perfusion more than in regions of lower perfusion.

The changes in CBF were anticipated due to the administration of carbogen, which has known vasodilating effects but the underlying mechanism of the changes in MTR_{asym} is less immediately obvious. This was interrogated through fitting analysis to identify where in the z-spectrum changes occur due to the inhalation of carbogen, and what the implications may be for future glucoCEST imaging.

CEST is sensitive to two main physiological parameters: metabolite concentration and pH (mediated through changes in the exchange rate). The ^{31}P spectroscopy data indicates that the pH remained stable when breathing different gases and showed no correlation with MTR_{asym}. This suggests that the observed CEST signal changes may be driven by an altered metabolomic profile. Shah *et al* have previously investigated changes in the CEST signal in fresh blood samples due to variations in oxygenation using a six-pool Lorentzian difference analysis method [153]. They observed that the amide (APT), amine, and NOE1 signals broadly tended to either increase or remain steady with increasing blood oxygenation and that the MT signal tended to decrease or remain steady. The NOE1 signal in our data behaves consistently with these findings in both the cortex and hippocampus and the amine signal is consistent in cortex but not hippocampus. It should be noted that the Lorentzian fitting model used here includes an additional hydroxyl pool which may affect the results and that the measurements from Shah *et al* were made in *ex vivo* samples of blood, not *in vivo* brains.

Z-spectrum features at 9.4T are more well-defined than at lower fields which makes fitting more robust and allows for easier visual interpretation of the spectra than previous in vivo work. Optimization of the fitting parameters was performed using the method outlined in chapter 6. The number of peaks and their offset frequencies were in keeping with literature values and produced good fits, with residuals typically less than 0.01. A previous study investigating z-spectrum changes in the rat brain at 9.4T when breathing different gases found similar offset frequencies for NOE signals [154].

MT data-points were not acquired for all rats so z-spectrum normalization was approximated based on data acquired in the rats that did have MT points. While this is a potential source of error it is thought that the vertical offset term in the fitting-model will have been able to account for this uncertainty.

The MTR_{asym} signal in both the cortex and hippocampus was found to decrease when breathing carbogen, with the effects in the cortex being most pronounced. Results from the fitting analysis suggest that these changes in MTR_{asym} are caused by several underlying pool-specific changes.

The amide signal increases when breathing carbogen, which would typically give rise to an increase in MTR_{asym} and a similar effect on the MTR_{asym} would occur due to the observed decrease of the NOE1 amplitude. It must then be the case that these two effects are primarily counteracted by the proportionally larger decrease in the amine amplitude and the sum of signal changes in the other pools over the asymmetry range.

Both the cortex and hippocampus data suggested sizeable changes in the NOE1 amplitude of approximately 0.05 when switching between gases. In the cortex, additional signal changes were observed in the amide and amine amplitudes and FWHM-values and the hydroxyl FWHM. This suggests that an altered NOE1 signal may be the most pronounced effect of switching to carbogen from oxygen and should be given due consideration when interpreting changes in CEST signal in future exogenous CEST experiments such as glucoCEST.

In the example shown in Figure 7-11 the NOE2 and MT signals appear to be complimentary suggesting that there is some interaction in the fitting. This is likely due to their very similar chemical shifts and broad FWHM values compared to the sampling range of the z-spectrum.

7.4.1 Sources of altered CEST signals when breathing carbogen

The concentrations of a range of metabolites have been found to be altered when breathing high concentrations of CO_2 [152][155]. Of this non-exhaustive list, those containing chemical groups with exchangeable protons are listed in Table 7-3.

Individual metabolite concentrations are plotted in Figure 7-14 along with a calculated summed concentration change for the amine and hydroxyl chemical groups. The calculated summed concentrations were calculated using the relevant stoichiometry of the number of amine and hydroxyl groups present in each molecule. None of the metabolites reported by Miller *et al* contained amide groups [152].

The net changes in amine and hydroxyl concentrations are very small (< 3% in both cases). The decrease in amine signal in the cortex is in consistent with the reduction in amine concentration reported by Miller et al but changes in the hydroxyl signal are very small and not consistent when alternating between breathing gases, or between brain regions.

Quantification of the changes that underpin the changes in the NOE signal are more challenging due to the fact that it can be mediated through multiple channels even within a single molecule, but it is clear that increased perfusion, possibly in conjunction with the metabolite changes outlined above, causes a reduction in the NOE signal reliably in both the cortex and hippocampus.

Metabolite	Control (21)	10% CO_2 (21)	30% CO_2 (8)	# Groups	
				Amine	Hydroxyl
Glucose	1.54 ± 0.05	2.83 ± 0.10 **	4.16 ± 0.10 **	0	5
Glucose 6-phosphate	0.180 ± 0.0005	0.188 ± 0.005	0.280 ± 0.003 **	0	5
Fructose 1,6-diphosphate	0.0131 ± 0.0004	0.0120 ± 0.009	0.0084 ± 0.0009 **	0	3
Dihydroxyacetone phosphate	0.0164 ± 0.0009	0.0122 ± 0.0009 **	0.0070 ± 0.0005 **	0	1
α-Glycerophosphate	0.103 ± 0.004	0.064 ± 0.007 **	0.056 ± 0.003 **	0	4
Pyruvate	0.0890 ± 0.0020	0.0463 ± 0.0031 **	0.0296 ± 0.0019 **	0	1
Lactate	1.36 ± 0.04	0.641 ± 0.054 **	0.407 ± 0.028 **	0	2
Citrate	0.298 ± 0.008	0.225 ± 0.009 **	0.170 ± 0.011 **	0	4
α-Oxoglutarate	0.209 ± 0.004	0.102 ± 0.008 **	0.0579 ± 0.0015 **	0	2
Malate	0.300 ± 0.008	0.159 ± 0.010 **	0.115 ± 0.007 **	0	3
Glutamate	11.7 ± 0.16	10.3 ± 0.19 **	8.80 ± 0.14 **	2	2
Aspartate	2.96 ± 0.04	3.76 ± 0.11 **	4.48 ± 0.10 **	2	2
NH_4^+	0.275 ± 0.0025(13)	0.339 ± 0.035(3)	0.304 ± 0.030	3	0
ATP	2.48 ± 0.05	2.48 ± 0.08	2.52 ± 0.04	2	2
ADP	0.591 ± 0.015	0.563 ± 0.014	0.545 ± 0.020	2	5
AMP	0.0577 ± 0.0028	0.0558 ± 0.0032	0.0566 ± 0.0044	2	1
Creatine phosphate	3.94 ± 0.05	3.62 ± 0.12 *	2.55 ± 0.12 **	1	3
HCO_{3-}	10.5 ± 0.5(8)	13.3 ± 0.6(4) **	18.1 ± 0.3(4) **	0	1
pH	7.1	7.0	6.6	N/A	N/A

***Table 7-3:** The effect of 10 and 30% CO2 exposure on brain metabolite concentration after 5 mins. All values are means ± standard error of the mean (S.E.M.) with the number of observations indicated in parentheses. Symbols * and ** indicate statistical significance at the 5% and 1% levels respectively. Figure reproduced and adapted from* [152].

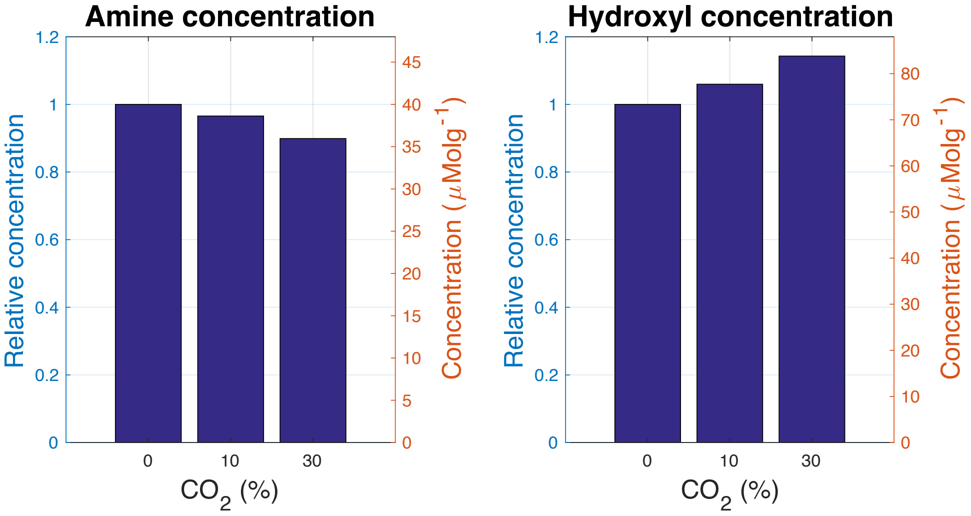

Figure 7-14: *Relative and absolute concentrations of amine and hydroxyl-containing metabolites when breathing different concentrations of* CO_2*. This study used 5%* CO_2 *which the data in this figure suggest would cause a reduction in the amine concentration and an increase in the hydroxyl concentration. Figure generated using data from* [152].

7.5 Conclusions

Changes in CEST signal in the healthy rat brain during carbogen challenge are not observed to correlate with measurements of T2 or tissue pH in this study. However, it has been observed that CEST asymmetry measurements correlate with levels of perfusion across the brain and that the magnitude of these effects in the cortex and the hippocampus are different. To understand the z-spectrum changes in more detail, a fitting algorithm was optimized and the fit results were analysed to identify which underlying exchange-related effects give rise to the asymmetry changes. The signals from multiple pools are seen to change with the inhalation of different gases affecting perfusion. This is significant for the future application of glucoCEST cancer imaging because tumours often display altered perfusion due to disrupted angiogenesis and leaky vasculature. In order to reliably distinguish between CEST effects caused by altered glucose concentrations and those caused by concomitant perfusion-related effects, it will therefore be pertinent to consider the correlation between perfusion effects and CEST effects when acquiring and analyzing data in future *in vivo* CEST imaging studies.

8 The effect of gadolinium contrast on the CEST signal in glioma patients

MRI contrast agents such as gadolinium are administered routinely in clinical glioma imaging protocols. Given that CEST is still an experimental technique, CEST research scans are typically performed at the end of clinical or research protocols, often after the administration of gadolinium. The question of whether or not gadolinium affects CEST measurements is therefore pertinent both for the practical design of current research protocols and potentially for future implementations of adaptive protocol design where CEST sequences may be added to protocols in real-time to obtain supplementary information.

In this chapter, CEST effects are evaluated both pre- and post-administration of gadolinium in a cohort of glioma patients [156]. Fitting of the data was performed to quantify effects on different CEST and NOE pools and in addition to evaluate changes in fitting contrast between tumour and healthy tissue at 3.0T.

Specific Chapter contributions:

I undertook all fitting-related analysis and subsequent interpretation and comparison with literature values.

Francisco Torrealdea (Clinical Scientist)[1,2]: Study design, patient recruitment and data acquisition.

Marilena Rega (Clinical Scientist)[3]: Study design, patient recruitment and data acquisition.

Joe Hearle[4]: Drawing regions of interest on images.

Moritz Zaiss[5]: Sequence development.

Ana Carvalho[3]: Research radiographer.

Anath Shankar[6]: Patient identification.

Harpreet Hyare[3]: Clinical oversight.

Anna Barnes[3]: PET-MR Research Unit Oversight.

Contributor affiliations:

[1] Centre for Medical Imaging, University College London, 43-45 Foley St, Fitzrovia, London, W1W 7TS, United Kingdom

[2] Department of Medical Physics and Biomedical engineering, University College Hospital, 235 Euston Road, London, NW1 2BU

[3] Institute of Nuclear Medicine, University College London Hospital NHS Foundation Trust, 5th Floor Tower, University College Hospital, 235 Euston Road, London, NW1 2BU

[4] UCL Medical School, UCL, London
[5]High Field Magnetic Resonance, Max Plank Institute, Tubingen, Germany
[6] Teenage Cancer Unit, UCLH, London

8.1 Introduction

Gadolinium (Gd) is one of the lanthanide rare-earth metals which have partially filled inner electron shells. This configuration renders it strongly paramagnetic which means it can influence tissue T1, T2 and T2* values, although its primary clinical purpose is for the shortening of tissue T1. Gd-based complexes are one of the most common types of MRI contrast media administrated during clinical scans and the *in vivo* kinematics (uptake and washout) depend on tissue-type, levels of perfusion and dosage.

Brain tumour imaging routinely involves comparisons of pre- and post-Gd images to identify regions with signal changes caused by the presence of Gd. In glioma imaging it allows for assessment of the blood-brain barrier (BBB) permeability, disruption of which is known to correlate with WHO tumour grades. Signal enhancement after Gd- administration may suggest increased microvascular permeability, which can be taken as a marker of malignancy in brain lesions [157] or an accumulation of Gd in tissue due to leaky blood vessels [158][159].

A growing literature suggests that CEST contrast in tumours may correlate with tumour aggressiveness [19][92][93][160]. However, as CEST signal is sensitive to changes in T1 and T2, it is important to understand the effects of gadolinium contrast administration. This chapter focuses on two main questions:

1) What is the effect of Gd-administration on the absolute CEST signal measurements (and the signal to noise ratio)?
2) How does it affect image contrast between regions of tumor and healthy tissue?

8.2 Materials and Methods

8.2.1 Study participants and ethics

Seven patients (age-range 17-20, three female, one WHO grade I, one WHO grade II and five WHO grade IV) with suspected glioma were recruited and provided written informed consent. In addition, five healthy volunteers (two females) were also scanned. Recruitment and scanning was performed under a sequence development ethics agreement in place at UCL/UCLH which was approved by the local ethics board.

8.2.2 MRI protocol

Data were acquired using a 3.0T Siemens mMR Biograph running software version VB20p. A 16 channel head coil was used with 12 head and 4 neck elements.

Patients were scanned using a standard clinical glioma protocol including pre- and post-gadolinium T1w MP-RAGE and T1 map acquisitions. Healthy volunteers were scanned using the same imaging protocol without the administration of gadolinium.

In addition to the standard clinical protocol, APT-CEST data were acquired twice using a gradient echo based snapCEST acquisition [161] with 3.0s saturation at 50% duty-cycle was applied at two different powers (B_1 = 0.75μT and 1.25μT) to allow for B_1 correction to 1.0μT. The time between the CEST scans was 12 minutes and the administration of Gd occurred half-way through this period. WASABI scans were also acquired for field homogeneity corrections [57].

Images were acquired at 41 offset frequencies evenly spaced between ±5ppm. The z-spectra were found to be especially smooth and were interpolated to 123 evenly spaced offset frequencies for post-processing. In one volunteer, additional MT points were acquired at ± 6ppm, ± 8ppm, ± 10ppm, ± 15ppm, ± 20ppm, ± 30ppm, ± 40ppm, ± 50ppm, ± 60ppm, ± 70ppm, ± 80ppm, ± 90ppm, ± 100ppm, ± 150ppm, ± 200ppm, ± 250ppm and ± 300ppm to allow for characterization of the MT contribution. The z-spectra from this volunteer were not interpolated as they were used as part of the peak-finder analysis outlined in section 8.2.3.2. More detail on this decision can be found in the discussion, section 8.4.1

The APT-CEST asymmetry was calculated by FT and MR from the B_0- and B_1-corrected data as the normalized asymmetry at 3.5ppm.

8.2.3 Fitting algorithm optimisation

8.2.3.1 MT Chemical Shift

Water, CEST and NOE resonances are nested close to the centre of the broad MT resonance. Therefore the first step in algorithm-tuning was to fix the central frequency of the MT effect for subsequent fitting. This was initially evaluated using data from the patient with MT points. A total of 96,678 brain voxels were fitted included both pre-Gd and post-Gd data. All points in the ±20ppm range were excluded and the remaining data points were fitted using a single Lorentzian lineshape. This was done to identify the offset frequency of the MT pool. The range of allowed offset frequencies was ±10ppm.

8.2.3.2 Fixing the CEST and NOE Chemical Shifts

With the MT offset fixed, the sum-of-amplitudes approach outlined in chapter 6 was applied in an attempt to identify the number and offset frequencies of CEST and NOE pools. Data from a volunteer were fitted using 24 Lorentzian lineshapes including a single Lorentzian lineshape to account for water and one to account for the MT pool.

A second, alternative chemical shift assignment for the CEST and NOE pools was also performed which started with the chemical shift values of the rat brain data from the previous chapter. Fits were performed with upper and lower bounds at ± 0.4ppm from the starting values. This was done in two iterations, the first of which was used to fix the amine and NOE2 pool offset frequencies, and the second used to fix the remaining offset frequencies.

8.2.3.3 MT fit-parameters in patients

As the patient data did not include MT points, it was necessary to restrict the amplitude and FWHM parameters of the MT pool to within an appropriate range for subsequent fits. This range was chosen based on analysis of a single volunteer dataset which included MT points. This rested on the assumption that MT values do not vary considerably between individuals and brain regions, although the ranges were chosen to be sufficiently large to allow for some variation. Subsequent boxplot analysis of the MT amplitudes in the patient data was performed to ascertain whether the distribution of the fitted amplitudes were hitting the max- or min-permitted values (as would be expected if the ranges were too constrained). The final algorithm was then applied to all voxels within fitting masks drawn in several brain regions.

8.2.4 Analysis and post-processing

Regions of interest were drawn in the necrotic core of the tumours by JH as well as in Gd-enhancing and non-Gd-enhancing regions and in healthy-appearing white-matter (WM), using T2w-FLAIR and T1w-post-Gd images. CEST signal was compared pre- and post-Gd. Data were tested for normality using the Kolmogorov-Smirnov test and significance testing was performed using a two-sample t-test.

8.3 Results

8.3.1 MT offset frequency

Analysis of the pre-Gd data suggested an MT offset frequency of -1.65ppm (25th and 75th percentiles: -2.40ppm, -0.84ppm), and for the post-Gd data -1.57ppm (25th and 75th percentiles: -2.19ppm, -0.93ppm). When combined the median value was -1.61ppm with 25th and 75th percentiles of -2.28ppm and -0.89ppm. These distributions are shown in boxplots in Figure 8-1 along with a histogram of the combined datasets.

Of the fitted voxels, 1,029 (~1%) had MT offset frequencies at the upper or lower boundaries (±9.99ppm), with 577 at the negative boundary and 452 at the positive boundary. To ensure that this was not introducing any sizeable skew to the mean and median values, the mean and median values were recalculated excluding the boundary results. This gave rise to the same mean and median values to 2.d.p. The median value was judged to be stable between both analysis methods and the median value of -1.61ppm was selected as the offset frequency of the MT pool for subsequent analysis.

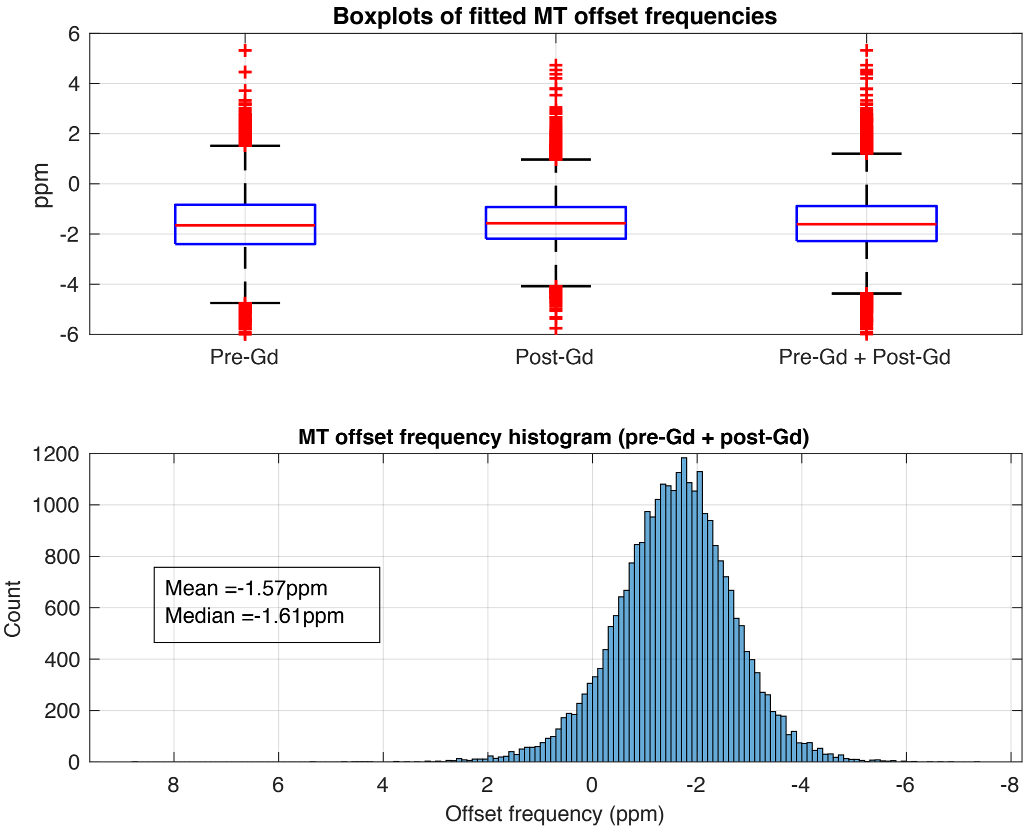

Figure 8-1: *Boxplots and a histogram showing the fitted MT offset frequencies from whole brain data of a single healthy volunteer. The median offset frequency of -1.63ppm was found to be stable both when including and excluding fit results at the boundary conditions (outside the*

±9.99ppm range). It was therefore selected as the offset frequency of the MT pool for subsequent fitting in this chapter.

8.3.2 Tuning of the fitting-algorithm using a sum-of-amplitudes approach

With the MT offset frequency fixed at -1.61ppm, a 23-lineshape sum-of-amplitudes fit was run over all voxels using data acquired without Gadolinium in the volunteer with MT points. Figure 8-2 shows the distribution of MT height and FWHM values over all voxels in the volunteer with MT points. The starting values and upper and lower limits for the MT heights in subsequent fits were chosen as the median and upper and lower adjacent values. The restriction on the FWHM was tighter, with the 25^{th} and 75^{th} percentiles chosen as the limits. These ranges were chosen to constrain the MT parameters enough to prevent unrealistic results, while still providing enough freedom for fitting over a reasonable range.

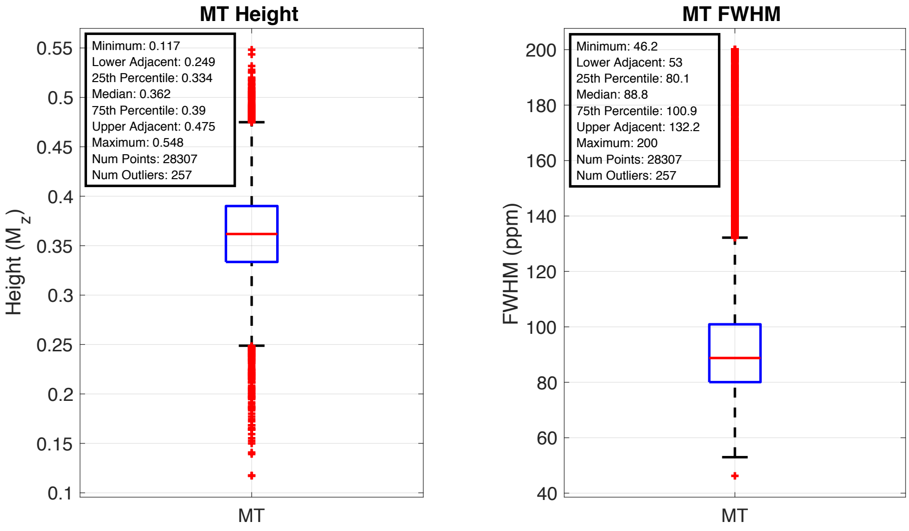

Figure 8-2: *Distribution of the fitted MT height and FWHM parameters from a single volunteer.*

In an attempt to identify the CEST and NOE chemical shifts, several iterations of the peak-finder method were performed using a range of starting values and parameter ranges and using data both including and excluding MT data-points. The results did not converge on CEST or NOE offset frequencies clearly enough to provide confidence in the results. The best sum-of-amplitudes result from these attempts is shown purely for illustration in Figure 8-3.

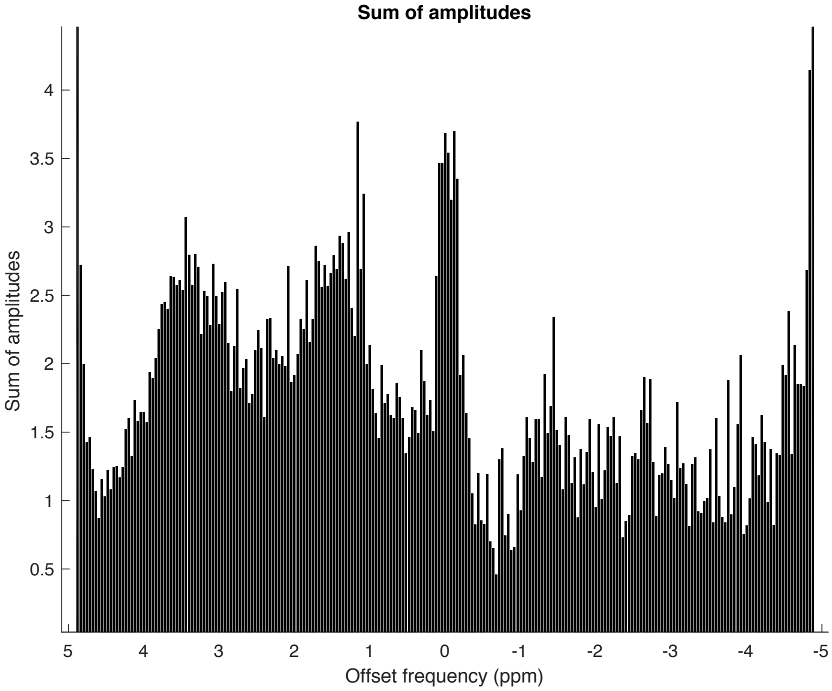

Figure 8-3: *Sum-of-amplitudes for a whole-brain fit using 23-Lorentzian lineshapes for each z-spectrum. Maxima are observed close to 3.5ppm, 1.5ppm, -1.5ppm which would be ascribed to amide, hydroxyl and NOE2 effects, but there is not sufficient resolution to select offset frequencies for further fitting with confidence based on these results. No clear contributions from the amine and NOE1 effects are observed.*

As the sum-of-amplitudes method did not converge, an iterative approach was performed (data not shown) where chemical shifts for each pool were identified using starting values based on the values found in the rat brain in the previous chapter. The upper and lower bounds for the chemical shift of each pool were set to be ±0.4ppm and a fit was performed. The chemical shifts of pools showing a clear maximum in the histogram analysis were fixed and the process was repeated until chemical shifts for all pools had been assigned. The finally selected fitting parameters for the Lorentzian lineshapes are given in Table 8-1.

Z-spectrum contributor	Lineshape	Parameter	Starting Value	Lower Bound	Upper Bound
Water	Lorentzian	ω_0 (ppm)	0.00	-	-
		Γ (ppm)	4	0.5	10
		A (A.U)	0.90	0.20	1.00
Amide	Lorentzian	ω_0 (ppm)	3.56	-	-
		Γ (ppm)	4	0.5	10
		A (A.U)	0.01	0.00	0.50
Amine	Lorentzian	ω_0 (ppm)	2.76	-	-
		Γ (ppm)	4	0.5	10
		A (A.U)	0.01	0.00	0.50
Hydroxyl	Lorentzian	ω_0 (ppm)	1.44	-	-
		Γ (ppm)	4	0.5	10
		A (A.U)	0.01	0.00	0.50
NOE1	Lorentzian	ω_0 (ppm)	-3.48	-	-
		Γ (ppm)	4	0.5	10
		A (A.U)	0.01	0.00	0.50
NOE2	Lorentzian	ω_0 (ppm)	-1.52	-	-
		Γ (ppm)	4	0.5	10
		A (A.U)	0.01	0.00	0.50
MT	Lorentzian	ω_0 (ppm)	-1.61	-	-
		Γ (ppm)	88.8	80.1	100.9
		A (A.U)	0.362	0.249	0.475
Horizontal Offset (whole-fit)	Constant	h (ppm)	0.0	-0.25	0.25
Vertical Offset (whole-fit)	Constant	v (A.U)	0.00	-0.05	0.05

Table 8-1: *Lorentzian fitting parameters for data acquired from brain glioma patients at 3.0T.*

8.3.3 Repeatability in healthy volunteers

The healthy volunteers were scanned twice with no administration of Gd therefore good agreement between both scans was expected. The median of the fitted peak heights in grey-matter and white-matter from the repeated scans are shown in Figure 8-4 for each of the four healthy volunteers without MT points both separately and also aggregated over all volunteers. The volunteer scanned with MT points was excluded from this analysis to ensure that all datasets being analysed were acquired in precisely the same way. All data are normalised to the mean of the two measurements. The standard deviations of the absolute values of the percentage variations for median peak heights between scans are shown in Table 8-2. All but one of the percentage standard deviation values lie between 0.3% and 4.7% and the grey-matter values are consistently lower than the white-matter values.

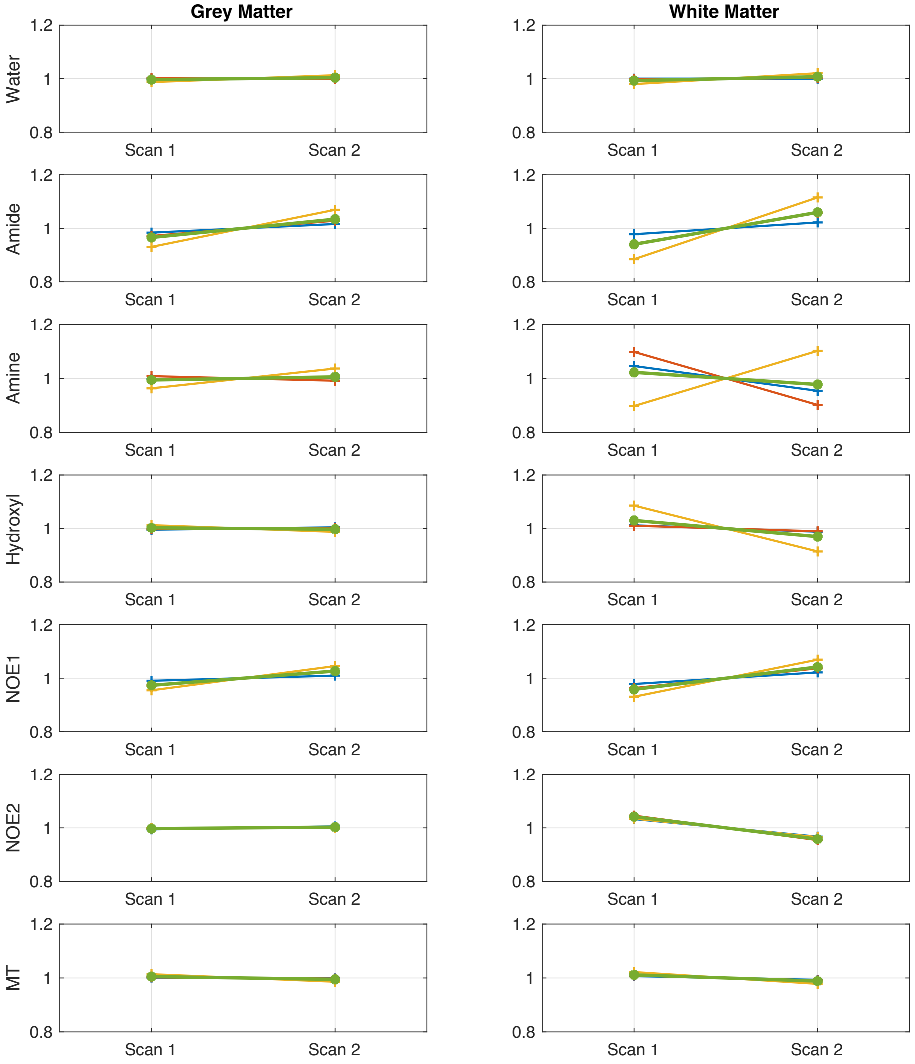

Figure 8-4: *Fitted peak heights derived from repeated measurements in four healthy volunteers. Results are shown for all seven pools in both grey and white-matter and are normalised to the mean of the two sets of measurements. Good agreement is observed on visual inspection.*

	S.D. between measurements (%)	
Peak	**Grey-matter**	**White-matter**
Water	0.8	1.1
Amide	2.8	4.7
Amine	2.4	10.4
Hydroxyl	0.9	4.3
NOE1	1.8	2.4
NOE2	0.3	0.7
MT	0.7	0.8

Table 8-2: *The standard deviation of the variation in median fitted peak heights over repeated scans in healthy volunteers expressed as a percentage.*

Now that we have quantified the degree to which the signal varies in repeated scans of the GM and WM in healthy volunteers we will move on to evaluate the signal changes observed pre- and post-Gd administration in various anatomical regions in patients.

8.3.4 Absolute peak heights pre- and post-Gd

Representative z-spectra from a Gd-enhancing voxel are shown in Figure 8-5.

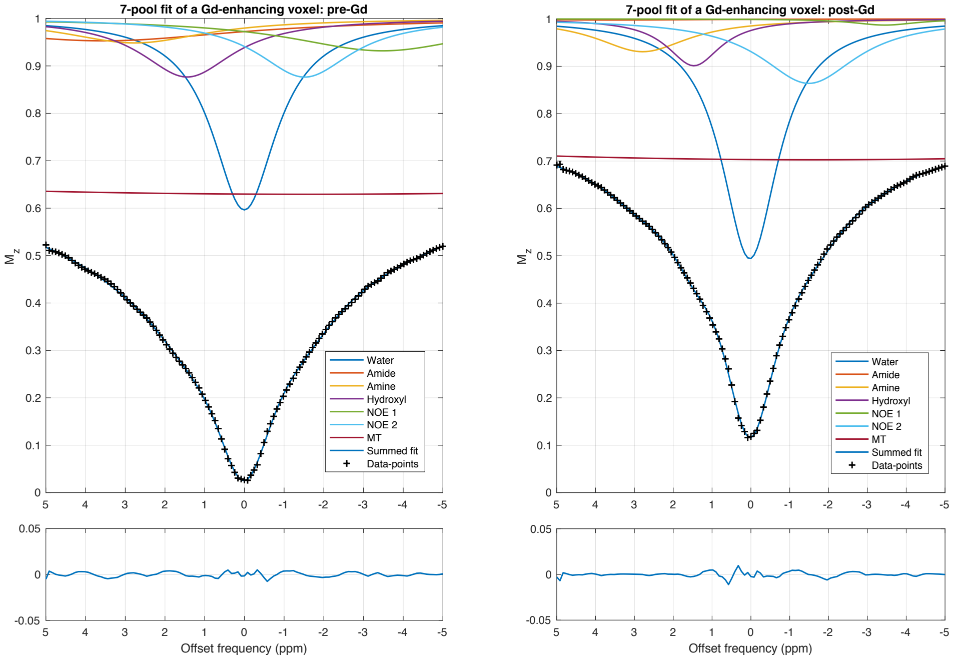

Figure 8-5: *Normalised z-spectra taken from a single voxel in a Gd-enhancing region both pre- and post-administration of Gd. The post-Gd z-spectrum appears less saturated than the pre-Gd z-spectrum which is consistent with a reduction in T1.*

The median absolute fitted peak heights for each, peak, volunteer and region of interest are shown in Figure 8-6 and voxel-wise data from Gd-enhancing regions are aggregated over all patient volunteers and shown in boxplot form in Figure 8-7 to inform the reader about the distribution of individual voxel values around the group median values.

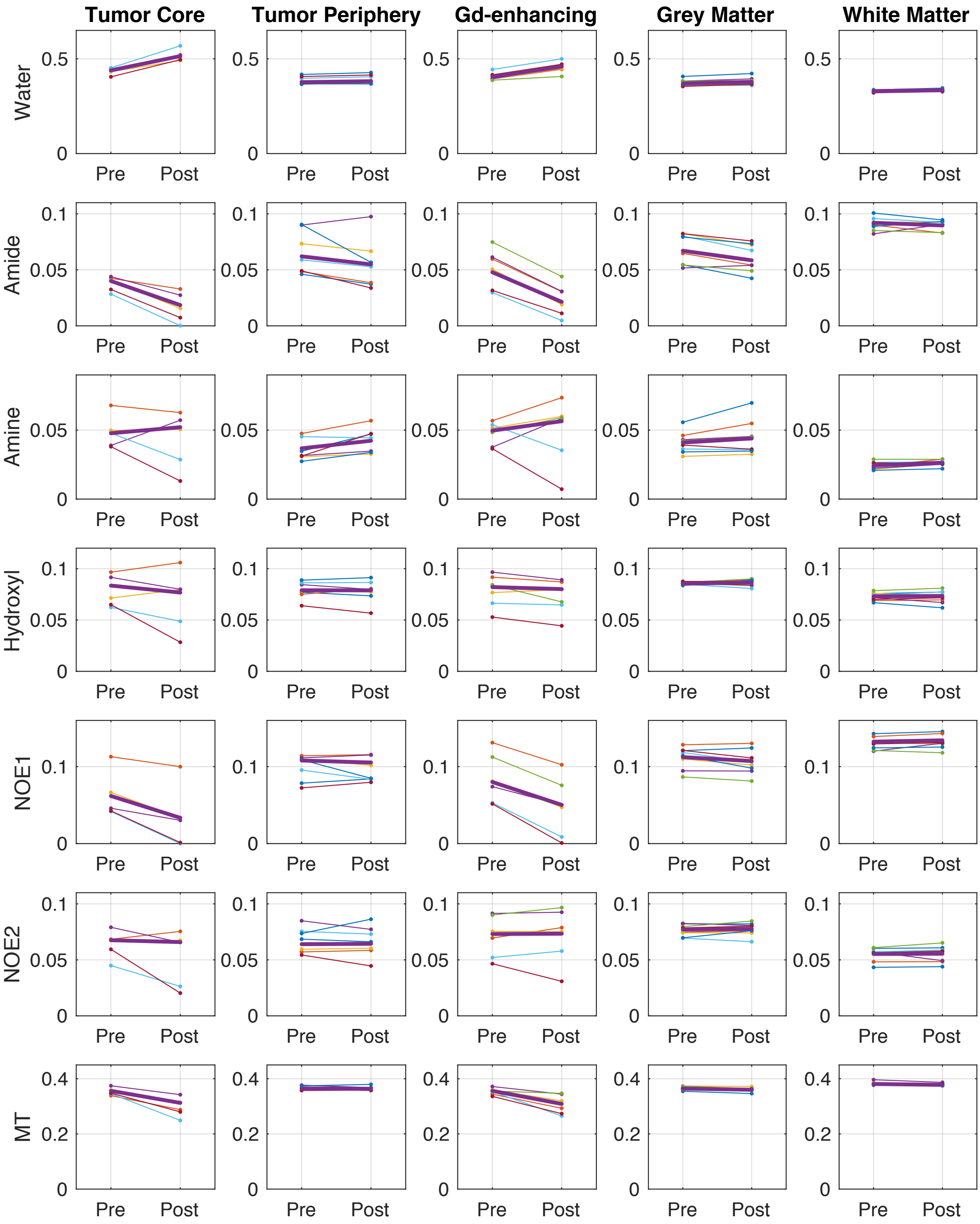

Figure 8-6: *The median absolute fitted peak heights, pre- and post-Gd administration, in five anatomical regions of interest over all five patients. The purple line with heavier weighting indicates the median of the heights aggregated over all patients. Post-Gd signal changes are larger in tumour and Gd-enhancing regions than in apparently uninvolved regions of grey and white-matter.*

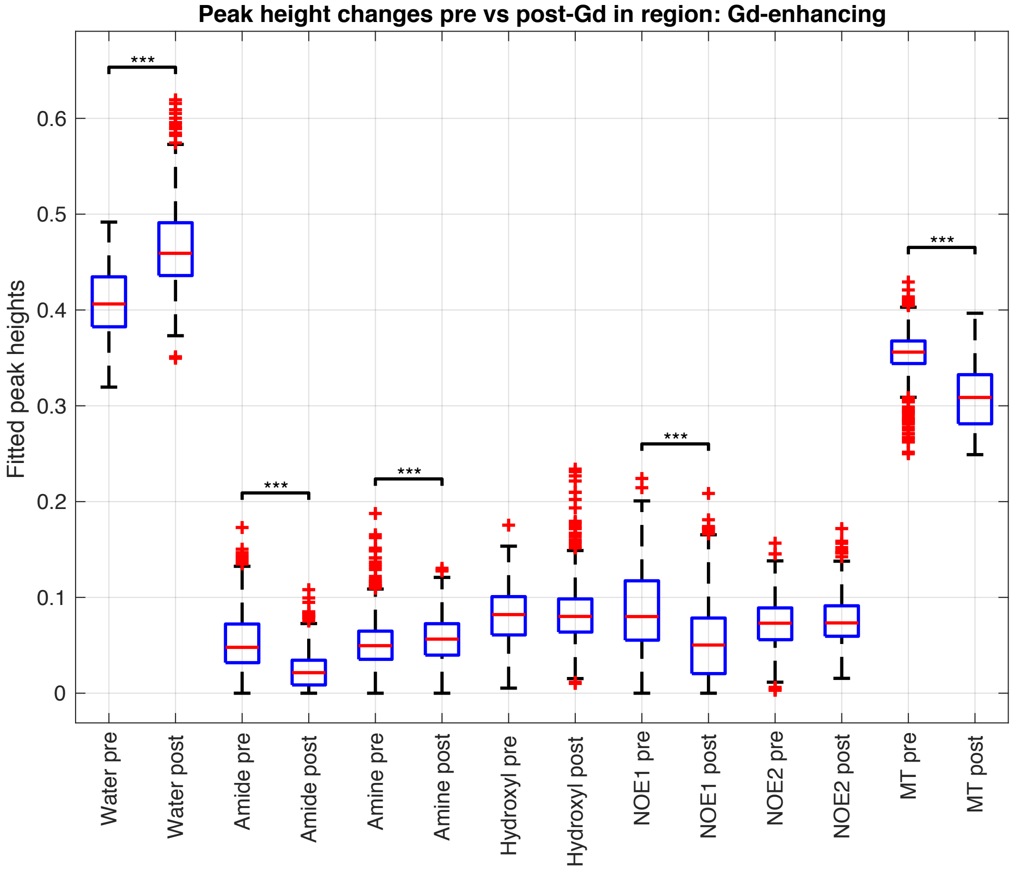

Figure 8-7: *Boxplots showing the distribution of fitted peak heights from all voxels in Gd-enhancing regions from all seven patients. Normality was checked using the Kolmogorov-Smirnov test and significance was calculated using a two-sample t-test.*

Based on the data underpinning Figure 8-6 and Figure 8-7, the signal changes observed in the Gd-enhancing regions and are especially pronounced and in the water, amide, NOE1 and MT pools, all of which are found to have significance levels of $p < 0.001$. The amine signal changes (~0.01) are also found to be statistically significant at the $p < 0.001$ level. This significance level is not obvious from visual inspection of the data but it is judged to be due to the differences in the variance of the two distributions.

The median absolute and percentage changes of fitted peak heights post-Gd administration, aggregated over all patients, are tabulated in Table 8-3. In cases where the percentage changes are larger than the greater of the two S.D. values calculated in healthy volunteers (see Table 8-2) these values are underlined and highlighted in bold.

The percentage changes in the water, amide, amine, NOE1 and MT signals in Gd-enhancing regions exceed the previously calculated percentage standard deviations for repeated scans. Similar signal changes are observed in the tumour core and, to a lesser degree, in the tumour periphery and grey and white-matter.

	Post-Gd signal changes									
	Tumour core		**Tumour Periphery**		**Gd-enhancing**		**Grey Matter**		**White Matter**	
Peak	**Abs**	**%**	**Abs**	**%**	**Abs**	**%**	**Abs**	**%**	**Abs**	**%**
Water	**+0.0754**	**+17.18**	**+0.0050**	**+1.32**	**+0.0529**	**+13.01**	**+0.0086**	**+2.31**	**+0.0051**	**+1.55**
Amide	**-0.0215**	**-53.70**	**-0.0071**	**-11.49**	**-0.0264**	**-55.21**	**-0.0085**	**-12.70**	-0.0024	-2.58
Amine	+0.0044	+9.15	**+0.0055**	**+15.04**	**+0.0068**	**+13.76**	+0.0030	+7.20	+0.0020	+8.38
Hydroxyl	**-0.0067**	**-8.06**	-0.0001	-0.14	-0.0019	-2.36	+0.0011	+1.24	+0.0004	+0.53
NOE1	**-0.0284**	**-45.87**	-0.0026	-2.40	**-0.0297**	**-37.14**	**-0.0051**	**-4.55**	+0.0017	+1.30
NOE2	**-0.0017**	**-2.47**	+0.0004	+0.55	+0.0003	+0.39	**+0.0007**	**+0.93**	+0.0002	+0.34
MT	**-0.0438**	**-12.30**	-0.0013	-0.35	**-0.0473**	**-13.29**	**-0.0043**	**-1.17**	**-0.0032**	**-0.84**

Table 8-3: *Absolute and percentage-changes in median signal post-Gd administration aggregated over all patient volunteers. Percentage-changes exceeding the maximum standard deviation values previously calculated in healthy volunteers are underlined and highlighted in bold.*

8.3.5 Tumour contrast pre- and post-Gd

Having assessed the absolute signal changes it is pertinent to assess whether they alter the CEST contrast between healthy tissue and tumour. Figure 8-8 shows ROI masks used in the analysis of slice 5 from patient 6 and Figure 8-9 shows maps of both the peak heights the FWHM values. Colorbar axes have been matched for easy comparison. Changes are seen in the heights of the amide, NOE1, NOE2 and MT contributions in the region of tumour and in the FWHM values of the amide, amine, NOE1, NOE2 and MT contributions. For easier visualization, Figure 8-10 shows the median signal differences between regions of tumour and apparently uninvolved grey and white-matter for each pool over all patients. Contrast is calculated as the median healthy signal (either GM or WM) minus the median tumour signal. It should be noted that in order to simplify this analysis, tumour core, periphery and Gd-enhancing regions of interest were combined and treated as unified ‘tumour’ ROIs (although the sub-regions may still be distinguished in the ROI masks shown in Figure 8-8).

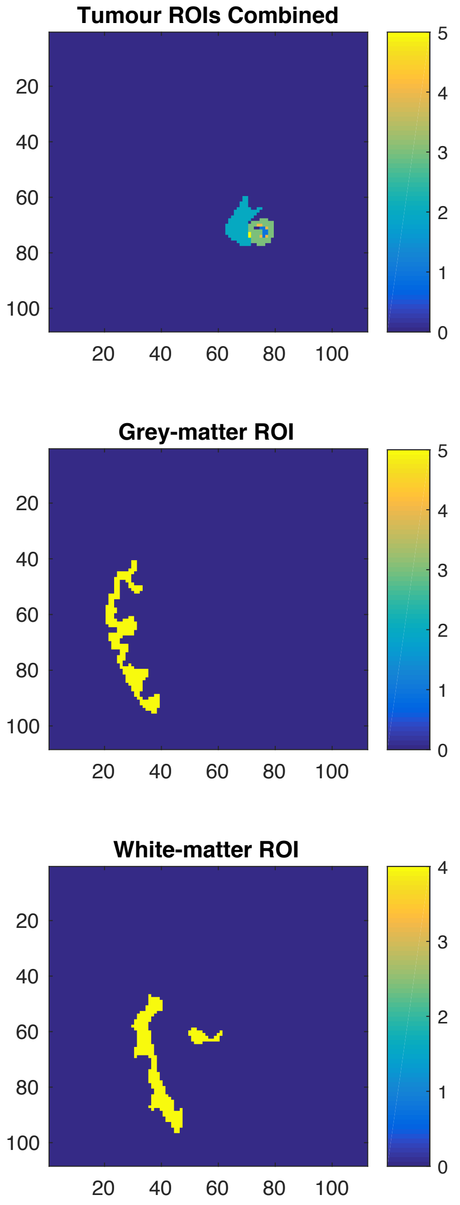
Tumour ROIs Combined
20
40
60
80
100
20
40
60
80
100
0
1
2
3
4
5
Grey-matter ROI
20
40
60
80
100
20
40
60
80
100
0
1
2
3
4
5
White-matter ROI
20
40
60
80
100
20
40
60
80
100
0
1
2
3
4

Figure 8-8: *Masks for the tumour-related ROIs, and grey and white-matter ROIs for slice 5 of volunteer 6. These are provided for reference to help with interpretation of the subsequent CEST maps.*

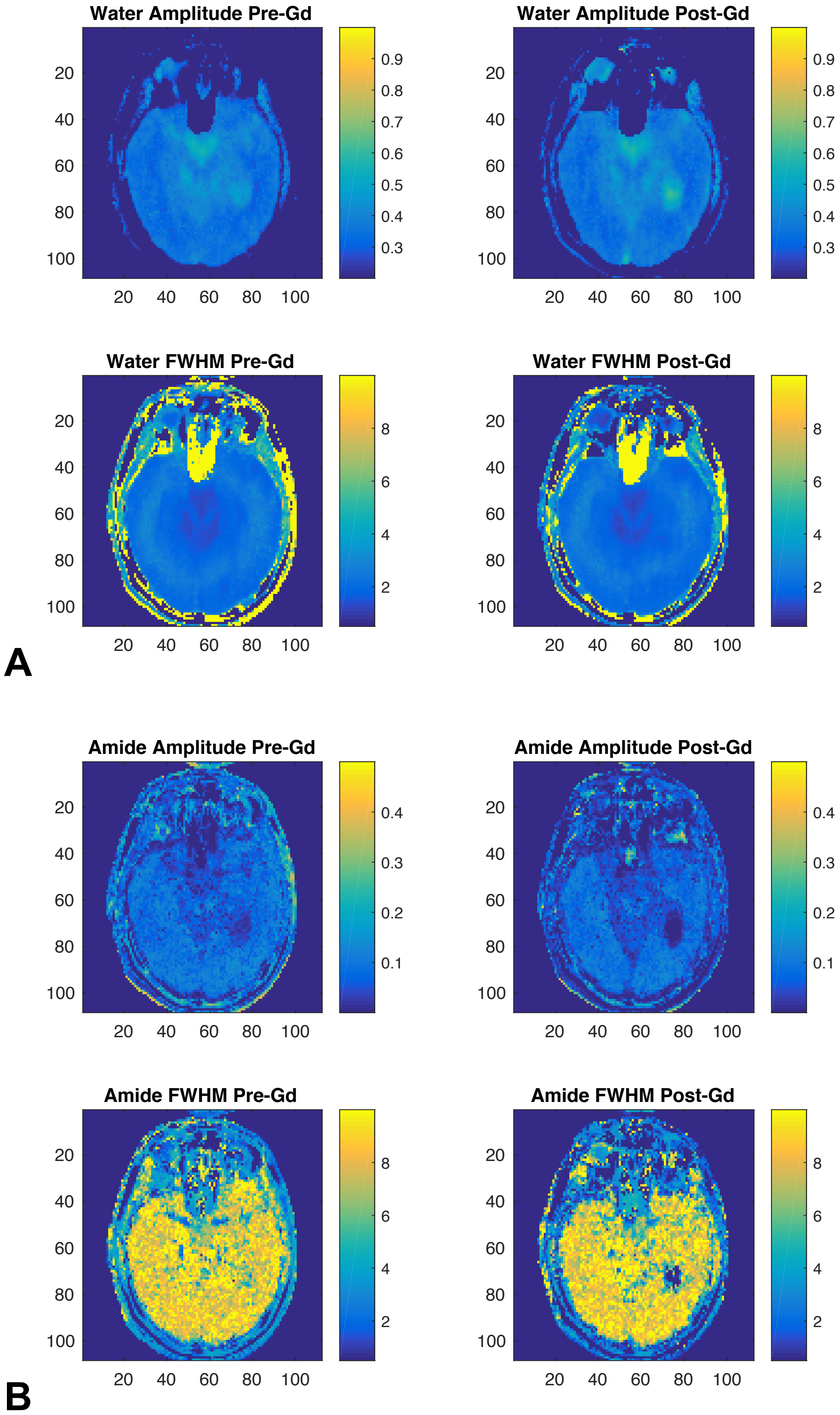
Water Amplitude Pre-Gd
Water Amplitude Post-Gd
20
40
60
80
100
0.9
0.8
0.7
0.6
0.5
0.4
0.3
Water FWHM Pre-Gd
Water FWHM Post-Gd
8
6
4
2
A
Amide Amplitude Pre-Gd
Amide Amplitude Post-Gd
0.4
0.3
0.2
0.1
Amide FWHM Pre-Gd
Amide FWHM Post-Gd
8
6
4
2
B

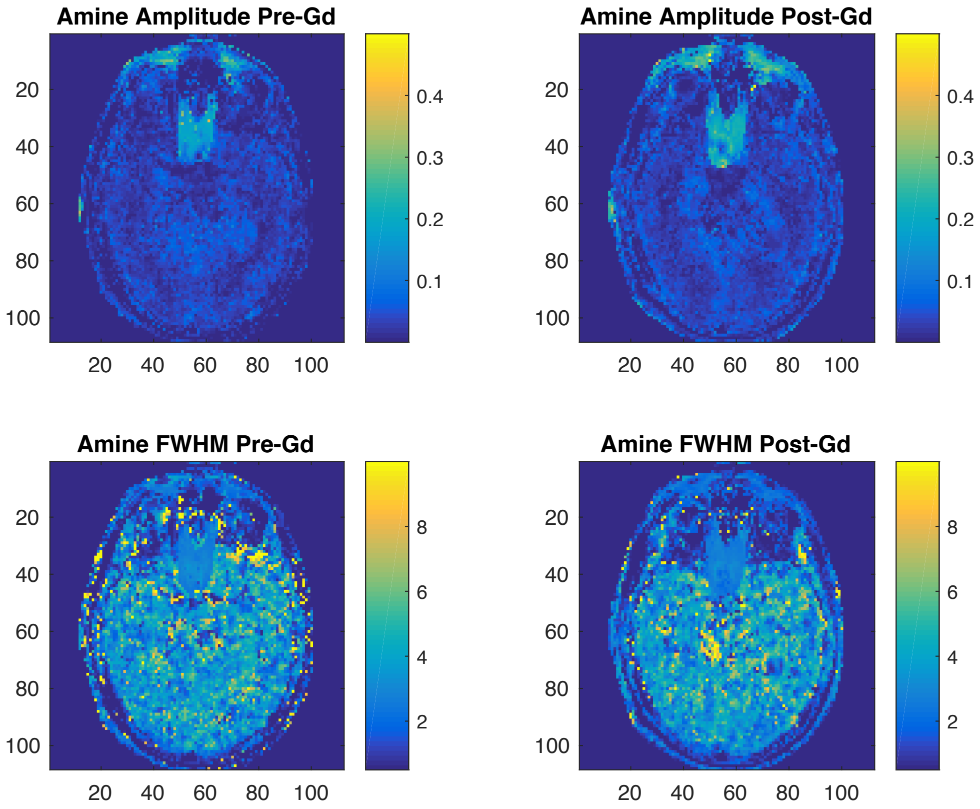
Amine Amplitude Pre-Gd
Amine Amplitude Post-Gd
Amine FWHM Pre-Gd
Amine FWHM Post-Gd
20
40
60
80
100
0.1
0.2
0.3
0.4
2
4
6
8

C

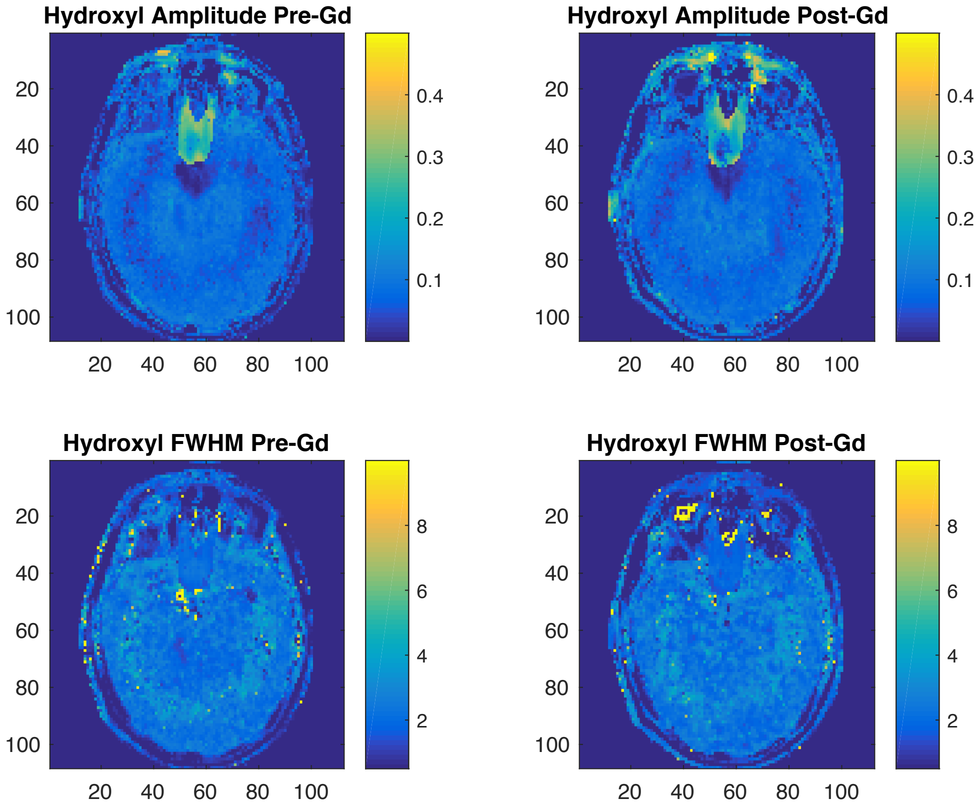
Hydroxyl Amplitude Pre-Gd
Hydroxyl Amplitude Post-Gd
Hydroxyl FWHM Pre-Gd
Hydroxyl FWHM Post-Gd
20
40
60
80
100
0.1
0.2
0.3
0.4
2
4
6
8

D

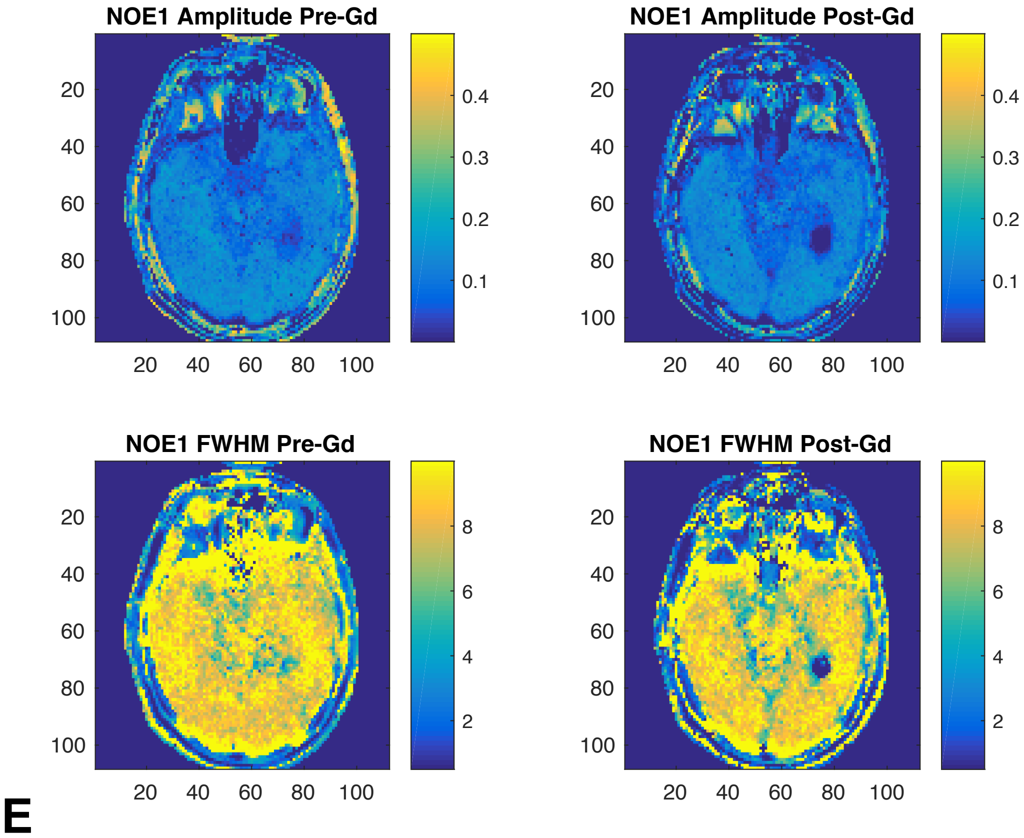
NOE1 Amplitude Pre-Gd
NOE1 Amplitude Post-Gd
NOE1 FWHM Pre-Gd
NOE1 FWHM Post-Gd
20
40
60
80
100
0.1
0.2
0.3
0.4
2
4
6
8
E

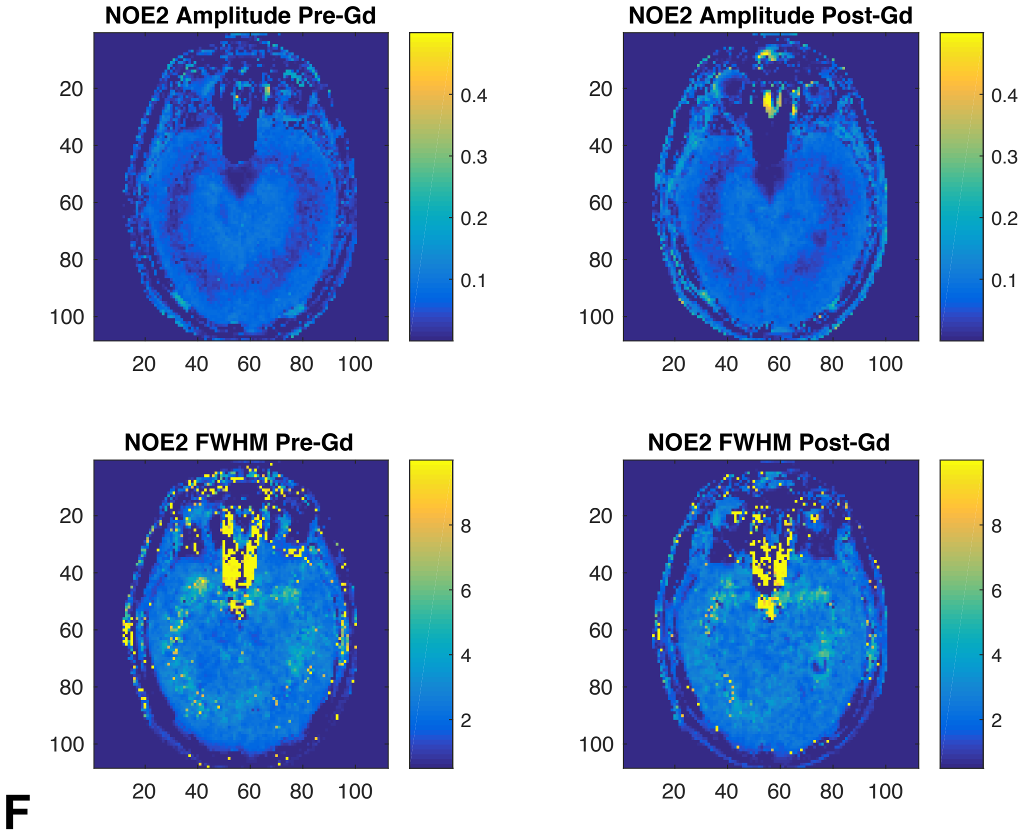
NOE2 Amplitude Pre-Gd
NOE2 Amplitude Post-Gd
NOE2 FWHM Pre-Gd
NOE2 FWHM Post-Gd
20
40
60
80
100
0.1
0.2
0.3
0.4
2
4
6
8
F

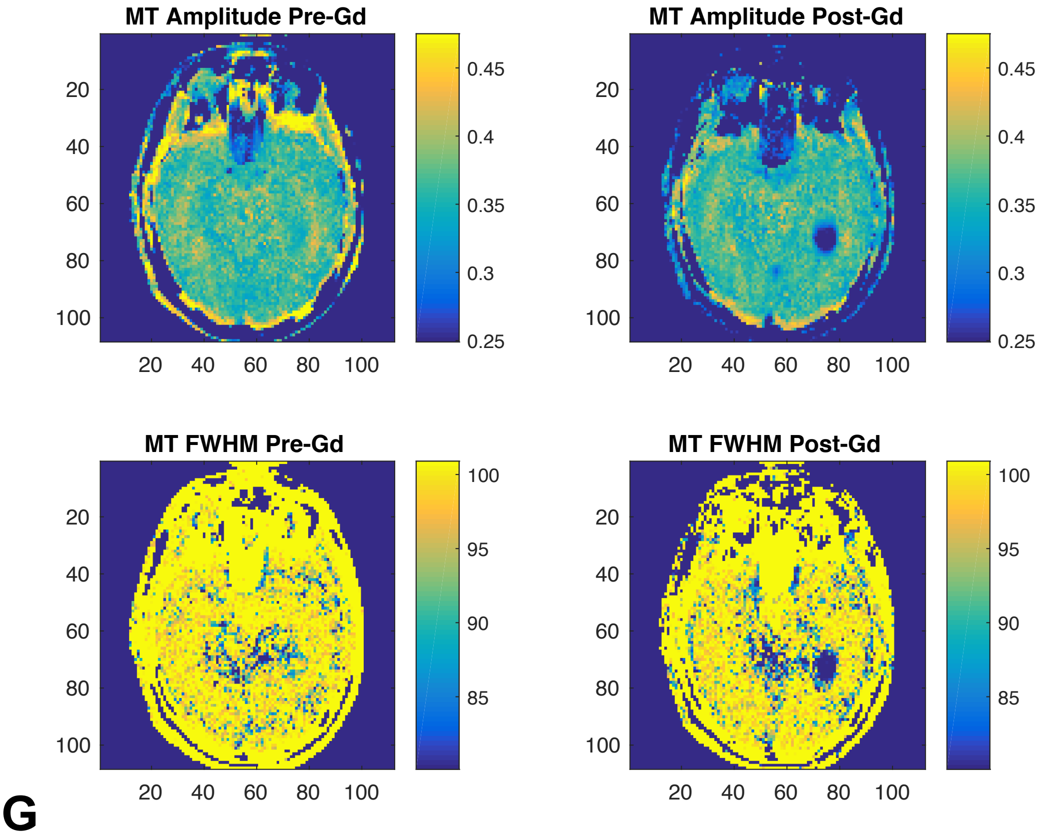
MT Amplitude Pre-Gd
MT Amplitude Post-Gd
MT FWHM Pre-Gd
MT FWHM Post-Gd
20
40
60
80
100
0.45
0.4
0.35
0.3
0.25
95
90
85
G

Figure 8-9: *CEST signal maps showing the amplitude and FWHM of the fitted lineshapes in volunteer 5 both pre-and post-Gd for* ***A*** *water,* ***B*** *amide,* ***C*** *amine,* ***D*** *hydroxyl,* ***E*** *NOE1,* ***F*** *NOE2 and* ***G*** *MT. The core of the tumour is most clearly identifiable in the post-Gd cases in the amplitude of the amide, NOE1, NOE2 and MT pools, and in the FWHM of the amide, amine, NOE1, NOE2 and MT pools. The FWHM of the NOE2 pool also shows some distinction between the tumour core and periphery.*

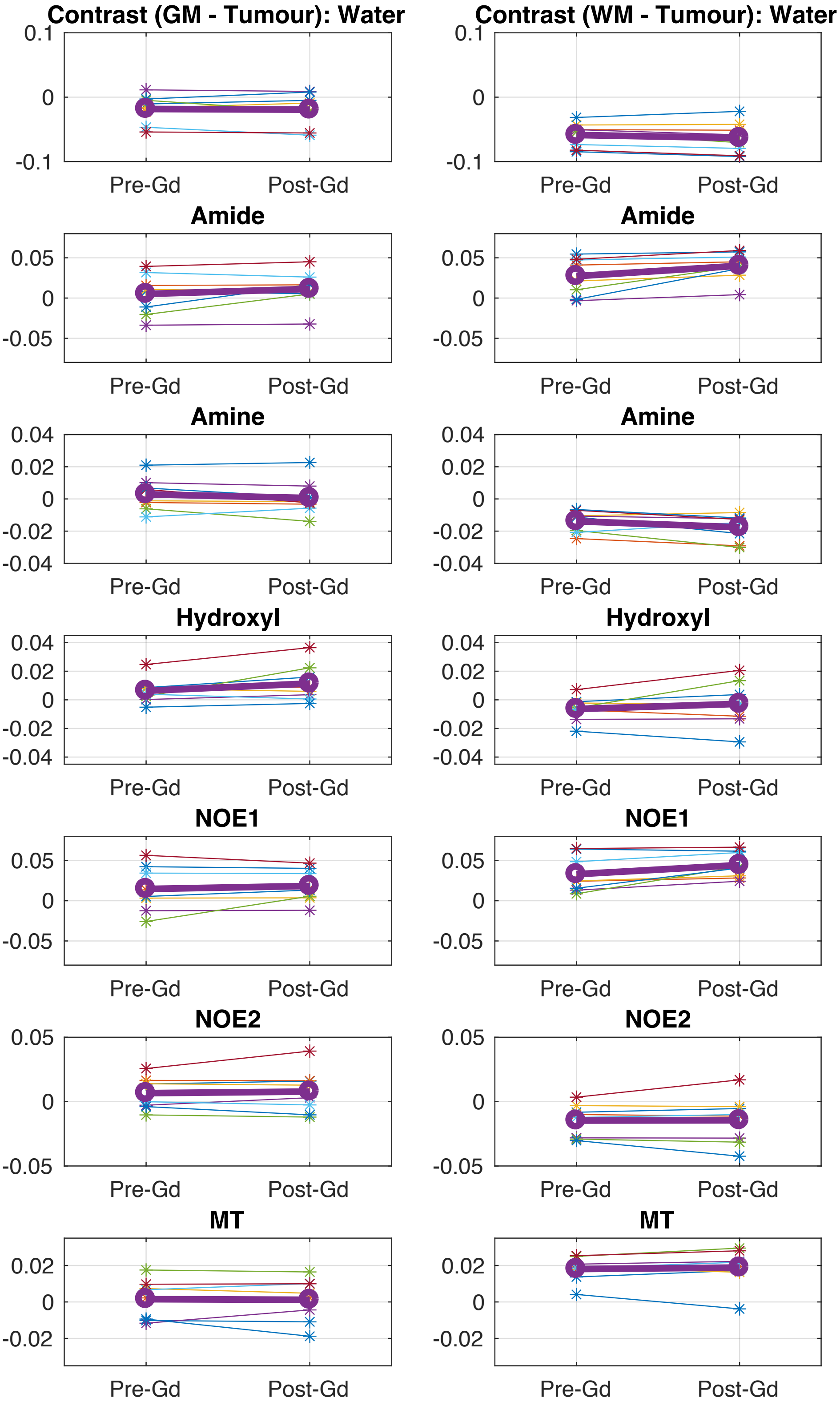

Figure 8-10: *Signal differences between regions of tumour and grey- and white-matter for all patients, pre- and post-Gd. In all cases apart from GM-tumour amine contrast, WM-tumour hydroxyl contrast and GM-tumour MT contrast, the administration of Gd increases the absolute signal differences between GM or WM, and tumour.*

The results shown in Figure 8-10 are striking as they suggest that in almost all cases (excluding GM-tumour contrast in the amine signal, WM-tumour contrast in the hydroxyl signal, and GM-tumour contrast in the MT signal) the absolute differences in median signal between tumour and grey or white-matter are increased after the use of Gadolinium. This is consistent with visual inspection of the signal maps shown in Figure 8-9 which show clearer delineation of the tumour in the post-Gd images.

8.4 Discussion

8.4.1 Peak-assignment

The sum-of-amplitudes analysis did not clearly identify CEST peaks in the z-spectra in this particular application. While the approach appeared to work well in phantoms and in the rat brain at 9.4T it may be that *in vivo* at 3.0T the sensitivity of the technique is limited due to the broadness and overlap of the z-spectrum features.

The dataset used for the sum-of-amplitudes analysis included the same chemical shift sampling as all other volunteers and patients, but with additional sampling points in the MT range. To avoid unexpected fit results this analysis was performed on non-interpolated data which meant that the B_0 field corrections could not be performed (as a key part of this process is to interpolate the z-spectra before shifting them voxel-by-voxel). The field correction could have applied by performing the correction and then un-interpolating the dataset again, but these steps would have yielded a dataset that was moving increasingly further from the raw measurements. The inclusion of the whole-fit horizontal offset and the requirement that the water peak should be fixed at 0ppm with an amplitude of at least 0.4 M_0 means that the fitting algorithm is able to account for some B_0-inhomogeneities, but it is likely that the lack of B_0 field corrections had some small impact on results of the sum-of-amplitudes analysis.

Performing the analysis on different brain regions would be beneficial in future work. While this would require additional segmentation steps, it would be useful to find out whether the separate analysis of grey-matter and white-matter produced clearer results. It was not carried out here due to the time and computational-cost of applying the method.

8.4.2 Absolute signal changes

Tumour core and Gd-enhancing regions showed the most sizeable changes in absolute signal magnitude. In over half of the measurements, for the core and Gd-enhancing regions, the changes in absolute signal were larger than the repeatability thresholds calculated from repeated scans in healthy volunteers for six of seven, and five of seven pools, respectively. Grey-matter and white-matter signal changes exceeded the respective thresholds in five of seven and two of seven pools, respectively although these differences were much smaller than in the tumour ROIs.

This suggests that longitudinal studies focused on making absolute measurements of CEST signal (as compared with image contrast) should utilise CEST data that was acquired prior to Gd-administration to ensure consistency between timepoints and subjects. An alternative would be to use data acquired at a prescribed time after administration however this would likely introduce additional sources of error due to variations in renal clearance between patients and examinations which would be a confounding effect within any such studies.

8.4.3 Contrast changes

Image contrast between tumour and both GM and WM appeared to be maximised post-Gadolinium. Given that all fitting was performed using the same algorithm, this is attributed to physical changes caused by the Gd. This finding is notable as it suggests not only that the addition of Gd does not reduce CEST contrast, but that it may act to enhance it. While it may be that maximising CEST image contrast is not the primary desired clinical goal, it appears that CEST scans focused on doing this could be inserted at any point during a glioma MRI protocol with no loss of contrast, and with a gain in contrast if added after the administration of Gadolinium.

Optimisation of the fitting parameters was done using pre-Gd data only because this was the only data with MT points as it was acquired in a healthy volunteer. Optimisation could be performed using post-Gd data for better characterisation, if MT points were to be acquired in subsequent patient scans.

In their study on the effect of Gd on asymmetry measurements in patients with internal carotid stenosis [162] Tee *et al* recommend that APT measurements should be acquired prior to administration of Gd to avoid misinterpretation of the signal. The results presented here lead to a similar conclusion. But an increase in CEST contrast with the use of Gadolinium has not been reported previously, including by Tee *et al*. However, several differences between the work of Tee *et al* and this study exist. They were not evaluating contrast between glioma and healthy grey and white-matter and their analysis was also focused on changes in the MTR_{asym} and was acquired using a saturation power ($0.535\mu T$) that was almost half of that used here. In order to perform the analysis contained here, it was necessary to deviate from the protocol used by Tee *et al*. The vast number of variables in the acquisition and post-processing of CEST data makes it difficult to directly compare results that are not acquired using standardised protocols.

8.4.4 Recommendations

These results suggest that the acquisition of CEST data for z-spectrum fitting is possible both pre- and post-administration of Gd. This allays previous concerns that Gd may reduce CEST contrast between tumour and healthy tissue. Based on this analysis it is also suggested that Gd could enhance CEST contrast when performing z-spectrum fitting although standardization of Gd doses and scan-timings must be carefully considered.

Researchers interested in pursuing this line of inquiry may wish to study larger cohorts of patients to better understand which pools or combinations of pools have the greatest diagnostic and prognostic power for glioma assessment. It would also be of interest to understand the physical basis of the effects in combination with histopathology and metabolomic data.

Two distinct conclusions are reached, depending on the aims of future studies. For research protocols aiming to maximise tumour contrast, it is tentatively suggested that CEST data are acquired after the administration of Gd. However, for studies aiming to characterize endogenous CEST contrast it is suggested that data are acquired without the administration of Gd to ensure the best possible consistency across all measurements without the added complications of Gd-kinematics.

9 Summary and future directions

9.1 Thesis summary

The work outlined in this thesis is intended to support the practical development of acquisition and post-processing of z-spectrum fitting methods for CEST data acquired at 3.0T.

In the prostate repeatability study it was found that the repeatability of fitting metrics were comparable to other mp-MRI acquisitions and fell within an acceptable range, comparable to those previously reported for other prostate imaging techniques. With improved optimization over time, the signal to noise ratio is likely to increase which may also improve repeatability scores which may act as a driver for increased adoption of the technique. The optimization processes are outlined thoroughly in the thesis. It will become increasingly important to be specific about optimization steps as CEST techniques are applied in a wider range of contexts as the future harmonisation of pulse sequences and protocols becomes more important for multi-centre trials.

The peak-finder method outlined worked well in simulated data with added noise, and in phantoms at 9.4T and 3.0T, demonstrating that a statistical approach to CEST peak identification and assignment of chemical shifts for fitting is possible and may be useful at lower field-strengths. At 9.4T in rat brain data it also suggested clear peak offset frequencies, consistent with literature values. At 3.0T *in vivo* the method was inconclusive but future work may enable improvements of the technique, thereby putting z-spectrum fitting at 3.0T on firmer footing as will be needed if it is to become used in clinical practice. If developed and tested to a clinical standard, and with sufficient computational speed or efficiency gains, the approach outlined in the thesis could be used to tune CEST fitting algorithms on a case-by-case basis to account for differences in physiology across patients.

In the chapter investigating concomitant CEST and ASL signal changes we have seen that z-spectrum fitting can add depth to existing CEST measurements. We establish that perfusion levels alter CEST signal, which is of particular relevance in cancer imaging where leaky bloody vessels due to disrupted angiogenesis and regions of necrosis both exhibit dramatically altered perfusion. This is of particular importance in techniques such as glucoCEST which rely on the addition of an exogenous contrast agent which may give rise to altered perfusion as well as an altered CEST profile. Understanding the underlying mechanics of CEST measurements and their interaction with other physical and physiological processes will be vital for the interpretation of any clinically implemented CEST protocol.

In human glioma studies we provide evidence suggesting that CEST contrast between tumour and healthy tissue is not only preserved after the administration of Gadolinium but may be increased when performing z-spectrum fitting although careful control of Gadolinium dosage and timings must be considered if this it to be done routinely.

9.2 Future directions

The growing body of existing CEST work is largely comprised of single-centre studies of novel methods, with very few validation or repeatability studies. In order to become clinically established, a multi-faceted effort will be required to understand the underlying basis of the contrasts observed, to optimize the sequences, and to shorten scan times. MRI scanner vendors will also need to (and indeed, have started to) integrate CEST software into their proprietary software offerings to ensure CE-marked scans can be performed clinically and compared across multiple sites.

An effort to understand precisely the benefits afforded by the unique CEST contrast, as well as interactions with other imaging methods and modalities such as PET would also help build a picture of where CEST may sit in the future diagnostic landscape. As MRI is a non-ionising imaging modality, any opportunity to supercede ionizing methods such as PET or CT should be exploited to maximum effect to minimise patient radiation exposure.

In terms of field strengths, there are two separate and important lines of inquiry. On the one hand, human-sized scanners at field-strengths above 3.0T are becoming more widespread. Therefore, the availability of high-field CEST data with improved spectral resolution will increase in the coming years allowing for greater insight into the CEST mechanics of tumours. On the other hand, lower-field scanners of 1.5T and 3.0T are prevalent globally therefore efforts should be made to maximise the usefulness of CEST data acquired at these field strengths. In reality both approaches will be pursued in tandem, with higher-field work feeding into the optimization of lower-field protocols.

For clinical adoption of CEST techniques to occur, researchers in the field must start working towards the standardisation of protocols for multi-centre trials. CEST sequence design involves exploring a vast multi-dimensional parameter space. It could be that, in a similar way to ASL, this space is reduced through the production of a consensus white-paper [141] resulting in a de-facto standard practice for clinical CEST imaging which could provide a template for future study protocols. The growing interest of MRI vendors in CEST, signifies a growing momentum for exploring its diagnostic potential and commercial involvement may be a spark for such a consensus meeting to be arranged.

Based on the work presented here and knowledge gained about the field of the course of my PhD I envisage that the integration of z-spectrum fitting into future clinical CEST imaging will necessitate a period of 'back to basics' experimentation. This will feature long, low-power saturation trains at 50% duty-cycle, acquiring the whole z-spectrum with sampling frequency spacings of no greater than 0.25ppm in the ±5ppm range. The sizeable effects of MT should also not be ignored so a minimum of 3 MT-points, and preferably more, should also be acquired on at least one side of the water resonance and preferably on both, for proper characterization of the effect. It may be that time savings can be made by dropping the acquisition of dedicated B_0 maps as fitting may be able to account for static-field inhomogeneities through the use of the whole-fit offset parameter, but this will need to be validated thoroughly. Alternative lineshapes or fitting algorithms may also be explored but Lorentzian fitting appears to be 'good enough' at this stage and manages to avoid the computational burden of calculating full numerical solutions to the BM equations. Once z-spectrum fitting analysis has been thoroughly tested and characterized in specific applications, the modifications and optimization gains can be attempted, but due to the broad features at 3.0T and below, a rigorous approach should be taken from the outset. It is hoped that the work contained in this thesis constitutes a modest contribution to this end.

10 References

[1] M. H. Levitt, *Spin Dynamics*, Second. London: Wiley, 2008.

[2] F. Torrealdea, “Investigation of cancer metabolism with glucoCEST MRI.”

[3] A. N. Dula, S. a Smith, and J. C. Gore, “Application of chemical exchange saturation transfer (CEST) MRI for endogenous contrast at 7 Tesla.,” *J. Neuroimaging*, vol. 23, no. 4, pp. 526–32, Oct. 2013.

[4] J. Zhou *et al.*, “Differentiation between glioma and radiation necrosis using molecular magnetic resonance imaging of endogenous proteins and peptides.,” *Nat. Med.*, vol. 17, no. 1, pp. 130–4, Jan. 2011.

[5] J. Zhou, J.-F. Payen, D. a Wilson, R. J. Traystman, and P. C. M. van Zijl, “Using the amide proton signals of intracellular proteins and peptides to detect pH effects in MRI.,” *Nat. Med.*, vol. 9, no. 8, pp. 1085–90, Aug. 2003.

[6] S. Walker-Samuel and R. Ramasawmy, “In vivo imaging of glucose uptake and metabolism in tumors,” *Nat. Med.*, vol. 19, no. 8, pp. 1067–1072, Aug. 2013.

[7] X. Xu *et al.*, “Dynamic Glucose-Enhanced (DGE) MRI: Translation to Human Scanning and First Results in Glioma Patients.,” *Tomogr. (Ann Arbor, Mich.)*, vol. 1, no. 2, pp. 105–114, Dec. 2015.

[8] P. Z. Sun, Y. Murata, J. Lu, X. Wang, E. H. Lo, and a. G. Sorensen, “Relaxation-compensated fast multislice amide proton transfer (APT) imaging of acute ischemic stroke,” *Magn. Reson. Med.*, vol. 59, no. 5, pp. 1175–1182, 2008.

[9] W. Ling, R. R. Regatte, G. Navon, and A. Jerschow, “Assessment of glycosaminoglycan concentration in vivo by chemical exchange-dependent saturation transfer (gagCEST).,” *Proc. Natl. Acad. Sci. U. S. A.*, vol. 105, no. 7, pp. 2266–70, Feb. 2008.

[10] A. Müller-lutz, C. Schleich, G. Pentang, B. Schmitt, and G. Antoch, “Magnetic Resonance gagCEST Imaging of the Human Lumbar Intervertebral Disc,” *Clin. Orthop. Imaging*, pp. 3–6, 2014.

[11] T. Towse *et al.*, “In Vivo Human Skeletal Muscle Glycogen Measured by Chemical Exchange Saturation Transfer (GlycoCEST) and 13 C MRS at 7T,” *Proc. Intl. Soc. Mag. Reson. Med.*, vol. 18, p. 415, 2010.

[12] P. C. M. van Zijl, C. K. Jones, J. Ren, C. R. Malloy, and a D. Sherry, “MRI detection of glycogen in vivo by using chemical exchange saturation transfer imaging (glycoCEST).,” *Proc. Natl. Acad. Sci. U. S. A.*, vol. 104, no. 11, pp. 4359–64, Mar. 2007.

[13] S. Aime, D. Delli Castelli, and E. Terreno, “Highly sensitive MRI chemical exchange saturation transfer agents using liposomes,” *Angew. Chemie - Int. Ed.*, vol. 44, no. 34, pp. 5513–5515, 2005.

[14] K. Cai *et al.*, “Mapping glutamate in subcortical brain structures using high-resolution GluCEST MRI.,” *NMR Biomed.*, vol. 26, no. 10, pp. 1278–84, Oct. 2013.

[15] C. Witte *et al.*, “Live-cell MRI with Xenon Hyper-CEST Biosensors Targeted to Metabolically Labeled Cell-Surface Glycans,” *Angew. Chemie Int. Ed.*, vol. 54, no. 9, pp.

2806–2810, Feb. 2015.

[16] I. Hancu, W. T. Dixon, M. Woods, E. Vinogradov, a D. Sherry, and R. E. Lenkinski, “CEST and PARACEST MR contrast agents.,” *Acta Radiol.*, vol. 51, no. 8, pp. 910–23, Oct. 2010.

[17] M. Haris, K. Cai, A. Singh, H. Hariharan, and R. Reddy, “In vivo mapping of brain myo-inositol.,” *Neuroimage*, vol. 54, no. 3, pp. 2079–85, Feb. 2011.

[18] C. K. Jones, M. J. Schlosser, P. C. M. van Zijl, M. G. Pomper, X. Golay, and J. Zhou, “Amide proton transfer imaging of human brain tumors at 3T.,” *Magn. Reson. Med.*, vol. 56, no. 3, pp. 585–92, Sep. 2006.

[19] J. Zhou *et al.*, “Practical data acquisition method for human brain tumor amide proton transfer (APT) imaging.,” *Magn. Reson. Med.*, vol. 60, no. 4, pp. 842–9, Oct. 2008.

[20] P. Z. Sun, T. Benner, A. Kumar, and a. G. Sorensen, “Investigation of optimizing and translating pH-sensitive pulsed-chemical exchange saturation transfer (CEST) imaging to a 3T clinical scanner,” *Magn. Reson. Med.*, vol. 60, no. 4, pp. 834–841, Oct. 2008.

[21] R. Scheidegger, E. T. Wong, and D. C. Alsop, “Contributors to contrast between glioma and brain tissue in chemical exchange saturation transfer sensitive imaging at 3Tesla,” *Neuroimage*, vol. 99, pp. 256–268, 2014.

[22] J. Yuan *et al.*, “Amide proton transfer-weighted imaging of the head and neck at 3 T: a feasibility study on healthy human subjects and patients with head and neck cancer.,” *NMR Biomed.*, vol. 27, no. 10, pp. 1239–47, Oct. 2014.

[23] G. Jia *et al.*, “Amide proton transfer MR imaging of prostate cancer: a preliminary study.,” *J. Magn. Reson. Imaging*, vol. 33, no. 3, pp. 647–54, Mar. 2011.

[24] Y. Takayama *et al.*, “Amide proton transfer (APT) magnetic resonance imaging of prostate cancer: comparison with Gleason scores,” *Magn. Reson. Mater. Physics, Biol. Med.*, vol. 29, no. 4, pp. 671–679, 2016.

[25] A. W. Overhauser, “Polarization of Nuclei in Metals,” *Phys. Rev.*, vol. 92, no. 2, pp. 411–415, Oct. 1953.

[26] E. Vinogradov, A. D. Sherry, and R. E. Lenkinski, “CEST: from basic principles to applications, challenges and opportunities,” *J. Magn. Reson.*, pp. 155–172, 2013.

[27] S. Forsén and R. Hoffman, “Study of Moderately Rapid Chemical Exchange Reactions by Means of Nuclear Magnetic Double Resonance,” *J. Chem. Phys.*, vol. 39, no. 11, pp. 2892–2901, 1963.

[28] F. Kogan, H. Hariharan, and R. Reddy, “Chemical Exchange Saturation Transfer (CEST) Imaging: Description of Technique and Potential Clinical Applications,” *Curr Radiol Rep*, pp. 102–114, 2013.

[29] A. D. Bain, “Modern Magnetic Resonance,” G. A. Webb, Ed. Dordrecht: Springer Netherlands, 2006, pp. 421–427.

[30] E. Liepinsh and G. Otting, “Proton exchange rates from amino acid side chains--implications for image contrast.,” *Magn. Reson. Med.*, vol. 35, no. 1, pp. 30–42, 1996.

[31] G. K. Schwalfenberg, “The alkaline diet: is there evidence that an alkaline pH diet

benefits health?," *J. Environ. Public Health*, vol. 2012, p. 727630, 2012.

[32] N. McVicar *et al.*, "Quantitative tissue pH measurement during cerebral ischemia using amine and amide concentration-independent detection (AACID) with MRI," *J. Cereb. Blood Flow Metab.*, vol. 34, no. 4, pp. 690–698, 2014.

[33] X. Zhang, Y. Lin, and R. J. Gillies, "Tumor pH and its measurement.," *J. Nucl. Med.*, vol. 51, no. 8, pp. 1167–70, 2010.

[34] P. Z. Sun, J. Cheung, E. Wang, and E. Lo, "Association between pH-weighted endogenous amide proton chemical exchange saturation transfer MRI and tissue lactic acidosis during acute ischemic stroke.," *J. Cereb. blood flow Metab.*, vol. 31, no. 8, pp. 1743–50, 2011.

[35] P. Z. Sun, J. Zhou, W. Sun, J. Huang, and P. C. M. van Zijl, "Detection of the ischemic penumbra using pH-weighted MRI.," *J. Cereb. Blood Flow Metab.*, vol. 27, no. 6, pp. 1129–1136, 2007.

[36] T. Jin, P. Wang, X. Zong, and S. G. Kim, "MR imaging of the amide-proton transfer effect and the pH-insensitive nuclear overhauser effect at 9.4 T," *Magn. Reson. Med.*, vol. 69, no. 3, pp. 760–770, 2013.

[37] M. Zaiss, G. Angelovski, E. Demetriou, M. T. McMahon, X. Golay, and K. Scheffler, "QUESP and QUEST revisited - fast and accurate quantitative CEST experiments," *Magn. Reson. Med.*, vol. 79, no. 3, pp. 1708–1721, Mar. 2018.

[38] M. T. McMahon, A. a. Gilad, J. Zhou, P. Z. Sun, J. W. M. Bulte, and P. C. M. Van Zijl, "Quantifying exchange rates in chemical exchange saturation transfer agents using the saturation time and saturation power dependencies of the magnetization transfer effect on the magnetic resonance imaging signal (QUEST and QUESP): pH calibration for poly," *Magn. Reson. Med.*, vol. 55, no. 4, pp. 836–847, 2006.

[39] K. M. Ward and R. S. Balaban, "Determination of pH using water protons and Chemical Exchange Dependent Saturation Transfer (CEST)," *Magn. Reson. Med.*, vol. 44, no. 5, pp. 799–802, 2000.

[40] X.-Y. Zhang *et al.*, "A new NOE-mediated MT signal at around −1.6ppm for detecting ischemic stroke in rat brain," *Magn. Reson. Imaging*, vol. 34, no. 8, pp. 1100–1106, Oct. 2016.

[41] M. Zaiss *et al.*, "Downfield-NOE-suppressed amide-CEST-MRI at 7 Tesla provides a unique contrast in human glioblastoma," *Magn. Reson. Med.*, vol. 00, no. June 2015, p. n/a-n/a, 2016.

[42] "Illustration: Hydration layers around a macromolecule." [Online]. Available: http://mri-q.com/macromolecule-effects.html. [Accessed: 16-Oct-2018].

[43] S. D. Swanson, D. I. Malyarenko, M. L. Fabiilli, R. C. Welsh, J.-F. Nielsen, and A. Srinivasan, "Molecular, dynamic, and structural origin of inhomogeneous magnetization transfer in lipid membranes," *Magn. Reson. Med.*, vol. 77, no. 3, pp. 1318–1328, Mar. 2017.

[44] J. Hua, C. K. Jones, J. Blakeley, S. A. Smith, P. C. M. van Zijl, and J. Zhou, "Quantitative

description of the asymmetry in magnetization transfer effects around the water resonance in the human brain," *Magn. Reson. Med.*, vol. 58, no. 4, pp. 786–793, Oct. 2007.

[45] P. C. M. van Zijl, A. A. Sehgal, P. C. M. Zijl, and A. A. Sehgal, "Proton Chemical Exchange Saturation Transfer (CEST) MRS and MRI," in *eMagRes*, Chichester, UK: John Wiley & Sons, Ltd, 2016, pp. 1307–1332.

[46] E. S. Yoshimaru, E. A. Randtke, M. D. Pagel, and J. Cárdenas-Rodríguez, "Design and optimization of pulsed Chemical Exchange Saturation Transfer MRI using a multiobjective genetic algorithm," *J. Magn. Reson.*, vol. 263, pp. 184–192, 2015.

[47] X.-Y. Zhang *et al.*, "MR imaging of a novel NOE-mediated magnetization transfer with water in rat brain at 9.4 T," *Magn. Reson. Med.*, vol. 78, no. 2, pp. 588–597, Aug. 2017.

[48] K. J. Ray *et al.*, "Determination of an optimally sensitive and specific chemical exchange saturation transfer MRI quantification metric in relevant biological phantoms," 2016.

[49] M. Zaiss, B. Schmitt, and P. Bachert, "Quantitative separation of CEST effect from magnetization transfer and spillover effects by Lorentzian-line-fit analysis of z-spectra," *J. Magn. Reson.*, vol. 211, no. 2, pp. 149–155, 2011.

[50] K. L. Desmond, F. Moosvi, and G. J. Stanisz, "Mapping of amide, amine, and aliphatic peaks in the CEST spectra of murine xenografts at 7 T," *Magn. Reson. Med.*, vol. 1853, pp. 1841–1853, 2013.

[51] M. Zaiss and P. Bachert, "Chemical exchange saturation transfer (CEST) and MR *Z* -spectroscopy *in vivo* : a review of theoretical approaches and methods," *Phys. Med. Biol.*, vol. 58, no. 22, pp. R221–R269, Nov. 2013.

[52] K. Cai *et al.*, "CEST signal at 2 ppm (CEST@2ppm) from Z -spectral fitting correlates with creatine distribution in brain tumor," *NMR Biomed.*, no. August 2014, p. n/a-n/a, 2014.

[53] R. M. Henkelman, G. J. Stanisz, and S. J. Graham, "Magnetization transfer in MRI: a review," *NMR Biomed.*, vol. 14, no. 2, pp. 57–64, Apr. 2001.

[54] J. G. Sled and G. B. Pike, "Quantitative imaging of magnetization transfer exchange and relaxation properties in vivo using MRI.," *Magn. Reson. Med.*, vol. 46, no. 5, pp. 923–31, Nov. 2001.

[55] J.-E. Meissner, J. Windschuh, M. Zaiss, D. Paech, A. Radbruch, and P. Bachert, "Multi-pool CEST imaging of glioblastoma at 7T," in *Proc. Intl. Soc. Mag. Reson. Med.*, 2014, vol. 22, p. 3152.

[56] M. Kim, J. Gillen, B. a Landman, J. Zhou, and P. C. M. van Zijl, "Water saturation shift referencing (WASSR) for chemical exchange saturation transfer (CEST) experiments.," *Magn. Reson. Med.*, vol. 61, no. 6, pp. 1441–50, Jun. 2009.

[57] P. Schuenke, J. Windschuh, V. Roeloffs, M. E. Ladd, P. Bachert, and M. Zaiss, "Simultaneous mapping of water shift and B $_1$ (WASABI)-Application to field-Inhomogeneity correction of CESTMRI data," *Magn. Reson. Med.*, vol. 00, p. n/a-n/a, 2016.

[58] A. Singh, K. Cai, M. Haris, H. Hariharan, and R. Reddy, “On B1 inhomogeneity correction of in vivo human brain glutamate chemical exchange saturation transfer contrast at 7T.,” *Magn. Reson. Med.*, vol. 69, no. 3, pp. 818–24, Mar. 2013.

[59] P. Z. Sun, C. T. Farrar, and a. G. Sorensen, “Correction for artifacts induced by B0 and B1 field inhomogeneities in pH-sensitive chemical exchange saturation transfer (CEST) imaging,” *Magn. Reson. Med.*, vol. 58, no. 6, pp. 1207–1215, 2007.

[60] P. Z. Sun, I. Y. Zhou, T. Igarashi, Y. Guo, G. Xiao, and R. Wu, “Simplified correction of B $_1$ inhomogeneity for chemical exchange saturation transfer (CEST) MRI measurement with surface transceiver coil,” vol. 9417, p. 94171H, 2015.

[61] K. M. Jones, A. C. Pollard, and M. D. Pagel, “Clinical applications of chemical exchange saturation transfer (CEST) MRI,” *J. Magn. Reson. Imaging*, vol. 47, no. 1, pp. 11–27, 2018.

[62] D. Hanahan and R. A. Weinberg, “The Hallmarks of Cancer,” *Cell*, vol. 100, pp. 57–70, 2000.

[63] D. Hanahan and R. A. Weinberg, “Hallmarks of cancer: the next generation.,” *Cell*, vol. 144, no. 5, pp. 646–74, Mar. 2011.

[64] N. N. Pavlova and C. B. Thompson, “Perspective The Emerging Hallmarks of Cancer Metabolism,” *Cell Metab.*, vol. 23, no. 1, pp. 27–47, 2016.

[65] B. P. Lucey, W. A. Nelson-Rees, and G. M. Hutchins, “HeLa Cells and Cell Culture Contamination-Lucey et al 1463,” 2009.

[66] M. G. Vander Heiden, L. C. Cantley, and C. B. Thompson, “Understanding the Warburg Effect: The Metabolic Requirements of Cell Proliferation,” *Science (80-.).*, vol. 324, no. 5930, pp. 1029–1033, 2009.

[67] T. Pfeiffer, S. Schuster, and S. Bonhoeffer, “Cooperation and Competition in the Evolution of ATP-Producing Pathways Cooperation and Competition in the Evolution of ATP-Producing Pathways,” *Science (80-.).*, vol. 292, no. April 2001, pp. 504–508, 2001.

[68] A. Snyder, “Donald F Gleason,” *Lancet*, vol. 373, no. 9663, p. 540, Feb. 2009.

[69] J. I. Epstein, W. C. Allsbrook, M. B. Amin, L. L. Egevad, and I. G. Committee, “Words of wisdom. The 2005 International Society of Urological Pathology (ISUP) Consensus Conference on Gleason Grading of Prostatic Carcinoma.,” *Eur. Urol.*, vol. 49, no. 4, pp. 758–759, 2006.

[70] J. I. Epstein, L. Egevad, M. B. Amin, B. Delahunt, J. R. Srigley, and P. A. Humphrey, “The 2014 International Society of Urological Pathology (ISUP) Consensus Conference on Gleason Grading of Prostatic Carcinoma,” *Am. J. Surg. Pathol.*, p. 1, Oct. 2015.

[71] N. Chen and Q. Zhou, “The evolving Gleason grading system.,” *Chin. J. Cancer Res.*, vol. 28, no. 1, pp. 58–64, Feb. 2016.

[72] B. Delahunt, R. J. Miller, J. R. Srigley, A. J. Evans, and H. Samaratunga, “Gleason grading: past, present and future,” *Histopathology*, vol. 60, no. 1, pp. 75–86, Jan. 2012.

[73] P. Harnden, M. D. Shelley, B. Coles, J. Staffurth, and M. D. Mason, “Should the Gleason grading system for prostate cancer be modified to account for high-grade tertiary

components? A systematic review and meta-analysis," *Lancet Oncol.*, vol. 8, no. 5, pp. 411–419, May 2007.

[74] J. L. Wright *et al.*, "Prostate cancer specific mortality and Gleason 7 disease differences in prostate cancer outcomes between cases with Gleason 4 + 3 and Gleason 3 + 4 tumors in a population based cohort.," *J. Urol.*, vol. 182, no. 6, pp. 2702–7, Dec. 2009.

[75] J. McBride and National Institute for Health and Care Excellence (Great Britain), *Prostate cancer : diagnosis and treatment*. National Institute for Health and Care Excellence, 2014.

[76] J. O. Barentsz *et al.*, "ESUR prostate MR guidelines 2012," *Eur. Radiol.*, vol. 22, no. 4, pp. 746–757, 2012.

[77] J. G. R. Bomers and J. O. Barentsz, "Standardization of multiparametric prostate MR imaging using PI-RADS.," *Biomed Res. Int.*, vol. 2014, p. 431680, 2014.

[78] H. U. Ahmed *et al.*, "Diagnostic accuracy of multi-parametric MRI and TRUS biopsy in prostate cancer (PROMIS): a paired validating confirmatory study.," *Lancet (London, England)*, vol. 389, no. 10071, pp. 815–822, Feb. 2017.

[79] T. Harada *et al.*, "Five-point Likert scaling on MRI predicts clinically significant prostate carcinoma.," *BMC Urol.*, vol. 15, p. 91, Sep. 2015.

[80] V. Kasivisvanathan *et al.*, "MRI-Targeted or Standard Biopsy for Prostate-Cancer Diagnosis," *N. Engl. J. Med.*, vol. 378, no. 19, pp. 1767–1777, May 2018.

[81] V. S. Evans *et al.*, "Optimization and Repeatability of Multipool Chemical Exchange Saturation Transfer MRI of the Prostate at 3.0 T," *J. Magn. Reson. Imaging*, p. jmri.26690, Feb. 2019.

[82] G. Jia *et al.*, "Amide proton transfer MR imaging of prostate cancer: a preliminary study," *J. Magn. Reson. Imaging*, vol. 33, no. 3, pp. 647–654, 2011.

[83] Q. T. Ostrom *et al.*, "The epidemiology of glioma in adults: a &quot;state of the science&quot; review," *Neuro. Oncol.*, vol. 16, no. 7, pp. 896–913, Jul. 2014.

[84] N. Upadhyay and A. D. Waldman, "Conventional MRI evaluation of gliomas," *Br. J. Radiol.*, vol. 84, no. special_issue_2, pp. S107–S111, Dec. 2011.

[85] S. C. Thust, M. J. van den Bent, and M. Smits, "Pseudoprogression of brain tumors.," *J. Magn. Reson. Imaging*, vol. 48, no. 3, p. 571, May 2018.

[86] B. Ma *et al.*, "Applying amide proton transfer-weighted MRI to distinguish pseudoprogression from true progression in malignant gliomas.," *J. Magn. Reson. Imaging*, vol. 44, no. 2, pp. 456–62, 2016.

[87] H. Mehrabian, K. L. Desmond, H. Soliman, A. Sahgal, and G. J. Stanisz, "Differentiation between Radiation Necrosis and Tumor Progression Using Chemical Exchange Saturation Transfer," *Clin. Cancer Res.*, vol. 23, no. 14, pp. 3667–3675, Jul. 2017.

[88] I. Y. Zhou, E. Wang, J. S. Cheung, X. Zhang, G. Fulci, and P. Z. Sun, "Quantitative chemical exchange saturation transfer (CEST) MRI of glioma using Image Downsampling Expedited Adaptive Least-squares (IDEAL) fitting.," *Sci. Rep.*, vol. 7, no. 1, p. 84, 2017.

[89] A. Deshmane *et al.*, “3D gradient echo snapshot CEST MRI with low power saturation for human studies at 3T,” *Magn. Reson. Med.*, Nov. 2018.

[90] R. J. Harris *et al.*, “pH-weighted molecular imaging of gliomas using amine chemical exchange saturation transfer MRI.,” *Neuro. Oncol.*, vol. 17, no. 11, pp. 1514–24, Nov. 2015.

[91] H.-Y. Heo *et al.*, “Whole-Brain Amide Proton Transfer (APT) and Nuclear Overhauser enhancement (NOE) Imaging in Glioma Patients Using Low-Power Steady-State Pulsed CEST Imaging at 7T HHS Public Access,” *J Magn Reson Imaging*, vol. 44, no. 1, pp. 41–50, 2016.

[92] C. Su *et al.*, “Amide Proton Transfer Imaging Allows Detection of Glioma Grades and Tumor Proliferation: Comparison with Ki-67 Expression and Proton MR Spectroscopy Imaging.,” *AJNR. Am. J. Neuroradiol.*, vol. 38, no. 9, pp. 1702–1709, Sep. 2017.

[93] J. E. Park, H. S. Kim, K. J. Park, S. J. Kim, J. H. Kim, and S. A. Smith, “Pre- and Posttreatment Glioma: Comparison of Amide Proton Transfer Imaging with MR Spectroscopy for Biomarkers of Tumor Proliferation,” *Radiology*, vol. 278, no. 2, pp. 514–523, Feb. 2016.

[94] L. Dang *et al.*, “Cancer-associated IDH1 mutations produce 2-hydroxyglutarate.,” *Nature*, vol. 462, no. 7274, pp. 739–44, 2009.

[95] T. L. Perry, S. Hansen, K. Berry, C. Mok, and D. Lesk, “Free Amino Acids and Related Compounds in Biopsies of Human Brain,” *J. Neurochem.*, vol. 18, no. 3, pp. 521–528, 1971.

[96] D. Paech *et al.*, “Assessing the predictability of IDH mutation and MGMT methylation status in glioma patients using relaxation-compensated multipool CEST MRI at 7.0 T,” *Neuro. Oncol.*, vol. 20, no. 12, pp. 1661–1671, 2018.

[97] B. M. Ellingson *et al.*, “Consensus recommendations for a standardized Brain Tumor Imaging Protocol in clinical trials.,” *Neuro. Oncol.*, vol. 17, no. 9, pp. 1188–98, Sep. 2015.

[98] D. Abergel and A. G. Palmer, “Approximate Solutions of the Bloch–McConnell Equations for Two-Site Chemical Exchange,” *ChemPhysChem*, vol. 5, no. 6, pp. 787–793, Jun. 2004.

[99] M. Zaiss *et al.*, “A combined analytical solution for chemical exchange saturation transfer and semi-solid magnetization transfer,” *NMR Biomed.*, vol. 28, no. 2, pp. 217–230, Feb. 2015.

[100] T. Jin, J. Autio, T. Obata, and S.-G. Kim, “Spin-locking versus chemical exchange saturation transfer MRI for investigating chemical exchange process between water and labile metabolite protons.,” *Magn. Reson. Med.*, vol. 65, no. 5, pp. 1448–60, May 2011.

[101] “Anatomy of the Prostate Gland | Johns Hopkins Medicine Health Library.” [Online]. Available: https://www.hopkinsmedicine.org/healthlibrary/conditions/prostate_health/anatomy_of_the_prostate_gland_85,P01257. [Accessed: 11-Feb-2019].

[102] S. W. Hayward and G. R. Cunha, “THE PROSTATE: DEVELOPMENT AND PHYSIOLOGY,” *Radiol. Clin. North Am.*, vol. 38, no. 1, pp. 1–14, Jan. 2000.

[103] “The prostate - Canadian Cancer Society.” [Online]. Available: http://www.cancer.ca/en/cancer-information/cancer-type/prostate/prostate-cancer/the-prostate/?region=on. [Accessed: 11-Feb-2019].

[104] S. J. Berry, D. S. Coffey, P. C. Walsh, and L. L. Ewing, “The Development of Human Benign Prostatic Hyperplasia with Age,” *J. Urol.*, vol. 132, no. 3, pp. 474–479, Sep. 1984.

[105] H.-Y. Heo *et al.*, “Whole-brain amide proton transfer (APT) and nuclear overhauser enhancement (NOE) imaging in glioma patients using low-power steady-state pulsed chemical exchange saturation transfer (CEST) imaging at 7T,” *J. Magn. Reson. Imaging*, vol. 44, no. 1, pp. 41–50, Jul. 2016.

[106] C. K. Jones *et al.*, “Nuclear Overhauser enhancement (NOE) imaging in the human brain at 7T.,” *Neuroimage*, vol. 77, pp. 114–24, Aug. 2013.

[107] M.-C. Ng, J. Hua, Y. Hu, K. D. Luk, and E. Y. Lam, “Magnetization transfer (MT) asymmetry around the water resonance in human cervical spinal cord.,” *J. Magn. Reson. Imaging*, vol. 29, no. 3, pp. 523–8, Mar. 2009.

[108] P. C. M. van Zijl, W. W. Lam, J. Xu, L. Knutsson, and G. J. Stanisz, “Magnetization Transfer Contrast and Chemical Exchange Saturation Transfer MRI. Features and analysis of the field-dependent saturation spectrum,” *Neuroimage*, Apr. 2017.

[109] C. M. J. de Bazelaire, G. D. Duhamel, N. M. Rofsky, and D. C. Alsop, “MR Imaging Relaxation Times of Abdominal and Pelvic Tissues Measured in Vivo at 3.0 T: Preliminary Results,” *Radiology*, vol. 230, no. 3, pp. 652–659, Mar. 2004.

[110] J. Martin Bland and D. Altman, “STATISTICAL METHODS FOR ASSESSING AGREEMENT BETWEEN TWO METHODS OF CLINICAL MEASUREMENT,” *Lancet*, vol. 327, no. 8476, pp. 307–310, Feb. 1986.

[111] A. Fedorov, M. G. Vangel, C. M. Tempany, and F. M. Fennessy, “Multiparametric Magnetic Resonance Imaging of the Prostate: Repeatability of Volume and Apparent Diffusion Coefficient Quantification.,” *Invest. Radiol.*, vol. 52, no. 9, pp. 538–546, 2017.

[112] L. R. Arlinghaus, R. D. Dortch, J. G. Whisenant, H. Kang, R. G. Abramson, and T. E. Yankeelov, “Quantitative Magnetization Transfer Imaging of the Breast at 3.0 T: Reproducibility in Healthy Volunteers.,” *Tomogr. (Ann Arbor, Mich.)*, vol. 2, no. 4, pp. 260–266, Dec. 2016.

[113] T. Barrett *et al.*, “Diagnostic evaluation of magnetization transfer and diffusion kurtosis imaging for prostate cancer detection in a re-biopsy population,” *Eur. Radiol.*, vol. 28, no. 8, pp. 3141–3150, Aug. 2018.

[114] A. N. Dula *et al.*, “Amide proton transfer imaging of the breast at 3 T: Establishing reproducibility and possible feasibility assessing chemotherapy response,” *Magn. Reson. Med.*, vol. 70, no. 1, pp. 216–224, 2013.

[115] J. Yuan *et al.*, “Amide proton transfer-weighted imaging of the head and neck at 3 T: a

feasibility study on healthy human subjects and patients with head and neck cancer," *NMR Biomed.*, vol. 27, no. 10, pp. 1239–1247, Oct. 2014.

[116] T. Wech and H. K€ Ostler, "Robust motion correction in CEST imaging exploiting low-rank approximation of the z-spectrum Magnetic Resonance in Medicine."

[117] O. Togao *et al.*, "Scan-rescan reproducibility of parallel transmission based amide proton transfer imaging of brain tumors," *J. Magn. Reson. Imaging*, vol. 42, no. 5, pp. 1346–1353, Nov. 2015.

[118] C. H. Pernar, E. M. Ebot, K. M. Wilson, and L. A. Mucci, "The Epidemiology of Prostate Cancer," *Cold Spring Harb. Perspect. Med.*, vol. 8, no. 12, p. a030361, Dec. 2018.

[119] H. Grönberg, "Prostate cancer epidemiology," *Lancet*, vol. 361, no. 9360, pp. 859–864, Mar. 2003.

[120] R. S. Kelly, M. G. Vander Heiden, E. Giovannucci, and L. A. Mucci, "Metabolomic Biomarkers of Prostate Cancer: Prediction, Diagnosis, Progression, Prognosis, and Recurrence.," *Cancer Epidemiol. Biomarkers Prev.*, vol. 25, no. 6, pp. 887–906, 2016.

[121] H. Augustin *et al.*, "Biochemical recurrence following radical prostatectomy: a comparison between prostate cancers located in different anatomical zones.," *Prostate*, vol. 55, no. 1, pp. 48–54, Apr. 2003.

[122] M. E. Chen, D. A. Johnston, K. Tang, R. J. Babaian, and P. Troncoso, "Detailed mapping of prostate carcinoma foci," *Cancer*, vol. 89, no. 8, pp. 1800–1809, Oct. 2000.

[123] J. E. McNeal, E. A. Redwine, F. S. Freiha, and T. A. Stamey, "Zonal distribution of prostatic adenocarcinoma. Correlation with histologic pattern and direction of spread.," *Am. J. Surg. Pathol.*, vol. 12, no. 12, pp. 897–906, Dec. 1988.

[124] R. J. Cohen, B. A. Shannon, M. Phillips, R. E. Moorin, T. M. Wheeler, and K. L. Garrett, "Central Zone Carcinoma of the Prostate Gland: A Distinct Tumor Type With Poor Prognostic Features," *J. Urol.*, vol. 179, no. 5, pp. 1762–1767, May 2008.

[125] J. C. Weinreb *et al.*, "PI-RADS Prostate Imaging – Reporting and Data System: 2015, Version 2," *Eur. Urol.*, vol. 69, no. 1, pp. 16–40, Jan. 2016.

[126] "PI-RADS | American College of Radiology." [Online]. Available: https://www.acr.org/Clinical-Resources/Reporting-and-Data-Systems/PI-RADS. [Accessed: 12-Feb-2019].

[127] K. L. Wallitt, S. R. Khan, S. Dubash, H. H. Tam, S. Khan, and T. D. Barwick, "Clinical PET Imaging in Prostate Cancer," *RadioGraphics*, vol. 37, no. 5, pp. 1512–1536, Sep. 2017.

[128] A. Briganti *et al.*, "Active Surveillance for Low-risk Prostate Cancer: The European Association of Urology Position in 2018.," *Eur. Urol.*, vol. 74, no. 3, pp. 357–368, Sep. 2018.

[129] G. L. Lu-Yao *et al.*, "Fifteen-Year Survival Outcomes Following Primary Androgen-Deprivation Therapy for Localized Prostate Cancer," *JAMA Intern. Med.*, vol. 174, no. 9, p. 1460, Sep. 2014.

[130] J. C. Weinreb *et al.*, "Prostate Cancer: Sextant Localization at MR Imaging and MR

Spectroscopic Imaging before Prostatectomy—Results of ACRIN Prospective Multi-institutional Clinicopathologic Study," *Radiology*, vol. 251, no. 1, pp. 122–133, Apr. 2009.

[131] B. Birdsall, J. Feeney, and P. Partington, "Ionisation, self association, and proton exchange studies of nicotinamide in aqueous solution using nuclear magnetic resonance spectroscopy," *J. Chem. Soc. Perkin Trans. 2*, vol. 0, no. 15, p. 2145, Jan. 1973.

[132] A. Kujawa *et al.*, "Assessment of a clinically feasible Bayesian fitting algorithm using a simplified description of Chemical Exchange Saturation Transfer (CEST) imaging," *J. Magn. Reson.*, vol. 300, pp. 120–134, Mar. 2019.

[133] "Nicotinamide(98-92-0)1HNMR." [Online]. Available: https://www.chemicalbook.com/SpectrumEN_98-92-0_1HNMR.htm. [Accessed: 18-Feb-2019].

[134] Z. Zu, V. a. Janve, J. Xu, M. D. Does, J. C. Gore, and D. F. Gochberg, "A new method for detecting exchanging amide protons using chemical exchange rotation transfer," *Magn. Reson. Med.*, vol. 69, no. 3, pp. 637–647, 2013.

[135] F. Torrealdea, M. Rega, M. Tachrount, M. Sokolska, and X. Golay, "Understanding concomitant effects between CEST and ASL contrast," in *Proc. Intl. Soc. Mag. Reson. Med. 25 Abstract 0200*, 2017.

[136] J. Wang *et al.*, "Magnetic Resonance Imaging of Glucose Uptake and Metabolism in Patients with Head and Neck Cancer," *Sci. Rep.*, vol. 6, no. April, p. 30618, 2016.

[137] X. Xu *et al.*, "Dynamic Glucose-Enhanced (DGE) MRI: Translation to Human Scanning and First Results in Glioma Patients," *Tomography*, vol. 1, no. 2, pp. 105–114, Dec. 2015.

[138] J. M. HARVEY, M. C. R. SYMONS, and R. J. NAFTALIN, "Proton magnetic resonance study of the hydration of glucose," *Nature*, vol. 261, p. 435, Jun. 1976.

[139] J. A. Detre, J. S. Leigh, D. S. Williams, and A. P. Koretsky, "Perfusion imaging," *Magn. Reson. Med.*, vol. 23, no. 1, pp. 37–45, Jan. 1992.

[140] D. S. Williams, J. A. Detre, J. S. Leigh, and A. P. Koretsky, "Magnetic resonance imaging of perfusion using spin inversion of arterial water.," *Proc. Natl. Acad. Sci. U. S. A.*, vol. 89, no. 1, pp. 212–6, Jan. 1992.

[141] D. C. Alsop *et al.*, "Recommended implementation of arterial spin-labeled perfusion MRI for clinical applications: A consensus of the ISMRM perfusion study group and the European consortium for ASL in dementia.," *Magn. Reson. Med.*, vol. 73, no. 1, pp. 102–16, Jan. 2015.

[142] E. C. Wong, "An introduction to ASL labeling techniques," *J. Magn. Reson. Imaging*, vol. 40, no. 1, pp. 1–10, Jul. 2014.

[143] X. Golay, J. Hendrikse, and T. C. C. Lim, "Perfusion Imaging Using Arterial Spin Labeling," 2004.

[144] W. Dai, D. Garcia, C. de Bazelaire, and D. C. Alsop, "Continuous flow-driven inversion for arterial spin labeling using pulsed radio frequency and gradient fields," *Magn. Reson. Med.*, vol. 60, no. 6, pp. 1488–1497, Dec. 2008.

[145] Y. Liu, Y. Gu, and X. Yu, “Assessing tissue metabolism by phosphorous-31 magnetic resonance spectroscopy and imaging: a methodology review.,” *Quant. Imaging Med. Surg.*, vol. 7, no. 6, pp. 707–726, Dec. 2017.

[146] J. Ren, A. D. Sherry, and C. R. Malloy, “^{31} P-MRS of healthy human brain: ATP synthesis, metabolite concentrations, pH, and T_1 relaxation times,” *NMR Biomed.*, vol. 28, no. 11, pp. 1455–1462, Nov. 2015.

[147] T. Burt, T. Glonek, and M. Barany, “Analysis of Phosphate Metabolites, the Intracellular pH, and the State of Adenosine Triphosphate in Intact Muscle by Phosphorus Nuclear Magnetic Resonance,” *J. Biol. Chem.*, vol. 251, no. 9, pp. 2584–2591, 1976.

[148] M. E. B. Powell, S. A. Hill, M. I. Saunders, P. J. Hoskin, and D. J. Chaplin, “Effect of carbogen breathing on tumour microregional blood flow in humans,” *Radiother. Oncol.*, vol. 41, no. 3, pp. 225–231, Dec. 1996.

[149] A. Rojas *et al.*, “Radiosensitisation in normal tissues with oxygen, carbogen or nicotinamide: therapeutic gain comparisons for fractionated x-ray schedules,” *Radiother. Oncol.*, vol. 39, no. 1, pp. 53–64, Apr. 1996.

[150] D. J. Honess and N. M. Bleehen, “Perfusion changes in the RIF-1 tumour and normal tissues after carbogen and nicotinamide, individually and combined.,” *Br. J. Cancer*, vol. 71, no. 6, pp. 1175–80, Jun. 1995.

[151] F. Nasrallah, G. Pagès, and P. Kuchel, “Imaging brain deoxyglucose uptake and metabolism by glucoCEST MRI,” *J. Cereb. …*, vol. 33, no. 8, pp. 1270–1278, Aug. 2013.

[152] A. L. Miller, R. A. Hawkins, and R. L. Veech, “DECREASED RATE OF GLUCOSE UTILIZATION BY RAT BRAIN IN VIVO AFTER EXPOSURE TO ATMOSPHERES CONTAINING HIGH CONCENTRATIONS OF CO_2,” *J. Neurochem.*, vol. 25, no. 5, pp. 553–558, Nov. 1975.

[153] S. M. Shah *et al.*, “The z-spectrum from human blood at 7T,” *Neuroimage*, vol. 167, pp. 31–40, Feb. 2018.

[154] Z. Zu, “Toward more reliable measurements of NOE effects in CEST spectra at around −1.6 ppm (NOE (−1.6)) in rat brain,” *Magn. Reson. Med.*, vol. 81, no. 1, pp. 208–219, Jan. 2019.

[155] J. Folbergrovaa, U. Pontean, and B. K. Siesjou, “PATTERNS OF CHANGES IN BRAIN CARBOHYDRATE METABOLITES, AMINO ACIDS AND ORGANIC PHOSPHATES AT INCREASED CARBON DIOXIDE TENSIONS,” *J. Neurochem.*, vol. 22, no. 6, pp. 1115–1125, Jun. 1974.

[156] F. Torrealdea *et al.*, “APT-CEST post Gadolinium. Should it be avoided? Comparison of pre- & post-Gadolinium CEST on glioma at 3T,” in *Proc. Intl. Soc. Mag. Reson. Med. 26*, 2018, p. 5109.

[157] M. Bergamino, L. Barletta, L. Castellan, G. Mancardi, and L. Roccatagliata, “Dynamic Contrast-Enhanced MRI in the Study of Brain Tumors. Comparison Between the Extended Tofts-Kety Model and a Phenomenological Universalities (PUN) Algorithm.,” *J. Digit. Imaging*, vol. 28, no. 6, pp. 748–54, Dec. 2015.

[158] C. L. Merten, H. O. Knitelius, J. Assheuer, B. Bergmann-Kurz, J. P. Hedde, and H. Bewermeyer, “MRI of acute cerebral infarcts, increased contrast enhancement with continuous infusion of gadolinium.,” *Neuroradiology*, vol. 41, no. 4, pp. 242–8, Apr. 1999.

[159] Z. Zhou and Z.-R. Lu, “Gadolinium-based contrast agents for magnetic resonance cancer imaging.,” *Wiley Interdiscip. Rev. Nanomed. Nanobiotechnol.*, vol. 5, no. 1, pp. 1–18, 2013.

[160] X. Zhao *et al.*, “Saturation power dependence of amide proton transfer image contrasts in human brain tumors and strokes at 3 T,” *Magn. Reson. Med.*, 2011.

[161] M. Zaiss, P. Ehses, and K. Scheffler, “Snapshot-CEST: Optimizing spiral-centric-reordered gradient echo acquisition for fast and robust 3D CEST MRI at 9.4 T,” *NMR Biomed.*, vol. 31, no. 4, p. e3879, Apr. 2018.

[162] Y. K. Tee, M. J. Donahue, G. W. J. Harston, S. J. Payne, and M. A. Chappell, “Quantification of amide proton transfer effect pre- and post-gadolinium contrast agent administration,” *J. Magn. Reson. Imaging*, vol. 40, no. 4, pp. 832–838, Oct. 2014.

[163] C. M. J. de Bazelaire, G. D. Duhamel, N. M. Rofsky, and D. C. Alsop, “MR Imaging Relaxation Times of Abdominal and Pelvic Tissues Measured in Vivo at 3.0 T: Preliminary Results,” *Radiology*, vol. 230, no. 3, pp. 652–659, Mar. 2004.

11 Appendix A – Sequence optimization in the prostate at 3.0T

The aim of the optimization was to decide on a set of sequence parameters that would allow for maximum observable fitted peak heights and acceptable fit quality in the shortest amount of time. As with all MRI there were several trade-offs to be made in order to preserve a clinically feasible scan-time. An upper limit on the scan-time was set at 6 minutes. The total scan-time is determined by the product of the dynamic scan time and the number of dynamics. It was estimated that a minimum of 50 dynamics would be required for a reasonable fit, with more to be acquired if possible. Optimization data were acquired on multiple occasions from several healthy volunteers.

11.1.1 Readout

Turbo-spin-echo (TSE) and turbo-field-echo (TFE) readouts were initially compared for image quality. The signal-to-noise ratio (SNR) was higher in the TSE so therefore it was chosen as we are interested in the best-case scenario for CEST repeatability.

11.1.2 Saturation Scheme

11.1.2.1 Dynamic Scan Time and estimate of SNR

The T1 of prostate was taken from [163] to be 1,597 ± 42ms meaning that, with exponential recovery of signal, 99% of signal lost due to the TSE readout will have recovered after 5 x T1 = 7985ms. This was verified experimentally by acquiring unsaturated images with a dynamic scan time of 2, 3, 4, 5 or 6 seconds and evaluating the relative absolute signal acquired in a small prostate ROI. Data are presented in Figure 11-1 normalized to the TR=6s data. The standard deviations of the 39 acquisitions are all less than 1.3% of the mean signal for each respective TR. And the standard deviations are all less than 1.05% of the maximum observed signal of the TR=6s data.

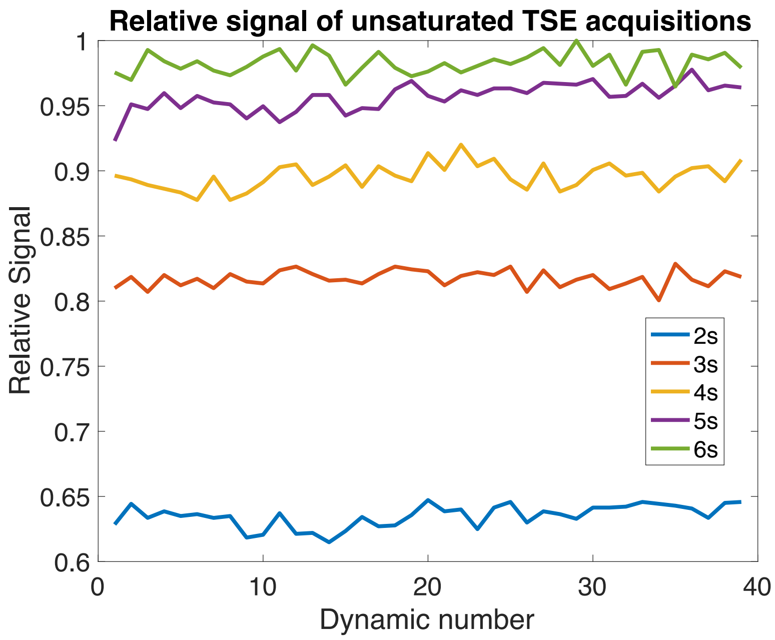

Figure 11-1: *measured signal from repeated measurements for a range of TR values.*

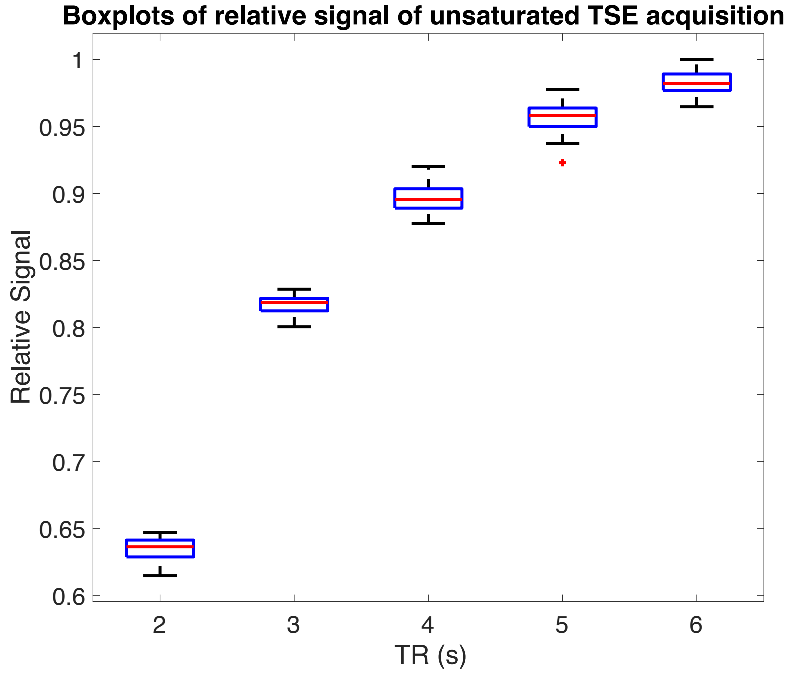

Figure 11-2: *Repeated unsaturated acquisitions showing that longer TR's yield higher absolute signal.*

The 5s and 6s TR data show a similar absolute signal and SNR. As N=60 was seen to be optimal (4800ms of saturation), and the shot length is 245ms, a TR of 5.1s was selected as optimal to allow for an increased offset-frequency sampling rate while preserving absolute signal and the pseudo-steady-state.

11.1.2.2 Offset frequency sampling strategy

Sampling strategies in the literature are varied and application specific. For MTR_{asym} applications, the sampling is typically within the ± 5ppm range, with a reference scan for normalization (although wider sampling ranges are sometimes used). In some cases, to speed up acquisition times, the central region close to 0ppm is excluded. However, for z-spectrum fitting, sampling of the whole z-spectrum is required to ensure that the contribution from the MT pool is able to be fitted. The trade-off is between acquiring finely-sampled data, which allows for improved resolution of peaks in the z-spectrum, and scan-time.

A finely sampled z-spectrum (192 offset frequencies) was acquired on a healthy volunteer. The offset frequencies, centred at 0ppm, were spaced at intervals of 0.125ppm in the ±5ppm range, at intervals of 0.25ppm in the ±(5 to 10)ppm range, at intervals of 1ppm in the ±(10 to 30)ppm range, at intervals of 10ppm in the the ±(30 to 100)ppm range, and at intervals of 25ppm in the the ±(100 to 300)ppm range.

An under-sampling exercise was performed in an effort to understand what offset sampling frequencies were required to ensure consistent fit results. 7 offset ranges were defined – 0 to 1ppm, 1 to 5ppm, 5 to 7.5ppm, 7.5 to 10ppm, 10 to 30ppm, 30 to 100ppm and 100 to 300ppm. Within each range, several possible sampling intervals were defined. The first sampling interval in each range is to use all of the acquired points. The second is to use every second point (counting outwards from 0ppm), then every third point etc. The finally chosen offset frequencies were based on the results from this analysis combined with the requirement that the CEST scan duration be no longer than 6 minutes. [Note: data is not shown for this analysis as it was contained on a laptop which was damaged before having been backed up]

12 Appendix B – ISMRM 2018 (Paris) Interactive e-Poster

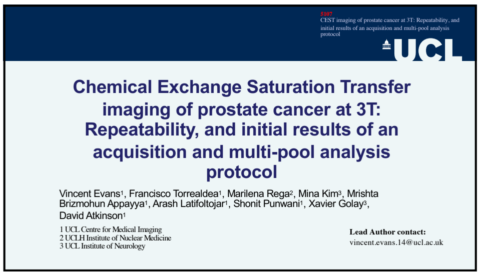

Chemical Exchange Saturation Transfer imaging of prostate cancer at 3T: Repeatability, and initial results of an acquisition and multi-pool analysis protocol

Vincent Evans[1], Francisco Torrealdea[1], Marilena Rega[2], Mina Kim[3], Mrishta Brizmohun Appayya[1], Arash Latifoltojar[1], Shonit Punwani[1], Xavier Golay[3], David Atkinson[1]

1 UCL Centre for Medical Imaging
2 UCLH Institute of Nuclear Medicine
3 UCL Institute of Neurology

Lead Author contact:
vincent.evans.14@ucl.ac.uk

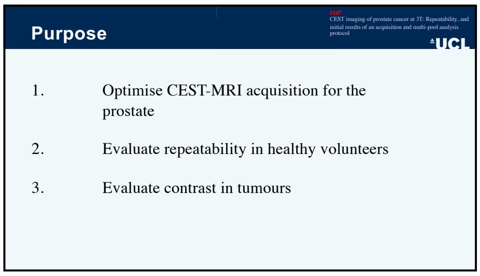

Purpose

1. Optimise CEST-MRI acquisition for the prostate
2. Evaluate repeatability in healthy volunteers
3. Evaluate contrast in tumours

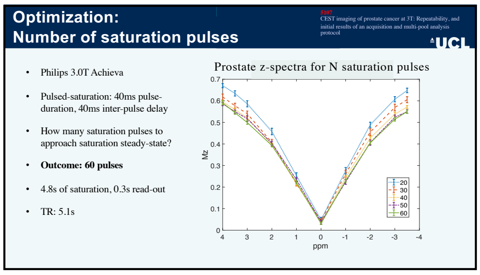

Optimization:
Number of saturation pulses

- Philips 3.0T Achieva
- Pulsed-saturation: 40ms pulse-duration, 40ms inter-pulse delay
- How many saturation pulses to approach saturation steady-state?
- **Outcome: 60 pulses**
- 4.8s of saturation, 0.3s read-out
- TR: 5.1s

Prostate z-spectra for N saturation pulses

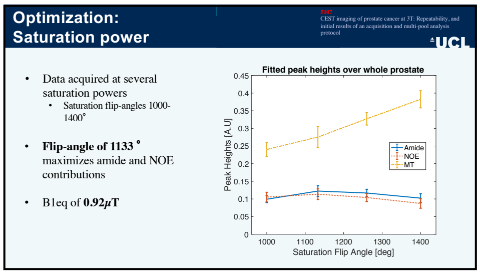

Optimization:
Saturation power

- Data acquired at several saturation powers
  - Saturation flip-angles 1000-1400°
- **Flip-angle of 1133 °** maximizes amide and NOE contributions
- B1eq of **0.92μT**

Fitted peak heights over whole prostate

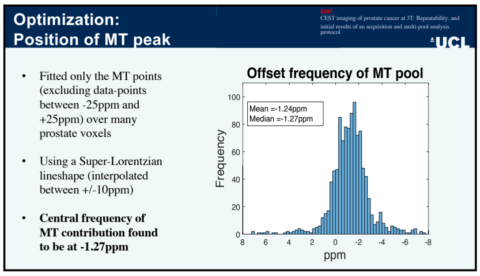

Optimization:
Position of MT peak

- Fitted only the MT points (excluding data-points between -25ppm and +25ppm) over many prostate voxels
- Using a Super-Lorentzian lineshape (interpolated between +/-10ppm)
- **Central frequency of MT contribution found to be at -1.27ppm**

Offset frequency of MT pool

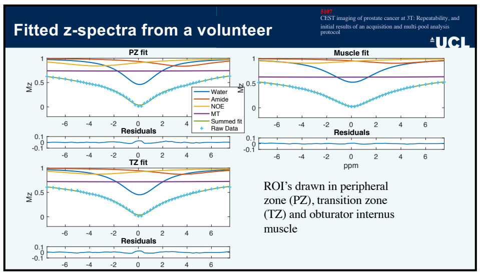

Fitted z-spectra from a volunteer

ROI's drawn in peripheral zone (PZ), transition zone (TZ) and obturator internus muscle

Intra-session Repeatability Correlation and Bland-Altman plots

5107
CEST imaging of prostate cancer at 3T: Repeatability, and initial results of an acquisition and multi-pool analysis protocol

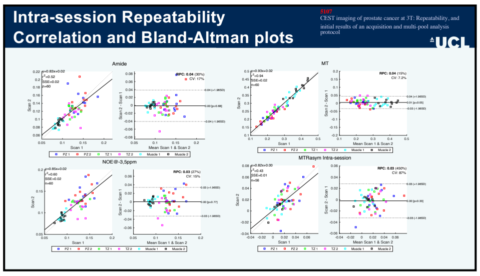

Inter-session Repeatability Correlation and Bland-Altman plots

5107
CEST imaging of prostate cancer at 3T: Repeatability, and initial results of an acquisition and multi-pool analysis protocol

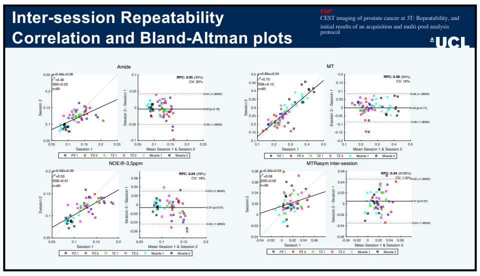

Coefficients of variation

5107
CEST imaging of prostate cancer at 3T: Repeatability, and initial results of an acquisition and multi-pool analysis protocol

UCL

	Intra-session COV	Inter-session COV
Amide	17%	20%
NOE	15%	16%
MT	7.2%	16%
MTRasym	87%	110%

In all cases, intra-session variability < inter-session variability

Tumour signal changes: Patient 1 – TZ tumour

5107
CEST imaging of prostate cancer at 3T: Repeatability, and initial results of an acquisition and multi-pool analysis protocol

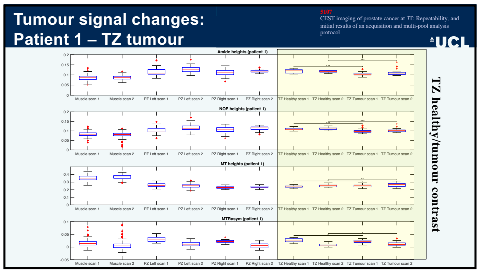

Tumour signal changes: Patient 2 – PZ tumour

5107
CEST imaging of prostate cancer at 3T: Repeatability, and initial results of an acquisition and multi-pool analysis protocol

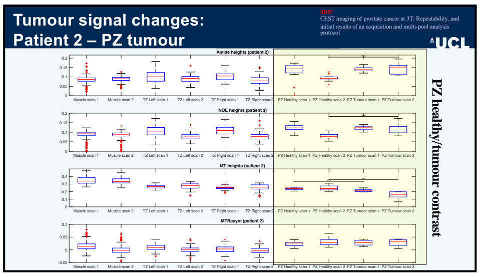

Tumor image contrast: Patient 1 TZ tumour

5107
CEST imaging of prostate cancer at 3T: Repeatability, and initial results of an acquisition and multi-pool analysis protocol

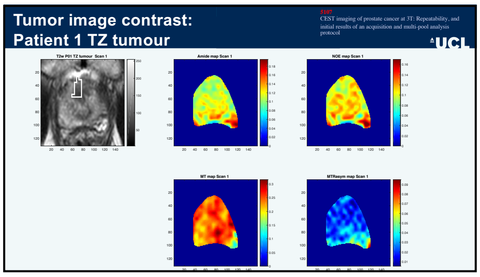

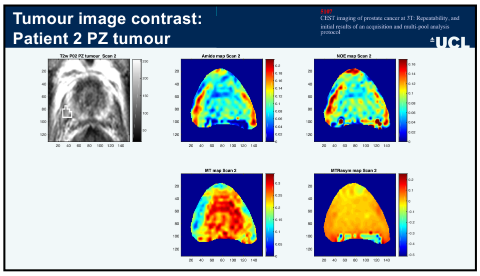

Tumour image contrast: Patient 2 PZ tumour

T2w P02 PZ tumour Scan 2
Amide map Scan 2
NOE map Scan 2
MT map Scan 2
MTRasym map Scan 2
20
40
60
80
100
120
140
250
200
150
100
50
0.2
0.18
0.16
0.14
0.12
0.1
0.08
0.06
0.04
0.02
0
0.3
0.25
0.15
0.05
0.1
-0.1
-0.2
-0.3
-0.4
-0.5

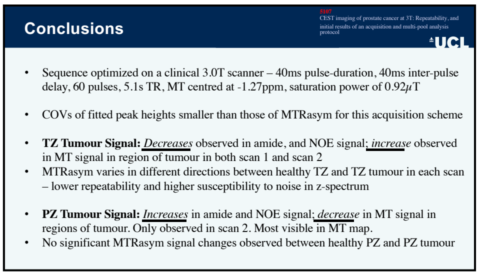

Conclusions

- Sequence optimized on a clinical 3.0T scanner – 40ms pulse-duration, 40ms inter-pulse delay, 60 pulses, 5.1s TR, MT centred at -1.27ppm, saturation power of 0.92μT

- COVs of fitted peak heights smaller than those of MTRasym for this acquisition scheme

- **TZ Tumour Signal:** *Decreases* observed in amide, and NOE signal; *increase* observed in MT signal in region of tumour in both scan 1 and scan 2
- MTRasym varies in different directions between healthy TZ and TZ tumour in each scan – lower repeatability and higher susceptibility to noise in z-spectrum

- **PZ Tumour Signal:** *Increases* in amide and NOE signal; *decrease* in MT signal in regions of tumour. Only observed in scan 2. Most visible in MT map.
- No significant MTRasym signal changes observed between healthy PZ and PZ tumour

Acknowledgements

CANCER RESEARCH UK

NHS
National Institute for Health Research

PHILIPS
Healthcare

IOP Institute of Physics

GLINT.
GLUCOCEST IMAGING IN NEOPLASTIC TUMOURS

Lead Author contact:
vincent.evans.14@ucl.ac.uk

13 Appendix C – ESMRMB 2017 (Barcelona) e-Poster

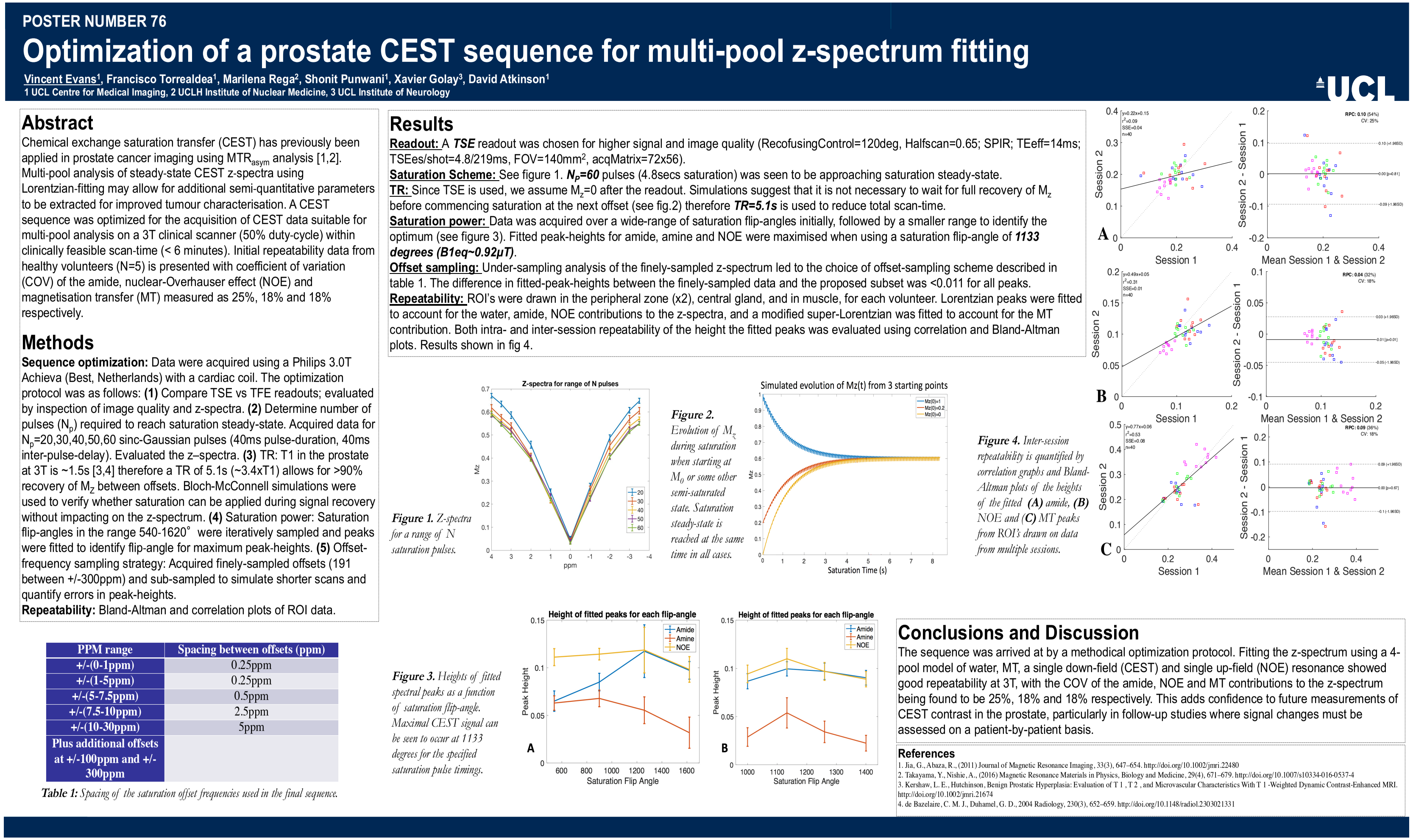

POSTER NUMBER 76

Optimization of a prostate CEST sequence for multi-pool z-spectrum fitting

Vincent Evans[1], Francisco Torrealdea[1], Marilena Rega[2], Shonit Punwani[1], Xavier Golay[3], David Atkinson[1]
1 UCL Centre for Medical Imaging, 2 UCLH Institute of Nuclear Medicine, 3 UCL Institute of Neurology

Abstract

Chemical exchange saturation transfer (CEST) has previously been applied in prostate cancer imaging using MTR_{asym} analysis [1,2]. Multi-pool analysis of steady-state CEST z-spectra using Lorentzian-fitting may allow for additional semi-quantitative parameters to be extracted for improved tumour characterisation. A CEST sequence was optimized for the acquisition of CEST data suitable for multi-pool analysis on a 3T clinical scanner (50% duty-cycle) within clinically feasible scan-time (< 6 minutes). Initial repeatability data from healthy volunteers (N=5) is presented with coefficient of variation (COV) of the amide, nuclear-Overhauser effect (NOE) and magnetisation transfer (MT) measured as 25%, 18% and 18% respectively.

Methods

Sequence optimization: Data were acquired using a Philips 3.0T Achieva (Best, Netherlands) with a cardiac coil. The optimization protocol was as follows: **(1)** Compare TSE vs TFE readouts; evaluated by inspection of image quality and z-spectra. **(2)** Determine number of pulses (N_p) required to reach saturation steady-state. Acquired data for N_p=20,30,40,50,60 sinc-Gaussian pulses (40ms pulse-duration, 40ms inter-pulse-delay). Evaluated the z–spectra. **(3)** TR: T1 in the prostate at 3T is ~1.5s [3,4] therefore a TR of 5.1s (~3.4xT1) allows for >90% recovery of M_z between offsets. Bloch-McConnell simulations were used to verify whether saturation can be applied during signal recovery without impacting on the z-spectrum. **(4)** Saturation power: Saturation flip-angles in the range 540-1620° were iteratively sampled and peaks were fitted to identify flip-angle for maximum peak-heights. **(5)** Offset-frequency sampling strategy: Acquired finely-sampled offsets (191 between +/-300ppm) and sub-sampled to simulate shorter scans and quantify errors in peak-heights.
Repeatability: Bland-Altman and correlation plots of ROI data.

PPM range	Spacing between offsets (ppm)
+/-(0-1ppm)	0.25ppm
+/-(1-5ppm)	0.25ppm
+/-(5-7.5ppm)	0.5ppm
+/-(7.5-10ppm)	2.5ppm
+/-(10-30ppm)	5ppm
Plus additional offsets at +/-100ppm and +/-300ppm	

Table 1: *Spacing of the saturation offset frequencies used in the final sequence.*

Results

Readout: A ***TSE*** readout was chosen for higher signal and image quality (RecofusingControl=120deg, Halfscan=0.65; SPIR; TEeff=14ms; TSEes/shot=4.8/219ms, FOV=$140mm^2$, acqMatrix=72x56).
Saturation Scheme: See figure 1. ***N_P=60*** pulses (4.8secs saturation) was seen to be approaching saturation steady-state.
TR: Since TSE is used, we assume M_z=0 after the readout. Simulations suggest that it is not necessary to wait for full recovery of M_z before commencing saturation at the next offset (see fig.2) therefore ***TR=5.1s*** is used to reduce total scan-time.
Saturation power: Data was acquired over a wide-range of saturation flip-angles initially, followed by a smaller range to identify the optimum (see figure 3). Fitted peak-heights for amide, amine and NOE were maximised when using a saturation flip-angle of ***1133 degrees (B1eq~0.92µT)***.
Offset sampling: Under-sampling analysis of the finely-sampled z-spectrum led to the choice of offset-sampling scheme described in table 1. The difference in fitted-peak-heights between the finely-sampled data and the proposed subset was <0.011 for all peaks.
Repeatability: ROI's were drawn in the peripheral zone (x2), central gland, and in muscle, for each volunteer. Lorentzian peaks were fitted to account for the water, amide, NOE contributions to the z-spectra, and a modified super-Lorentzian was fitted to account for the MT contribution. Both intra- and inter-session repeatability of the height the fitted peaks was evaluated using correlation and Bland-Altman plots. Results shown in fig 4.

Figure 1. *Z-spectra for a range of N saturation pulses.*

Figure 2. *Evolution of M_z during saturation when starting at M_0 or some other semi-saturated state. Saturation steady-state is reached at the same time in all cases.*

Figure 3. *Heights of fitted spectral peaks as a function of saturation flip-angle. Maximal CEST signal can be seen to occur at 1133 degrees for the specified saturation pulse timings.*

Figure 4. *Inter-session repeatability is quantified by correlation graphs and Bland-Altman plots of the heights of the fitted* ***(A)*** *amide,* ***(B)*** *NOE and* ***(C)*** *MT peaks from ROI's drawn on data from multiple sessions.*

Conclusions and Discussion

The sequence was arrived at by a methodical optimization protocol. Fitting the z-spectrum using a 4-pool model of water, MT, a single down-field (CEST) and single up-field (NOE) resonance showed good repeatability at 3T, with the COV of the amide, NOE and MT contributions to the z-spectrum being found to be 25%, 18% and 18% respectively. This adds confidence to future measurements of CEST contrast in the prostate, particularly in follow-up studies where signal changes must be assessed on a patient-by-patient basis.

References

1. Jia, G., Abaza, R., (2011) Journal of Magnetic Resonance Imaging, 33(3), 647–654. http://doi.org/10.1002/jmri.22480
2. Takayama, Y., Nishie, A., (2016) Magnetic Resonance Materials in Physics, Biology and Medicine, 29(4), 671–679. http://doi.org/10.1007/s10334-016-0537-4
3. Kershaw, L. E., Hutchinson, Benign Prostatic Hyperplasia: Evaluation of T 1 , T 2 , and Microvascular Characteristics With T 1 -Weighted Dynamic Contrast-Enhanced MRI. http://doi.org/10.1002/jmri.21674
4. de Bazelaire, C. M. J., Duhamel, G. D., 2004 Radiology, 230(3), 652–659. http://doi.org/10.1148/radiol.2303021331

14 Appendix D – BC-ISMRM 2016 (Leeds) Traditional Poster

POSTER B30

Improved fitting of CEST z-spectra using Bloch-McConnell simulations for the water peak

VINCENT EVANS[1], FRANCISCO TORREALDEA[1], MARILENA REGA[2], SHONIT PUNWANI[1], XAVIER GOLAY[3], DAVID ATKINSON[1]
1 UCL Centre for Medical Imaging; 2 UCLH Institute of Nuclear Medicine; 3 UCL Institute of Neurology

KEY POINTS

- Fitting the z-spectrum using a Lorentzian lineshape to account for the water resonance introduces significant errors in measurements of the heights of more clinically relevant fitted peaks (eg amides)
- An improved fitting method is suggested, where the water is modelled using a Bloch simulation
- This method produces more accurate height measurements and improved overall goodness of fit compared to the Lorentzian method when applied to data from simulations

INTRODUCTION

CEST is sensitive to the presence of endogenous molecules. Fitting to the CEST z-spectrum allows for semi-quantitative measurement of the contributions from overlapping and competing chemical groups on both side of the water resonance and provides more information than a simple asymmetry analysis. Pools have been modelled using Lorentzian lineshapes [1,2]. However, the pulsed-saturation schemes used on clinical scanners produce a complex 'zig-zag' behaviour of the water signal close to 0 ppm, see figures 1 and 2. Lorentzians do not account for this complexity and the current work proposes an improved fitting method using a Bloch-McConnell (BM) model for the water peak.

Methods

Simulations: Z-spectra were generated using a numerically-solved 2-pool (water and amide) BM model in Matlab. Saturation parameters: 60 sinc-Gaussian pulses, pulse duration = 40 ms, inter-pulse delay = 40 ms. Z-spectra were generated for a range of saturation flip-angles (900° to 1800°) with corresponding powers ($B1_{eff}$: 0.93μT to 2.08μT).

Fitting method A: Lorentzians for both water and amide pools.
Fitting method B: BM model for water, Lorentzian for amide.
Analysis: Compare fitted amide peak heights from each method to the height of the z-spectrum asymmetry at 3.5 ppm – which is taken to be the gold standard when modelling only two pools (water and amide). Mean absolute differences (MAD) of the fit residuals are calculated for the whole z-spectrum as a measure of the overall goodness of fit.

RESULTS

See figure 3.

Method A: Amide peak height over-estimates the asymmetry values in the studied range by up to 62% and shows a strong dependence on flip angle with 360° periodicity. Maximum MAD = 1.9%.

Method B: Amide peak height shows good agreement with the asymmetry value with a maximum deviation of 8.3%. Maximum MAD = 0.2%.

DISCUSSION

The results suggest that the 'zig-zag' effects cause sizeable deviations in the height of the fitted amide peak when using a Lorentzian for the water peak, and that the deviations are strongly dependent on flip-angle. Model-based fitting produces amide peak heights that are closer to the gold standard, and minimises fitting errors across the whole z-spectrum. Further testing will help to validate the approach in phantoms and in vivo with more pools.

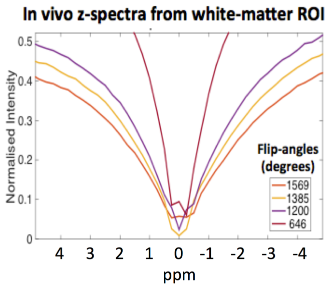

Figure 1 *Motivation for the current work. Zig-zag patterns close to 0 ppm observed in z-spectra from white matter*

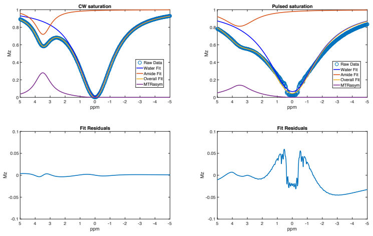

Figure 2 *Simulated z-spectra and fitted Lorentzians for a two pool model (water and amides) using both CW and pulsed saturation. There are sizeable residuals in the pulsed case.*

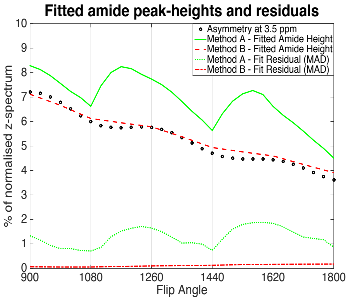

Figure 3 *Height of the fitted amide Lorentzians for a range of saturation flip angles and powers using both methods, along with the mean absolute difference of the fits. The asymmetry at 3.5ppm is taken as the gold standard for the fitted amide peak height.*

CONCLUSION

In simulations, using the Bloch-McConnell equations to fit the water peak reduces amide-peak fitting errors compared to the more conventional Lorentzian lineshape approach.

References

[1] Desmond KL et al. Magn Reson Med.2013;1853:1841–53 [2] Zaiß M et al.J Magn Reson.2011;211(2):149–55

Acknowledgements

The author acknowledges funding from Cancer Research UK (CRUK) through the Comprehensive Cancer Imaging Centre (CCIC) and the Department of Health's NIHR-funded Biomedical Research Centre at (University College London Hospitals).

15 Contributions from this work and funding

Publications, conference abstracts and other presentations stemming from this work are listed in Table 15-1.

Type	Reference	Contribution	Comments
Journal Article	"Optimization and repeatability of multi-pool chemical exchange saturation transfer MRI of the prostate at 3.0T"	Lead author	Article published in the *Journal for Magnetic Resonance Imaging* (JMRI) in February 2019. DOI: 10.1002/jmri.26690 Thesis chapters 4 and 5 are based on this work.
Journal Article (submission pending)	"Challenges in glucoCEST MR body imaging at 3 Tesla"	Contributing author	Article published in *Quantitative Imaging in Medicine and Surgery (QIMS)* in October 2019. DOI: 10.21037/qims.2019.10.05
Journal Article (submission pending)	"Translating pH-sensitive PROgressive saturation for Quantifying Exchange using Saturation Times (PRO-QUEST) MRI to a 3 T Clinical Scanner"	Contributing author	Manuscript accepted for publication in *Magnetic Resonance in Medicine (MRM)* in February 2020.
Conference Abstract	"Chemical Exchange Saturation Transfer imaging of prostate cancer at 3T: Repeatability, and initial results of an acquisition and multi-pool analysis protocol" Proc. Intl. Soc. Mag. Reson. Med. 26 (2018) Abstract 5107	Lead author	e-Poster presentation at ISMRM 2018, Paris. Thesis chapters 4 and 5 are based on this work. See appendix B for e-Poster.
Conference Abstract	"Optimisation of a prostate CEST MRI sequence for multi-pool analysis of z-spectra on a 3T clinical scanner" Magn Reson Mater Phy (2017) 30(Suppl 1): 1. https://doi.org/10.1007/s10334-017-0632-1 Abstract 76.	Lead author	Oral lightning talk and e-Poster at ESMRMB 2017, Barcelona. Chapter 4 is based on this work. See appendix C for e-Poster.
Conference Abstract	"Improved fitting of CEST z-spectra using Bloch-McConnell simulations for the water peak" 22nd Annual Scientific Meeting of the British Chapter of the International Society for Magnetic Resonance in Medicine, 2016.	Lead author	Traditional poster presentation with poster pitch at BC-ISMRM 2016, Leeds. See appendix D for poster.
Conference Abstract	"Translating pH-sensitive PROgressive saturation for Quantifying Exchange using	Contributing author	Presentation at ISMRM 2019, Montreal.

	Saturation Times (PRO-QUEST) MRI to a 3T Clinical Scanner" Proc. Intl. Soc. Mag. Reson. Med. 27 (2019) Abstract 2082		
Conference Abstract	"APT-CEST post Gadolinium. Should it be avoided? Comparison of pre- & post-Gadolinium CEST on glioma at 3T" Proc. Intl. Soc. Mag. Reson. Med. 26 (2018) Abstract 5109	Contributing author	Thesis chapter 8 is based on my contributions to this work.
Conference Abstract	"Understanding concomitant effects between CEST and ASL contrast" Proc. Intl. Soc. Mag. Reson. Med. 25 (2017) Abstract 0200.	Contributing author (named on presentation slides but not on abstract)	Thesis chapter 7 is based on my contributions to this work.
Conference Abstract	"Optimisation of glucoCEST MRI signal for applications in tumours" Magn Reson Mater Phy (2015) 28(Suppl 1): 277. https://doi.org/10.1007/s10334-015-0489-0 Abstract 440.	Contributing author	Poster presented by postdoc colleagues at ESMRMB 2015.
International Workshop	GlucoCEST in Neoplastic Tumours (GLINT) workshop 2017, Barcelona	Workshop attendee	Contributing the Horizon 2020 GLINT Project
International Workshop	GlucoCEST in Neoplastic Tumours (GLINT) workshop 2016, Vienna	Workshop attendee	Contributing the Horizon 2020 GLINT Project
Departmental Away Day Abstract	"Fitting the water direct saturation peak in the CEST z-spectrum: Lorentzian lineshapes vs Bloch simulations" Oral presentation at the UCL Institute of Neurology "Neuroradiology Away Day" 2017	Lead author	Abstract printed in "2017 Academic Away Day Report"
Departmental Away Day Abstract	"Optimisation of pulsed-saturation flip-angles for multi-pool endogenous CEST in vivo at 3T" Oral presentation at the UCL Institute of Neurology "Neuroradiology Away Day" 2016	Lead author	Abstract printed in "2016 Academic Away Day Report"
PhD Upgrade Presentation	Division of Medicine Seminar Programme, 11th March 2016	Presenting	-

Research Group Internal Presentation	Presentation at Centre for Medical Imaging (CMI) Research Meeting, 28th July 2015	Presenting	-

Table 15-1: *Contributions from this work.*

The work described in this thesis would not have been possible without the studentship provided via the Comprehensive Cancer Imaging Centre (CCIC) which is a collaboration between University College London and King’s College London. I was also generously funded on several occasions by the EU Horizon 2020 GLINT programme and by my supervisors David Atkinson, Xavier Golay and Shonit Punwani.